UCRL-LR-107524

The Radiative Properties and Optical Constants of Liquid Metals

Mark Alan Havstad
(Ph.D. Dissertation)

June 1991

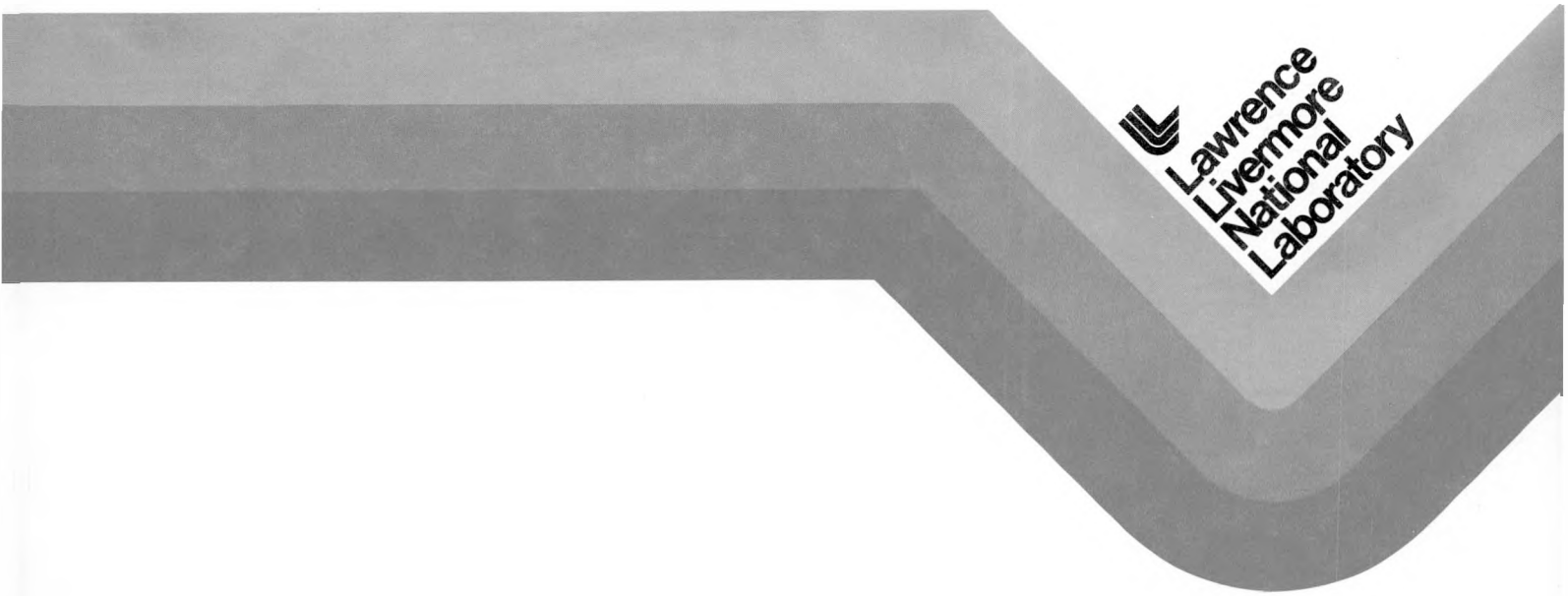

Work performed under the auspices of the U.S. Department of Energy by Lawrence Livermore National Laboratory under Contract W-7405-Eng-48.

Dist UCRL-LR--107524

DE91 016874

The Radiative Properties and Optical Constants of Liquid Metals

Mark Alan Havstad
(Ph.D. Dissertation)

Manuscript date: June 1991

LAWRENCE LIVERMORE NATIONAL LABORATORY
University of California • Livermore, California • 94551

THE RADIATIVE PROPERTIES AND OPTICAL CONSTANTS OF LIQUID METALS

A DISSERTATION

SUBMITTED TO THE DEPARTMENT OF

MECHANICAL ENGINEERING

AND THE COMMITTEE ON GRADUATE STUDIES

OF STANFORD UNIVERSITY

IN PARTIAL FULFILLMENT OF THE REQUIREMENTS

FOR THE DEGREE OF DOCTOR OF PHILOSOPHY

BY

MARK ALAN HAVSTAD

JUNE 1991

SIGNATURE PAGE

I certify that I have read this dissertation and that in my opinion it is fully adequate, in scope and quality, as a dissertation for the degree of Doctor of Philosophy.

Sidney A. Self (Principal Advisor)

I certify that I have read this dissertation and that in my opinion it is fully adequate, in scope and quality, as a dissertation for the degree of Doctor of Philosophy.

Steven J. Niksa

I certify that I have read this dissertation and that in my opinion it is fully adequate, in scope and quality, as a dissertation for the degree of Doctor of Philosophy.

Ronald K. Hanson

Approved for the University Committee on Graduate Studies:

Dean of Graduate Studies

Acknowledgment

This report is the Ph. D. thesis of the author who was advised by Professor Sidney A. Self. This work was funded by the Lawrence Livermore National Laboratory (LLNL).

I am most grateful to my advisor, Professor Self, for his guidance over the past five years. His review of this manuscript was particularly important to the successful completion of this work.

There are several co-workers here at LLNL whose assistance has been essential. Don Brown supported me over the long period which began after the initial most valuable results were obtained. Without Don the study would have been terminated in a very incomplete form.

Bill McLean insisted adamantly and correctly at the start that the only way to do this was in a way not yet attempted; with surface science tools. Bill then provided the tools and vigorously supported the effort to do a little good science within the rush of engineering development.

I wish to thank the Laser Isotope Separation Program at LLNL for their financial support. Originally Richard Stern was the programmatic proponent of this study but with managerial changes many others took his place.

In the initial stages of apparatus assembly, Thom Hawley's assistance was invaluable. His facility with mechanical design and vacuum practice were particularly helpful for building and modifying the apparatus.

The technical information department at LLNL has been very helpful with the manuscript and the figures. Sandy Bishop and Catherine Ulatowski skillfully prepared many of the figures.

Lastly, I thank my wife, Cindy, for patiently enduring the stress and disruption this undertaking has wrought over the past five years.

Abstract

Measurements of the optical constants and thermal radiative properties of three metals; tungsten (in the solid phase) and uranium and aluminum (both in the liquid phase) have been made using a new instrument which includes two independent optical systems and surface control and analysis capability. The two optical systems, one for measuring the complex index of refraction by ellipsometry, the other for measuring the normal spectral emissivity by direct comparison to an integral blackbody cavity, operate over the wavelength range 0.4 to 10 μm with sample temperatures between 940 and 1630 K.

The surface science capabilities of the instrument permit the preparation of high purity samples of known composition in-situ. The device includes two 5 KeV argon ion sputter guns, an ultra-high vacuum pumping system and an Auger spectrometer. The two sputter guns allow surface cleaning to occur while optical measurements are being made or while Auger spectroscopy is determining the surface composition of solid or liquid samples.

The ellipsometric optical system uses a novel radiation source (a carbon composite filament), refractive optics (CaF_2) and both calcite and wire grid polarizers to cover the extended wavelength range. The system for measuring the normal spectral emissivity uses reflective optics and an integral blackbody cavity which is located in the wall of the crucible holding the liquid sample. The use of two measurement techniques allows independent determinations of the normal spectral emissivity, and thus allows unbiased estimation of experimental errors.

The sensitivity of six techniques for determining the complex index of refraction of molten metals (including the ellipsometric method used here) is analyzed over the wavelength range of interest. It is shown that only methods measuring both the phase shift and the amplitude attenuation upon reflection provide adequate accuracy over the entire

spectral range of interest here. Methods measuring only amplitude attenuation on reflection, such as polarized reflectivity measurements at multiple angles, are shown to be sensitive only in the visible or from the ultra-violet to the near infrared, with their sensitivity declining rapidly with increasing wavelength in the infrared.

For tungsten, the measurements made using the two optical systems agreed well with each other and with previously published works. For aluminum, only the ellipsometric technique was employed, because the vapor pressure of aluminum prevented the use of sample temperatures high enough for accurate emissivity measurements, but these agreed well with expectations from the Drude model and with published results for the optical constants of molten aluminum. For uranium, for which published values for the optical constants of the liquid do not exist, the results from the two techniques agree well.

Table of Contents

Page

List of Tables

List of Figures

Nomenclature

a	term in the Fresnel equations
a_0,a_1,a_2,a_3	constants in fit of emissivity vs. wavelength
A	Area
b	term in the Fresnel equations
B	oscillator amplitude
c	speed of light
C	one component of the Stokes vector
C_1	the first radiation constant
C_2	the second radiation constant
C_3	the third radiation constant
D	damping constant
e	elementary charge
e	emissive power
E	energy
E	electric field vector
f	sputter rate
F	polarizer extinction ratio
g_1	polarizer transmission in pass direction
g_2	polarizer transmission in extinction direction
G	amplifier gain
h	Planck's constant
H	magnetic field vector
i	spectral radiance
i	imaginary number

I	electric current
I	intensity
I_o	reference intensity in ellipsometric technique
I_1,I_2,I_3,I_4	measured variables in ellipsometric technique
J	ion current density
k	extinction coefficient
K	Kelvin
K_{spr}	spring constant
L	detector sensitivity
m	mass
m"	complex index of refraction
M	one component of the Stokes vector
M	molecular mass
M_1,M_2	measured value in an ellipsometric technique
n	index of refraction
N	number density of gas molecules
N_e	number density of free electrons
p	pressure
P	cauchy principle value
P	power
P_h	peak height
P_{hn}	normalized peak height
q	number density of particles in a gas
Q	energy rate
Q_1,Q_2	measured variables in an ellipsometric technique
r	amplitude reflection coefficient
r_e	direct current electrical resistivity

R	sputter rate
R_o	outer radius
S	Poynting vector
S	one component of the Stokes vector
S_f	sensitivity factor
t	time
T	temperature
u	mean thermal molecular speed
U	degree of polarization
V	Voltage
x,y,z	rectilinear coordinates
x_1,x_2,x_3	dummy variables
Z	impedance

GREEK

α	absorptivity
$\alpha^{\wedge}$	attenuation coefficient
$\alpha\sim$	absorption coefficient
β	wave number
γ	damping factor
δ	phase angle

δ	skin depth
ε	emissivity
κ	boltzmann constant
ζ	azimuth angle of an ellipse
η	ellipticity of an ellipse
θ	angle
λ	wavelength
μ	permeability
μ_o	permeability of free space
υ	frequency in hertz
ρ	intensity reflection coefficient
ρ	mass density
$\rho\hat{}$	the ratio of amplitude reflection coefficients
$\rho\sim$	average of polarized reflectivities
ξ	degree of polarization
σ	Stefan-Boltzmann constant
σ	optical conductivity
σ_{dc}	direct current electrical conductivity
τ	mean collision time
χ	angle of refraction
Ψ	angle used in ellipsometry
Ψ_N	azimuth of analyzer in ellipsometry
Ψ_A	azimuth of polarizer in ellipsometry
ω	angular frequency in radians per second
Γ	gas molecule flux
Δ	relative phase shift on reflection
Θ	oscillator phase angle

Ω	solid angle
ϵ	real part of complex dielectric function
ϵ'	imaginary part of complex dielectric function
ϵ''	complex dielectric function
ϵ_0	permittivity of free space
ϕ	azimuthal angle
Φ	work function

SUBSCRIPTS

A	analyzer of ellipsometer
b	black body
dc	direct current
e	electronic
i	incident
imag	the imaginary part of a complex number
local	local rather than an average or macroscopic value
max	maximum value
n	normal
N	polarizer of ellipsometer
o	free space value
p	parallel component
pl	plasma
proj	projected
r	reflected

real	the real part of a complex number
res	resonance
s	perpendicular component
sam	sample
scat	scattered
spr	spring
sub	substitute
x,y,z	coordinate directions
x_o,y_o	amplitude along specified axis
λ	wavelength

SUPERSCRIPTS

b	blackbody
r	reflected
'	directional quantity, except when used with $\in$ when it signifies the imaginary part of a complex number
"	bidirectional quantity, except when used with $\in$ and m when it signifies a complex number
-	the mean value
$\rightarrow$	a vector quantity

1. Introduction

The thermal radiative properties of the surfaces of various metals at high temperature, both below and above the melting point, are of importance to a wide range of research and development activities, including laser welding, metal refining, electron beam processing, vacuum arc remelting, and laser isotope separation. These properties, namely the reflectivity, emissivity and absorptivity, influence the energy balance and heat transfer in such applications and thereby determine performance and even economic viability. Thermal radiative properties are often vital input data for heat transfer computations performed during development of a process. The accuracy of the input data determines the results of calculations that provide the understanding needed to make design changes and successfully complete development.

Accurate information is required on surface absorptivity, reflectivity, and emissivity as a function of wavelength, temperature, and angle relative to the surface normal. These properties are known to be strong functions of surface condition, such as oxidation, roughness, composition, and, for solids, crystalline orientation [1]. The depth to which such properties are sensitive to these conditions is determined by the skin depth, δ, which is directly proportional to the wavelength of the radiation and inversely proportional to the imaginary part of the complex refractive index, the extinction coefficient k [2].

In most prior studies of thermal radiative properties, insufficient attention has been paid to the surface condition. In the few instances where surfaces have been well characterized and controlled, the measurements have been made over narrow parameter ranges or only at low temperature. Studies of liquid metals are relatively rare and have most often been made in inadequate vacuum environment. Very low pressures [~10^{-9} torr, i.e., ultra-high vacuum (UHV)] are necessary in studies of molten metals because liquid metal surfaces are often highly reactive. A review of the reported work in this area leads to very low confidence in the results (because of the large scatter in the data) to the point where the results from various workers rarely agree within their stated uncertainty limits. Estimates of surface contamination based on the reported system pressures often indicate a high probability of inadequately controlled surface condition.

The present work began with two precepts. First, surface science techniques would be employed so that extreme sample purity could be produced, maintained, and quantitatively determined *in-situ*. Second, two independent measurement methods would be used to allow reliable error estimates to be made.

The focus on surface science led to the design of a UHV vacuum system having two ion sputter guns for surface cleaning and an Auger spectrometer for surface mass analysis. The focus on the use of two independent methods led to the selection of emissivity and ellipsometric optical techniques. The normal spectral emissivity apparatus employs an arrangement similar to systems commonly used for thermal radiative property studies, except for the crucible design and the blackbody cavity integral to it. The ellipsometric apparatus is, in principle, similar to others used in studies of the electronic structure of metals and alloys but it was designed to work over a wider spectral band than its predecessors. Commonly, ellipsometers are used over narrow spectral ranges to obtain the complex index of refraction of a surface at low or moderate temperatures. In this work,

metals at high temperatures (as high as 1630 K) have been studied over an extended wavelength range (0.4-10μm).

The present work applies these techniques to the study of the thermal radiative properties of three metals, tungsten, uranium, and aluminum. Tungsten was chosen because the large body of high quality data available could serve as a calibration check. Uranium was selected for its importance to a number of Department of Energy (DOE) programs and because of the paucity of reliable data on it. Aluminum is of interest because of its wide range of applications within DOE and in technology in general.

The interest in the optical properties as they influence heat transfer led to the choice of 0.4 to 10 μm as the wavelength range of interest. This range makes the results more generally useful than is typical, and can be reasonably accommodated with calcium fluoride (CaF_2) or reflective optics. The full angular range from $\theta = 0^o$ (normal to the surface) to 90^o (grazing incidence) was also studied. The tendency of the radiative property literature to be restricted to normal emission and near normal reflection makes much of such available data of limited value. In nearly all applications, off-normal and even oblique radiant properties can have a considerable impact on the results.

In summary, this work is unusual among studies of thermal radiative properties in four respects. First, high-temperature surface conditions have been controlled and measured with extreme care. Second, two independent measurement systems were used to permit unbiased estimation of errors. Third, a general measurement method (ellipsometry) has been applied over much wider parameter ranges than previously used. (Ellipsometry is a powerful general method because it yields a basic material property, the complex refractive index, from which thermal radiative properties can be calculated.) Fourth, the search for a general measurement method led to a more complete evaluation of the sensitivity of potential measurement techniques than has been reported to date.

1.1 Evolution of the experimental approach

This study began with efforts to obtain the emissivity and reflectivity of liquid uranium as functions of angle, wavelength and temperature. These quantities were to be measured relative to standards: a blackbody cavity and a reference reflector respectively. The first system for measuring emissivity compared sample emission to that from a separate blackbody but was abandoned due to its complexity and the difficulty of maintaining the sample and cavity at sufficiently similar temperatures. The crucible was subsequently redesigned to include an integral blackbody cavity. This improvement provided a greatly simplified and accurate system, although it only allowed determination of the sample emissivity as a function of wavelength in the normal direction.

The initial configuration for measurement of spectral reflectivity was also impractical, because of the curvature of the molten sample surface. In this first version, the variation in the optical signal through the instrument due to sample surface curvature could not be matched when the reference reflector replaced the sample.

The need for a reference reflector was eliminated in the second version of the reflectivity measurement scheme, which measured the ratio of the two polarized reflectivities, again as a function of angle relative to the surface normal. (The ratio of the polarized reflectivities was used to compute the desired absolute reflectivities using the Fresnel equations described in chapter 2). Although this second system was adequate in the visible spectrum, it had poor sensitivity in the infrared and it required computed corrections to the measurements (due to polarization produced by optical elements other than the sample). However, this second approach emphasized more fundamental aspects of the physics of reflection which led to the selection of the third and final system

employing an ellipsometric technique (where both the amplitude attenuation and the phase shift on reflection are measured). The ellipsometric technique was in many ways simpler than its predecessors and calculations of its sensitivity (see chapter 7) indicated it would be superior to the other options considered. This method yielded the optical constants of the reflecting substrate from which all of the thermal radiative properties can be calculated. For uranium, the results from this third system have agreed well with measurements of normal spectral emissivity and have been used extensively in development efforts for the laser isotope separation process at Lawrence Livermore National Laboratory (LLNL).

In summary, practical problems with the original scheme for measuring reflectivity led to a more fundamental and generally useful approach: the ellipsometric technique where the complex index of refraction was measured and from which the other quantities of interest could be computed.

1.2 Organization of the thesis

Chapters 2 through 6 present background material for the varied disciplines applied in this study. Chapter 2 includes the relevant fundamentals of electromagnetic theory and thermal radiation. Classical theories of the optical constants of solids are discussed in chapter 3. Although quantum band theory is now used to interpret measurements of the optical properties, the classical theories are useful in providing physical insight into the optical constants by using simple intuitive models. Chapter 4 describes the large body of previously reported work on measurement methods for the optical constants and thermal radiative properties of metals but leaves for chapter 5 a detailed description of the ellipsometric methods applied here.

Previously reported measurements of the optical constants and thermal radiative properties of the three metals treated here are described in chapter 6. For tungsten, the literature review focuses on the precision high temperature work which made it an attractive

material for checking the measurement techniques. For uranium, the review includes all of the reported citations in detail because so few works have treated this metal even cursorily. For aluminum, the review focuses on the reported measurements of the optical constants for the molten state. (More than 100 studies treating solid aluminum have been reported and well summarized [3].) The two principal citations [4,5] for liquid aluminum (which treat much of the wavelength range of interest in this study) are discussed in detail.

Following the background material of chapters 2 to 6, the subsequent five chapters describe new work. Chapter 7 presents calculations comparing the sensitivity of the measurement methods considered for use in this work. These computations assisted in both measurement technique selection and interpretation of the results. In chapter 8 the apparatus is described; the principal subjects being the optical systems and the surface science equipment. Chapters 9, 10 and 11 present the results of the measurements with tungsten, uranium and aluminum samples respectively. Extensive references are made to chapter 3 in the discussion of results because the classical optical theories provide useful insight. Chapter 12 summarizes the accomplishments of the study and describes areas where continuing work has begun or is warranted.

2. The theoretical basis of the optical properties of opaque surfaces

2.1 Electromagnetic theory and electromagnetic waves

Classical electromagnetic theory describes the propagation of electromagnetic waves in a medium in terms of its macroscopic electrical and magnetic properties. It predicts the velocity and absorption of such waves as well as their reflection and refraction at an interface between two media and hence provides the theoretical basis for methods of measuring the radiative properties of opaque surfaces in terms of the optical constants of the material.

Unlike longitudinal waves, e. g. sound waves in fluids, electromagnetic waves are transverse waves in which the electric and magnetic field vectors are perpendicular to each other and to the direction of propagation. Being transverse waves, they exhibit phenomena related to the polarization state of the wave.

2.1.1 Maxwell's equations. The basis of electromagnetic theory is the set of Maxwell's equations. For a homogenous, isotropic medium (neglecting space charge effects) they can be written in SI (mks) units:

$$\nabla \cdot \vec{H} = 0 \qquad \nabla \times \vec{E} = -\mu \frac{\partial \vec{H}}{\partial t}$$

$$\nabla \cdot \vec{E} = 0 \qquad \nabla \times \vec{H} = \epsilon \frac{\partial \vec{E}}{\partial t} + \frac{1}{r_e} \vec{E} \qquad (2\text{–}1)$$

Here E (V/m) and H (A/m) are the electric and magnetic field vectors, while ϵ (F/m), μ (H/m) and r_e (ohm-m) are respectively the permittivity, the permeability and the electrical resistivity of the medium. For an isotropic medium they are scalars which are

generally functions of frequency. For non-magnetic materials $\mu = \mu_o$, the vacuum permeability [6].

The term, $\epsilon \partial E/\partial t$, is the displacement current density, while (E/r_e) is the conduction current density due to the motion of free charges. Basically, Maxwell's curl equations state that a time varying electric field produces a spatially varying magnetic field and vice versa. This fact gives rise to solutions in the form of propagating waves.

Most materials can be classed as insulators (dielectrics) for which the electrical conductivity $(1/r_e) \sim 0$ or conductors (metals, semiconductors) containing free electrons for which $(1/r_e) \neq 0$. The former support undamped waves while in the latter case the waves are damped by absorption due to collisions of electrons with lattice defects and vibrations (phonons).

2.1.2 The general wave equation. By taking the time derivative of one of the Maxwell curl equations and the curl of the other, E (or H) may be eliminated to yield a general wave equation which both field vectors satisfy.

$$\nabla^2 \vec{E} = \epsilon \mu \frac{\partial^2 \vec{E}}{\partial t^2} + \frac{\mu}{r_e} \frac{\partial \vec{E}}{\partial t}$$

$$\nabla^2 \vec{H} = \epsilon \mu \frac{\partial^2 \vec{H}}{\partial t^2} + \frac{\mu}{r_e} \frac{\partial \vec{H}}{\partial t} \qquad (2\text{–}2)$$

The first order time derivatives imply damping of the wave.

For an insulator ($r_e \sim \infty$) and with no dielectric or magnetic loss (ϵ and μ purely real), the wave equations may be written:

$$\nabla^2 \vec{E} = \frac{1}{c^2} \frac{\partial^2 \vec{E}}{\partial t^2} \quad ; \quad \nabla^2 \vec{H} = \frac{1}{c^2} \frac{\partial^2 \vec{H}}{\partial t^2} \tag{2–3}$$

where $c = (\epsilon \mu)^{-1/2}$ is the (phase) speed of propagation.

The ratio

$$Z \equiv (E/H) = (\mu/\epsilon)^{1/2} \tag{2–4}$$

is the characteristic impedance (ohms) of the medium [7].

For vacuum, $\mu_o = 4\pi \times 10^{-7}$ (H/m), $\epsilon_o = 1/(c_o^2 \mu_o) \approx 8.85 \times 10^{-12}$ (F/m), $c_o \approx 2.998 \times 10^8$ m/s is the vacuum speed of light and $Z_o = 377$ ohms. The refractive index of the medium is defined by

$$n = c_o/c = (\epsilon \mu / \epsilon_o \mu_o)^{1/2} \tag{2–5}$$

and is in general a function of frequency.

2.1.3 Linearly-polarized, plane harmonic waves in lossless dielectrics. For a linearly-polarized plane harmonic wave propagating in the z direction we may take

$$\vec{E}_x = \vec{x} E_x \exp i(\omega t - \beta z) \quad ; \quad \vec{H}_y = \vec{y} H_y \exp i(\omega t - \beta z) \tag{2–6}$$

Here, E_x and H_y are the field amplitudes (independent of x and y), x and y are unit vectors, $\omega = 2\pi\upsilon$ is the angular frequency (υ being the frequency in hertz) and $\beta = 2\pi/\lambda$ is the wavenumber (λ being the wavelength).

Substituting these forms into the wave equation (2-3) we find $\omega^2 = \beta^2 c^2$, so that $c = (\omega/\beta) = \lambda\upsilon$, and $n = \lambda_o/\lambda$. Since, for a lossless dielectric, ϵ and μ are real positive quantities, β (and n) are real. The complex notation exp $i(\omega t - \beta z)$ can then be interpreted as

$$\cos(\omega t - \beta z + \delta) = \cos 2\pi(\upsilon t - z/\lambda + \delta) \qquad (2\text{–}7)$$

where δ is an arbitrary phase angle, being the same for both E_x and H_y. The positive root of $\beta^2 = \omega^2/c^2$ corresponds to waves propagating to +z, while the negative root corresponds to propagation to –z.

E_x and H_y are in phase as shown in the "snapshot" of Fig. 2-1. With increasing time the whole pattern moves along the z axis with the phase velocity c.

2.1.4 Linearly-polarized, plane harmonic waves in conducting media.

Substituting the assumed expression (2-6) for E_x and H_y into the general wave equations (2-2), we obtain

$$\beta^2 = \omega^2 \epsilon \mu (1 - i/\omega \epsilon r_e) \qquad (2\text{–}8)$$

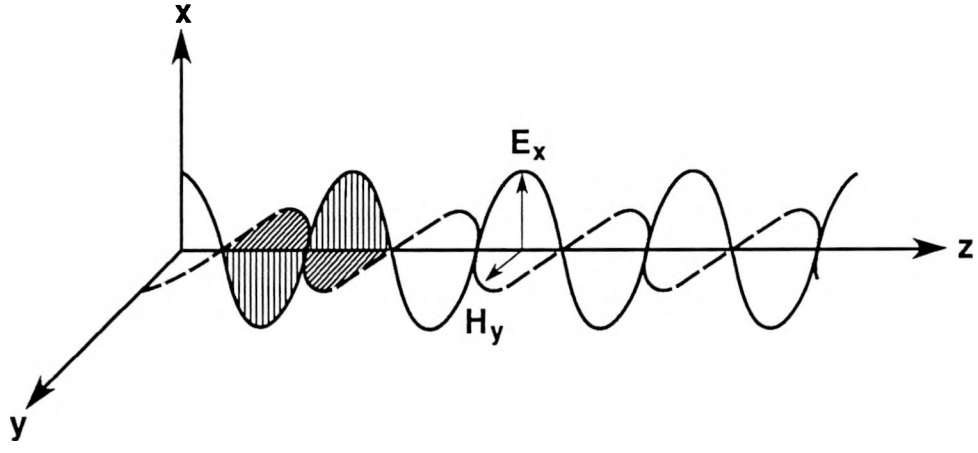

Fig. 2-1. A plane transverse wave propagating in the z direction. Amplitude oscillations are in the x and y directions.

To make the treatment for conductors formally identical to that for insulators, it is convenient to subsume the contribution of the conduction current into a complex permittivity defined by

$$\epsilon'' \equiv \epsilon - i\epsilon' \equiv \epsilon - i/\omega r_e \qquad (2\text{–}9)$$

(use of $\epsilon = \epsilon' + i\epsilon''$ is also common) so that

$$\beta^2 = \omega^2 \epsilon'' \mu \qquad (2\text{–}10)$$

Correspondingly, it is convenient to define a complex refractive index:

$$m'' \equiv (n - ik) \equiv (\epsilon'' \mu / \epsilon_o \mu_o)^{1/2} \qquad (2\text{–}11)$$

Here k is called the extinction coefficient and the real and imaginary parts (n,k) of the complex refractive index are known as the optical constants of the medium [8].

The real and imaginary parts of the complex permittivity and refractive index are related by

$$\epsilon = [\epsilon_o \mu_o / \mu][n^2 - k^2] \; ; \; \epsilon' = [\epsilon_o \mu_o / \mu][2nk] \qquad (2\text{–}12)$$

Moreover, the optical constants (n,k) are given in terms of the electrical and magnetic properties of the medium [9] by:

$$n^2=\frac{\epsilon\mu c_o^2}{2}\{+1+[1+(\omega\epsilon r_e)^{-2}]^{1/2}\}$$

$$k^2=\frac{\epsilon\mu c_o^2}{2}\{-1+[1+(\omega\epsilon r_e)^{-2}]^{1/2}\} \qquad (2\text{–}13)$$

Clearly in (2-10), the wavenumber β is also complex and given by

$$\beta=\omega(\epsilon''\mu)^{1/2}=\omega(\epsilon_o\mu_o)^{1/2}m''=(\omega/c_o)(n-ik) \qquad (2\text{–}14)$$

The wave dependence on z and t can then be written

$$\exp i(\omega t-\beta z)=\exp(-\omega kz/c_o)\cos(\omega t-\omega nz/c_o+\delta)$$
$$\equiv\exp(-\hat{\alpha}z)\cos 2\pi(\upsilon t-z/\lambda+\delta) \qquad (2\text{–}15)$$

Here $\alpha\hat{}$ (m^{-1}) is the attenuation coefficient for the wave amplitude, and $1/\alpha\hat{}$ is the distance in which the amplitude is attenuated by a factor 1/e. However, because at optical frequencies, radiation detectors measure the power in the wave, which is proportional to the square of the wave amplitude (see sec. 2.1.6 below), the power is attenuated as $\exp(-\tilde{\alpha}x)$ where $\tilde{\alpha}=2\alpha\hat{}$. Here, $\tilde{\alpha}$ (m^{-1}) is known as the absorption coefficient, given by

$$\tilde{\alpha}=2\omega k/c_o=4\pi k/\lambda \qquad (2\text{–}16)$$

Its inverse is known as the skin depth

$$\delta=\frac{\lambda}{4\pi k} \qquad (2\text{–}17)$$

2.1.5 Polarization state of plane waves. In the above, a linearly-polarized plane harmonic wave was considered having its electric vector directed along the x axis. Equally well the electric vector could have been taken along the y axis. In fact, the wave equation admits of two linearly-independent solutions, so the general solution for a plane harmonic wave may be taken as

$$\vec{E}=\vec{x}\,E_x\cos(\omega t-\beta z+\delta_x)+\vec{y}\,E_y\cos(\omega t-\beta z+\delta_y) \qquad (2-18)$$

Here E_x,E_y and δ_x, δ_y are arbitrary constants [10].

If $(\delta_x - \delta_y) = 0,\pi$ the two component waves can be combined to form a single linearly-polarized wave with amplitude $(E_x^2 + E_y^2)^{1/2}$ oriented at an (azimuth) angle $\Psi = \arctan(E_y/E_x)$ as shown in Fig. 2-2. If however, $E_x = E_y$ and $(\delta_x - \delta_y) = (\pi/2,3\pi/2)$, the combined wave is circularly polarized. The electric vector of constant amplitude rotates about the z axis with angular frequency ω, while at a given instant it rotates along z with pitch equal to the wavelength. The sense of rotation is right or left handed depending on whether the phase difference is $\pi/2$ or $3\pi/2$.

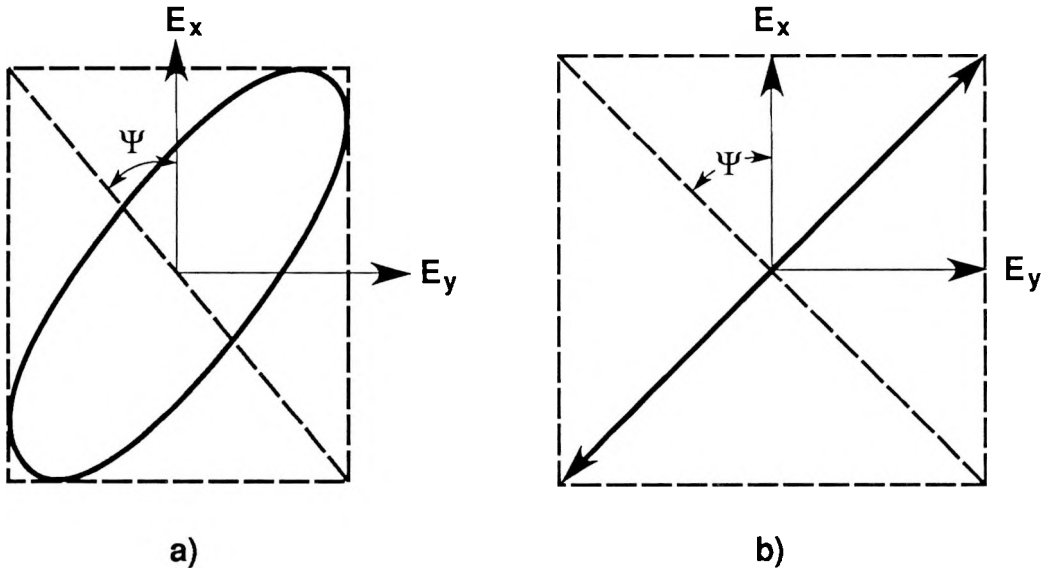

Fig. 2-2. Elliptical and linear polarization.

In the general case when $E_x \neq E_y$ and $(\delta_x - \delta_y) \neq m\pi/2$ (m = 0,1,2,3), the wave is elliptically polarized. As shown in Fig. 2-2, the electric vector rotates with angular frequency ω, while its length varies periodically, tracing out an ellipse in the (x,y) plane. Elliptical polarization, characterized by its handedness, ellipticity and azimuth is the general case of a plane harmonic wave; circular and linear polarization are special cases.

Of course, a harmonic (i.e. monochromatic) wave is an abstraction which, however, is closely approximated in some gas lasers. Radiation from a narrow spectral line (e.g. from a low pressure glow discharge lamp) may be termed quasi-monochromatic. In this case the amplitude E_x and E_y vary slowly with time (compared to the wave period). However, over long times (wave periods) the amplitudes fluctuate in some manner which is more or less correlated.

So called natural light i.e. broad band radiation from an incandescent source, is completely uncorrelated (unless passed through a very narrow band filter) and is said to be unpolarized (or randomly polarized). Over long times the vibration ellipse varies over all shapes, and orientations.

2.1.6 Energy and power flow (the Poynting vector). The rate of energy flow per unit area in an electromagnetic wave is described by the Poynting vector, **S**

$$\vec{\mathbf{S}} = \vec{E} \times \vec{H} \tag{2–19}$$

The direction of **S** gives the direction of energy flow [11]. The instantaneous values of E and H at a given point determine the instantaneous magnitude and direction of **S**, but most often an average of **S** taken over one or more cycles of the wave is of greater interest. Any measurement of wave energy arriving at a detector yields such an average **S**

$$\bar{S} = \frac{1}{2} E_x H_y \qquad (2\text{–}20)$$

where E_x and H_y are the amplitudes of the two vectors. Since the intrinsic impedance of a medium relates the E and H vectors, as described in sec 2.1.3, the Poynting vector can be written in terms of E or H alone. Because the magnetic forces and polarization caused by the oscillating magnetic fields in traveling electromagnetic waves are very small at optical frequencies it is typical to write the Poynting vector in terms of just the electric field vector. The energy flux expressed in this way is of particular interest in ellipsometry and thermal radiative property studies because radiation detectors sense the energy arrival rate per unit time.

2.1.7 The Kramers-Kronig relations. The Kramers-Kronig equations are integral relations which relate the real and imaginary parts of the complex index of refraction (or dielectric constant) to each other. These equations follow from 1) the causal relation between the polarization within a material and the electric field and 2) the fact that the complex refractive index is an analytic function. The relations express mathematically the fact that an appropriate integration over all frequencies of one part of the complex function yields the other part. These relations can be written in various forms of which the most basic is:

$$n(\omega) = 1 + \frac{2}{\pi} \mathbf{P} \int_0^\infty \frac{\omega' k(\omega') \, d\omega'}{\omega'^2 - \omega^2}$$

$$k(\omega) = \frac{-2\omega}{\pi} \mathbf{P} \int_0^\infty \frac{n(\omega') \, d\omega'}{\omega'^2 - \omega^2} \qquad (2\text{–}21)$$

where **P** indicates the Cauchy principal value of the integral and ω is the angular frequency. In practice one never obtains either part of the analytic function over the full spectral range but when one is obtained over a large enough spectral interval, the Kramers-Kronig relations can be applied to give the other part. The Kramers-Kronig relations and their applications are more fully treated in many publications [12,13,14].

2.1.8 The Hagen-Rubens relations. The Hagen-Rubens relations describe the interaction of electromagnetic waves and conducting materials at long wavelengths. These relations were derived theoretically by Drude [15] and confirmed experimentally by Hagen and Rubens [16]. At low frequencies (or long wavelengths), the components of the complex index of refraction become equal and >> 1. The equivalence of the refractive index components leads to the following result:

$$n = k = (\lambda_o \mu_o c_o / 4\pi r_e)^{1/2} \qquad (2\text{–}22)$$

For λ_o in m and r_e in ohm-m a simpler form is:

$$n = k = (30\lambda_o / r_e)^{1/2} \qquad (2\text{–}23)$$

This relation is sometimes accurate at wavelengths as small as 2 μm but agreement should not be expected until well beyond 10 μm. Derivation of the Hagen-Rubens approximation from classical theories of the optical constants is treated in chapter 3.

2.1.9 Plane wave reflection and refraction. The reflection and refraction of light waves are familiar phenomena. Consider a plane wave incident on a planar interface between two materials as represented in Fig. 2-3. The interface normal and the

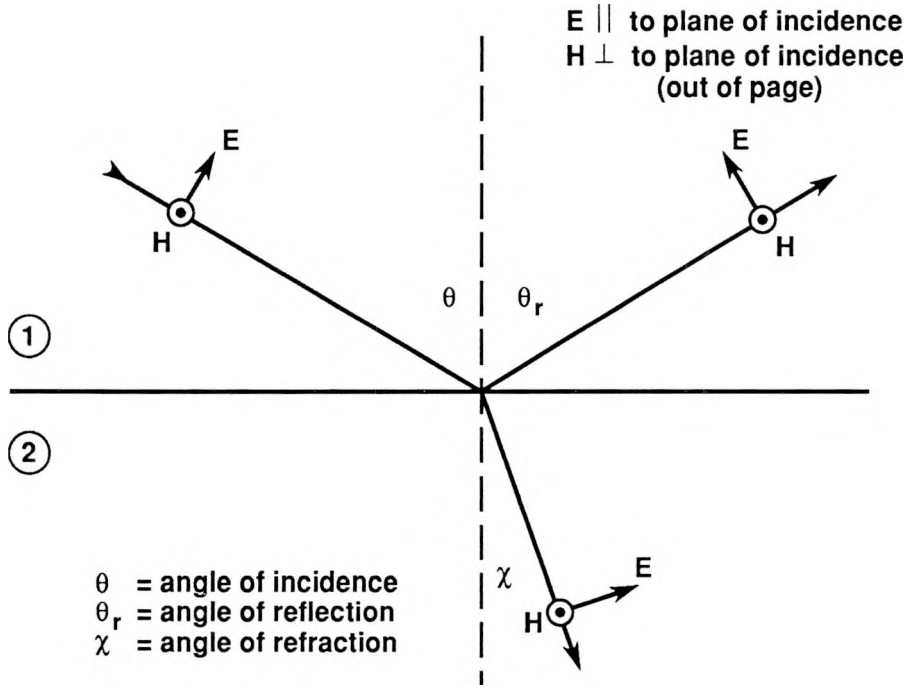

Fig. 2-3. Plane wave reflection with incident electric field vector parallel to plane of incidence.

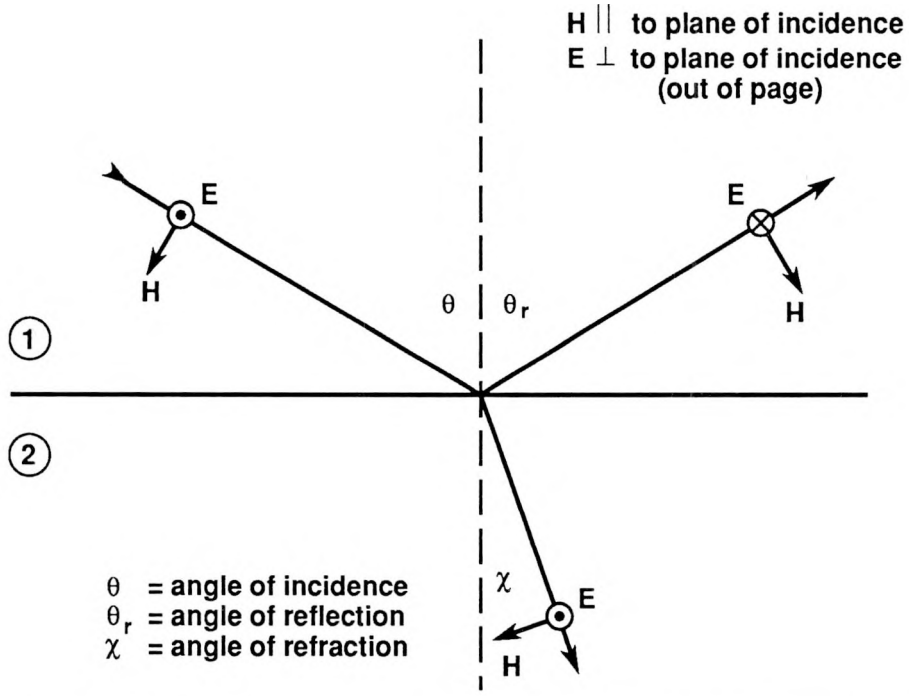

Fig. 2-4. Plane wave reflection with incident electric field vector perpendicular to plane of incidence.

direction of wave propagation define the plane of incidence and for a smooth interface both the reflected and refracted beams lie in this plane. It is common to distinguish two cases with the electric vector of the incident wave either parallel or perpendicular to the plane of incidence. The two sets of results are denoted p and s for parallel and perpendicular (s from the german word senkrecht for perpendicular). Figures 2-3 and 2-4 show the incident, reflected and refracted waves for the two cases. The properties of the reflected and refracted waves are determined by the polarization of the incoming wave, the complex indices of refraction of the materials on either side of the interface, the angle of incidence and the boundary conditions. Applying the boundary conditions that the components of E and H parallel to the surface are continuous across the interface, it can be shown that the amplitude reflection coefficients for the two polarizations are given by:

$$r_{\lambda,p} = \frac{E_p^r}{E_p} = \frac{\cos\theta / \cos\chi - (n_1 - ik_1)/(n_2 - ik_2)}{\cos\theta / \cos\chi + (n_1 - ik_1)/(n_2 - ik_2)}$$

$$r_{\lambda,s} = \frac{E_s^r}{E_s} = \frac{\cos\chi / \cos\theta - (n_1 - ik_1)/(n_2 - ik_2)}{\cos\chi / \cos\theta + (n_1 - ik_1)/(n_2 - ik_2)} \qquad (2\text{–}24)$$

where θ is the angle of incidence, χ is the angle of refraction and the superscript r denotes the reflected wave [9]. The subscript λ indicates r depends on wavelength because in general n and k are functions of wavelength. These equations relate the incident and reflected electric field vector amplitudes. For the familiar case of an incident wave in vacuum striking a metal substrate, the refracted wave is damped rapidly and the reflected wave amplitude is less than but comparable to that of the incident wave.

2.1.10 Amplitude reflection by perfect dielectrics (k=0). For reflection by dielectrics (non-conductors or insulators) from incidence in vacuum (or air), $n_1 = 1$ and $k_1 = 0$, Snell's law describes the bending of the incident rays toward the surface normal.

$$n_1 \sin\theta = n_2 \sin\chi \tag{2–25}$$

The special case of normal incidence does not display bending. For incidence from the dielectric to vacuum or any medium of lower index of refraction the bending is away from the surface normal and increases with angle of incidence until a critical value is reached, when $\chi = \pi/2$. Beyond this angle of incidence there is no refracted wave and total internal reflection occurs. Figures 2-5 and 2-6 display these phenomena for a typical insulator (n = 1.5,k = 0). The negative values for amplitude reflection correspond to phase changes of π on reflection (These are immaterial to the reflected intensity which depends on the amplitude squared) [17]. The angle at which the parallel polarized reflectivity passes through zero is termed the Brewster angle.

The relations for the amplitude reflection coefficients can also be written in terms of the angle of incidence and the angle of refraction:

$$r_{\lambda,p} = \frac{\tan(\theta - \chi)}{\tan(\theta + \chi)} \quad ; \quad r_{\lambda,s} = \frac{-\sin(\theta - \chi)}{\sin(\theta + \chi)} \tag{2–26}$$

These forms are equivalent to the general form (2-24).

2.1.11 The Fresnel equations. The results, (2-24), for the amplitude reflection coefficients, when squared, yield the intensity reflection coefficients. The results of this operation (for incidence from vacuum) are termed the Fresnel equations:

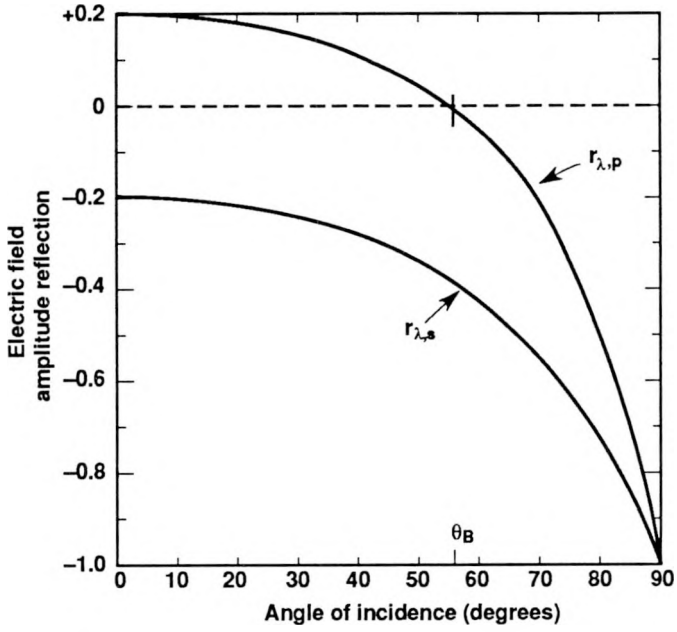

Fig. 2-5. Amplitude reflection coefficients for light incident from air on a dielectric with n = 1.5. The Brewster angle θ_B marks where the reflection of the parallel component is zero.

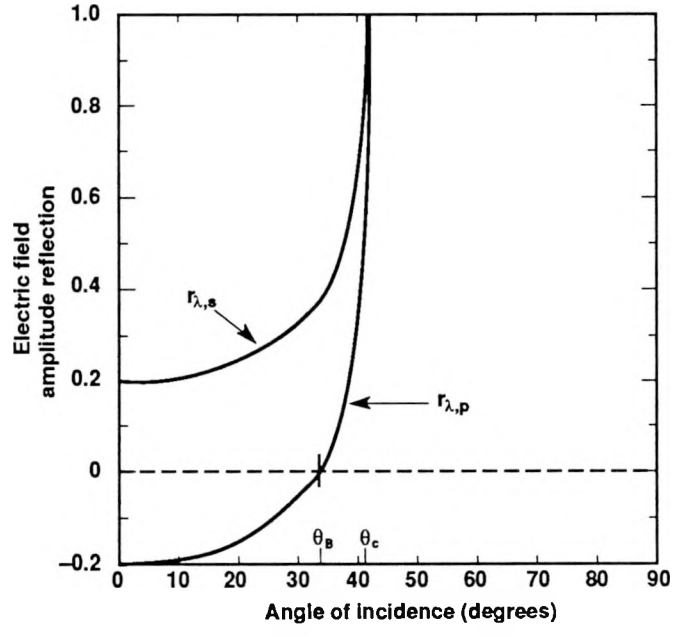

Fig. 2-6. Amplitude reflection coefficients for light incident from a dielectric to air (internal reflection). The dielectric has n, index of refraction, = 1.5. The critical angle, θ_C marks where total internal reflection occurs for both components of polarization. The Brewster angle, θ_B , marks where the parallel polarized component is zero.

$$\rho_{\lambda,p} \equiv r^2_{\lambda,p}(\lambda,\theta) = \frac{a^2 + b^2 - 2a\sin\theta\tan\theta + \sin^2\theta\tan^2\theta}{a^2 + b^2 + 2a\sin\theta\tan\theta + \sin^2\theta\tan^2\theta} r^2_{\lambda,s}$$

$$\rho_{\lambda,s} \equiv r^2_{\lambda,s}(\lambda,\theta) = \frac{a^2 + b^2 - 2a\cos\theta + \cos^2\theta}{a^2 + b^2 + 2a\cos\theta + \cos^2\theta}$$

where $2a^2 = [(n^2 - k^2 - \sin^2\theta)^2 + 4n^2k^2]^{1/2} + (n^2 - k^2 - \sin^2\theta)$

and $2b^2 = [(n^2 - k^2 - \sin^2\theta)^2 + 4n^2k^2]^{1/2} - (n^2 - k^2 - \sin^2\theta)$ (2–27)

Figures 2-7 and 2-8 display these reflection coefficients for material parameters typical of insulators and metals respectively. The Brewster and pseudo-Brewster angles define the angles where the reflected light has a zero or a minimum respectively in the parallel component of reflectivity. For randomly polarized incident light, the reflected light is partially polarized since the two polarized reflectivities are unequal (except at normal incidence).

For normal incidence, the reflectivities are:

$$\rho_p = \rho_s = \frac{(n-1)^2 + k^2}{(n+1)^2 + k^2} \tag{2–28}$$

For heat transfer purposes, however, the effects of polarization are most often neglected and the average of the two polarized reflectivities is used:

$$\tilde{\rho_\lambda} = \frac{1}{2}(\rho_{\lambda,p} + \rho_{\lambda,s}) \tag{2–29}$$

2.1.12 Practical aspects of optical reflection. The Fresnel equations consider an idealized reflection interface. The vacuum to material boundary is assumed to

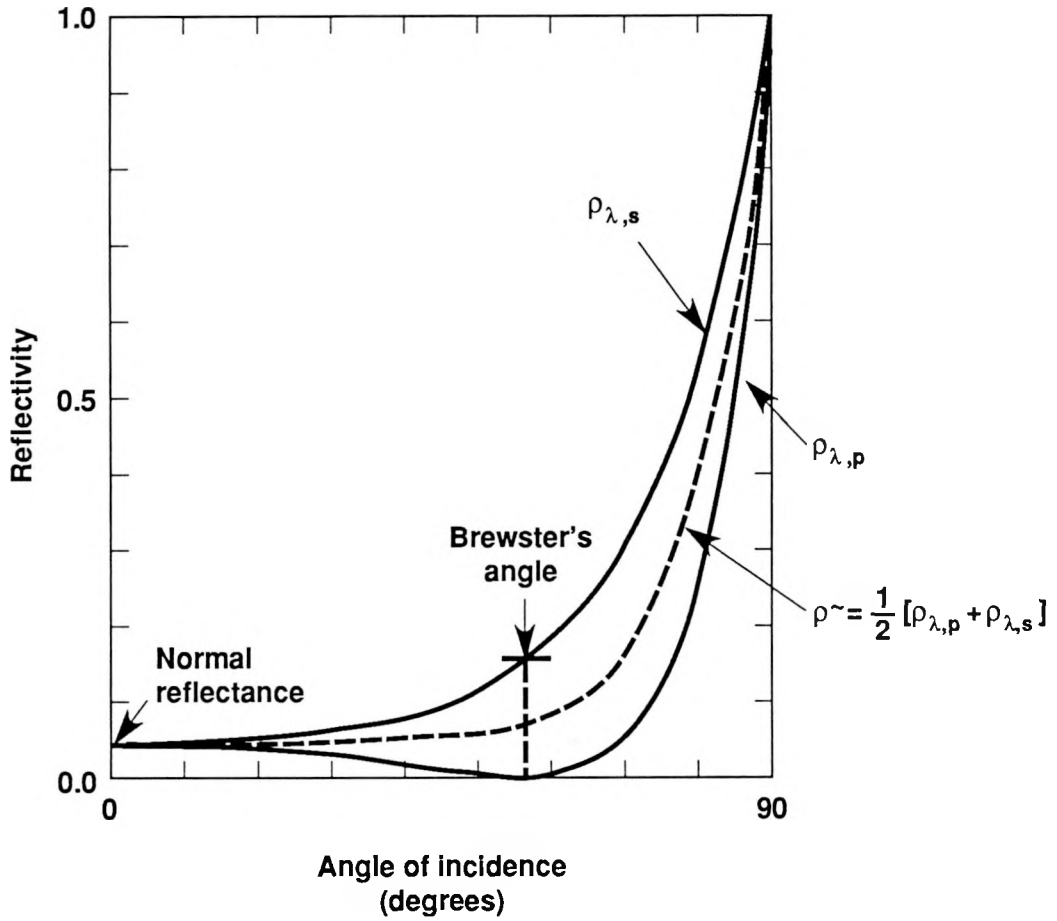

Fig. 2-7. Reflectivity vs angle typical of dielectrics. (n=1.5,k=0)

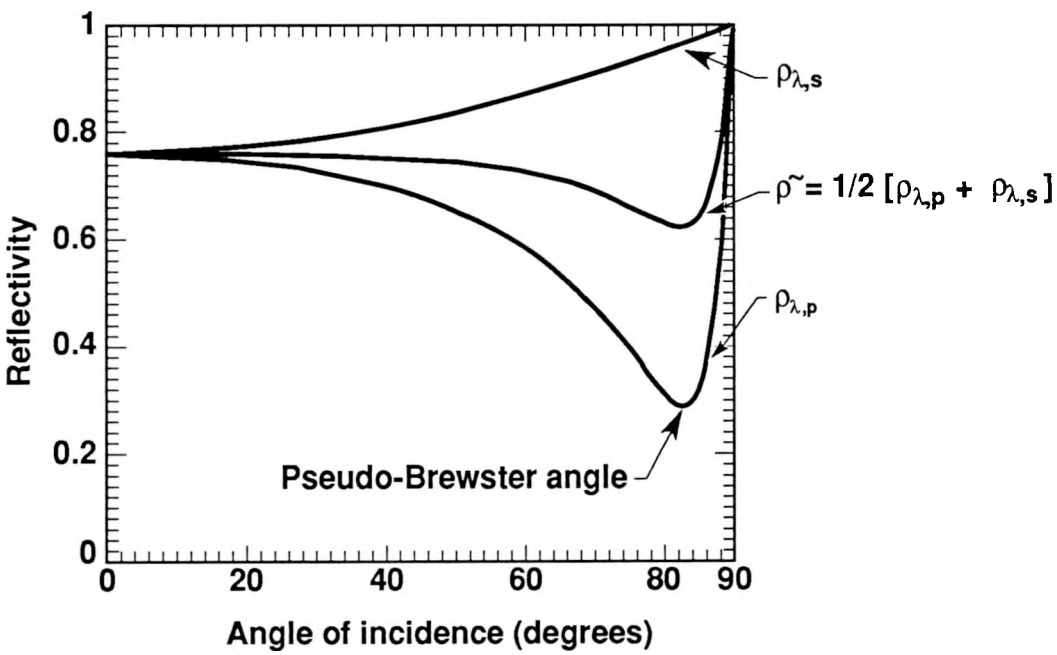

Fig. 2-8. Reflectivity vs angle typical of metals. (n=4.25,k=6.62)

be perfectly smooth, whereas real surfaces have varying degrees of roughness (down to the atomic level). The effects of surface roughening on reflection measurements have been addressed by numerous studies [18,19,20,21]. Roughening tends to increase absorption and decrease reflectivity. It causes a spreading of the reflected light about the specular angle, i.e. scattering which can be distinguished from specular reflection. For liquids, of particular interest to this thesis, roughness is not a consideration provided there are no mechanical vibrations of the sample surface which lead to fluid wave motion at the liquid-vacuum interface.

The Fresnel equations also assume that the vacuum to material interface is sharp and that the material properties, n and k, begin at the interface and are constant with depth into the material. One might expect a transition distance because the surface atoms have no neighboring atoms on their surface side while all of the sub-surface atoms possess a full array of neighbors on all sides. It is known that atomic spacing influences lattice properties and therefore the optical constants [22] and the lack of a full set of neighbors makes the surface atom spacings atypical.

The Fresnel equations, as given here, also assume an isotropic material, which leads to a dependence only on θ (the polar angle) in the results for the polarized reflectivity. Most real materials are not isotropic so that a full description of their properties also involves the azimuthal angle. In the following work, the azimuthal angle is dropped from the notation for simplicity.

The principal way in which real materials are not isotropic is in crystallinity. Metallic solids are commonly polycrystalline. The individual crystals are oriented randomly and their sizes vary from μm to even several millimeters across. Polycrystalline grain effects influence the results of radiant property measurements. For the special case of a single crystal sample the refractive index must be regarded as a tensor. It is well known that electronic band structure is a strong function of direction within the crystal lattice so that one expects optical absorption and therefore reflection to be strongly

dependent on the orientation of the crystal lattice relative to the vacuum to material surface interface[23,24].

Most real surfaces are thinly covered with a layer of foreign atomic species determined by the material's processing history and present environment. The thickness and composition of this layer, often an oxide, can have great influence on the optical properties of an interface. It is the lack of control of such surface layers which has made much of the reported radiant property work of questionable value, especially at high temperatures.

Many of the problems arising from real surface effects are not found when treating liquid samples. Surface roughness is eliminated if the sample is not vibrating. Grain boundaries, a principal cause of surface roughness with polished solid samples are absent. The amorphous condition of the liquid material in the bulk makes the subsurface region essentially isotropic. With liquids, thin surface oxides are often visible as they migrate over the surface or break up when the sample is intentionally vibrated. A non-ideality particular to liquids is the meniscus where the surface contacts a solid boundary. This problem is actually a practical one to be addressed by the optical system rather than a fundamental aspect related to the assumptions inherent in the Fresnel equations. For molten samples which wet the solid crucibles (pool diameter ~6 mm) described in this work, vacuum to material surface curvature is small. This issue will be more thoroughly discussed in the sections describing the optical system.

2.2 Blackbody radiation

2.2.1 The definition of a blackbody. A blackbody is a theoretical construct with special ideal properties: it reflects no incident radiation and emits the maximum possible radiation from its surface as determined by the Planck function (to be given later). All incident radiation is absorbed internally by a blackbody so that it is an ideal absorber for

all wavelengths of incoming radiation and for all angles of incidence. Similarly, the emission from a blackbody is the maximum possible in all directions and at all wavelengths. Real surfaces display less emission than ideal at all wavelengths and in all directions and exhibit non-zero reflection. The blackbody concept is useful to heat transfer analysis and the laboratory approximation of blackbody radiation is useful for thermal radiation measurements. The device employed to produce a laboratory approximation of a blackbody is shown in Fig. 2-9. The cavity walls are often coated with highly absorbing paint. An opening whose area is small compared to the total cavity wall area allows radiation to enter and to escape. Blackbody radiation is necessarily isotropic because a lack of isotropy implies less than maximum in a particular direction [9].

The notation of Siegel and Howell [9] is followed here, i. e. a subscript λ indicates a spectral quantity, a superscript b indicates a blackbody quantity and a superscript ' indicates a directional quantity.

2.2.2 Spectral radiance. In general, a radiation field consists of electromagnetic waves distributed continuously over wavelength and direction of propagation and it is impractical to decompose it into separate monochromatic plane waves specified by their electric and magnetic field vectors. Instead, the radiation field at a given spatial location is specified in terms of its spectral radiance (also known as its spectral intensity in older texts).

The spectral radiance i_λ' is defined as the radiant power flux per unit wavelength range per unit solid angle in a given direction specified by its polar and azimuthal angles (θ,ϕ) relative to a spherical coordinate system (shown in Fig. 2-10) and per unit

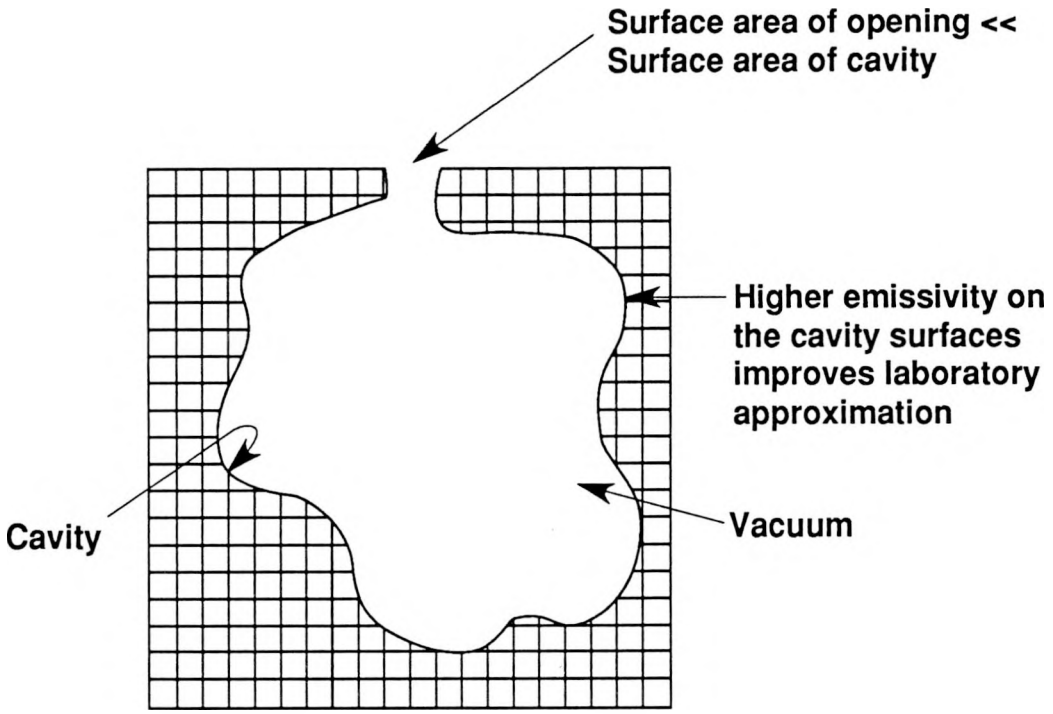

Surface temperature is uniform so that radiation emitted from infinitesimal opening is isotropic and in equilibrium with cavity walls

Fig. 2-9. Schematic representation of a blackbody cavity.

projected area normal to the (θ,ϕ) direction. For an elementary area dA, a wavelength interval λ to $(\lambda + d\lambda)$, a solid angle $d\Omega = \sin\theta\, d\theta d\phi$, and a power flux dP^b the spectral radiance is:

$$i'_\lambda(\lambda,\theta,\phi) \equiv \frac{dP}{dA\cos(\theta)\, d\Omega\, d\lambda} \tag{2–30}$$

Convenient units of spectral radiance are watts $m^{-2}(\mu m)^{-1}Sr^{-1}$. The projected area in the denominator of (2-30) is given by:

$$dA_p = dA\cos(\theta) \tag{2–31}$$

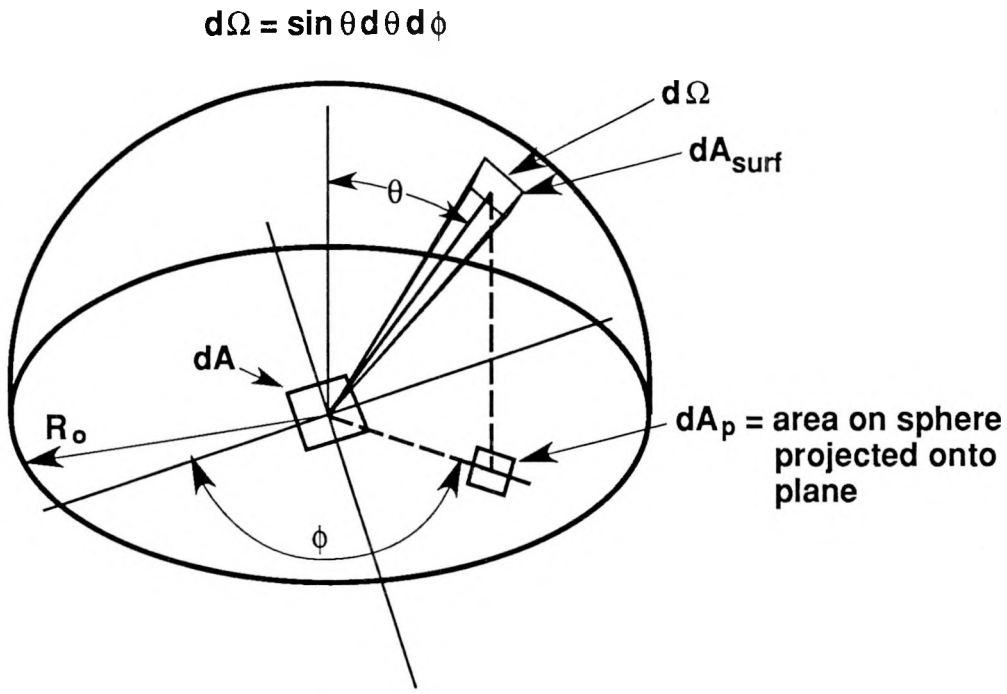

Fig. 2-10. The polar coordinate system relative to a surface area element dA.

2.2.3 Blackbody spectral radiance. A blackbody emits the maximum possible radiation in every direction and at all wavelengths as determined by its temperature. This emitted radiation can be characterized by its spectral radiance, i_λ^b:

$$i_\lambda^b(\lambda,T) \equiv \frac{dP^b}{dA\cos(\theta)\,d\Omega\,d\lambda} \tag{2-32}$$

The total radiance of a blackbody is the integral over all wavelengths of the spectral radiance:

$$i^b(T)=\int_o^\infty i_\lambda^b(\lambda,T)d\lambda \tag{2-33}$$

2.2.4 Blackbody emissive power. The definition of spectral emissive power uses actual rather than projected surface area so its relation to spectral radiance is given by:

$$e_\lambda^b(\theta,T,\lambda)=i_\lambda^b(T,\lambda)\cos\theta \tag{2–34}$$

This formulation leads to what is referred to as Lambert's Law of emission: the radiant emission from an ideal emitter varies as the cosine of the angle of emission [25]. Lambert's law describes the properties of diffuse surfaces: surfaces with no angular dependence of emission, reflection or absorption. Emissive power can also be evaluated on a hemispherical spectral basis.

$$e_\lambda^b(\lambda,T)=\int_0^{2\pi}\int_0^{\pi/2} i_\lambda^b(\lambda,T)\cos\theta\sin\theta d\theta d\phi = \pi i_\lambda^b(\lambda,T) \tag{2–35}$$

2.2.5 Planck's Law. The spectral distribution of blackbody emissive power was derived by Planck using quantum arguments [26]. For a blackbody in vacuum the hemispherical spectral emissive power is

$$e_\lambda^b(\lambda,T)=\frac{2\pi C_1}{\lambda^5(\exp(C_2/\lambda T)-1)} \tag{2–36}$$

Where $C_1 = 0.59544 \times 10^8$ W $\mu m^4/m^2$ and C_2= 14,388 μm K. This distribution is shown for three separate temperatures in Fig. 2-11. The peak in the distribution shifts to shorter wavelengths with higher temperature. The emissive power falls off very rapidly on the short wavelength side of the spectrum, while the long wavelength portion of the spectrum

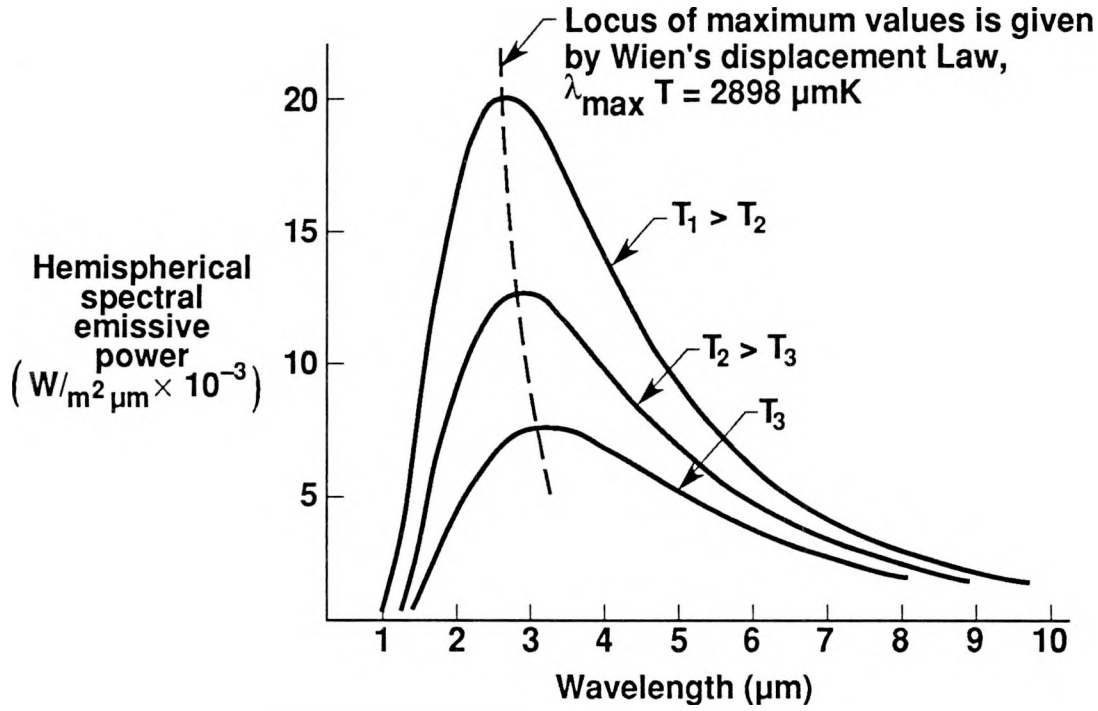

Fig. 2-11. The Planck function gives the spectral distribution of emitted energy from a blackbody.

shows a more gradual decrease in power. The peak in the Planck function (versus wavelength) is given by the Wien displacement law:

$$(\lambda,T)_{max} \equiv C_3 \approx 2898\ \mu m\ K \tag{2–37}$$

This result is readily obtained by differentiating the Planck function. Approximately 25% of the energy in the Planck distribution is at $\lambda < \lambda_{max}$.

The short and long wavelength asymptotes of the Planck function (actually known prior to Planck's work) are also important. In the short wavelength limit ($C_2/\lambda T >> 1.$) Wien's law holds:

$$e_\lambda^b(\lambda,T) \approx \frac{2\pi C_1}{\lambda^5(\exp(C_2/\lambda T)} \tag{2–38}$$

This result is much used in optical pyrometry where the instrumentation typically works on short wavelength emission. It gives results which are in error by less than 1% when λT is less than 2898 μm K [1].

At long wavelengths ($C_2/\lambda T << 1$.)the classical Rayleigh-Jeans law holds:

$$e_\lambda^b(\lambda,T) \approx \frac{2C_1 \pi T}{C_2(\lambda)^4} \tag{2–39}$$

At λT = 10,000 μm K this relation gives ~29% error. For longer wavelengths and/or higher temperatures, the error decreases so that this relation is most often useful at very long wavelengths, such as in radio, radar and television.

2.2.6 Total blackbody emissive power. When the Planck distribution is integrated over all wavelengths a particularly simple result is obtained, the Stefan-Boltzmann equation. The hemispherical total emissive power of a blackbody into vacuum is given by

$$e_b(T) = \sigma T^4 \tag{2–40}$$

The Stefan-Boltzmann constant, σ, is 5.67×10^{-8} watts/m^{2}K^4. The blackbody emissive power into any fraction of the hemisphere above a surface or in any wavelength range within the full spectrum can be found by constraining the integrations to the desired limits. When the Planck function is divided by the fifth power of temperature, the result is a function of only the product λT.

$$\frac{e_\lambda^b(\lambda,T)}{T^5} = \frac{2\pi C_1}{(\lambda T^5)(\exp(C_2/\lambda T)-1)} \tag{2–41}$$

The integral of this function over the integration limits 0 to λT is tabulated in numerous references [1,9,25] and is very useful for calculations of radiation heat transfer.

2.3 Definitions of the thermal radiative properties of non-black surfaces and relations between them

2.3.1 Introduction. Real surfaces have non-ideal surface properties which depend on many factors. Whereas blackbodies show the maximum possible thermal emission, real surfaces display less emission which generally depends on wavelength, direction of emission, temperature, and surface condition. Similarly, real surfaces have non-zero reflection which generally depends on wavelength, direction of incident radiation and surface condition. Real surfaces also show less than ideal (i. e. perfect) absorption with similar dependent factors.

The three principal quantities used in specifying the thermal radiative properties of opaque real surfaces are the reflectivity, the emissivity and the absorptivity. (Surface properties are defined for samples thick enough that negligible incident radiation penetrates to the sample lower surface.) Generally, reflectivity is defined as the fraction of incoming radiant energy which is reflected by a surface. Some of the various specific definitions of reflectivity, spectral or total for example, will be noted briefly below. Emissivity is defined as the fraction of maximum possible emission, blackbody emission, displayed by a surface. Absorptivity is defined as the fraction of incoming radiation absorbed by a surface. Specific definitions of emissivity and absorptivity are also discussed.

From the definitions given here it is clear that all three of the surface properties are defined so that they may vary between zero and unity. Blackbody surface properties are then recognized as special cases of general surface properties. The ideal or black surface has emissivity of unity, reflectivity of zero and absorptivity of unity. No real

surface can replicate these properties but with careful design it is often possible to construct an approximation to a blackbody which is sufficiently close to ideal to be useful as a reference in experimental work.

2.3.2 Notation. The various independent variables influencing the thermal radiative properties of surfaces cause any notation system to be somewhat cumbersome. Here, functional notation is used to indicate the dependent variables. For example, if an absorptivity depends on wavelength, surface temperature and incident polar and azimuthal angles it is called the directional spectral absorptivity, and written

$$\alpha'_{\lambda}(\lambda,T,\theta,\phi) \tag{2–42}$$

The use of the prime (to denote directional dependence) and the lambda subscript are redundant but it is useful to retain them. Absorption generally depends on the polarization of the incoming wave relative to the surface normal. In this case the two absorptivities are written:

$$\alpha'_{\lambda,s}(\lambda,T,\theta,\phi) \qquad \alpha'_{\lambda,p}(\lambda,T,\theta,\phi) \tag{2–43}$$

As with the reflectivity, in radiation heat transfer, the average of the polarized absorptivities is most often used.

2.3.3 Emissivity. The most basic emissivities, the polarized directional spectral emissivities are denoted:

$$\varepsilon'_{\lambda,s}(\lambda,T,\theta,\phi) \qquad \varepsilon'_{\lambda,p}(\lambda,T,\theta,\phi) \tag{2–44}$$

For randomly polarized radiation in heat transfer, it is more common to work with the average of these two quantities [1] and call it the directional spectral emissivity:

$$\varepsilon'_{\lambda}(\lambda,T,\theta,\phi) = \frac{1}{2}\left[\varepsilon'_{\lambda,s}(\lambda,T,\theta,\phi) + \varepsilon'_{\lambda,p}(\lambda,T,\theta,\phi)\right] \tag{2–45}$$

For a perfectly smooth isotropic surface, the azimuthal angle, ϕ does not appear. However, real surfaces do sometimes show dependence on azimuthal angle and a complete rendering must include it. Similarly, real surfaces may show partially polarized emission so that a complete formulation should strictly include both the parallel and perpendicular polarized emissivities.

It is common in engineering heat transfer to work with emissivities averaged over wavelength and/or direction. The hemispherical spectral emissivity, (i. e. the spectral emissivity averaged over the hemisphere) is defined as:

$$\varepsilon_{\cap,\lambda}(T,\lambda) \equiv \int_{\cap} \varepsilon'_{\lambda}(\lambda,T,\theta,\phi)\cos\theta \, d\Omega = \int_0^{2\pi}\int_0^{\pi/2} \varepsilon'_{\lambda}\sin\theta\cos\theta \, d\theta \, d\phi \tag{2–46}$$

The integral is over the entire hemisphere for emission.

The total directional emissivity (integrated over wavelength) is given by:

$$\varepsilon'(\theta,\phi,T) = \frac{\int_0^{\infty} \varepsilon'_{\lambda}(\lambda,\theta,\phi,T)\, e^{b}_{\lambda}(\lambda,\theta,T)d\lambda}{\int_0^{\infty} e^{b}_{\lambda}(\lambda,\theta,T)d\lambda} = \frac{\int_0^{\infty} \varepsilon'_{\lambda}(\lambda,\theta,\phi,T)\, e^{b}_{\lambda}(\lambda,\theta,T)d\lambda}{\sigma T^4} \tag{2–47}$$

The hemispherical total emissivity is readily obtained by performing both integrations described above. Thus:

$$\varepsilon_{\Omega} = \frac{\int_{\Omega} \cos\theta \, d\Omega \int_{0}^{\infty} \varepsilon'_{\lambda}(\lambda,\theta,\phi,T)\, i_{\lambda}^{b}(\lambda,\theta,T) d\lambda}{\int_{\Omega} \cos\theta d\Omega \int_{0}^{\infty} e_{\lambda}^{b}(\lambda,\theta,T) d\lambda} \tag{2–48}$$

Of course the order of integration can be reversed or either of the earlier averaged results can be integrated over the other independent variable to give the fully averaged result.

2.3.4 Absorptivity. The formulations for absorptivity closely follow those given for emissivity. However a significant difference arises from the fact that absorption depends on the spectral content of the incident light as well as the surface properties.

As before, the directional spectral absorptivity is the average of the polarized components of absorptivity:

$$\alpha'_{\lambda}(\lambda,\theta,\phi,T) = \frac{1}{2}\left[\alpha'_{\lambda,s}(\lambda,\theta,\phi,T) + \alpha'_{\lambda,p}(\lambda,\theta,\phi,T)\right] \tag{2–49}$$

This more commonly used unpolarized quantity is defined by

$$\alpha'_{\lambda}(\lambda,\theta,\phi,T) = \frac{d^{3}Q'_{\lambda,a}(\lambda,\theta,\phi,T)}{i'_{\lambda,i}(\lambda,\theta,\phi)\, dA \cos\theta \, d\Omega d\lambda} \tag{2–50}$$

The numerator gives the absorbed power in the wavelength range of interest from the incident direction of interest and at the sample surface temperature. The denominator gives the incident power in that same wavelength range and from the same direction within an infinitesimal solid angle. For the special case of energy incident from a

blackbody the denominator can be replaced by the appropriate form of the Planck distribution.

The directional total absorptivity is formulated by integrating over all wavelengths of incident light:

$$\alpha'(\theta,\phi,T) = \frac{\int_0^\infty \alpha'_\lambda(\lambda,\theta,\phi,T)\, i'_{\lambda,i}(\lambda,\theta,\phi)d\lambda}{\int_0^\infty i'_{\lambda,i}(\lambda,\theta,\phi)d\lambda} \tag{2–51}$$

The hemispherical spectral absorptivity is given by integrating the directional spectral result over angles of incidence:

$$\alpha_{\lambda,\cap}(\lambda,T) = \frac{\int_\cap \alpha'_\lambda(\lambda,\theta,\phi,T)\, i'_{\lambda,i}(\lambda,\theta,\phi,T)\cos\theta\, d\Omega}{\int_\cap i'_{\lambda,i}(\lambda,\theta,\phi,T)\cos\theta\, d\Omega} \tag{2–52}$$

This result cannot be reduced further in the general case because the incident radiation may not be isotropic. The corresponding hemispherical total result is obtained by performing both integrals described above.

2.3.5 Kirchoff's Law. Kirchoff's law states that (without restriction) the spectral directional emissivity and absorptivity are equal. It is widely used in engineering heat transfer both for simplifying calculations and for utilizing measurements of one property in calculations where another is required. Other forms of emissivity and absorptivity are also equated in special cases of Kirchoff's law but these hold given specific restrictions which are particular to the types of emissivity and absorptivity being equated [9].

In its most general form, Kirchoff's law applies to directional spectral properties and this form applies without restriction:

$$\alpha'_\lambda(\lambda,\theta,\phi,T) = \varepsilon'_\lambda(\lambda,\theta,\phi,T) \tag{2–53}$$

For properties integrated over wavelength the following holds under the restriction on the incident radiation given below:

$$\alpha'(\theta,\phi,T) = \varepsilon'(\theta,\phi,T) \tag{2–54}$$

The incident radiation must have a spectral distribution proportional to that of a blackbody at the surface temperature. A second special case where the above holds is for a directional gray surface. Such a surface has absorptive and emissive properties which are independent of wavelength so that this case follows directly from the general form of Kirchoff's law.

For properties averaged over direction Kirchoff's law takes the form given below with the restriction noted:

$$\alpha_\lambda(\lambda,T) = \varepsilon_\lambda(\lambda,T) \tag{2–55}$$

The incident radiation must be independent of direction. This form of the law also applies when the surface is a diffuse spectral surface. This case is again a special case of the most general form.

When equating emissivity and absorptivity averaged over both wavelength and angle the restrictions on validity are then compound versions of the restrictions formulated for the single parameter averages:

$$\alpha(T) = \varepsilon(T) \tag{2–56}$$

— for incident radiation independent of angle and with a spectral distribution proportional to that of blackbody

or — incident radiation independent of angle and surface properties independent of wavelength (gray)

or — incident radiation has spectral distribution proportional to that of a blackbody and surface properties are independent of angle

or — surface properties are independent of both wavelength and angle i.e., the surface is a diffuse-gray surface.

Kirchoff's law is exceedingly useful for simplifying radiation heat transfer calculations. The shortage of complete data on the radiant properties of common engineering materials often makes its use necessary even when the restrictions do not strictly apply.

2.3.6 Reflectivity. Reflectivity is the most complicated of the radiative properties to define because for non-specular surfaces it depends on both the incoming and outgoing directions as well as other properties of the incident radiation. The most basic reflection quantity is the bidirectional spectral reflectivity:

$$\rho''_{\lambda}(\lambda,\theta_r,\phi_r,\theta,\phi) = \frac{i''_{\lambda,r}(\lambda,\theta_r,\phi_r,\theta,\phi)}{i'_{\lambda,i}(\lambda,\theta,\phi)\cos\theta\, d\Omega} \tag{2–57}$$

The notation, pictured in Fig. 2-12, indicates that there can be dependence on both the incident angles and both the reflected angles as well as the surface temperature and wavelength. The reflectivity can also depend on the polarization of the incident radiation

as described earlier in this chapter. For smooth specular surfaces ($\theta_r = \theta$ and $\phi_r = \phi + \pi$), the quantity defined above is the arithmetic average of the two polarized reflectivities.

The directional-hemispherical reflectivity is given by:

$$\rho'_\lambda(\lambda,\theta,\phi) = \frac{\int_\Omega i''_{\lambda,r}(\lambda,\theta_r,\phi_r,\theta,\phi)\cos\theta_r\, d\Omega_r}{i'_{\lambda,i}(\lambda,\theta,\phi)\cos\theta\, d\Omega} \qquad (2\text{–}58)$$

For a specular surface this reflectivity becomes equal to the reflectivity given earlier by the Fresnel equations.

Real surfaces exhibit several types of reflection, in contrast to the ideal smooth surfaces discussed earlier which display only specular reflection. Diffuse surfaces scatter any incident light into the hemisphere above them isotropically, with no angular dependence. Thus, diffuse surfaces are anything but specular; they take whatever directional dependence exists in the incident radiation and spread it out into a uniform fan

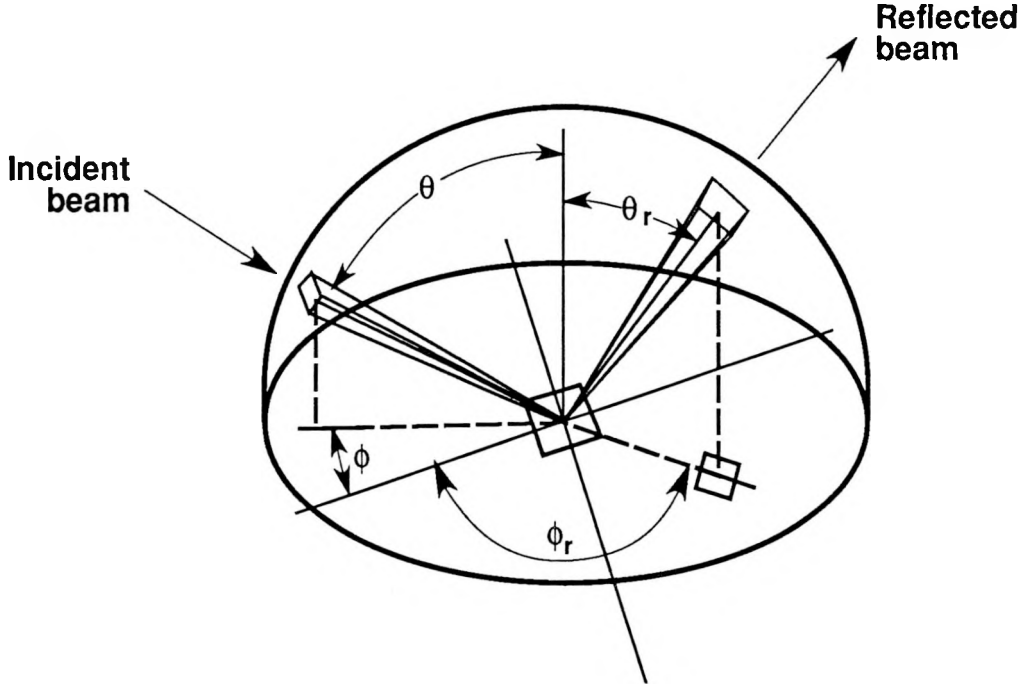

Fig. 2-12. Schematic representation of the bidirectional reflectivity.

of rays. Surfaces which are randomly rough on a scale small compared to the radiation wavelength are good approximations to the diffuse concept.

Real surfaces often exhibit a mixture of diffuse and specular reflection. It is not uncommon to find that reflected radiation is heavily centered on the specular direction but that there is significant reflected (or scattered) radiation over all outgoing angles for a given angle of incidence.

There are also real surfaces with general reflection properties which are neither specular nor diffuse nor a combination of the two. Such surfaces have been reported in the literature but are not a principal concern here where smooth pure liquid metals are of interest and one expects specular behaviour conforming to the predictions of Maxwell's relations and wave reflection theory.

The general form for the bidirectional reflectance given above is rarely used because it is computationally unwieldy as well as very difficult to measure. Calculations using the bidirectional reflectance are complex and require significant computing power. In practice the integrated forms of the reflectivity are often used to allow reasonable estimation of radiation heat transfer. These averages are formed much like those described for the absorptivity. Once again the spectral and directional properties of the incident radiation must be considered but the possibility of integrating over outgoing directions also exists. The integrated forms of reflectivity are given in detail in thermal radiation texts [9,25].

2.3.7 Relations among reflectivity, absorptivity and emissivity. All three of the thermal radiative properties of opaque surfaces can be related when conservation of energy and Kirchoff's laws are applied. If a version of Kirchoff's law other than the most general is applied, the relation is subject to the previously discussed conditions.

When conservation of energy is applied to the radiation incident on an opaque surface the following can be written:

$$\rho'_{\lambda}(\lambda,\theta,\phi,T) + \alpha'_{\lambda}(\lambda,\theta,\phi,T) = 1 \qquad (2\text{–}59)$$

where the reflectivity given above is in general the directional-hemispherical reflectivity. For an opaque surface, all the incident radiation is either reflected or absorbed. For a transparent or translucent body a third term describing transmissivity should be added to the left hand side of the equation but for the materials of interest here only very thin sections would allow for non-zero transmission. Since the most general form of Kirchoff's law applies without restriction the emissivity can be substituted to give:

$$\rho'_{\lambda}(\lambda,\theta,\phi,T) + \varepsilon'_{\lambda}(\lambda,\theta,\phi,T) = 1 \qquad (2\text{–}60)$$

These relations are appropriate for a general reflecting surface. For smooth clean metallic surfaces the reflectivity in eqns.(2-57) and (2-60) becomes the (specular) directional spectral reflectivity calculated from the Fresnel equations. These equalities are used in this work to compare the two independent measurement techniques applied for measurements of the thermal radiant properties of liquid metals.

Using quantities averaged over wavelength and/or direction one can write similar equations relating the thermal radiative properties. Whenever Kirchoff's law is applied to form such equalities, the result is only valid under the conditions for which Kirchoff's law holds. A more complete listing of these relations and their limits of validity are given in Siegel and Howell [9].

3. Classical theories of the optical constants of materials

The interaction of visible light with everyday materials includes many familiar but seemingly disparate phenomena. Ordinary window glass transmits well but is also weakly reflecting. A chrome automobile bumper is highly reflective and not transmissive while an iron skillet is neither strongly reflective nor transmissive. The interaction of light with these everyday items is determined by the optical constants of the materials of which they are composed. This chapter describes some simple models of the microscopic structure of materials which help in understanding the variation of optical constants.

Although other optical constant conventions exist, the two forms most often used are the complex refractive index and the complex dielectric function (also called the relative permittivity). The relations between these were given in chapter 2:

$$\epsilon_{real} = \epsilon/\epsilon_o = n^2 - k^2 \qquad \epsilon_{imag} = \epsilon'/\epsilon_o = 2nk$$

$$n = \left[\frac{\sqrt{\epsilon^2/\epsilon_o^2 + \epsilon'^2/\epsilon_o^2} + \epsilon'/\epsilon_o}{2} \right]^{1/2}$$

$$k = \left[\frac{\sqrt{\epsilon^2/\epsilon_o^2 + \epsilon'^2/\epsilon_o^2} - \epsilon'/\epsilon_o}{2} \right]^{1/2} \qquad (3\text{–}1)$$

Intuitive understanding of n and k is facilitated by their role in plane wave refraction and attenuation, and for specification of reflective and emissive properties in thermal radiation heat transfer, this pair is preferred. However, when considering the microscopic processes which govern optical effects, the complex dielectric function is preferred.

Therefore, this chapter uses both conventions even though most of the work presented in this dissertation will focus on the complex refractive index.

3.1 The Lorentz model

In about 1880, Lorentz explained optical absorption in dielectrics with a theory in which the electrons and ions of the material were treated as simple harmonic oscillators [8,27]. The driving force for the oscillators were electromagnetic fields such as those of light or thermal radiation. Lorentz's model postulated that matter is a collection of harmonic oscillators which are identical, independent and isotropic (generalization to multiple types of oscillator and anisotropy is possible). Each oscillator has mass m and charge e and is acted upon by a linear restoring force $K_{spr}x$, where K_{spr} is a spring constant and x is the displacement from equillibrium. The damping force on the oscillator is Dx' with D the damping constant. The driving force is caused by the local electric field E_{local} (magnetic forces are small relative to electric forces in most materials at optical frequencies). The equation of motion of this oscillator is :

$$m\ddot{\vec{x}} + D\dot{\vec{x}} + K_{spr}\vec{x} = e\vec{E} \qquad (3\text{–}2)$$

For interactions of the oscillator and electromagnetic radiation, the oscillator is driven by a time harmonic with the frequency of the radiation, ω:

$$E = E_o \exp\{-i\omega t\} \qquad (3\text{–}3)$$

Of the transient and oscillatory portions of the solution to this model, only the oscillatory part is of interest:

$$\vec{x} = \frac{e/m\,\vec{E}}{\omega_{res}^2 - \omega^2 - i\gamma\omega} \tag{3–4}$$

Where $\omega_{res} = K_{spr}/m$ and $\gamma = D/m$. For a non-zero damping constant γ, the displacement and field are not in phase. The displacement is then written in terms of a phase angle, Θ and a real amplitude factor, B (both of which are frequency dependent):

$$B = \frac{1}{[(\omega_{res}^2 - \omega^2)^2 + \gamma^2\omega^2]^{1/2}} \tag{3–5}$$

$$\Theta = \tan^{-1}\left[\frac{\gamma\omega}{\omega_{res}^2 - \omega^2}\right] \tag{3–6}$$

The phase angle and amplitude are shown as functions of frequency in Fig. 3-1. At low frequencies the oscillator is in phase with the driving force and at high frequencies the two are 180°. out of phase. The amplitude peak is at $\omega \sim \omega_{res}$ with height proportional to γ^{-1}.

The solution for the oscillator displacement leads to the following form for the complex dielectric function of a material composed of an aggregate of oscillators:

$$\epsilon''/\epsilon_o = 1 + \frac{\omega_{pl}^2}{\omega_{res}^2 - \omega^2 - i\omega\gamma}\ ;\ \omega_{pl}^2 = \frac{N_e e^2}{m\epsilon_o} \tag{3–7}$$

where N_e is the number density of bound electrons. (The plasma wavelength, λ_{pl}, is also used, where $\lambda_{pl} = c/2\pi\omega_{pl}$.) The real and imaginary parts of the dielectric function for the Lorentz model are then:

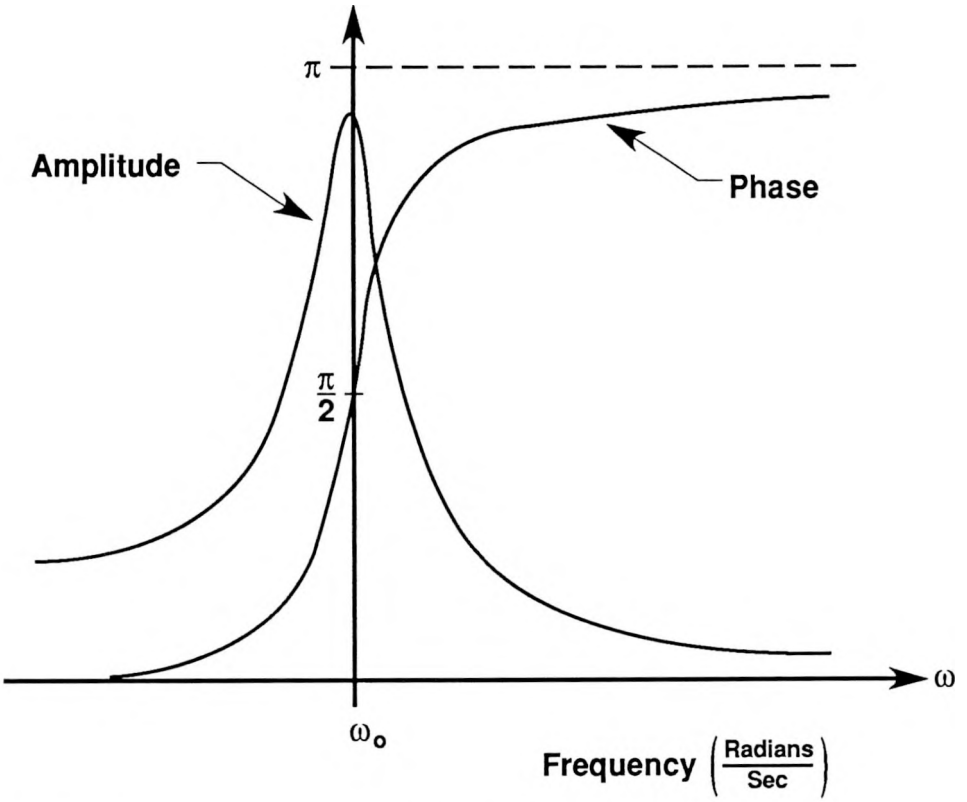

Fig. 3-1. Oscillator displacement of the Lorentz model.

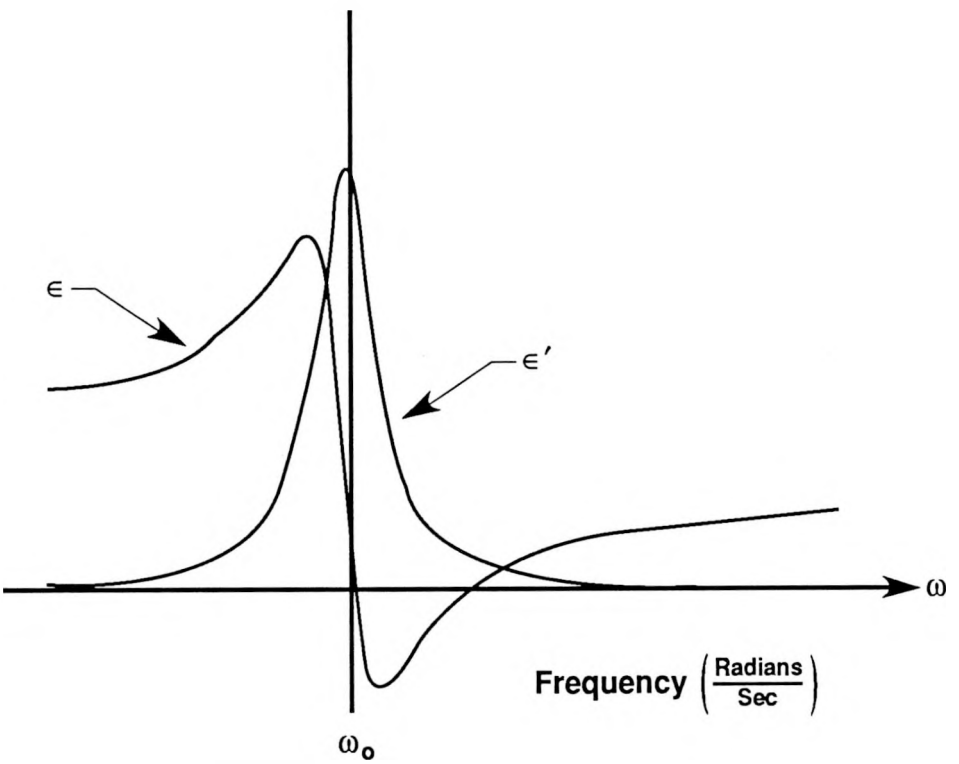

Fig. 3-2. Complex dielectric function of the Lorentz model.

$$\epsilon/\epsilon_o = 1 + \frac{\omega_{pl}^2(\omega_{res}^2-\omega^2)}{(\omega_{res}^2-\omega^2)^2 + \omega^2\gamma^2} \tag{3–8}$$

$$\epsilon'/\epsilon_o = \frac{\omega_{pl}^2\omega\gamma}{(\omega_{res}^2 - \omega^2)^2 + \omega^2\gamma^2} \tag{3–9}$$

Their frequency dependence is shown in Fig. 3-2 and that of the corresponding n and k is given in Fig. 3-3. The reflectance at normal incidence computed from the n and k shown in Fig. 3-3 is given in Fig. 3-4. Around the resonant frequency there is a peak in the reflectance (as long as the oscillator parameters are such that $k >> 1$ there) so that only a small fraction of incident radiation enters the material. That which does enter is rapidly attenuated, as evidenced by the peak in k. On either side of the resonance, n increases with increasing frequency, which behaviour is termed normal dispersion. Close to the resonance where n decreases with ω the dispersion is said to be anomalous.

The Lorentz model is valuable for understanding some of the optical properties of insulators. In some instances, it is both qualitatively and quantitatively applied. The variation of n and k for silicon nitride (given by Phillips [28]) is shown in Fig. 3-5. The general features of the ideal oscillator of Fig. 3-3 are apparent. For some materials, more complex oscillator models provide even better agreement with experiments.

The classical picture of bound electrons assumed by the Lorentz model and the modern picture of energy bands given by the quantum theory of solids are not mutually exclusive [29]. The bound electron effects described here correspond to the interband transitions described by quantum mechanics. Similarly, the free electron effects of the classical Drude model (described below) correspond to intraband transitions. This work emphasizes the classical viewpoint and terminology, partly due to its success in treating molten aluminum and partly due to its physical insight, but the quantum picture is

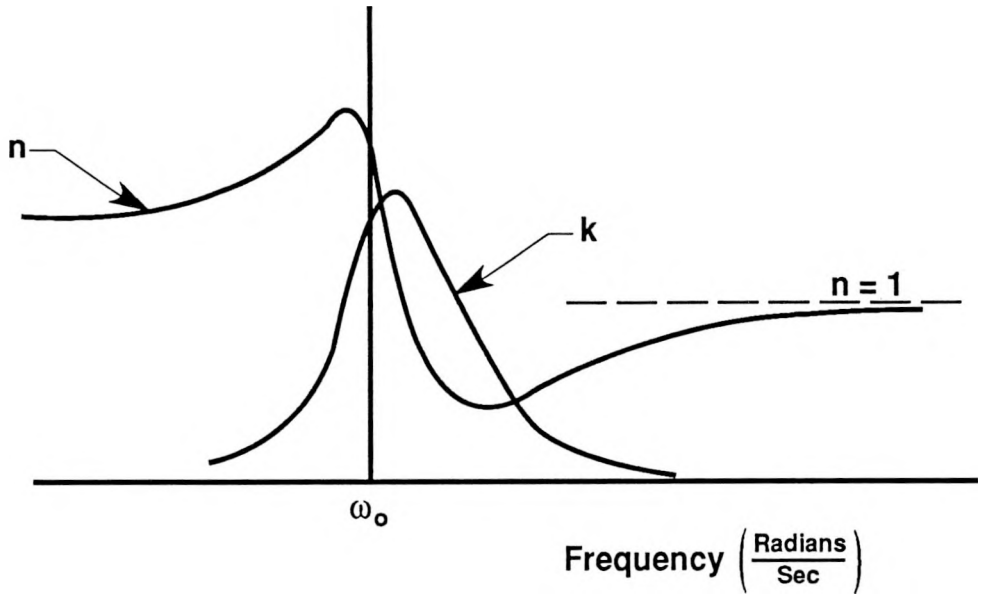

Fig. 3-3. Complex refractive index of the Lorentz model.

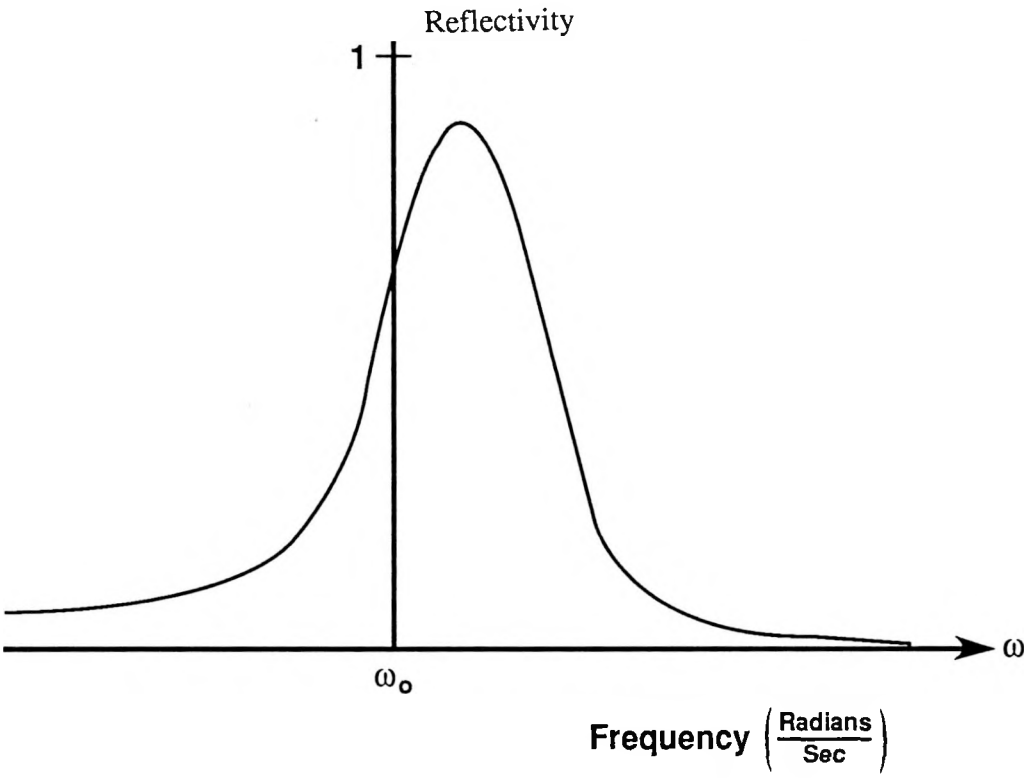

Fig. 3-4. Reflectivity of the Lorentz model.

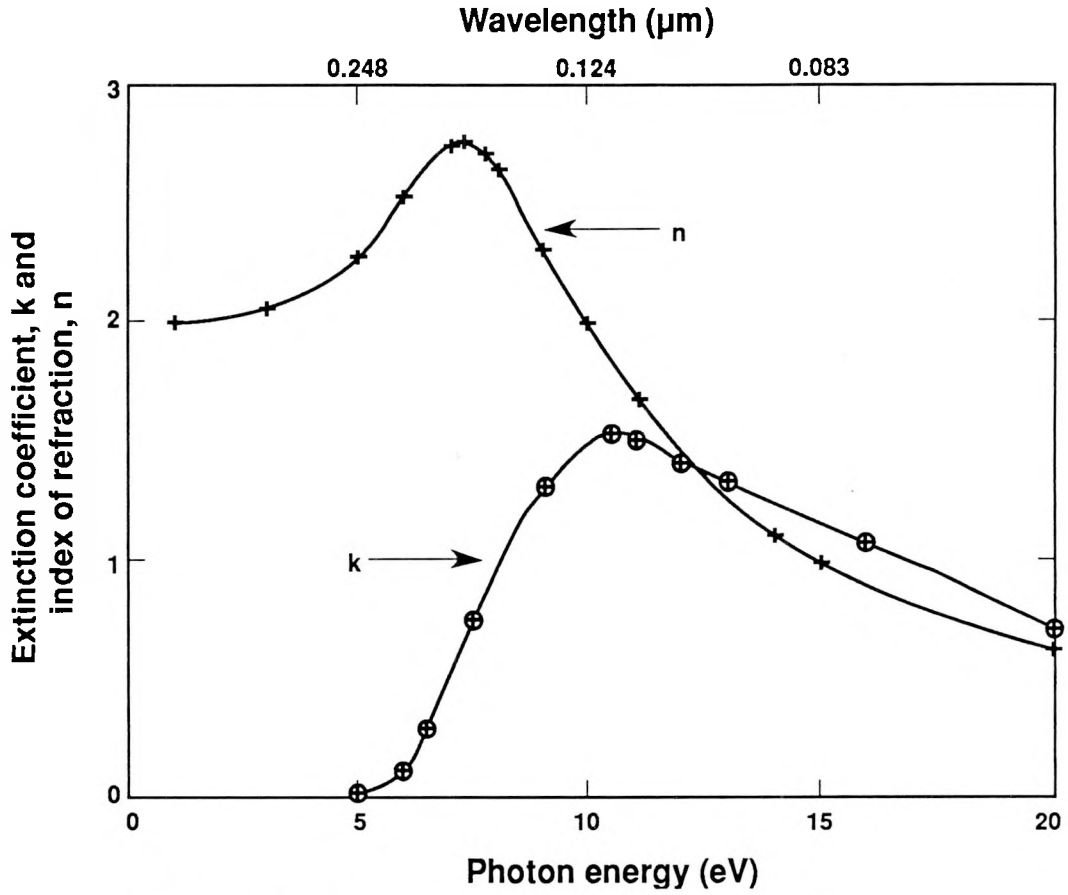

Fig. 3-5. Complex index of refraction measured for Silicon Nitride at room temperature. (from Phillips [28])

sometimes referred to also, particularly for explaining deviations from the simple classical models.

3.2 The Drude model

Drude proposed to treat the unbound (free) charges within conducting materials by allowing the restoring force $K_{spr}x$ of the Lorentz model to go to zero [30]. Thus the equation of motion for the electrons in a "Drude metal" is :

$$m\ddot{\vec{x}} + D\dot{\vec{x}} = e\vec{E}_{local} \qquad (3\text{–}9)$$

The dielectric function for this case is obtained by setting the resonant frequency, ω_{res}, to zero in the Lorentz solutions above:

$$\epsilon/\epsilon_o = 1 - \omega_{pl}^2/(\omega^2 + \gamma^2) \tag{3–11}$$

$$\epsilon'/\epsilon_o = \omega_{pl}^2 \gamma/[\omega(\omega^2 + \gamma^2)] \tag{3–12}$$

The frequency dependence of ϵ/ϵ_o and ϵ'/ϵ_o are given in Fig. 3-6, where the range of photon energies shown corresponds to the wavelength range of interest here (0.4–10 μm).

The Drude model features the restoring force removed, so the possibility of a resonance with the forcing function is gone and ϵ/ϵ_o and ϵ'/ϵ_o no longer possess sharp peaks. In some works ϵ/ϵ_o and the optical conductivity, σ, are reported. The relation between ϵ'/ϵ_o and σ is:

$$\sigma = \omega\epsilon' = \epsilon_o\omega_{pl}^2\gamma/(\omega^2 + \gamma^2) \tag{3–13}$$

The units of σ are $(\text{ohm-m})^{-1}$ or mhos/m. Its dependence on photon energy is given in Fig. 3-7.

The components of the complex refractive index corresponding to the ϵ/ϵ_o and ϵ'/ϵ_o of Fig. 3-6 are shown in Fig. 3-8, in this case as functions of wavelength. Both n and k increase monotonically with wavelength over this range. Although n is smaller than k everywhere, by 10 μm n is beginning to converge toward equality with k, as predicted by the Hagen-Rubens relation in chapter 2.

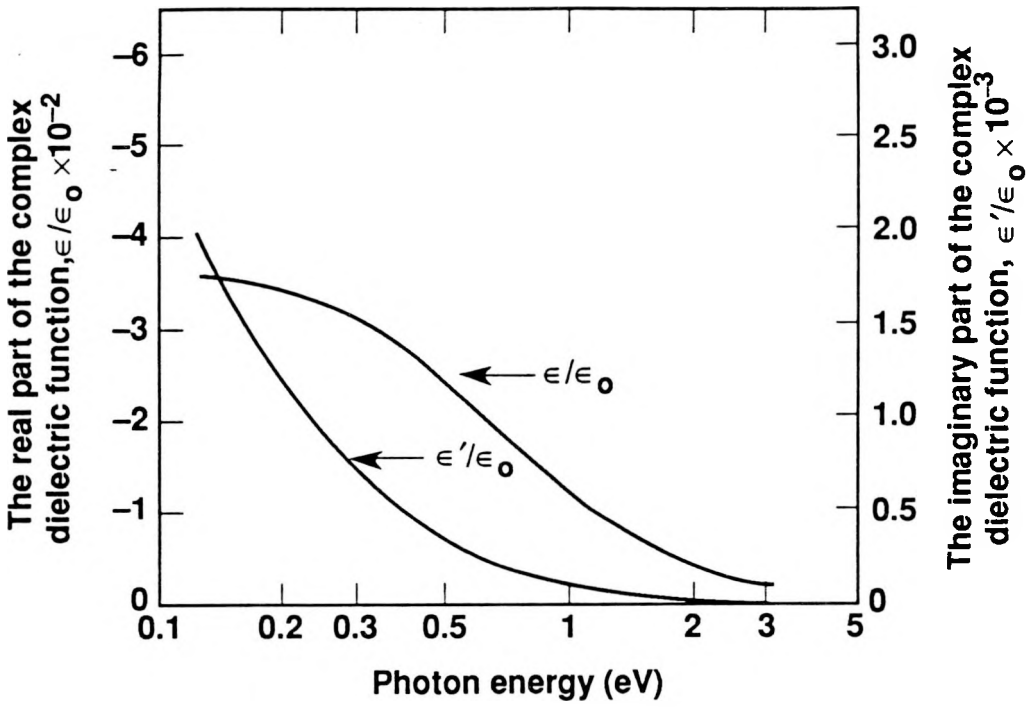

Fig. 3-6. The complex dielectric function for the Drude model with representative input parameters.

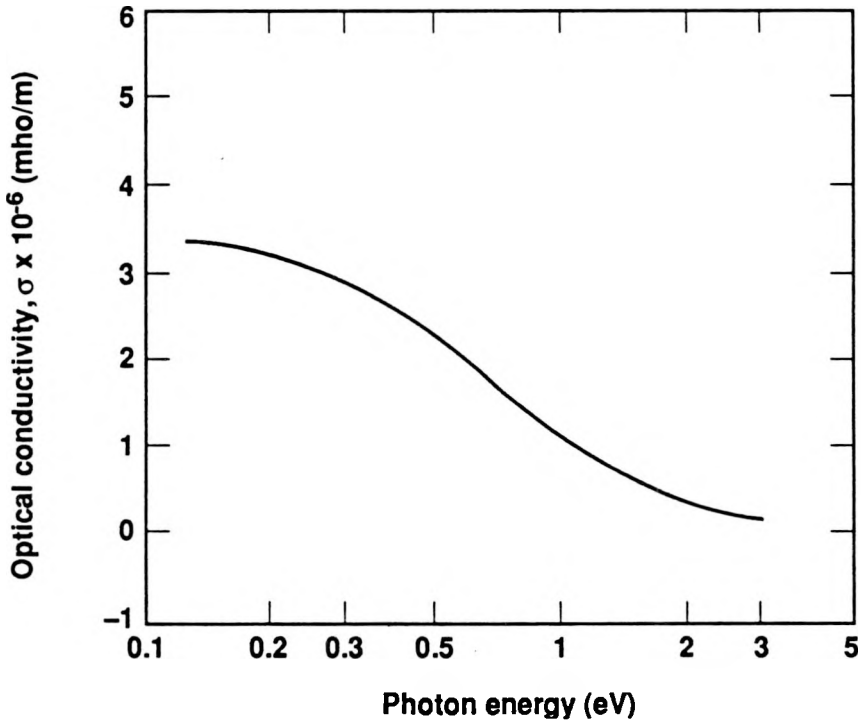

Fig. 3-7. Optical conductivity for the Drude model with representative input parameters.

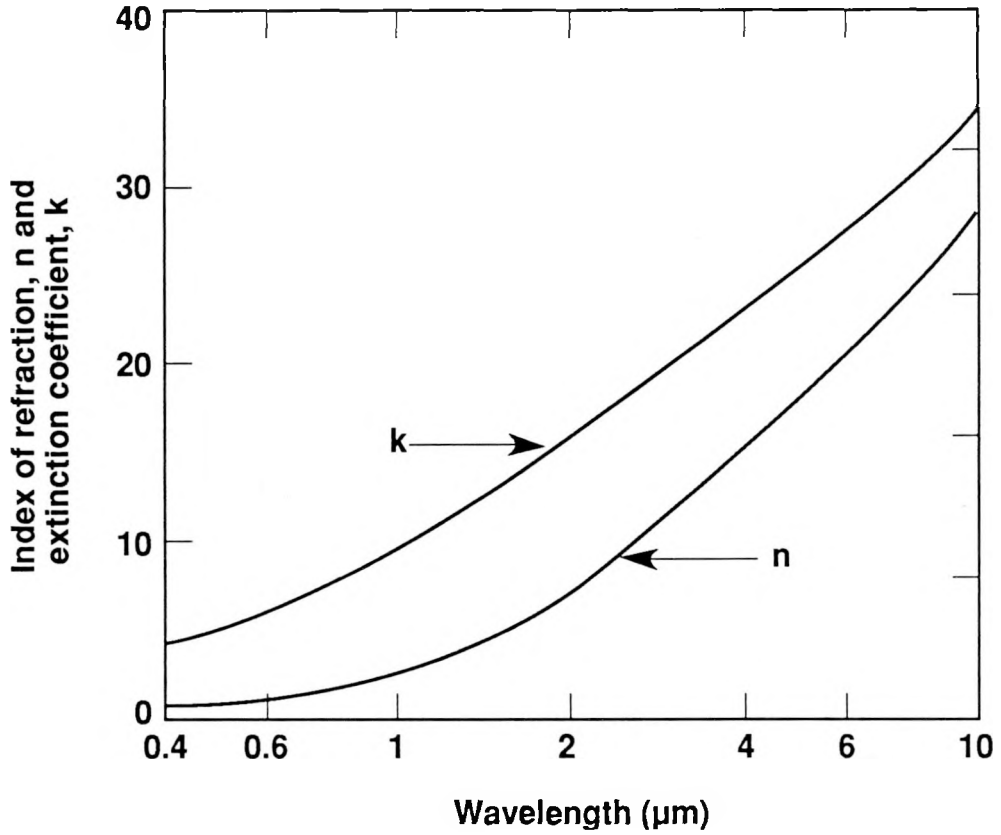

Fig. 3-8. Complex refractive index for the Drude model with representative input parameters.

The normal spectral emissivity and reflectivity computed from the n and k pair above are given in Fig. 3-9. Drude metals are highly reflective, particularly in the infrared, in agreement with experience for many common metals.

In the Lorentz model, peaks in reflectivity corresponded to local peaks in extinction coefficient k. In the Drude model, high reflectivity corresponds to uniformly high and increasing values of k. As in the Lorentz model, the higher rates of wave damping signified by high values of k coincide with lower fractions of incident radiation entering the material.

In Figs. 3-6 to 3-9, the Drude model described the variation in the optical constants with frequency in terms of fundamental constants, the optical frequency, and two parameters, sometimes called the "Drude parameters." In the solutions for ϵ/ϵ_0 and

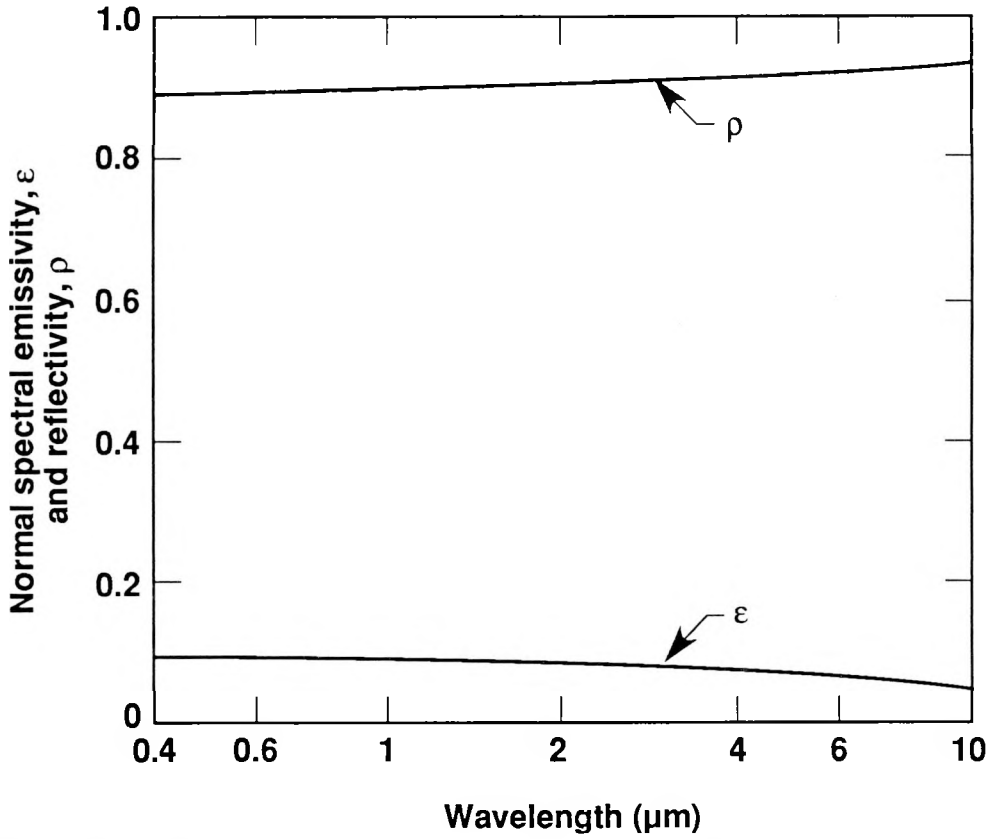

Fig. 3-9. Emissivity and reflectivity for the Drude model with representative input parameters.

ϵ'/ϵ_o (given by equations 3-10 and 3-11) these parameters were γ and ω_{pl}. Another common formulation which provides more insight into the underlying mechanisms uses the collision time for electrons, τ, and N_e, the density of free electrons [31,32,33]. The collision time is the average time between scattering events for the free electrons as they move in a lattice of ions, and is the inverse of the damping constant , D, in the equation of motion. Using τ and N_e, the optical constants are given by:

$$\epsilon/\epsilon_o = 1 - \frac{N_e e^2 \tau^2}{m\epsilon_o(1+\omega^2\tau^2)} \; ; \epsilon/\epsilon_o = \frac{N_e e^2 \tau}{m\epsilon_o \omega (1+\omega^2\tau^2)} \qquad (3\text{–}14)$$

In this form, metals vary according to their concentration of free electrons and the frequency with which scattering impedes their motion in the presence of an electric field. In terms of τ and N_e, the optical conductivity is:

$$\sigma = \frac{N_e e^2 \tau}{m(1 + \omega^2 \tau^2)} \qquad (3\text{–}15)$$

For most real metals, the Drude model provides only a qualitative description of the variation of complex index of refraction with wavelength (It is quantitative only for long wavelengths, $\lambda > \sim 10\mu m$). The components of the complex index of refraction of room temperature molybdenum from the Handbook of Optical Constants of Solids [34] are shown in Fig. 3-10 for qualitative comparison with the Drude model results shown in Fig. 3-8. For wavelengths less than 2 μm, the variation of n and k is similar to that given by the Lorentz model, with peaks in n and k, although very broad ones. Beyond 2 μm both n and k increase monotonically, and after 3 or 4 μm the similarity between the Drude prediction (Fig. 3-8) and the measurements for molybdenum (Fig. 3-10) is obvious. In both figures the curves for n and k tend to converge to the Hagen-Rubens asymptote (n = k) noted earlier.

Although the variation of n and k beyond ~3 μm in Fig. 3-10 qualitatively matches the Drude picture, quantitative correspondence is not obtained until beyond 10 μm, because bound electron effects (or interband transitions in quantum terminology) persist in molybdenum to very long wavelengths (or low energies). Quantum calculations of the energy band structrure of molybdenum [35] and optical measurements [36] indicate principal interband effects between 1.0 and 5.5 eV (0.22 to 1.24μm) but lesser effects also, at energies as low as 0.17 eV (7.3 μm). Although

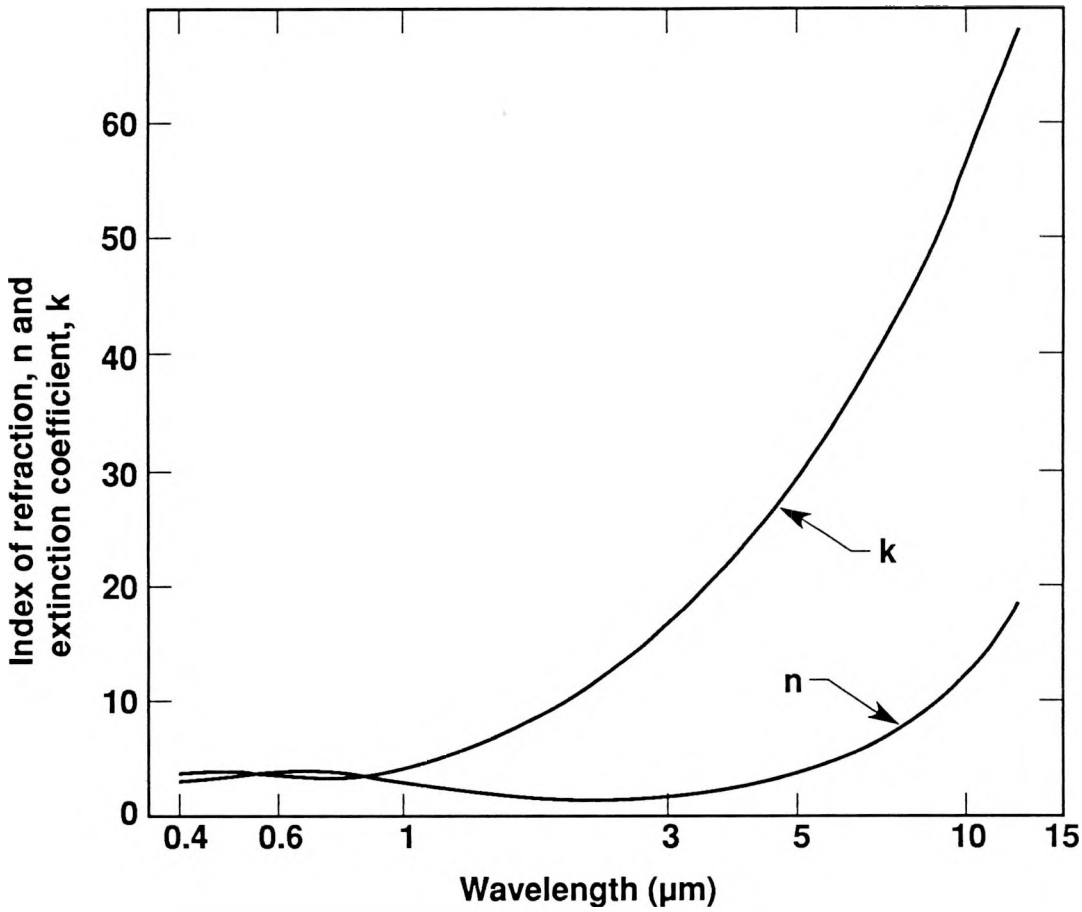

Fig. 3-10. Complex refractive index measured for Molybdenum at room temperature.

intraband optical effects (corresponding to the free carrier absorption described by the Drude relations) are stronger than the bound electron effects in the 2 to 8 μm spectral range, the low energy interband effects are large enough to require optical constant data from the 10 to 20 μm range to be used when determining the Drude parameters (τ and N_e, for example) of molybdenum. Similar effects will be noted for tungsten and uranium in chapters 9 and 10.

Although the transition metals such as molybdenum, uranium and tungsten commonly show rather poor correspondence with the Drude model, the alkali and the noble metals are often much more amenable to such fits. The lack of low energy

interband (or bound charge) effects makes metals such as sodium, gold and silver Drude-like for wavelengths greater than 1 or 2 μm. As will be discussed in ch. 11, aluminum is also such a metal and the Drude relations are particularly successful above the melting point.

3.3 The Hagen-Rubens relation

The long wavelength limit of the Drude model can be used to obtain the Hagen-Rubens approximation described in chapter 2. At low frequencies ($\omega^2 << \omega_{pl}^2$), inertial forces on the free electrons in metals become negligible [37] so that their equation of motion simplifies to:

$$D\vec{x} = e\vec{E} \tag{3–18}$$

The solutions for ϵ/ϵ_o,ϵ'/ϵ_o and σ become:

$$\epsilon/\epsilon_o = 1 \tag{3–19}$$

$$\epsilon'/\epsilon_o = \frac{N_e e^2 \tau}{\omega \epsilon_o m} \tag{3–20}$$

$$\sigma = \frac{N_e e^2 \tau}{m} \tag{3–21}$$

Since ϵ'/ϵ_o is much larger than ϵ/ϵ_o the forms for n and k in terms of ϵ'/ϵ_o and ϵ/ϵ_o (equation 3-1) become identical. In terms of the direct current conductivity the Hagen-Rubens relation is:

$$n = k = \sqrt{\frac{\epsilon'}{2\epsilon_o}} = \sqrt{\frac{\sigma_{dc}}{2\omega\epsilon_o}} = \sqrt{\frac{\sigma_{dc}\lambda}{4\pi\epsilon_o c_o}} \qquad (3\text{–}22)$$

For λ_o expressed in μm and the electrical resistivity in ohm-cm this becomes:

$$n = k = \sqrt{\frac{0.003\lambda_o}{r_e}} \qquad (3\text{–}23)$$

as given in chapter 2.

The normal spectral emissivity which follows from (3-21) above, the result for the normal spectral reflectivity (2-28) and $\rho_n = 1 - \varepsilon_n$ is:

$$\varepsilon_n(\lambda_o) = 0.365\sqrt{\frac{r_e}{\lambda_o}} - 0.0464\frac{r_e}{\lambda_o} \qquad (3\text{–}24)$$

Once again λ_o is given in μm and r_e in ohm-cm [1,38]. For solid metals this equation is sometimes qualitatively accurate to wavelengths as short as 5 μm, but such agreement should be regarded as fortuitous. With decreasing wavelength the Hagen-Rubens relation over-predicts the emissivity values measured for highly smooth, pure and stress free surfaces. However, most non-ideal surface effects arising during sample preparation (among these effects are surface damage caused by polishing, grain growth and roughening due to prolonged heating and oxidation due to exposure to air) serve to increase sample emissivity, and hence bring measurements and the predictions of the Hagen-Rubens relation into agreement at shorter wavelengths than is truly justified [39]. Real surface effects, such as these are not present with liquid samples such as those produced here.

The Hagen-Rubens relation is also of interest because it predicts the variation of n, k and ε_n with temperature through the variation of the electrical resistivity with

temperature. For metals at elevated temperature (600 to 1600 K), the resistivity generally increases approximately linearly with temperature. Thus, the long wavelength asymptote predicts both n and k decreasing inversely as the square root of temperature and the normal spectral emissivity increasing as the square root of temperature. The magnitude of this dependence is shown in Fig 3-11. The resistivities used for the curves are measured values for high purity tungsten formed by hot pressing and reported in Touloukian [40]. The wavelength range shown in the figure is the range of interest to this work rather than a range in which the Hagen-Rubens relation strictly applies ($\lambda > 10$ μm). The predicted dependence of spectral emissivity on temperature is weak and decreases with wavelength, trends which are in qualitative agreement with experimental work.

The dependence of n and k on wavelength and temperature indicated above (by equation 3-21) is shown in Fig. 3-12. The same values of resistivity are used as in the previous figure. A stronger dependence on temperature is indicated in the long wavelength extreme where the approximation begins to apply. Only qualitative correspondence with measurements is again observed.

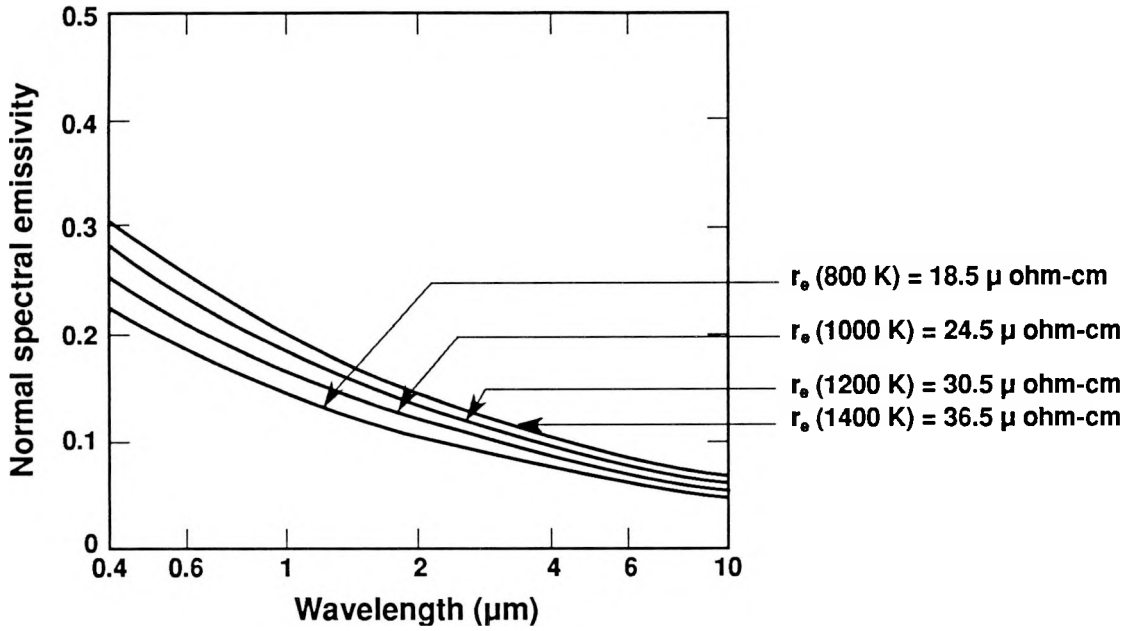

Fig. 3-11. The normal spectral emissivity of tungsten predicted by the Hagen-Rubens approximation.

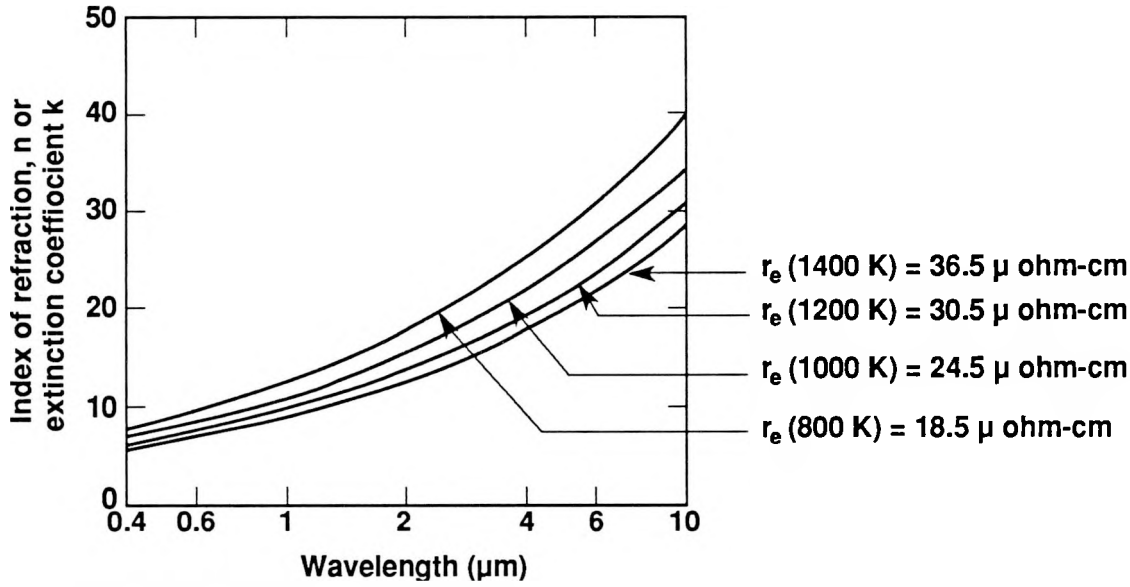

Fig. 3-12. The predicted variation in either component of the complex index of refraction of tungsten using the Hagen-Rubens approximation and published data for the resistivity as a function of temperature.

4. A review of measurement methods for the thermal radiative properties of smooth surfaces

4.1 Classification of measurement methods

Techniques for determining the thermal radiative properties of surfaces may be based on measuring any of the three related properties, emissivity, absorptivity and reflectivity. In each case there are a variety of measurement schemes, and the choice depends on the spectral range of interest, the sample temperature and material properties, and the level of detail required, i. e. whether the directional-spectral quantity is required or some integral property will suffice.

Measurement of one of the directional-spectral properties ε_λ', α_λ', or ρ_λ' allows the others to be determined from the unrestricted form of Kirchoff's law (2-49) and from such measurements over sufficient ranges of angle and wavelength, all of the integral forms of the three properties may be calculated by suitable integration over angle and/or wavelength. Moreover, for a smooth surface, a knowledge of ρ_λ' allows the Fresnel relations to be used to calculate the optical constants (n,k) as a function of wavelength, which completely characterizes the optical radiative properties of the material. The optical constants (n,k) are of great scientific interest since they can be related to the microscopic physics of the material, (e. g. the electronic band structure of metals).

On the other hand, for many engineering purposes in radiation heat transfer, values of some integral property are sufficient, and techniques for measuring such properties are generally simpler to implement than those for directional-spectral properties. However, the measurement of one integral property does not allow the others to be calculated from Kirchoff's law except under the restrictions noted in chapter 2, so such measurements are less general and complete. Moreover, they do not allow the optical constants to be determined.

All measurement techniques may be generally classified as either radiometric or calorimetric methods, or some combination of the two. Radiometric methods involve the use of optical systems to generate beams of radiation from a suitable source and/or detectors to measure the power in such beams. They therefore require relatively sophisticated equipment and techniques. Calorimetric methods are based on measuring radiant heat fluxes thermometrically using a heat balance equation allowing carefully for non-radiant heat gains or losses [1]. Generally, reflectivity measurements are purely radiometric, while absorptivity and emissivity measurements may be entirely calorimetric or some combination of the two.

There are two other important general distinctions between measurements of the three quantities ε_λ', α_λ', and ρ_λ'. Emissivity measurements are generally used and become more sensitive at high temperatures when the radiant power to be measured becomes larger and can be more accurately measured. On the other hand, absorptivity measurements , since they involve calorimetric measurements of small absorbed powers, become more sensitive at low temperatures and are most commonly used at cryogenic temperatures. In contrast, radiometric measurements of reflectivity are applicable at all sample temperatures although detection of the reflected power at high temperatures in the presence of high radiant emission from the sample poses problems. However, this can be alleviated by maximizing the ratio of the source to sample temperatures, by modulating (chopping) the incident beam and by using a phase sensitive detector (a lock-in amplifier) to improve the signal to noise ratio.

A most important distinction between direct measurements of ε on the one hand and measurements of ρ or α on the other is that in emissivity measurements the radiant power varies as a high power of the sample surface temperature (T^4 to T^5), which must therefore be measured with high precision. On the other hand, since ρ and α are weak functions of temperature, the sample temperature does not have to be known precisely.

A distinction can also be made between absolute and relative measurement techniques, which terms can be used in two senses. With regard to radiometric detection, the detector output voltage V is related to the incident radiance by

$$V=L(\lambda)i'_{\lambda}dAd\Omega d\lambda \qquad (4-1)$$

where $dA,d\Omega,d\lambda$ are respectively the effective area, solid angle and wavelength interval of the radiation received by the detector and $L(\lambda)$ is the detector sensitivity or responsivity in volts/watt. Generally, these quantities are not known with any precision which makes absolute measurements of radiant power very difficult. For this reason, radiometers are invariably used in a relative sense, by comparing the output voltages from measurements at two angles, two polarizations, etc., while keeping $\lambda,d\lambda,dA$, and $d\Omega$ accurately constant.

The term relative measurement may also be applied to the case where measurements on the unknown sample are compared with those on a reference surface whose properties are accurately known. For instance, for reflectivity measurements, reference surfaces of accurately specified reflectivity are available from NBS, but only for rather limited spectral ranges and for ambient temperatures [41]. Relative measurement techniques may also be used for emission by comparison with a well designed blackbody source operated at the same temperature as the sample surface. However, it is generally difficult to set the two temperatures the same with sufficient precision unless a sufficiently good blackbody cavity can be realized that is integral with the sample itself (or its crucible).

Also, in general, spectral measurements become more difficult at long wavelengths in the infrared because the emissive power is low both from the sample (for emissivity measurements) or from available sources (for reflection and absorption measurements). Also, for metals at long wavelength, when $\rho \rightarrow 1$, the reflectivity must

be measured precisely to infer accurate values of $\alpha'_\lambda = \varepsilon'_\lambda = (1 - \rho'_\lambda)$. Equivalently, for metals at long wavelengths when k , n >> 1, one needs precise measurements to infer reliable results for n and k. An analysis of the sensitivity of the infrared values of n and k to uncertainties in the measured quantities can be calculated from the Fresnel equations and is a useful indicator for various measurement techniques. Such calculations are presented in chapter 7.

Measurements at high temperatures, which is the focus of the present work, pose a number of problems related to the stability of the surface with regard to metallurgical and chemical changes. Polished polycrystalline metal surfaces exhibit 1) grain growth, 2) migration of impurities to the surface along grain boundaries and 3) chemical change (or even phase change) of the surface due for example to oxidation. For liquid metals, impurities rise to the surface and chemical reactivity increases. To control such changes the hot sample must be contained in a non-reactive crucible and placed in either an inert, or preferably, an ultra-high vacuum environment. In general, because the radiative properties of the surface are very sensitive to its chemical and physical condition, the surface must be maintained in a stable, well characterized state, (preferably ultra pure), if the measured properties are to be meaningful and useful. For this reason, in the measurements on high temperature metals reported here, the sample was enclosed in an ultra-high vacuum system equipped with techniques for cleaning the surface and characterizing its surface composition. An additional difficulty peculiar to measurements on liquid surfaces is the maintainance of a sufficiently flat surface. The meniscus causes curvature of the surface which, acting as a concave or convex mirror can strongly affect the optical geometry in reflectivity measurements.

Besides the general characteristics of the various measurement techniques discussed above, in practice they also vary widely in their precision due to various experimental factors. Errors and uncertainties may generally be classed as random or systematic. The former, e.g. due to signal to noise considerations, are relatively

straightforward to estimate and minimize. However, it is generally difficult to track down and control systematic errors. For this reason it is highly desirable to compare measurements of radiative properties by two (or more) independent techniques as a way of guarding against systematic errors.

4.2 Reflectivity measurements

4.2.1 Reflection methods designed to give various forms of directional and hemispherical spectral reflectivity. Reflection measurement methods vary with application and sample properties. Reviews have been published by Touloukian [1], Dunkle [42], and Dunn,Richmond and Parmer [43]. Touloukian classified reflection methods into five groups; 1) specular reflectometers 2) integrating mirror reflectometers 3) integrating sphere reflectometers 4) heated cavity reflectometers and 5) gonioreflectometers.

The Strong (or V-W) reflectometer is a specular reflectometer which has yielded highly accurate reflectivity results for specular samples [44,45,46,47]. The concept of this apparatus is shown in Fig. 4-1. The reference signal is obtained while the device is in the v configuration. The optical beam forms a v shape by making a single reflection at a subsidiary mirror. The sample signal is obtained while the device is in the w configuration. Here the optical beam forms a w shape by reflection from the sample then the subsidiary mirror and then the sample mirror again. Since the beam makes a single reflection off the subsidiary mirror in both configurations, the subsidiary mirror does not need to be a standard mirror. The ratio of the two signals is computed to cancel the attenuation due to reflection off the subsidiary mirror in the w configuration. Thus the technique measures the absolute rather than the relative reflectivity. Since the beam makes two reflections from the sample surface in the w position the square of the reflectivity is measured and accuracy is improved for highly reflecting samples. The total

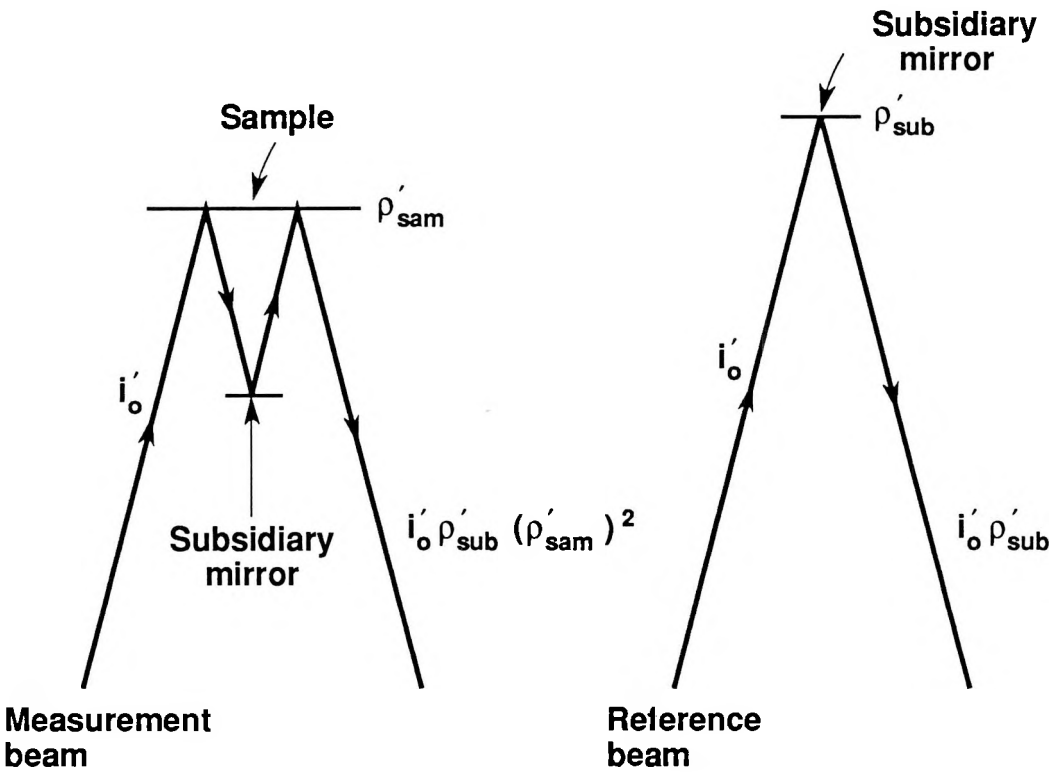

Fig. 4-1. Optical layout of the Strong (or V-W) reflectometer. The standard mirror pivots between the two positions shown so that with either the measurement beam or the reference beam the subsidiary mirror provides a single reflection.

path length is the same for the v and w configurations, a condition which preserves the imaging at the detector. Many other specular reflectometers have been used [1,42,43,48,49].

Integrating mirror reflectometers are useful with both diffuse and specular reflectors. Many of these devices have been built to treat a wide variety of engineering materials. Their optics are complex but they are often capable of precise measurements. Both spectral and directional selectivity can be obtained by the use of monochromators with bright incandescent light sources and simple high precision mechanical movements. Absolute and relative reflectivity measurements have been made using various types of integrating spheres [50] as well as ellipsoidal [51], parabaloidal [52] and hemispherical

[53] integrating mirror systems. Some of these devices use polarizers to measure both components of polarized reflectivity.

A paraboloidal reflectometer is shown in Fig. 4-2. The movable mirror between the paraboloids allows the sample to be irradiated over a wide range of angles. The reflected radiation is collected over the entire hemisphere above the sample and focused at the detector. Any type of reflecting surface can be measured; diffuse, specular or one having a completely arbitrary reflectivity. This system and variations of it have only been used at room temperature. They could be used at higher temperatures but with difficulty because the sample heating system would have to be contained in the small space between the two parabolic mirrors. At higher temperatures a modulated input beam and phase sensitive detection would be required to isolate the reflected signal from sample emission.

The first hemispherical mirror reflection system was developed by Coblentz [54] and later refined [55,56]. This arrangement, (Fig. 4-3), places the sample and the detector at conjugate focal points of a hemispherical mirror. Like the paraboloidal system

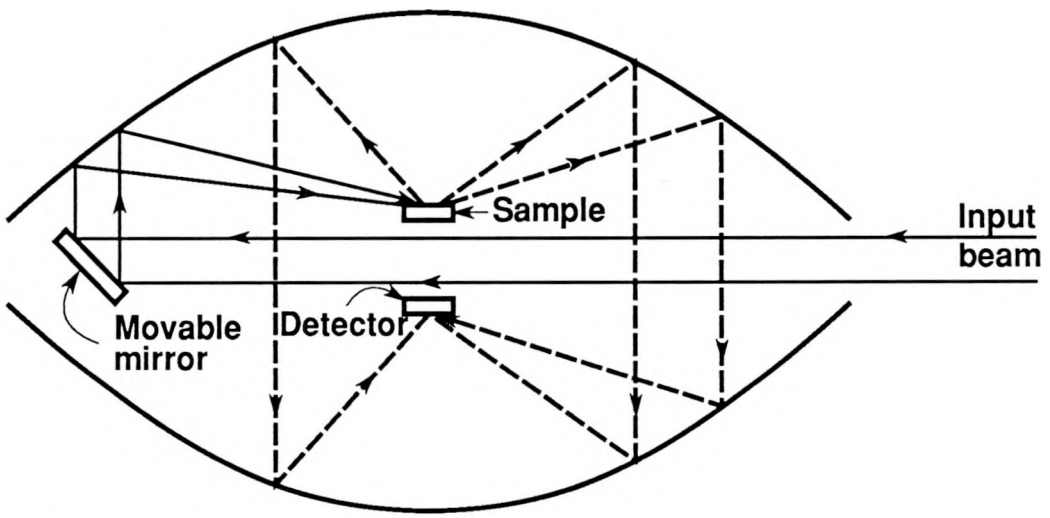

Fig. 4-2. Optical layout of a parabaloidal reflectometer.

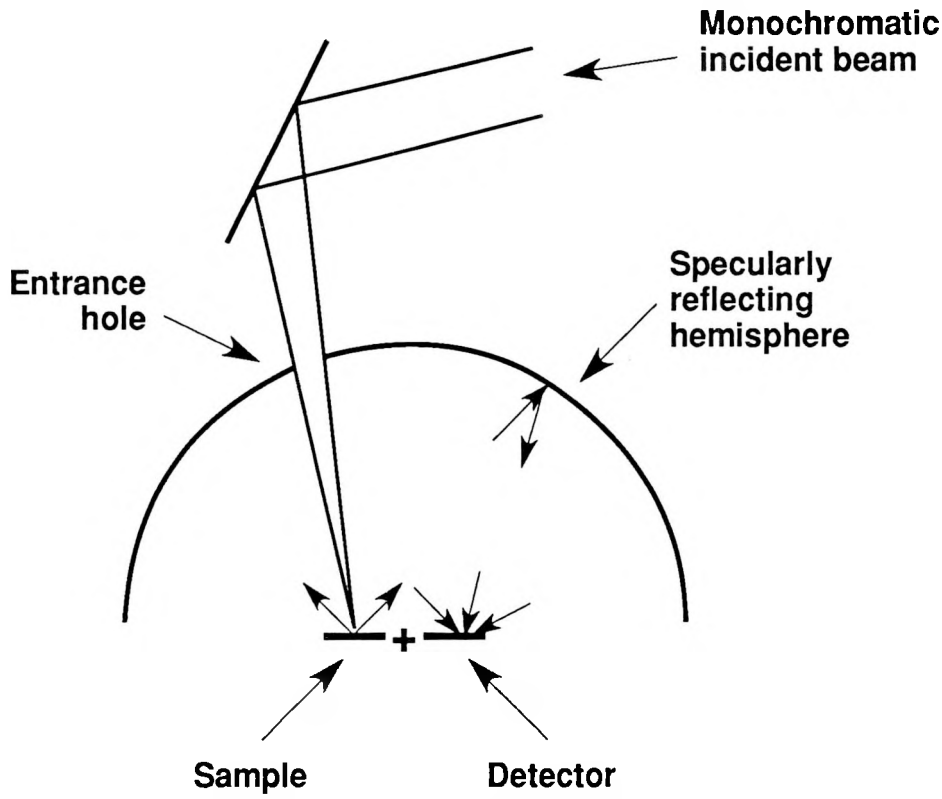

Fig. 4-3. Optical layout of the Coblentz-hemisphere reflectometer. The sample and detector are located at conjugate focal points.

described above, this apparatus measures the directional-hemispherical reflectance of samples with an arbitrary reflection distribution. The hemispherical arrangement readily permits sample heating, so that radiant properties can be measured at elevated sample temperatures. Results for samples as hot as 1273 K have been reported [57]. Unfortunately aberrations due to the hemispherical mirrors lead to significant errors.

Ellipsoidal integrating mirror systems greatly reduce aberrations compared to their hemispherical counterparts [51]. Their optics are otherwise similar to the hemispherical systems and they can readily accommodate sample heating. These systems are also able to measure both directional-hemispherical and hemispherical-directional reflectance by interchanging the positions of the light source and detector.

Integrating sphere reflectometers are widely used for directional-hemispherical reflection measurements on engineering materials [50,58,59,60,61]. In these systems the sphere surrounding the sample is coated with a material of high and diffuse reflectance. The sample is irradiated at normal incidence or over various angles around the hemisphere. The reflected light is diffused by the sphere and sampled by a detector on the sphere surface. Most often this device is used to measure reflectance relative to a standard, (usually smoked magnesium oxide or barium sulfate), but it has also been modified to give absolute reflectance results with good precision [62].

Heated cavity reflectometers use a hohlraum or blackbody around a sample so that the sample is irradiated over the entire hemisphere [63,64]. The reflected light from the sample is then focused onto a detector. By rotating the sample or the detector the total hemispherical-directional reflectance can be measured. In a more refined version of this method the sample is centered in the heated blackbody rather than along a wall and several contributions to errors are thereby reduced [65].

Gonioreflectometers use multiple rotation mechanisms to measure the bidirectional reflectance as a function of angle for any angle of incidence. When used over a wide spectral range, they give the most general and complete radiant property measurements [66]. With polarizing filters, gonioreflectometers measure the bidirectional reflectivity for both the perpendicularly and parallel polarized components [67]. Data in this form can be used to compute the sample's complex refractive index but the sensitivity of this approach in some of the spectral ranges of interest here is poor. The sensitivity of these and other methods is the subject of chapter 7.

Unfortunately, none of the methods for reflectivity measurement discussed above is applicable to the present purpose due to one or more of the following factors:

- not practical for liquid samples with surface curvature
- too complex for use inside a UHV system
- incompatible with high temperature

- too large to use with surface analysis equipment
- too limited for computing the complex index of refraction (to give a complete radiant property set)

These problems with the methods described above led to the consideration of more general measurement methods which could allow determination of the optical constants of the sample surface.

4.2.2 Reflection methods designed for determination of the complex refractive index. There are two basic approaches to measuring the optical constants of highly reflecting surfaces. The first approach measures the magnitude of the reflection coefficient as it varies with angle of incidence, for linearly polarized or unpolarized incident light. This approach will be discussed here. The second approach uses ellipsometry to measure both the amplitude and the relative phase change of a reflected beam. Ellipsometric methods and their significance to this work are the subject of chapter 5.

In the 1920s, efforts to obtain the complex refractive index from reflection measurements without considering phase change on reflection involved solving the Fresnel equations using unpolarized reflection data taken for two angles [68, 69]. These efforts were hampered by the complexity of the Fresnel equations and the lack of computers. Tousey and several others suggested computational methods to assist the work [70,71,72,73]. A major advance occurred when Avery [74] suggested using the ratio of the polarized reflectivities as a function of angle, rather than the average reflectivity or its individual polarized components. This approach increased the sensitivity for determining n and k for metals at long wavelength (where n and k become large and $\rho \rightarrow 1$). Avery's method and the other extant techniques were reviewed by Humphreys-Owen in 1960 [75] and later by Hunter in 1982 [76]. The nine methods compared by Humphreys-Owen involved measurements of:

(A) Reflectivity at two angles of incidence using natural (unpolarized) incident radiation.

(B) $\rho_{\lambda,p}$ at two angles of incidence.

(C) $\rho_{\lambda,s}$ at two angles of incidence.

(D) $\rho_{\lambda,p}/\rho_{\lambda,s}$ at two angles of incidence.

(E) $\rho_{\lambda,p}$ and $\rho_{\lambda,s}$ separately at one angle of incidence.

(F) Pseudo-Brewster angle and $\rho_{\lambda,p}$ at that angle.

(G) Pseudo-Brewster angle and $\rho_{\lambda,s}$ at that angle.

(H) Pseudo-Brewster angle and $\rho_{\lambda,p}/\rho_{\lambda,s}$ at that angle.

(I) Pseudo-Brewster angle and either $\rho_{\lambda,s}$, $\rho_{\lambda,p}/\rho_{\lambda,s}$, or $\rho_{\lambda,p}$ at any other angle.

The pseudo-Brewster angle was defined in chapter 2 as the angle of incidence at which the parallel polarized component of reflection from a conductor has a minimum. Of methods A through E only method D is practical for small liquid samples because the meniscus makes determination of absolute reflectivity impractical. The methods which work with the pseudo-Brewster angle, F through I are not options with a liquid metal sample because they would require continuous manipulation of optics inside a UHV chamber to find the minimum in reflectivity versus angle. [Method A was used by Simon [77] with an inert liquid where UHV conditions were not required.] Method D is valuable for work in the visible spectral range, but its sensitivity declines rapidly as the components of the complex refractive index increase, so that in the infrared range (with metallic specimens) this approach is not useful. This dependence of method sensitivity on spectral range is discussed further in chapter 7.

Humphreys-Owen did not include in his review the use of wide-band normal reflection data for the determination of the complex refractive index by use of the Kramers-Kronig approach (described in chapter 2). This method is also widely used despite the fact that it requires very wide spectral data and assumptions regarding the optical properties outside the range of measurement [78,79,80,81,82]. The Kramers-

Kronig approach is often used with a synchrotron radiation source for the ultraviolet spectral range.

Avery's method, several other reflection and emission methods, and two polarimetric methods are analyzed for sensitivity in detail in chapter 7. The analyses given there are similar to those performed by Humphreys-Owen but the presentation is modified to facilitate comparison with ellipsometric methods and the wavelength range investigated is extended further into the infrared (to 10 μm).

4.3 Emissivity measurement methods

4.3.1 Methods ignoring polarization effects. Both calorimetric and radiometric emissivity measurements are common [83,84,85,86] with samples at elevated temperatures (since signal strength generally increases with at least the fourth power of temperature). Calorimetric measurements of emissivity are necessarily total rather than spectral so they do not provide general and widely applicable results. However, calorimetry is simple and reliable. It is usually free of large systematic errors and therefore well suited for many applications to engineering heat transfer.

In calorimetric emission studies the sample's thermal connection to its surroundings is controlled. Power supplied to or removed from the sample is related to its radiant emission. In high temperature work the power is often supplied electrically. The steady state heat balance of the sample is given by:

$$IV = \varepsilon\sigma A\,(T_1^4 - T_2^4) \qquad (4\text{–}2)$$

The electrical heating is given by the current-voltage product, IV, ε is the total hemispherical emissivity of the sample, σ is the Stefan-Boltzmann constant, A is the surface area, and the temperatures, T_1 and T_2, are those of the sample surface and its

surroundings respectively. Alternative techniques involve measuring the sample's rate of cooling or heating and equating its thermal inertia to the radiative heat loss [87,88]. With all such techniques, particular care must be taken in measuring T_1 (because of T^4_1). Usually one uses thermocouples embedded in the sample when working with good thermal conductors. If measurements go through a melting point, the plateau in a cooling curve can be used to check the thermocouple calibration.

Many systems for radiometric emission measurement were developed in the 1960's when materials for space and aeronautical applications were actively investigated. The most common methods compared a sample's emission to that from an integral blackbody cavity [89, 90] but there has also been work using a separate blackbody [91]. An integral cavity is easier to maintain at the same temperature as the sample, a critical consideration for work at short wavelengths and/or high temperatures.

The most accurate measurements of spectral emissivity by radiometric means are made by the "hole-in-tube" technique [92,93,94,95]. The sample is formed into a tube (usually directly heated electrically) and emission from its surface is compared with that from a hole drilled in the side of the tube which forms an integral blackbody cavity. This arrangement produces a cavity with nearly the same temperature as the sample surface and the blackbody cavity quality is high because the tubular shape makes the cavity surface area large compared to its hole area. The tube is also drilled with a through hole (Fig. 4-4), which is usually backed by a cooled blackened appendage. When the optical system collects light for the detector from this position, it collects neither sample emission nor blackbody emission but background scattered light which may enter the optical system anywhere between the sample and the detector. When computing emissivity from the data, the scattered signal is subtracted from both the sample signal and the blackbody signal before the two are ratioed. Further refinements of the scattered signal measurement and allowance for other non-ideal effects have made these methods the most accurate to date [95]. The agreement between the results from hole-in-tube

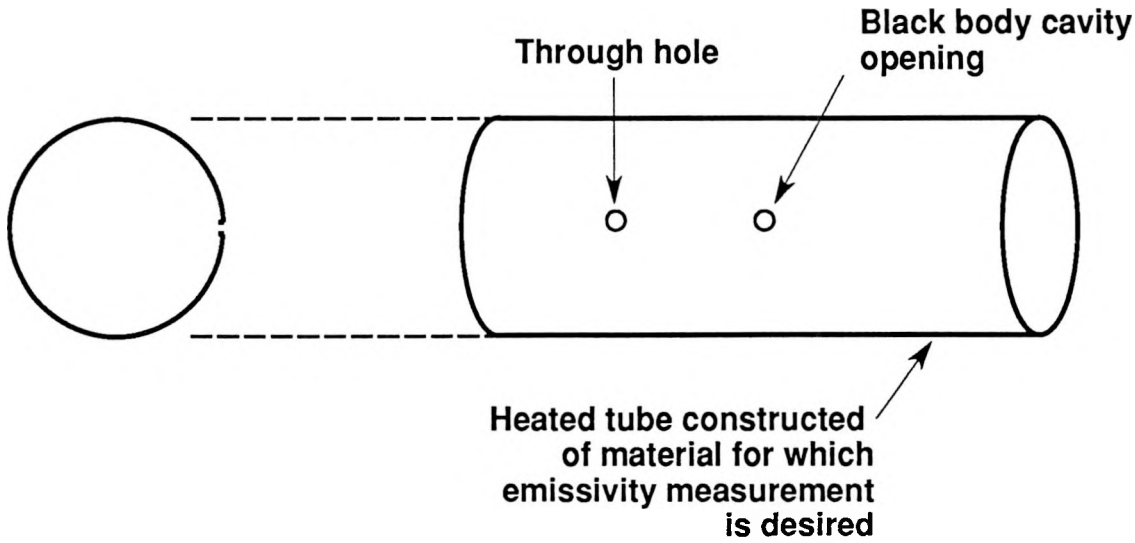

Fig. 4-4. The hole-in-tube method of emissivity measurement. The heated tube includes a blind hole for the blackbody signal and a through hole for the scattered signal.

studies is far better than is observed with other measurement methods in this field. Tungsten has been particularly well studied at high temperatures because of its use in tungsten filament lamps - as reference sources in radiometric measurements of temperature.

4.3.2 Emission methods using polarization effects. Kinbara was the first to measure a sample's polarized emission to determine its optical constants [96]. He made polarized emission measurements (at ~0.6 μm) on iron as a function of angle relative to the surface normal and used the Fresnel equations to determine n and k, the components of the complex index of refraction. In Kinbara's apparatus the parallel and perpendicularly polarized emission components were directed to separate photomultipliers and the two signals compared. The ratio of the photocurrents from the two detectors was measured every 10^{o}. Although it may be simpler to rotate a polarizer in front of a single detector (there are many possible refinements to this simple original

approach), this work represents a major improvement because it uses emission measurements to give n (λ,T) and k (λ,T) which then allow calculation of thermal radiant properties in full, $\varepsilon'_\lambda(\lambda,T)$, $\alpha'_\lambda(\lambda,T)$ and $\rho''_\lambda(\lambda,T)$. An important advantage of this approach is its elimination of the requirement for accurate knowledge of the sample surface temperature.

Several investigators varied Kinbara's approach [97, 98, 99]. Shestakov, Latyev and Chekhovskoi reviewed the topic [100] and also used the method [101]. Shestakov et. al. called the technique the self radiation method and noted that as a sample's temperature increases its higher emission increases the method's sensitivity.

Self radiation methods are also simpler than many alternatives. There is no input optical system to be aligned and tested. Often it is possible to simply rotate a polarizer in front of a detector. With solids, the sample may be rotated at the focus of the collection optics with a simple precision mechanism to obtain the angular dependence of emission. Mattei, Masclet and Herve recently reported the results of such work on gold and copper [102]. Unfortunately the sensitivity of the self radiation method for determining the complex index of refraction of metals also decreases in the infrared. Again, the sensitivites of the various techniques will be discussed in more detail in chapter 7.

4.4 Absorptivity measurement methods

Property measurements using absorption are necessarily calorimetric because absorbed radiation is converted to heat. As with calorimetric emissivity measurements, the sample's interaction with its surroundings is controlled so that a simple energy balance can be used to determine the absorbed power. The incident power is usually measured with a cavity calorimeter so the absorptivity is given by comparing the absorption of the sample surface with that of a black surface ($\alpha \sim 1$). However, calorimetric absorptivity measurements are not necessarily total (as for emissivity)

because the incident radiation can be passed through a monochromator. Similarly, calorimetric absorption work can also be directional. These two facts have made calorimetric absorbtivity measurements common. When combined with a Kramers-Kronig analysis, one can obtain a sample's complex refractive index from normal spectral absorptivity measurements [103,104].

Absorptivity measurements are most commonly performed at room temperature or lower to obtain adequate sensitivity of the calorimetric technique. Measurements at liquid nitrogen and liquid helium temperature give much increased sensitivity because the sample temperature rise due to the incident light is proportionally greater at these low temperatures. Unfortunately, extrapolation of low temperature absorption results to the temperatures of the liquid metals of interest here is not reliable. However, such measurements are relevant to radiative heat transfer when designing cryogenic equipment.

5. Selected fundamentals of ellipsometry

5.1 Purpose

Ellipsometry is the central measurement technique applied in this work. It has been used extensively as a tool for thin film characterization and as a means of probing the solid state of thick substrates. However it has only rarely been used for the determination of the thermal radiative properties of metals at high temperatures. This technique offers the possibility of high precision and detailed data on the surface radiative properties of clean and smooth metal surfaces. It yields the complex index of refraction which when used with the Fresnel equations gives the polarized reflectivity as a function of angle. Kirchoff's laws and other results quoted in chapter 2 also allow computation of spectral and directional emissivity and absorptivity from the complex refractive index.

5.2 Definitions and idealizations

Ellipsometry is defined as those optical measurement techniques which determine the intensity, shape, azimuth and polarization handedness of a beam of light. Strictly speaking polarimetry refers to measurements of shape and azimuth only, such as those performed in this work, but it has become common to refer to both polarimetric and ellipsometric methods with the term ellipsometry. Handedness and intensity were not required in the present work because measurements of the other two quantities, shape and azimuth, were sufficient to determine the two parameters of interest, the index of refraction and the extinction coefficient.

The derivation which follows assumes perfect polarizers. Although calcite polarizers for the visible have excellent polarization properties even they are not perfect.

In spectral regions outside of the visible the polarization properties of most common devices are far inferior to that of calcite.

Wave plates are common to many ellipsometers. These are devices which retard the phase of one component of polarization relative to the other by transmission through a birefringent material. The ideal wave plate has this sole effect on a beam during transmission. In practice, wave plates are useful only over narrow spectral ranges because the retardation varies with wavelength. The broad spectral range of interest to this work made wave plates impractical.

5.3 Polarizers and the law of Malus

A polarizer is any optical device that can produce a light beam which is appreciably polarized. Circular and elliptical polarizers exist but the linear type is of principal interest to this work. An ideal linear polarizer gives a linearly polarized beam, a beam with polarization fixed in one line within the plane perpendicular to the direction of beam propagation. All components of the original beam which lay out of this line are rejected by the perfect polarizer, either by reflection, absorption or separate direction of transmission (birefringence). The performance of polarizers is given by several sets of interrelated indices. The principal transmittances of a linear polarizer, g_1 and g_2, are defined as the maximum and minimum intensities transmitted by a polarizer when rotated in a perfectly polarized beam. Thus g_1 gives the fraction of a linearly polarized beam which is transmitted by a polarizer when its axis of transmission is coincident with the polarization of the beam incident on it. The second parameter, g_2, is the fraction of the same beam which is transmitted when the polarizer transmission axis is orthogonal to the incident beam polarization. For an ideal polarizer g_1 is 1 and g_2 is 0 so that the radiation whose polarization lies in the transmission axis is perfectly transmitted and all other components of polarization are extinguished. The extinction ratio, also commonly used,

is defined as the ratio between the maximum and minimum transmission through a pair of polarizers illuminated by a perfectly polarized beam when one is rotated [105]. In terms of g_1 and g_2 the extinction ratio (or polarization ratio) is:

$$F \equiv \frac{g_1^2 + g_2^2}{2\, g_1\, g_2} \cong \frac{g_1}{2\, g_2} \quad (\text{when } g_2 << g_1) \tag{5–1}$$

The term degree of polarization is also used:

$$\xi \equiv \frac{g_1 - g_2}{g_1 + g_2} \cong 1 - \frac{2g_2}{g_1} \text{ when } (g_2 << g_1) \tag{5–2}$$

Manufacturers differ on which performance index they quote for their equipment.

Calcite ($CaCO_3$) polarizers provide excellent extinction properties from approximately 0.2 μm to 2.3 μm. A typical extinction ratio, produced by the birefringence of the calcite crystal, is 1×10^5 or better. Transmission polarizers typically used in the infrared have much lower extinction ratios. Fig. 5-1 shows performance curves for five types of commercially available wire grid polarizers. The much lower extinction ratio of these units relative to calcite can make their performance in ellipsometric systems rather inferior. The only alternative, however, is the pile of plates polarizer, which works by reflection and is much more cumbersome to use. By using transmission polarizers over the full wavelength range of interest one can realize a simple experimental arrangement, such as that used here. Bennett and Bennett have given a comprehensive review of the different types of polarizing devices available [106].

The Law of Malus describes the attenuation properties of an ideal polarizer when rotated in a beam of linearly polarized light. The law is expressed mathematically as:

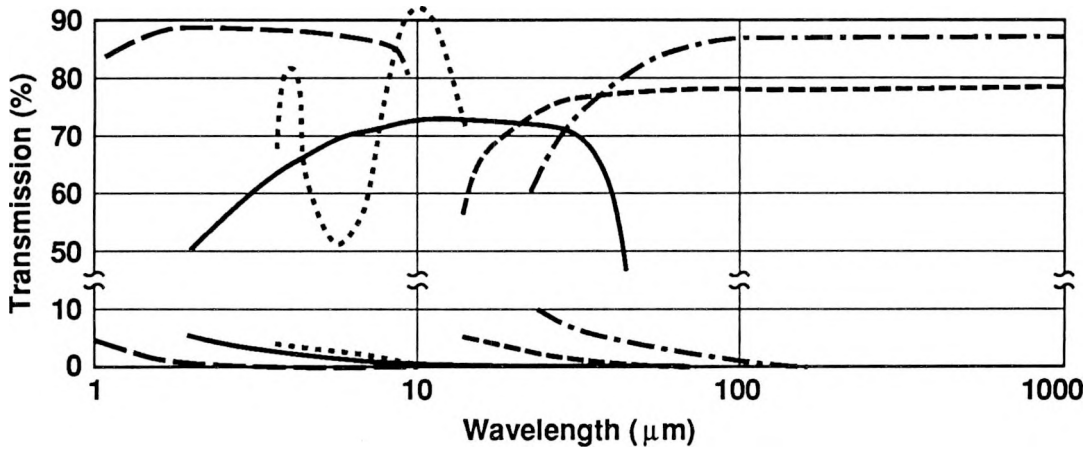

Lines above 50% transmission are g_1, transmission of electric field parallel to polarizer transmission axis

Lines below 50% transmission are g_2, transmission of electric field perpendicular to polarizer transmission axis

Line	Polarizer substrate
———	KRS-5
— — — —	Calcium fluoride
- - - - - -	Polyethylene
.....	AR coated Ge
—·—·—·—	Polyester

Fig. 5-1. Performance data for typical wire grid polarizers. Transmission parameters vary with wire size and spacing and substrate material.

$$I = I_o \cos^2(\theta) \qquad (5\text{–}3)$$

The law states that a perfect polarizer passes only that portion of the radiation incident on it which has electric field vector parallel to the polarizer's transmission axis. Hence, the cosine squared dependence of intensity is obtained.

5.4 General description of elliptically polarized light

A complete characterization of an elliptically polarized beam of light requires the specification of four parameters. The intensity of the beam gives the magnitude of the polarization ellipse. The azimuth gives the inclination of the polarization ellipse relative to a line perpendicular to the direction of beam propagation. The shape of the ellipse is given by the ratio of the major to minor axes of the ellipse. Lastly, the handedness determines in which direction the tip of the electric field vector is rotating about the ellipse, either clockwise or counterclockwise. For partially polarized elliptical beams, a fifth parameter is required giving the degree of polarization of the beam (not to be confused with the degree of polarization used to evaluate polarizer performance). This last parameter, not of interest to this work because fully polarized beams are always used, gives the fraction of the intensity of a beam which has non-random polarization.

For a quasi-monochromatic beam of radiation travelling in the z direction the two field components which combine to give elliptical polarization are:

$$E_x = E_{x_0} \cos\left(\omega t - \frac{2\pi z}{\lambda} + \delta_x \right) \tag{5–4}$$

$$E_y = E_{y_0} \cos\left(\omega t - \frac{2\pi z}{\lambda} + \delta_y \right) \tag{5–5}$$

At any point along the propagation direction z, say z = 0, the equations simplify to:

$$E_x = E_{x_0} \cos(\omega t + \delta_x) \tag{5–6}$$

$$E_y = E_{y_0} \cos(\omega t + \delta_y) \tag{5–7}$$

When these equations are combined to eliminate t the equation of the polarization ellipse is obtained:

$$\frac{E_x^2}{E_{x_0}^2} + \frac{E_y^2}{E_{y_0}^2} - \frac{2E_x E_y \cos(\delta_y - \delta_x)}{E_{x_0} E_{y_0}} = \sin^2(\delta_y - \delta_x) \qquad (5\text{–}8)$$

The presence of the third term on the left hand side, the cross product term, indicates that the reference axes, x and y, do not coincide with the major and minor axes of the ellipse. For $\delta_y - \delta_x = (m+1/2)\pi$ [m = 0,1,2,...] the cross product term vanishes and the more familiar ellipse equation results:

$$\frac{E_x^2}{E_{x_o}^2} + \frac{E_y^2}{E_{y_o}^2} = 1 \qquad (5\text{–}9)$$

The general polarization ellipse equation shows that four quantities specify the ellipse, E_{x_0} E_{y_0}, δ_y and δ_x. However these forms are not convenient because they are related to an arbitrary reference frame rather than the frame defined by the major and minor axes.

A more convenient set of parameters is given by

1) the beam intensity, I
2) its ellipticity, 1-η
3) its azimuth, ζ
4) its handedness, the sign of η.

These four quantities are related to the reference frame quantities as follows [10]:

$$I = E_{x_o}^2 + E_{y_o}^2 \qquad (5\text{–}10)$$

$$\tan 2\zeta = \frac{2\,E_{x_o}\,E_{y_o}\cos(\delta_y - \delta_x)}{E_{x_o}^2 - E_{y_o}^2} \tag{5–11}$$

$$\frac{2\eta}{1+\eta^2} = \frac{2E_{x_o}\,E_{y_o}\sin(\delta_y - \delta_x)}{E_{x_o}^2 + E_{y_o}^2} \tag{5–12}$$

$$\text{Handedness} = \text{sign of } \eta \tag{5–13}$$

The intensity is the sum of the squares of the component amplitudes. The ellipticity is one minus the ratio of the semiminor to semimajor axes. The azimuth is the inclination of the semimajor axis to the x axis. The handedness is the sign of η [10].

5.5 Fundamentals of the ellipsometric method due to Beattie and Conn

A convenient and practical ellipsometric method for determining the optical constants of metallic conductors in the infrared was developed simultaneously by Beattie and Conn [107,108] and Hodgson [109] in 1955. Because it does not employ the narrow band wave plates common in many ellipsometers, this method is readily applied over the broad spectral regions for which polarizers are available. A large number of subsequent workers have used this method [110–117]. Although several variants of the method have been proposed and used, the basic original approach itself remains popular.

The method can be explained with the help of Fig. 5-2. A beam of arbitrary polarization passes through a linear polarizer and reflects off the material of interest. This first linear polarizer, called the polarizer, is rotatable with rotation axis coincident with the beam axis. After reflection the beam passes through a second polarizer, referred to as the analyzer, which is also rotatable about an axis coincident with the axis of the

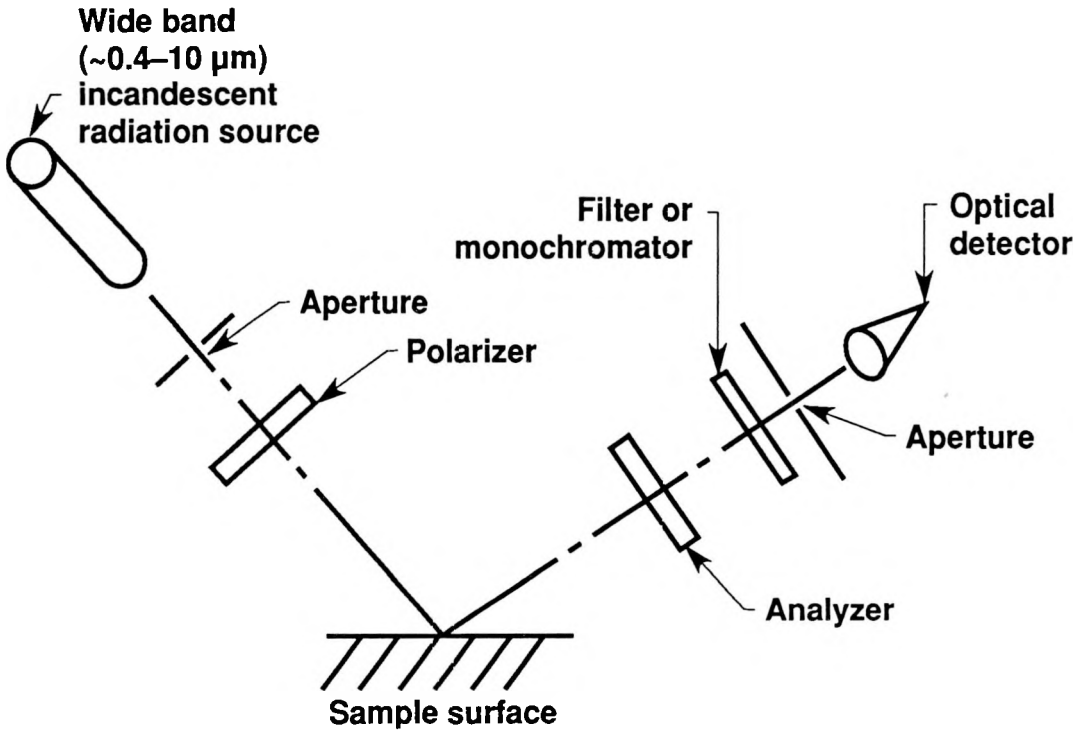

Fig. 5-2. Principal components of a spectroscopic ellipsometer.

reflected beam. The linearly polarized beam becomes an elliptically polarized beam after reflection from the sample surface, and the intensity variation of the radiation transmitted by the analyzer can yield the salient parameters of the polarization ellipse of the reflected radiation [118]. When the first polarizer is assumed ideal the wave it transmits can be written:

$$E \cos \psi_N \cos(\omega t) + E \sin \psi_N \cos(\omega t) \qquad (5\text{–}14)$$

where polarizer azimuth is ψ_N. The zero azimuth for the polarizer rotation is generally arbitrary but the mathematics is simpler if it is taken in the plane of incidence (defined by the beam axis and the surface normal). After reflection the wave can be described as:

$$E r_p \cos \psi_N \cos(\omega t + \delta_p) + E r_s \sin \psi_N \cos(\omega t + \delta_s) \qquad (5\text{–}15)$$

This expression allows for the reflection coefficient and phase shift incurred by each component of polarization upon reflection at the conductor surface. After passing through the analyzer the beam can then be written:

$$E\, r_p \cos\psi_N \cos\psi_A \cos(\omega t + \delta_p) + E\, r_s \sin\psi_N \sin\psi_A \cos(\omega t + \delta_s) \qquad (5\text{–}16)$$

The angle ψ_A is the azimuth of the analyzer and it is again defined to be zero in the plane of incidence. This last expression results from a double application of the law of Malus with an intermediate reflection (expressed as 2 phase shifts and 2 amplitude attenuations). The intensity is found by squaring the electric field vector amplitude given by (5-16):

$$I = E^2 [\ r_p^2 \cos^2\psi_N \cos^2\psi_A + r_s^2 \sin^2\psi_N \sin^2\psi_A + \frac{1}{2}\, r_p\, r_s \sin 2\psi_N \sin 2\psi_A \cos\Delta\ ] \qquad (5\text{–}17)$$

where

$$\Delta = \delta_p - \delta_s \qquad (5\text{–}18)$$

Equation (5-17) is relevant because at optical frequencies detectors measure intensity rather than amplitude. Further simplification of this relation results when the ratio of polarized reflection amplitudes is introduced:

$$\rho\hat{} = \frac{|r_p|}{|r_s|} \qquad (5\text{–}19)$$

The intensity leaving the analyzer can then be written:

$$\frac{I}{E^2 r_s^2} = \sin^2 \psi_N \sin^2 \psi_A + \rho\hat{}^2 \cos^2 \psi_N \cos^2 \psi_A + \frac{1}{2} \rho\hat{} \sin(2\psi_N) \sin(2\psi_A) \cos \Delta \quad (5\text{–}20)$$

This relation is symmetric in ψ_N and ψ_A so that the roles of the two polarizers are interchangable. This fact can be useful when either polarization sensitive detectors or polarized light sources must be used. With polarized light sources the polarizer should be held fixed and the analyzer rotated. Then the variation in intensity with analyzer azimuth can be used with the above equation to deduce Δ and $\rho\hat{}$. For polarization sensitive detectors the polarizer should be rotated and the analyzer held fixed. If the polarizer is fixed and the analyzer is rotated while using a polarization sensitive detector, the detector's response will alter the transmitted intensity variation and errors will be introduced.

In ellipsometry it is common to work in terms of ψ and Δ, where Δ is defined above and ψ is given by:

$$\tan \psi = \rho\hat{} \quad (5\text{–}21)$$

The method of Beattie and Conn gives ψ and Δ for a particular set of intensity measurements at two pairs of ψ_N and ψ_A settings, as described in section 5.7.

5.6 Computation of the complex refractive index from ψ and Δ

Price gave a derivation of the complex index of refraction from ψ and Δ measurements in 1946 [119] but the version given in Sokolov [120] is more complete. The derivation combines Snell's law, the Fresnel equations and the definitions of ψ and Δ given above. Sokolov's results are:

$$\epsilon/\epsilon_o = (n^2 - k^2) = \sin^2\theta\left[1 + \tan^2\theta\left[\frac{\cos^2 2\psi - \sin^2 2\psi \sin^2\Delta}{(1 + \sin 2\psi \cos\Delta)^2}\right]\right] \qquad (5\text{–}22)$$

$$(\epsilon' / \epsilon_o) = 2nk = 2\sin^2\theta \tan^2\theta\left[\frac{\cos 2\psi \sin 2\psi \sin\Delta}{(1 + \sin 2\psi \cos\Delta)^2}\right] \qquad (5\text{–}23)$$

with $\tan\psi = |r_p| / |r_s|$

and θ = angle of incidence

and Δ = relative phase shift on reflection

The standard texts can be consulted for a complete treatment of the other common formulations of the optical constants [6,7,8].

5.7 Computation of ψ and Δ from the measured quantities in the method of Beattie and Conn

The dependence of the detected intensity on the azimuths of the polarizer and analyzer was given above (5-20). Beattie and Conn proposed to fix the polarizer at 45° to the plane of incidence and determine ψ by making intensity readings at two azimuths of the analyzer, namely zero and 90°. Thus, from (5-20) one obtains:

$$I_1 \equiv I(\psi_N{=}45°, \psi_A{=}90°) = I_o \sin^2(45°) = \frac{I_o}{2} \qquad (5\text{–}24)$$

$$I_2 \equiv I(\psi_N{=}45°, \psi_A{=}0°) = I_o \rho^{\wedge 2} \cos^2 45° = \frac{I_o}{2} \rho^{\wedge 2} \qquad (5\text{–}25)$$

where $I_o = I(\psi_N{=}90°, \psi_A{=}90°)$

From the ratio of these two equations one obtains:

$$\rho\hat{}(\theta) = \tan\psi = \sqrt{I_2 / I_1} \tag{5–26}$$

Thus, the first ellipsometric parameter, $\rho\hat{}$, is determined from the ratio of two intensity measurements. The second two intensity readings are taken with the analyzer at $\pm 45^{o}$ relative to the plane of incidence with the polarizer position unchanged. These readings give:

$$I_3 \equiv I(\psi_N = 45^{o}, \psi_A = 45^{o}) = I_o (1 + \rho\hat{}^2 + 2\rho\hat{} \cos\Delta)/4. \tag{5–27}$$

$$I_4 \equiv I(\psi_N = 45^{o}, \psi_A = -45^{o}) = I_o (1 + \rho\hat{}^2 - 2\rho\hat{} \cos\Delta)/4. \tag{5–28}$$

In principle either I_3 or I_4 can be used seperately with I_1 and I_2 to obtain the phase shift Δ. However, when the reflectivity is high, as it is for metals at long wavelengths, determining Δ in this way makes its value sensitive to the small difference $\varepsilon \equiv (1 - \rho\hat{})$. For this reason, it is better to determine the phase shift Δ from I_3 and I_4 using the equation:

$$\cos\Delta = \left\{ \frac{1}{2}\left(\rho\hat{} + \frac{1}{\rho\hat{}}\right) \right\} \left\{ (I_3 - I_4) / (I_3 + I_4) \right\} \tag{5–29}$$

Here, when $\varepsilon \equiv (1 - \rho\hat{}) << 1$, the first bracket becomes $\{1 + 1/2(\varepsilon^2 + \varepsilon^3 + \cdots)\}$ which differs from unity by ε^2 and higher order terms. Thus use of (5-29) to determine Δ is insensitive to the exact value of $\rho\hat{}$ determined from I_1 and I_2 via (5-26).

For instance, for $\rho\hat{} = 0.8$ the first term in brackets is 1.025. Thus, the use of I_3 and I_4 makes the result for $\cos(\Delta)$ only weakly dependent on the value of $\rho\hat{}$ determined from I_1 and I_2 (for good reflectors).

The use of (5-29) for the relative phase shift may however lead to measurement sensitivity problems in the classical long wavelength limit for conductors, $\rho\hat{} \rightarrow 1$ and

$\Delta \rightarrow 0$. However, all methods become insensitive in this limit and the method of Beattie and Conn allows one to go to longer wavelengths than methods developed earlier.

5.8 Practical considerations with the method of Beattie and Conn

The method of Beattie and Conn is limited to spectral ranges where polarizers with high extinction ratios are available. As discussed above this is the visible range and longer. The technique also assumes a detector with linear response over the intensity range of the four measurements. Miller [4] was sufficiently concerned about linearity to develop a variant of the Beattie and Conn approach which involved finding polarizer angles for which intensities were equal. This technique eliminated nonlinear detector effects but was less convenient than the original approach. Sensitivity effects and measurement procedures in the Miller approach are analyzed in chapter 7.

Ellipsometric methods in general are sensitive to the presence of surface films. This topic was discussed by Hodgson [2]:

> The reflection coefficients of a liquid metal are determined by the properties of a surface layer a few hundred atoms thick. If the optical constants calculated from the reflection coefficients are to represent the properties of the bulk liquid metal, it is important that the surface be free from contamination. A visual inspection of the surface under a strong beam of light will detect any contamination which causes diffuse scattering of light. A coherent layer of contamination, such as oxide, will not be seen and even a 10 angstrom layer will appreciably change the measured n and k. Measurements at various angles of incidence are not very helpful in detecting such a layer because the deviations from the Fresnel equations are very small. It is more useful to look at the variation with wavelength since the

effects of a surface layer should have a strong and predictable wavelength dependence.

For the oblique angles of incidence commonly used, even very thin surface films overlying very clean substrates can alter the (ψ, Δ) parameters of a surface.

The method of Beattie and Conn is dependent on accurate knowledge of the angle of incidence. The relations given above for the complex refractive index as a function of ψ and Δ include the angle of incidence as $\sin^2$ and $\tan^2$ dependences. The tangent is a rapidly varying function at the oblique angles of incidence often used.

The solid angle of illumination is also a concern. For whatever solid angle is used the results will be a weighted average over that solid angle. Clearly smaller solid angles are preferred, neglecting other effects (such as decrease in signal magnitude and reduced signal/noise with decreased illumination cone angle) of course.

Polarizer mounting effects and uniformity are a concern. Calcite polarizers are available in very high grade crystals but wire grid polarizers often have visually noticeable transmission variation across their working surface [121]. When the polarizer is exactly centered in a uniform beam this variation has no influence on the recorded intensities but for a noncentered polarizer the four recorded intensities are derived from a polarizer having four different transmission loss values. Care must be exercised when positioning the polarizer mount. Lack of alignment is readily checked by comparing intensity readings between polarizer positions 180^o apart.

The axis of polarizer rotation must also be carefully aligned to the beam axis. For differing beam and rotation axes the beam transmitted by the polarizer precesses on the detector surface, leading to measurement errors. The optical path length in the polarizer influences the magnitude of this effect and for polarizers manufactured with any wedge (non parallel edge faces) this effect is essentially unavoidable. Clearly the polarizer

mounting mechanisms are critical. These are discussed in the optical system description of Chapter 8.

Once the polarizers are mounted adequately, their orientation must be registered relative to the plane of incidence. Procedures for accomplishing this have been given in the literature [122,123,124].

When the method of Beattie and Conn is applied with the sample in vacuum and portions of the optical system at ambient pressure, the possibility of stress birefringence in the optical access ports exists [121]. Common viewports are made of quartz which can exhibit significant stress birefringence. This study used calcium fluoride windows and stress birefringence was shown experimentally to be small. Ellipsometric data was recorded throughout the wavelength range of interest with the apparatus under vacuum and with the chamber filled with dry nitrogen at one atmosphere. There were no significant differences between the two sets of measurements on the solid, polished metal sample under study.

5.9 Fundamentals of the Stokes' vector

The Stokes vector, a construct used to aid in the understanding and mathematical manipulation of polarized light, consists of four parameters which uniquely specify the intensity and polarization of any incoherent beam of quasi-monochromatic light. The four components, I, M, C, and S are related to the wave amplitudes and phase angles by the following relations:

$$I = E_{x_o}^2 + E_{y_o}^2 \qquad M = E_{x_o}^2 - E_{y_o}^2$$

$$C = 2E_{x_o} E_{y_o} \cos(\delta_y - \delta_x) \qquad S = 2E_{x_o} E_{y_o} \sin(\delta_y - \delta_x) \qquad (5\text{–}30)$$

The four Stokes parameters are related to the polarization ellipse discussed earlier as follows:

$$\text{Size } I \quad ; \quad \text{Azimuth} \quad C/M = \tan 2\zeta$$

$$\text{Shape } \frac{|S|}{I} = \frac{2\eta}{1+\eta^2} \; ; \; \text{Handedness } \frac{|S|}{I} = \text{sign of } S \qquad (5\text{–}31)$$

Stokes vectors are quantitatively useful when applied with Mueller matrices. A Mueller matrix expresses the intensity and polarization modifying properties of an optical element so that when the Stokes vector of a beam entering an optical element is pre-multiplied by the element's Mueller matrix, the resulting Stokes vector expresses the properties of the beam which exits the optical element. This formalism, known as the Mueller calculus, is described in detail in ellipsometry texts [10,125] as well as the classical works on optics [126]. This procedure for treating the polarization properties of incoherent beams using vectors parallels the Jones calculus [127,128,129] which treats coherent beams.

6. A review of optical property literature for tungsten, uranium and aluminum

6.1 Overview

Measurements of the optical properties of metallic surfaces are reported in many sources. The engineering literature includes reflectivity, emissivity and absorptivity data for use in radiative heat transfer calculations. The physics literature includes similar data as well as optical constant measurements for investigation of the electronic structure of the substrate. The surface science literature includes reflection and ellipsometric studies for studies of surface chemistry effects and process control uses. Fortunately, the many sources include review articles; some describe the present status of the field and others provide compilations of property results.

This summary of literature for the three elements of interest here, is limited to the review papers, the most significant early works and the most recent works.

6.2 Tungsten

6.2.1 Review papers treating tungsten. The thermal radiative properties of tungsten are included in the data compilation by Touloukian [1]. This document compiles reports from the engineering literature and includes results for many materials and on all three radiative properties as a function of angle, wavelength and temperature. The review includes data from many sources in which various surface preparations and material processing techniques were used so that the presented results possess a large amount of scatter. These data are useful when the composition and surface condition of a particular sample seem to match an application.

The American Institute of Physics Handbook [130] includes a compilation of the complex index of refraction of the elements. The results for tungsten given there come from a wide range of sources. Some of the works were performed at cryogenic temperatures and others at ambient temperatures. This compilation is adequate for these temperature ranges but for higher temperatures, other references are appropriate.

The Physics Daten series published in Karlsruhe, Germany includes two volumes on the optical properties of metals [12]. The review of tungsten optical properties given in volume two is the most complete available. The review gives information from thirty six citations including specification of the wavelength range, temperature, sample type, data presentation and measurement method. The results of selected low temperature studies are tabulated.

The optical constants of solids were reviewed in a volume edited by Palik [34]. The section concerning tungsten was written by D. W. Lynch, a coauthor of the Physics Daten volumes. This review, including 37 references, is far briefer than the Karlsruhe review, but does include a few citations of work peformed at high temperatures. These will be discussed below.

Ordal et al. have reviewed the infrared optical properties of tungsten in two recent articles [131,132]. The majority of the wavelength range of interest in these works is beyond 10 μm, so that detailed comparisons to the Hagen-Rubens approximation could be made.

The optical properties of tungsten were also reviewed by Latyev et. al. in a volume hitherto only available in Russian [133]. Since these workers have performed the most accurate studies of high temperature tungsten [94,95,134] and their review of high temperature methods of determining optical properties [100] is the most complete extant, this is a valuable article.

6.2.2 Principal works on the optical properties of high temperature tungsten.

The most valuable studies of the emissivity of tungsten were made by DeVos [92], Larrabee [93] and Latyev, Shestakov and Chekhovskoi [94,95]. These works, summarized in the discussion below and in Table 6.1, utilized much improved experimental methods to obtain accuracy and precision superior to their predecessors.

TABLE 6.1

Principal studies of the normal spectral emissivity of tungsten at high temperature

Date (-)	Authors (-)	Temperature Range (K)	Wavelenth Range (μm)	Pressure (torr)
1954	De Vos [92]	1600–2800	0.23–2.7	5×10^{-6}
1959	Larrabee [93]	1600–2400	0.31–0.8	1×10^{-8}
1966	Dreshfield & House [194]	1360–2480	0.42–15	5×10^{-7}
1967	Dmitriev [195]	(Ph.D. Thesis, not obtained)		
1968	Thomas [189]	2000–3000	0.35–6	1×10^{-5}
1970	Latyev, Chekhovskoi & Shestakov [95]	1200–2600	0.4–4	2×10^{-7}
1970	Kovalev and Muchnik [197]	1400–3000	0.66–5.12	not reported

As early as 1954, it was recognized by De Vos that " . . . the values of the emissivity of tungsten which are adopted by the principal standard laboratories show

considerable differences." De Vos avoided many of the systematic errors of his predecessors by using an emission measurement scheme of improved design. In this apparatus a blockbody cavity is integral to the tungsten sample so that the temperature differences between the sample and the cavity are small. De Vos used 0.051 mm thick tungsten ribbon shaped into a triangular tube. The tube length was 160 mm, each leg of the triangle was 4.0 mm wide and the blackbody holes were 0.012 mm in diameter. In a separate publication [135] , De Vos calculated the cavity emissivity for the above geometry, to be better than 0.997 in the wavelength range of interest (0.2 to 2.7 μm, 1600 to 2800 K). Several holes were drilled in the tube to check if multiple holes or their positioning could effect the radiant output of the cavity and a nicol prism was used to check the polarization of the cavity emission. Only hole placement very near the tube seams was found to effect cavity emission and no polarization was observed.

De Vos considered sample and surface preparation and composition in much more detail than his predecessors. The root mean square uncertainty of the average emissivity results at several wavelengths was reported as 1.1% or less. At the time these were the most reliable tungsten measurements reported, possibly even the best emissivity measurements for any material. Larrabee [93] followed De Vos with a similar configuration but covered a smaller parameter range (0.3 to 0.8 μm, 1600 K to 2400 K). The blackbody cavity was a round tube of 3.2 mm diameter, 102 mm length, 0.025 mm wall thickness and 0.33 mm hole diameter. However, Larrabee found that there was a third optical signal to be considered. He considered not only the cavity emission and the sample emission but also the light scattered into the optical system. The latter signal was subtracted from each of the other signals before taking their ratio to obtain the emissivity. Larrabee drilled a through hole in his tube and mounted a cold and blackened appendage behind the hole. This addition gave a high quality but essentially non-emitting cavity behind the through hole. Any signal obtained from the optical system while viewing the

through hole was then due to light scattered into the optical system. The normal spectral emissivity was computed from the three measured signals from:

$$\varepsilon_{n,\lambda}(\lambda,T) = \frac{V_{sam} - V_{scat}}{V_b - V_{scat}} \qquad (6\text{–}1)$$

Larrabee also considered sample and surface purity and reported system vacuum levels of 3×10^{-9} at sealoff and less than 9.5×10^{-8} torr during testing. Larrabee's results were consistently lower than those of De Vos and other predecessors, a fact he ascribed to the scattered signal subtraction (For reference, the scattered signal correction changes the emissivity result from 0.483 to 0.471 at 0.4 μm and 1800 K or a change of 2.5%.).

Latyev, Chekhovskoi and Shestakov [94] improved upon the work of Larrabee and De Vos by studying a greater wavelength range 0.4 to 4.0 μm and analyzing the scattered signal and other non ideal effects in more detail. Latyev et al., used the hole in tube approach again with similar but slightly greater dimensions (260 mm long circular tube of 8 mm diameter, material thickness of 0.05 mm and cavity diameter of 0.5 mm). Their vacuum level was 3×10^{-7} torr during testing and the sample bulk was 99.95% pure.

The data reduction involved: (1) the dark signal of the radiation detector; (2) the radiation scattered in the optical system; (3) reflected radiation from the sighting glass (vacuum system viewport) and the vacuum chamber walls; and (4) the effective emissivity of the blackbody. A detailed description of this procedure appeared in Latyev et al.'s earlier publication [95] on tungsten properties over a reduced wavelength range (0.40 to 0.76 μm).

Latyev et al., reasoned that De Vos's results were 2 to 3% higher than theirs because of the ignored scattered signal and the smaller grain sizes typical of De Vos's

material. Their approximate correction of De Vos's results for these effects brought the two sets of measurements into agreement within their limits of accuracy.

Latyev et al., also reasoned that Larrabee's work was systematically in error for several reasons. Larrabee did not correct for reflections from his sighting glass and his measurement of the scattered light component was larger than estimates of the maximum possible value. Once again, when Latyev et al. corrected Larrabee's results the two works agreed within their estimated accuracy. Figures 6-1 and 6-2, reproduced from Latyev et al., compare the various principal tungsten studies at 1600 K and 2400 K. Errors increase with wavelength in the infrared because sample signal is declining as given by the Planck function.

6.2.3 Recent work on tungsten optical properties. Recent studies of the optical constants of tungsten in the infrared have been made by Ordal et. al. [131,132], Aksyutov [136], and Nomerovannaya et. al. [137]. Ordal's data covers the 2.5 to 25 μm region and was done at room temperature. Aksyutov reported the normal spectral emissivity and the complex index of refraction in the 3.8 to 6 μm region . This wavelength range has not been much studied at the temperatures Aksyutov used, (453 K, 553 K and 623 K). Nomerovannaya's data, which covers from 0.265 to 20 μm and was obtained at room temperature from single crystals cut parallel to the (110) and (100) planes. The two planes gave similar indices of refraction, within the limits of error and the results show good agreement with the older results of Roberts [138].

In recent work, Blanchet et. al., Pigeat et al. and Ramalingam and Jacobson investigated the effects of impurities. Blanchet et. al. [139] studied hydrogen chemisorbed on the tungsten (110) surface using reflectance measurements from 0.2 to 2.5 μm . They also used wave function calculations to interpret the experimental results. Pigeat et. al. [140] studied the influence of oxidation on the normal spectral emissivity of tungsten in the wavelength range 1.0 to 10.0 μm and the temperature range 800 to 1000

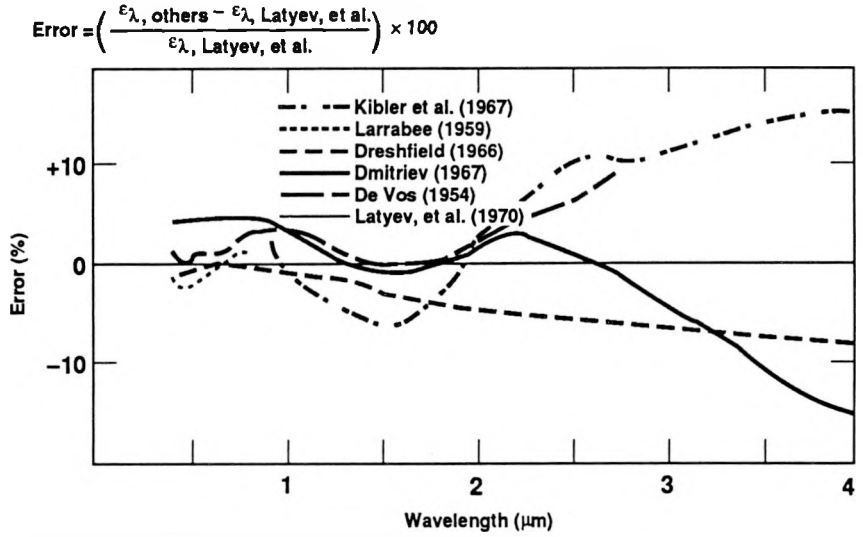

[Reproduced with permission from; Latyev, Chekhovskoi, and Shestakov, High Temperature-High Pressure, 2, pp. 175–181 (1970)].

Fig. 6-1. A comparison of emissivity results reported for tungsten at 1600 K.

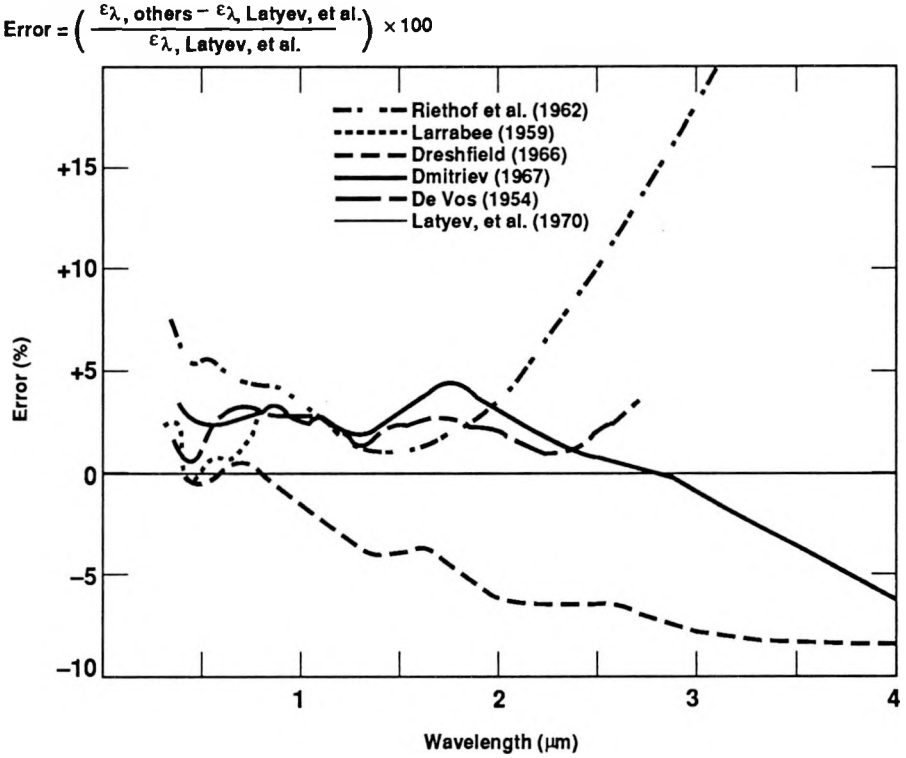

[Reproduced with permission from; Latyev, Chekhovskoi, and Shestakov, High Temperature-High Pressure, 2, pp. 175–181 (1970)].

Fig. 6-2. A comparison of emissivity results reported for tungsten for 2400 K.

K. An oxide island growth model and an optical model were used to predict the increase in emissivity with time of exposure to oxygen. Ramalingam and Jacobson [141] measured the variation in normal spectral (0.535 μm) emissivity with rhenium content of thoriated tungsten (1% mol ThO_2) in the temperature range of 1300 to 2300 K. The vacuum level was reported (~4.0×10^{-6} torr) but the surface composition of the sample was not.

Several recent studies have given emissivity results for tungsten at the melting temperature. Cezairliyan and Miller [142] measured the normal spectral emissivity of 23 specimens of molten tungsten and deduced a value of 0.404 at 0.653 μm . This value is in good agreement with values extrapolated from the solid tungsten studies discussed in the last section. However, Hiernaut,Sakuma and Ronchi [143] used a six-color pyrometer to obtain a value of 0.360 for the normal spectral emissivity at 0.655 μm. The pyrometer operates between 0.5 and 1 μm and is described in [144]. Hiernault et. al.'s results agree well with those of DeVos [92] but are not in agreement with Cezairliyan and Miller. Other efforts with molten tungsten are also conflicting. Arpaci, Betz and Frohberg [145] used a disappearing filament pyrometer calibrated at 0.547 and 0.65 μm to obtain the normal spectral emissivity of molten tungsten. They obtained a value of 0.378 at 0.650 μm and a value of 0.381 at 0.547 μm. The average normal spectral emissivity deduced from these three studies is 0.381 (at 0.65 μm) and the difference between the minimum and maximum values is 0.044. Thus, the range is 11.5 % of the average value. Clearly, experimental methods for liquids have not reached the level of precision demonstrated with solid samples.

In summary, recent work on the optical properties of tungsten have focused on a range of surface condition and purity issues with measurements in several narrow wavelength and temperature ranges. The complex index of refraction at high temperatures in the infrared remains uncertain and the range of results for the normal

spectral emissivity of liquid tungsten is the visible underscores the difficulties encountered with molten metals.

6.3 Aluminum

6.3.1 Review papers treating aluminum. Comments similar to those made above concerning review articles on tungsten apply here for aluminum. The review in the volume by Touloukian includes 25 citations [1] while that in the Physics Daten series [12] has 42. The review in The Handbook of Optical Constants of Solids [34], this time written by Smith, Shiles and Inokuti, includes 143 citations. A subsection describes the temperature dependence of the optical constants but neither of the two studies of molten aluminum [4,5] discussed below are referenced. A review by Ordal et. al. [131,132] considers long wavelengths (as with tungsten) and the compilation of data for room temperature and colder samples in the American Institute of Physics Handbook [130] is extensive. However, none of these reviews discusses liquid aluminum, which differs fundamentally from the solid phase.

The optical properties of molten aluminum were reviewed by Hodgson in the text "Liquid Metals" edited by Sylvan Beer [2]. Hodgson also provides some of his own data for solid aluminum and describes the study by Miller [4]. However, the continuation of Miller's work described by Comins [5] was not included in Hodgson's review.

Smith and Segall have reviewed intraband and interband processes in the infrared spectrum of metallic aluminum [3]. It uses the results of previous works to formulate a consistent picture of the infrared reflectance spectrum and dielectric function of solid aluminum.

6.3.2 Recent work on aluminum optical properties. Studies of the optical properties of pure aluminum have been published recently by Allen [146], Allen and

Sunderland [147], Halford, Chin and Norman [148], Churaeva and Zorin [149], Gergely and Croce [150], Decker and Hodgkin [151], and Masuda and Higano [152]. In 1976 Allen reported measurements on pure and oxidized samples of solid aluminum using a combined ellipsometer-Auger electron spectrometer system. The single wavelength ellipsometer (0.63 μm) was used to determine the complex index of refraction as the Auger spectrometer monitored the oxide film thickness. Allen's results are repeatedly referenced in the most recent literature [37,38,39], despite the many more recent studies, because of the demonstrated pure composition of his samples. In 1977 Allen and Sunderland published more aluminum results from a modified version of the same apparatus. A carbon dioxide laser was added to allow ellipsometry to be performed at 10.6 μm. Halford et. al. studied the effect of vacuum deposition conditions on the optical constants of ultrapure aluminum films. They found that bulk oxide contamination (as opposed to surface oxide) is a primary factor affecting optical properties. In 1987 Churaeva and Zorin reported ellipsometric work at 0.585 μm on aluminum films in media of different refractive index. They found that a transition layer model was required to explain the measurements when oxide layers or other media covered the pure metal surface. Gergely and Croce reported a study of aluminum using spectroscopic ellipsometry, x-ray specular reflection analysis, and plasmon energy loss spectroscopy. Decker and Hodgkin reported near normal reflectance data for pure aluminum mirrors. A wide spectral range (0.4 to 10 μm) was covered and the sample temperature was varied between 270 and 450 K. The results were interpreted with consideration of both inter- and intraband electronic transition effects. Masuda and Higano measured the total hemispherical emissivity of aluminum in the temperature range 330 to 630 K using a transient calorimetric technique.

A number of recent ellipsometeric studies have focused on the effects of oxidation on the optical constants of aluminum. Grimblot and Eldridge used in-situ ellipsometry at 0.546 micrometers to study the surface reaction with oxygen of the (111) aluminum

surface [153]. Bradshaw, Hofmann and Wyrobisch [154] and Hayden, Wyrobisch, Oppermann, Hachicha, Hofmann and Bradshaw [155] also studied the effect of oxygen on the (111), (100) and (110) surfaces. They used ellipsometry at 0.546 μm, Auger electron spectroscopy, low energy electron diffraction, surface plasmon spectroscopy and also studied changes of the work function. The ellipsometry was used to monitor the change in phase difference and ellipse azimuth on reflection as the surface exposure to oxygen increased.

As with tungsten, recent studies of the optical properties of solid aluminum have focused on surface effects. More sophisticated methods of surface analysis have been applied in conjunction with optical studies. However, the optical methods have been applied over spectral ranges yet narrower than those used with tungsten and the studies of liquid properties have been done only at single wavelengths. In general, the results are not of general use to radiative heat transfer.

6.3.3 Optical property studies of molten aluminum. The earliest study of molten aluminum was made by Miller in 1969 [4]. A variant of the method of Beattie and Conn was used to obtain the optical constants of aluminum, copper, gold, silver, iron, cobalt, and nickel in the 0.25 to 1.6 micrometer range. Sample temperature was as high as 1870 K , the vacuum level was 10^{-5} torr and hydrogen gas was used to remove surface oxide. Comins used the same apparatus and method to study molten aluminum in the range 3.3 to 8 micrometers [5]. He also studied copper, gold, mercury, gallium, tin, lead, bismuth, and copper-tin alloys in portions of the 0.9 to 8 μm range. Sample temperatures were as high as 1470 K. Wire grid polarizers were used for the infrared ellipsometry, as in this work. Since the present study covers the 0.45 to 9.5 μm range, comparisons are made to the results of both Miller and Comins.

Several reports of the optical properties of molten aluminum at 10.6 μm, the wavelength of carbon dioxide lasers, have been published. In 1989, Bruckner, Schaefer

and Uhlenbusch [156] used ellipsometry to measure the optical constants. Samples and the oven system for heating them were contained in ultra high vacuum (1×10^{-9} torr). A jump in the absorptivity (deduced from the optical constants) from 0.03 to 0.07 on melting was noted. Dreehsen, Hartwich, Schaefer and Uhlenbusch also published similar work at an earlier date (1984) [157] and noted a rise in absorptivity from 0.05 to 0.38. In 1983, Konov and Tokarev [158] reported absorption measurements at 10.6 μm in the temperature range 293 K to 1053 K. They also noted a jump in absorptivity, from 0.055 to 0.075, upon melting. The large changes noted on melting may imply that surface oxide effects are present.

6.4 Uranium

6.4.1 Review papers treating uranium. The Physics Daten volume devoted to the noble metals, the lanthanides and the actinides includes the only review of the optical properties of uranium. This review cites 5 works and notes good agreement between the results of Weaver [159] and Faldt and Nilsson [160]. The early works on uranium which are from somewhat obscure sources, are not listed. Of the five citations in this review, only 3 are in the wavelength range of interest here, the other two treat much greater photon energies.

6.4.2 Reported work on the thermal radiative properties and optical constants of uranium. An extensive literature search has revealed seven citations for the optical properties of uranium, only one of which is for the liquid. Of the remaining six citations only one presents measurements of the optical constants (the complex index of refraction), and this is for material at or below room temperature. Of the six references for solid uranium, only three are for elevated temperatures, 1100 K to 1406 K (the melting point), and are of particular interest here.

In 1915, Burgess and Waltenberg [161] reported the normal spectral emissivity of liquid uranium at 0.65 μm to be 0.34. The authors developed a micropyrometer for examining spots of molten metal on tungsten strips. The electrically heated tungsten strip, the molten metal sample supported on it, and a pyrometer filament could be viewed simultaneously while varying the filament current to match the brightness of either the strip or the sample. Provision was not made for removing surface oxide after melting or for preventing alloying between the strip and the sample. The vacuum system pressure was not reported. However, since Langmuir first reported the design of the mercury diffusion pump in 1916, the best vacuum pump available to Burgess and Waltenberg was probably a Toeppler pump. Consequently, the lowest pressure they could have produced in their apparatus was probably no better than 10^{-4} Torr. Calculations given later in this report show that, at this pressure, the surface contamination rate is so high that measurements on clean material were probably impossible. However, if Burgess and Waltenberg made their measurements very quickly after melting the sample so that the vacuum system base pressure was not a factor and they were careful to view a metallic surface rather than an oxide-coated one, their measurements may be reliable. Even so, the data is limited to one wavelength (0.65 μm) and the normal direction, which is insufficient for many purposes.

The most thorough work on the radiant properties of solid uranium at elevated temperatures is that of Lemmon [162] reported in the Battelle Memorial Institute reports series. Lemmon used the hole-in-tube method to obtain the normal spectral emissivity at 1125 K and 1325 K. He also used measurements of total electrical power input and a tube temperature measurement to calculate the total hemispherical emissivity. This work and those of the other references on uranium are summarized in Table 6.2. Lemmon's results show good correspondence with those of Burgess and Waltenberg for the liquid.

Fig. 6-3 gives an example of Lemmon's data. Both the spectral and total emissivity vary with the cooling and heating cycle. Because the spectral emissivity has

TABLE 6.2

Literature data on the emissivity of uranium

Date (–)	Authors (–)	Temperature (K)	Wavelength (μm)	Angle (degrees)	Pressure (torr)	Technique (–)	Emissivity at 0.65 μm (–)
1915	Burgess and Waltenberg	>1406	0.65	0	not reported	emission	0.34
		<1406	0.65	0	not reported	emission	0.55
1939	Hole and Wright	<1406	0.65	0	10^{-8}	emission	0.51
1956	Rauh	300	0.665	5	2×10^{-10}	reflection	0.265
1957	Lemmon	1123	0.65	0	2×10^{-5}	hole-in-tube	0.32
	Lemmon	1348	0.65	0	2×10^{-5}	hole-in-tube	0.38
	Lemmon	1123	total	hemispherical	2×10^{-5}	calorimetric	0.36
	Lemmon	1348	total	hemispherical	2×10^{-5}	calorimetric	0.34
1963	Baker	1273	total	hemispherical	3×10^{-7}	calorimetric	0.37
1980	Faldt and Nilson	293	0.05–0.4	0	10^{-10}	reflectance	
		10,77,293	0.05–2		10^{-10}	ellipsometry	0.33
1980	Weaver	4	0.6–8	near normal		absorptance	0.35

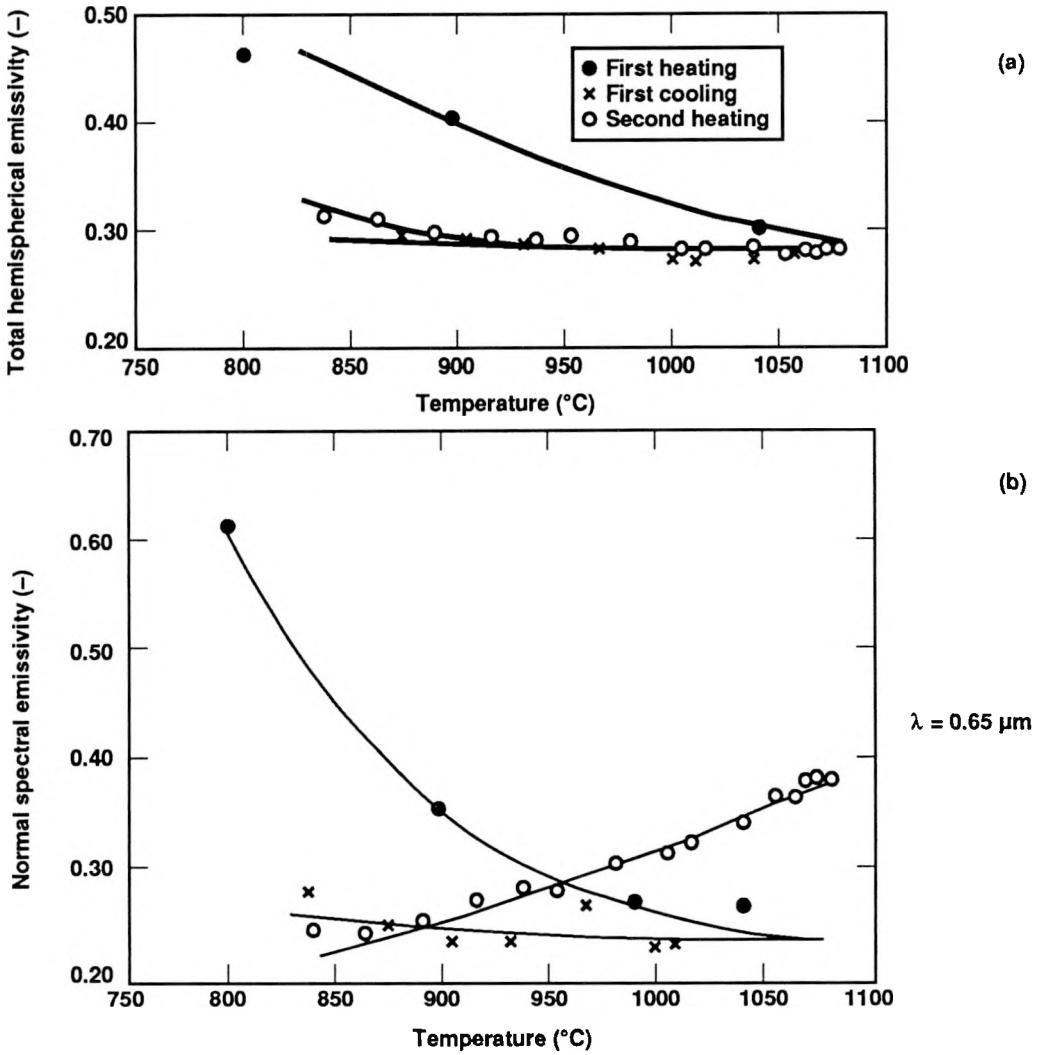

[Reproduced with permission from Battelle Memorial Institute. The citation is A. W. Lemmon, Battelle Memorial Institute, 1191, pp. 1–74 (1957)].

Fig. 6-3. a) Spectral and b) total emissivity vs temperature for uranium reported by Lemmon.

not stabilized, surface reactions are probably changing the sample surface composition during the measurement period (of unreported duration). The total hemispherical emissivity appears to have stabilized during the second heating.

The other two citations for high-temperature uranium are also of limited scope and questionable validity. Hole and Wright [163] measured the normal, spectral (0.67 μm) emissivity just below the melting point and obtained a value of 0.51, in reasonable

agreement with Burgess and Waltenberg's value of 0.55. Hole and Wright also measured the work function, the Richardson coefficient, and the melting point. Their results for the first two of these quantities disagree with the presently accepted value in a way suggesting oxygen contamination. Their measurement of the melting point of pure uranium is in error by 567 K. Little confidence in Hole and Wright's results is justified.

Baker, Mouradian, and Bingle [164] reported total hemispherical emission measurements in good agreement with Lemmon. This work was done at a base pressure of 3×10^{-7} Torr and probably involved oxidized material. In their discussion, they note that the originally highly polished cubes "appeared somewhat mottled after only slight heating, presumably because of anisotropic growth." Surface oxidation is a likely explanation given the system vacuum pressure.

In 1956, E. G. Rauh [165] published the results of a study of the near normal reflectivity of solid uranium at a wavelength of 0.665 μm. Rauh made extensive efforts to work with very clean material. The vacuum system pressure was 2×10^{-10} Torr after bakeout and measurements were made on freshly evaporated uranium condensed on a pyrex window. A removable nickel disc on the vacuum side of the window blocked the initially evaporated material which could have contained lower vapor pressure elements. Unfortunately, results were obtained at only one wavelength and the sample temperature was 300 K. Rauh's work function result, $\Phi = 3.47$ eV, compares well with the presently accepted value (3.54 eV) and indicates that he probably did maintain pure material.

In 1980, Faldt and Nilsson [160] reported optical constant measurements for uranium from 0.05 to 2.0 μm. Since the complex index of refraction determines not only the thermal radiative properties but also yields information on the electronic band structure of the crystal lattice, this study has broad value. Faldt and Nilsson made ellipsometric reflectance measurements on solid uranium at 293 K, 77 K, and 10 K as well as independent direct reflectance measurements at 293 K. Their results, by the two methods, show good agreement in the region of overlap, 3 to 4 eV (~0.3 to 0.4 μm), and

the form of the ellipsometric results allows computation of radiant properties over the full angular range. Unfortunately, the low temperature of their samples makes extrapolation to molten temperatures questionable. Also in 1980, J. H. Weaver [159] published the results of optical absorption measurements on clean polished uranium at 4.2 K for wavelengths from 0.6 to 8.0 μm. Although Weaver's results are much less general than Faldt and Nilsson's, they are valuable in that they agree with Faldt and Nilsson and cover the longer wavelength range that is often of considerable interest to high temperature development activities.

7. Sensitivity analyses of measurement methods for optical constants

7.1 Purpose

In general, for heat transfer calculations one needs, for a given material surface, a complete set of data for the radiative properties $\rho'_{\lambda,s}$, $\rho'_{\lambda,p}$, $\alpha'_{\lambda,s}$, $\alpha'_{\lambda,p}$, $\varepsilon'_{\lambda,s}$ and $\varepsilon'_{\lambda,p}$ as functions of (θ,ϕ) over an appropriately wide range of wavelength and temperature. In view of the unrestricted form of Kirchoff's law, $\varepsilon'_{\lambda,s} = \alpha'_{\lambda,s} = 1 - \rho'_{\lambda,s}$ and $\varepsilon'_{\lambda,p} = \alpha'_{\lambda,p} = 1 - \rho'_{\lambda,p}$, a complete set of data for one of these quantities implies knowledge of the others. Moreover, for the case of a smooth isotropic surface, when the radiative properties are independent of ϕ, the dependence on θ (at a given wavelength) must satisfy the Fresnel relations for appropriate values of the optical constants (n,k) (which are functions of λ and T).

In practice, it is impractical to make measurements of $\rho'_{\lambda,s}$, and $\rho'_{\lambda,p}$ (say) over the complete range of angles $0 < \theta < \pi/2$, at small intervals (as well as over a wide range of λ and T). For a set of measurements (for a given λ,T) at a limited number of angles, the appropriate method of smoothing the data is to make a best fit to the Fresnel relations (by varying n and k). This ensures that the smoothed results are consistent with the Fresnel relations, for instance that they satisfy the conditions $\rho'_{\lambda,s} = \rho'_{\lambda,p}$ at $\theta = 0$ and $\rho'_{\lambda,s} = \rho'_{\lambda,p}=1$ at $\theta = \pi/2$ (at which extreme angles measurements are difficult). In fact, the best fit values of n and k are a convenient and compact way of representing the data since all the radiative properties can be calculated as a function of θ from the Fresnel relations. Furthermore, a set of such measurements over a range of λ and T yields a set of n,k values which can be regarded as a complete specification of the radiative properties over that range. Moreover, since for metals at wavelengths through the visible and infrared there are no strong resonant absorption mechanisms, the functions $n(\lambda, T)$ and

k(λ ,T) are smooth functions, so that smoothing the data with respect to variation with λ and T can improve the quality of the results—or even indicate erroneous experimental results.

Since for given λ ,T, the radiative properties as a function of θ are completely determined by the two optical constants (n,k), the minimum set of measurements needed to determine n and k is just two independent measurements. There is a wide choice of the two independent measured quantities and a great variety of such pairs have been proposed and used (for reflection measurements, see the list of possibilities in section 4.2.2). The advantage of such methods is that they reduce the magnitude of the measurement task.

The purpose of this chapter is to evaluate several measurement methods for their suitability in determining the optical constants of clean metallic surfaces in the full wavelength range of interest to this work (0.4 to 10 μm). Of the many methods considered and used throughout the literature, the six discussed here were considered to have the greatest potential usefulness to the present objectives; a full specification of the thermal radiative properties of molten uranium and aluminum. The one method ultimately selected was unique for its sensitivity over the full spectral range.

Spectral range is critical to the choice of measurement method because of the variation of the components of the complex index of refraction with wavelength. Figures 7-1 and 7-2 display the variation of n, index of refraction, and k, extinction coefficient, with wavelength for platinum from two sources [117,167]. The rapid increase in both n and k with wavelength in the infrared range is typical of very good conductors and is the cause of the very high reflectivities common for this metal, gold, copper, aluminum and others. The agreement between the two sources is good, partly because platinum is inert. Thus, confidence in these results is high.

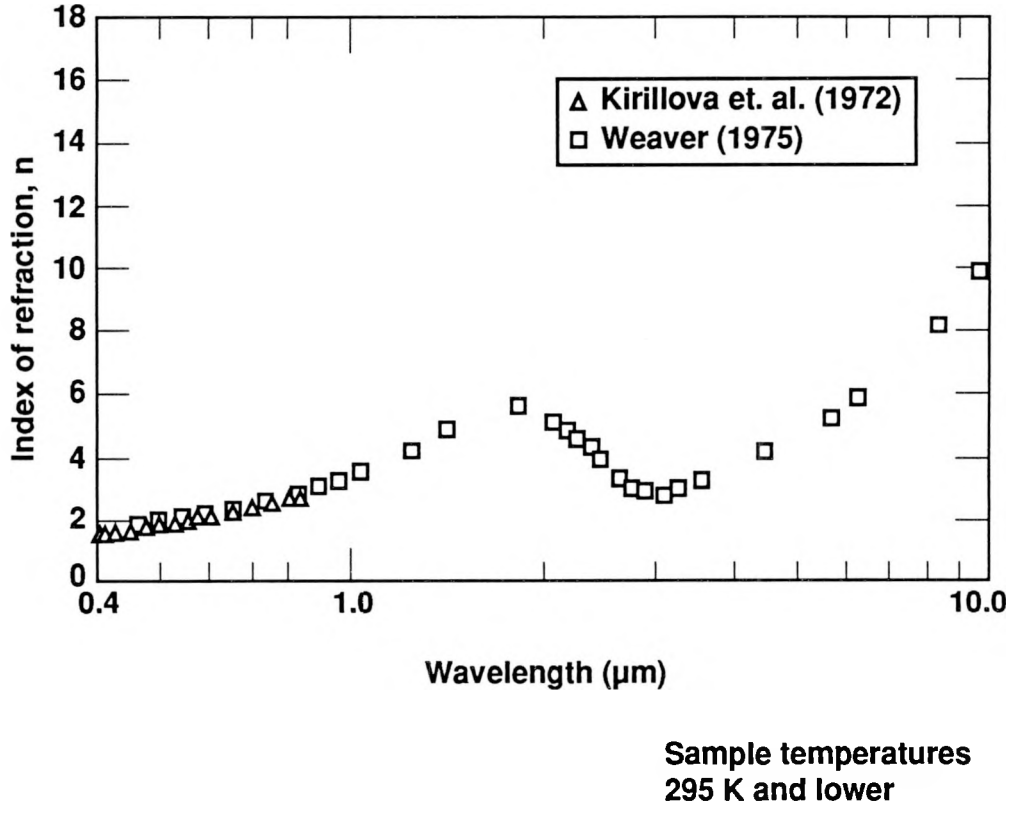

Fig. 7-1. Real part of platinum index of refraction. See text for full citations.

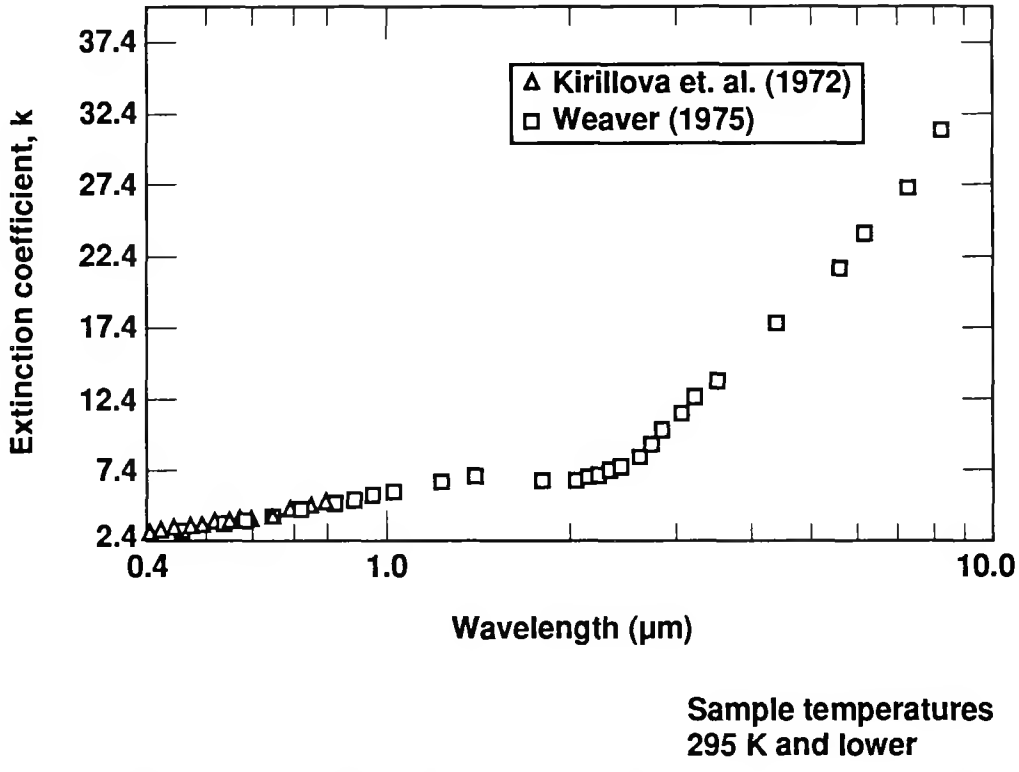

Fig. 7-2. Imaginary part of platinum index of refraction. See text for full citations.

Since good conductors such as platinum display the highest reflectivities and often the highest values for n and k at a given wavelength, it is reasonable to choose the maximum value from Fig. 7-2, 40.0, as an upper bound for k expected for the metals to be studied here. Since n is almost always smaller than k in the infrared for metals, it is conservative to take 40.0 as an upper bound for n also. Since tungsten and uranium are transition metals with lower conductivitiy and reflectivity than either platinum or aluminum, these upper bounds should be more than adequate for consideration of these metals. For the lower expectation bounds of n and k the value of 0.3 was chosen. This number is significantly lower than the lower limit in either Fig. 7-1 or 7-2 and avoids the possible complication to computation routines of selecting zero. The choice of lower bound is not critical because all six methods considered here displayed good sensitivity in the short wavelength extreme.

Previous studies of the choice of methods for measuring the components of the complex refractive index have considered narrower spectral ranges and a more limited set of potential methods. Most studies have focussed on measurements of reflectivity as a function of angle for obtaining the complex refractive index in the visible and ultraviolet spectral ranges. Humphries-Owen [75] did the original work in this area but did not treat methods which measured the relative phase shift on reflection. He considered index of refraction, n, from roughly 0.75 to 5.0 and extinction coefficient, k, from roughly 0.0 to 3.0. This range includes very little of the infrared for good conductors. In several papers [76,168,169] Hunter treated the visible to vacuum ultraviolet (VUV) range but ignored ellipsometric approaches because of the dearth of adequate polarizers for the VUV. He considered a subset of the methods covered by Humphries-Owen but used a different plotting approach.

Several other studies have treated this subject more briefly. Miller, Taylor and Julien [170] considered only measurements of reflectance versus angle and a wavelength range similar to that of Humphries-Owen. Their results were similar to those of

Humphries-Owen even though their methods were different. Field and Murphy [171] and Graves and Lenham [172] also considered aspects of these methods but the work of Humphries-Owen is clearly the most complete even though it does not cover the infrared spectral range and ellipsometric methods.

A thorough consideration of all the potential methods over the full spectral range of interest can help choose the best experimental method. Poor sensitivity, where errors in measured values are magnified by the data reduction process to give large uncertainty in the deduced complex index of refraction, should be avoided over the whole spectral range of interest. The use of a single technique for the full range is desirable to keep the experiment as simple, reliable and inexpensive as possible.

The sensitivity study given here is more complete in its consideration of methods and spectral range than prior work but is still limited in that it does not include many practical aspects of each method which are not readily quantified. Measurements of absolute values (such as reflectivity or emissivity in methods A and B below) are in general more difficult than measurements of ratios of such values (as in methods C through D below). The difficulty of working with a beam at angles extremely close to grazing incidence is another such practical aspect. At grazing incidence the elliptical "footprint" of an incident beam changes very rapidly as a function of angle. Measuring the average angle of incidence of a beam very near grazing is also difficult. Assessing these aspects along with the sensitivity constraints treated in this section is a matter of experimental judgement. Although there were many other judgemental considerations not treated by the analytic methods of this section, the sensitivity considerations evaluated here over the full wavelength range dictated which technique was ultimately selected.

The results of this sensitivity study also facilitated the understanding of the results. The regions of declining sensitivity at the extremes of the spectral range were manifested as regions of increased scatter in the measurement results. When this scatter

was greater than that inferred from the sensitivity analysis results, it was clear that other aspects of the measurement system should be examined to reduce uncertainty. This process assisted efforts to improve the measurement system.

7.2 Background

The six measurement methods considered here are:

A) measurements of unpolarized reflectivity at two angles of incidence which are fitted to the Fresnel equations to deduce n and k.

B) measurements of emissivity at two angles of emission which are fitted to the Fresnel equations to deduce n and k.

C) measurements of the ratio of perpendicular to parallel polarized reflectivity which are fitted to the Fresnel equations to deduce n and k.

D) measurements of the ratio of perpendicular to parallel polarized emissivity at two angles of incidence which are fitted to the Fresnel equations to deduce n and k.

E) the method of Beattie and Conn (discussed in Chapter 5) in which a single angle of incidence and a rotating polarizer are used to deduce amplitude attenuation and relative phase shift on reflection and thence the complex refractive index.

F) the method of Miller (also discussed in Chapter 5) in which two azimuths yielding equal intensity are obtained by rotating both the polarizer and the analyzer. The angles of equal intensity are then used to deduce the phase shift and amplitude attenuation on reflection and thence the complex index.

The fundamental relations bearing on methods A to D are the Fresnel equations. These were given in Chapter 2 and are repeated here:

$$\rho_{\lambda,p} \equiv r^2_{\lambda,p}(\lambda,\theta) = \frac{a^2 + b^2 - 2a\sin\theta\tan\theta + \sin^2\theta\tan^2\theta}{a^2 + b^2 + 2a\sin\theta\tan\theta + \sin^2\theta\tan^2\theta} r^2_{\lambda,s}$$

$$\rho_{\lambda,s} \equiv r^2_{\lambda,s}(\lambda,\theta) = \frac{a^2 + b^2 - 2a\cos\theta + \cos^2\theta}{a^2 + b^2 + 2a\cos\theta + \cos^2\theta} \qquad (7\text{–}1)$$

where $2a^2 = [(n^2 - k^2 - \sin^2\theta)^2 + 4n^2k^2]^{1/2} + (n^2 - k^2 - \sin^2\theta)$

and $2b^2 = [(n^2 - k^2 - \sin^2\theta)^2 + 4n^2k^2]^{1/2} - (n^2 - k^2 - \sin^2\theta)$

In method A, the average of the two polarized reflectivities is measured at two angles of incidence and a complex index (n and k) is computed which best fits the measurements. In method B, emissisity is measured at two angles of emission and a similar fit is performed to $(1 - (\rho'_{\lambda,s} + \rho'_{\lambda,p})/2)$, since on a directional spectral basis Kirchoff's law (see Chapter 2) holds without restriction. For method C, the ratio of the two Fresnel equations is used. The measured values for this ratio at two angles of incidence are then fit to the ratio equation to find the best n, k pair. For method D the ratio of 1 minus each of the polarized reflectivity components is formed so that a similar procedure can yield the best n, k pair.

For method E the results for phase shift and amplitude attenuation on reflection given in Chapter 5 are used. The four measured quantities of Beattie and Conn are related to ρ and Δ by the following equations:

$$\rho\hat{}(\theta) = \tan\psi = \sqrt{I_2/I_1}$$

$$\cos(\Delta) = \left\{\frac{1}{2}\left(\rho\hat{} + \frac{1}{\rho\hat{}}\right)\right\}\left\{\frac{I_3 - I_4}{I_3 + I_4}\right\} \qquad (7\text{–}2)$$

The measured quantities are I_1 to I_4 and ρ and Δ are functions of the angle of incidence, θ. The optical constants are related to ρ and Δ as follows:

$$\epsilon/\epsilon_o = (n^2 - k^2) = \sin^2\theta\left[1 + \tan^2\theta\left[\frac{\cos^2 2\psi - \sin^2 2\psi \sin^2\Delta}{(1 + \sin 2\psi \cos\Delta)^2}\right]\right] \qquad (7\text{–}3)$$

$$(\epsilon' / \epsilon_o) = 2nk = 2\sin^2\theta \tan^2\theta\left[\frac{\cos 2\psi \sin 2\psi \sin\Delta}{(1 + \sin 2\psi \cos\Delta)^2}\right] \qquad (7\text{–}4)$$

with $\tan\psi = |r_p| / |r_s|$

and θ = angle of incidence

and Δ = relative phase shift on reflection

For method F, the angles for equal intensity are each used to determine ρ and Δ and these are used to give n and k as in method E. The relations involving the polarizer azimuths for equal intensity, Q_1 and Q_2, were given by Miller [4]:

$$\rho\hat{}^2 = \tan|Q_2| \tan|Q_1|$$

$$\cos(\Delta) = \frac{1}{2\rho\hat{}}[\tan|Q_1| - \tan|Q_2|] \qquad (7\text{–}5)$$

In comparing the merits of the measurement schemes with regard to the accuracy of the inferred (n,k) values, two factors are involved. If the two measured quantities are represented by x_1 and x_2 and their estimated uncertainties by δx_1 and δx_2, then the uncertainties in the inferred n,k values, δn and δk are given by:

$$\delta n = \left(\frac{\partial n}{\partial x_1}\right)\delta x_1 + \left(\frac{\partial n}{\partial x_2}\right)\delta x_2$$

$$\delta k = \left(\frac{\partial k}{\partial x_1}\right)\delta x_1 + \left(\frac{\partial k}{\partial x_2}\right)\delta x_2 \qquad (7\text{–}6)$$

The quantities $(\partial n/\partial x_1)$, $(\partial n/dx_2)$, $(\partial k/\partial x_1)$ and $(\partial k/\partial x_2)$, which can be referred to collectively as sensitivity factors, can be found by differentiating the relevant equations (the Fresnel equations e.g. for methods A to D above). These factors are themselves functions of n and k as well as the angle or angles of incidence at which the measurements are made. In practice, because of the complexity of the Fresnel relations, it is difficult to derive the sensitivity factors analytically, and a more practical procedure is to compute plots of contours of constant (x_1,x_2) in the (n,k) plane as is done here.

There are, of course, a great number of methods not included among the six considered here. The principal reasons for rejecting most of the others were a) difficulty in applying them over the full spectral range or b) an obvious difficulty in applying them to molten metal samples. Several of the most recently developed ellipsometric methods use continuously rotating polarizers and/or analyzers to facilitate the data acquisition process. These methods did not allow sufficient integration time at the lock-in amplifier in the long wavelength extreme. In some ranges of this study 10 and 30 second integration times were required of the signal detection system to obtain the desired measurement accuracy.

Variations on methods A to D which use measurements at more than two angles are also not considered here even though many have been reported [97,99,173]. The use of statistics and more sophisticated fitting procedures makes these methods superior to their simpler counterparts but fundamentally the same. Constraints on sensitivity derived from analyses of the two angle methods will be largely unchanged for extra angle variations. Similar variations employing overdetermined systems could also be envisioned for methods E and F but only slight improvements in sensitivity and measurement spectral range are expected.

The results presented for method sensitivity in the next section treat each method over the full complex index of refraction range discussed above ($0.3 < n < 40$ and $0.3 < k < 40$). In each case there are contours of constant values of the measured

quantities placed over a grid of n (the x axis) and k (the y axis) values. Since n and k are the desired quantities in all of the methods, this choice of grid parameters puts all six methods on a similar footing. Preceeding works have most often plotted contours of constant values of the components of the complex refractive index so that the different methods are not as easily compared.

Several aspects of the sensitivity contours to be discussed below are common to all of the methods. A general grasp of these aspects facilitates understanding and interpretation of the results. The angle of intersection of the contours is critical when contours of the two measured variables within a given method are plotted on the same grid. For intersections which are near to orthogonal, the measured variables are largely independent. For contours which are nearly parallel, (intersections at angles of 20^{o} and less say), the two measured variables are strongly dependent. In the extreme limit of parallel contours of the two measured variables, the two quantities differ only by a multiplicative constant. In this condition, the method can not yield the two unknown components of the complex refractive index because only a single independent quantity is being measured. Thus, as the contours in a given plot become less and less orthogonal, the method becomes less and less sensitive for obtaining both n and k. All six of the methods described here display less and less orthogonal contours in the further extremes of the infrared but the performance of the ellipsometric methods is always superior to the others.

Another common feature to the sensitivity plots is contour spacing. For a constant numerical difference between plotted contours, there is more sensitivity in regions where contours are separated by smaller distances on the n,k grid. (In the plotting scheme given by Humphries-Owen the reverse is true because the contours are of n and k and the two orthogonal axes display the measured quantities.) Here, for a given uncertainty in the value of a measured quantity, the regions of closely spaced contours possess greater sensitivity because the corresponding uncertainty in the components of

the complex refractive index is less. When the uncertainty in both the measured quantities is considered at some position on a sensitivity plot, a corresponding uncertainty in both index components can be determined. In some of the earlier studies [75,76,168,169] these uncertainties have been plotted explicitly to compare some of the methods. However, as Humphries-Owen implied in his discussion, the sensitivity variations within a given method can be gauged with a simple understanding of these contour spacing and orthogonality arguments.

7.3 Sensitivity contours for candidate measurement techniques

7.3.1 Measurements of unpolarized reflectivity at two angles of incidence (method A). Contour plots for this method are given in Figs. 7-3 and 7-4. The contours are lines of constant value of the two measured reflectivities. The two angles chosen for the plot were 20 and 75°. Other pairs of angles would give rather different results but greatly improved results can only be obtained by making one angle even closer to grazing than 75°. Each of the figures covers a specified n,k range and therefore an approximate wavelength range (see Figs. 7-1 and 7-2 to estimate the wavelength range). Both n and k vary from 0.3 to 4.0 in Fig. 7-3. For many clean metals this figure covers the visible spectral region and part of the ultraviolet. The contours are well spaced in Fig. 7.3 indicating good sensitivity: small errors in measured quantities will not be greatly magnified to give large uncertainties in complex refractive index.

In the lower left corner of the figure (small n and small k) the contour lines are moderately orthogonal, indicating that the two measured variables are largely independent and two unknowns can be accurately determined from the two

Figure 7.3 Lines of constant $\rho(\theta_1)$ and $\rho(\theta_2)$ for 0.3<n,k<4.
$\theta_1=20^o$, solid lines; $\theta_2=75^o$, dashed lines

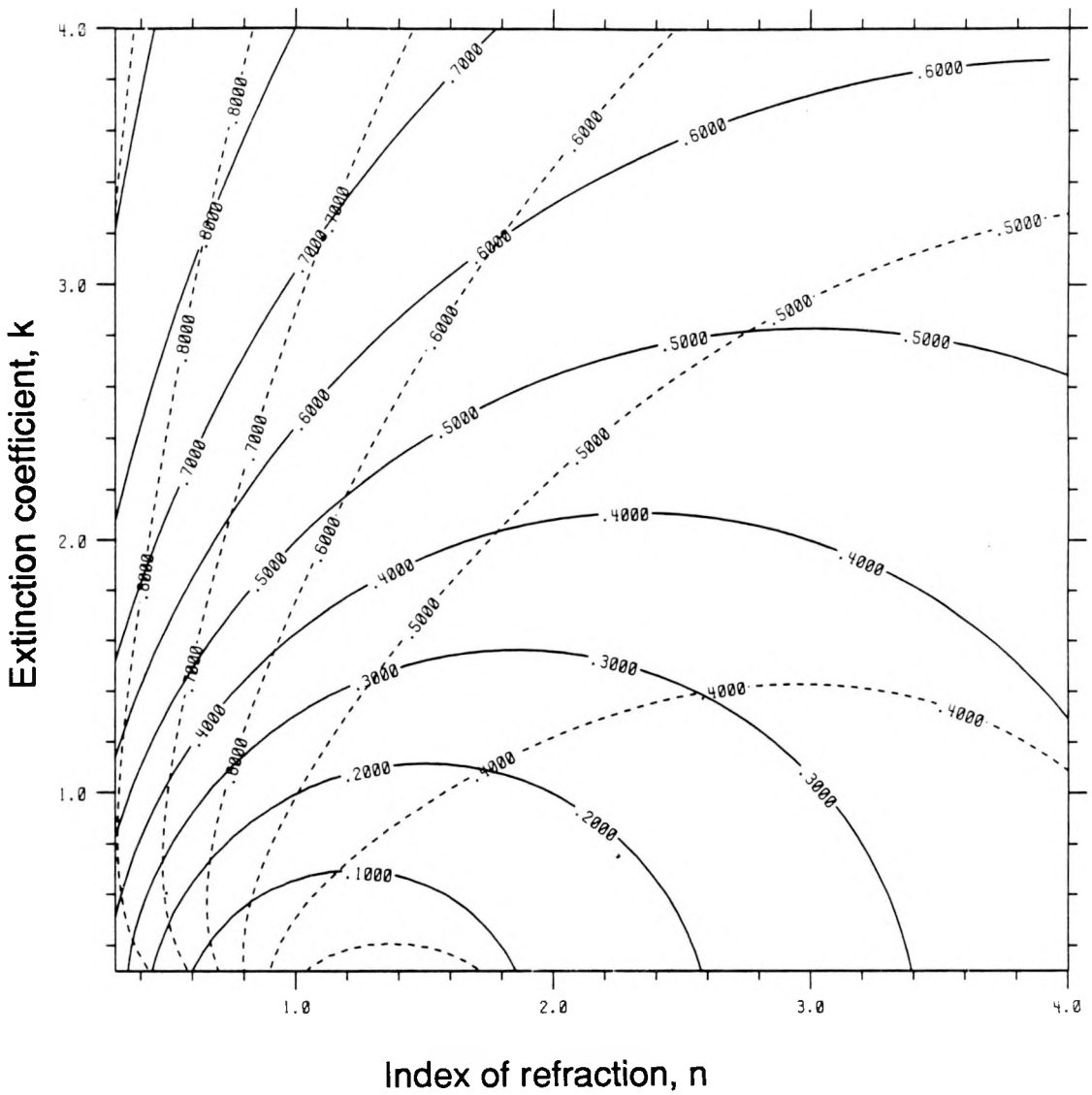

Figure 7.4 Lines of constant $\rho(\theta_1)$ and $\rho(\theta_2)$ for 4<n,k<10.
$\theta_1=20^o$, solid lines; $\theta_2=75^o$, dashed lines

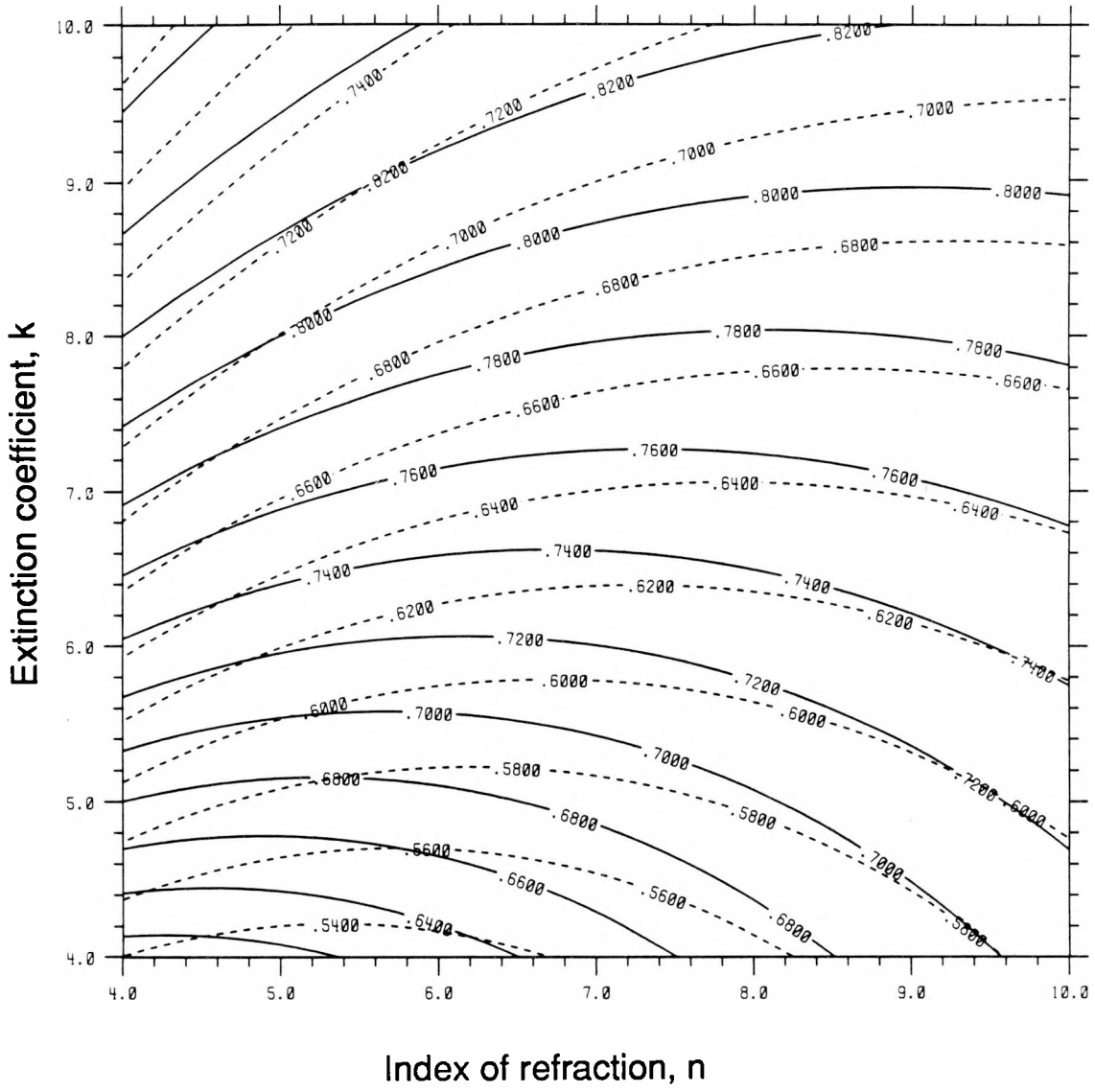

measurements. However, in the upper right corner of the figure (n and k approaching 4) the contour lines are far less orthogonal, indicating decreased sensitivity for discerning two unknowns. Both sets of contours are approaching a horizontal slope in this region of the figure. In the limit of equal slope, the two measured values are related by a constant and both components of the refractive index cannot be determined. Specifically, for zero slope of both contours, any uncertainty in either measured variable translates into an uncertainty in index of refraction but not in extinction coefficient. Thus, the method has little and declining sensitivity for the determination of n as n and k become larger than values typical of the visible region with metals.

Figure 7-4 presents results for the same method but larger values of n and k ($4 < n,k < 10$) corresponding to long infrared wavelengths. The contour lines are yet closer to parallel, particularly in the highest ranges of n and k. Clearly, this method is inadequate for complex index determination in the infrared. Historically, this method has been valuable in the ultraviolet where its sensitivity is high and the polarizing optics required of other methods are not available.

7.3.2 Measurement of emissivity at two angles of emission (method B). This method is very similar to method A because A works with $\rho'_\lambda(\theta)$ and B works with $1 - \rho'_\lambda(\theta) = \varepsilon'_\lambda(\theta)$ (using relations derived in Chapter 2). However, the methods are diverse when applied. Emission methods at angles close to 90^o are much more practical than their reflection counterparts: grazing incidence reflection experiments. For this reason, angles of emission of 70^o and 85^o have been chosen for the contour plots presented here. The choice of n and k range for Figs. 7-5 and 7-6 is the same as in Figs. 7-3 and 7-4 for easy comparison of the methods.

In Fig. 7-5 the contours display both adequate spacing and orthogonality over most of the plot. The lower left hand corner (small n and k) of the figure contains a

Figure 7.5 Lines of constant $\varepsilon(\theta_1)$ and $\varepsilon(\theta_2)$ for $0.3<n,k<4$.
$\theta_1=70^o$, solid lines; $\theta_2=85^o$, dashed lines

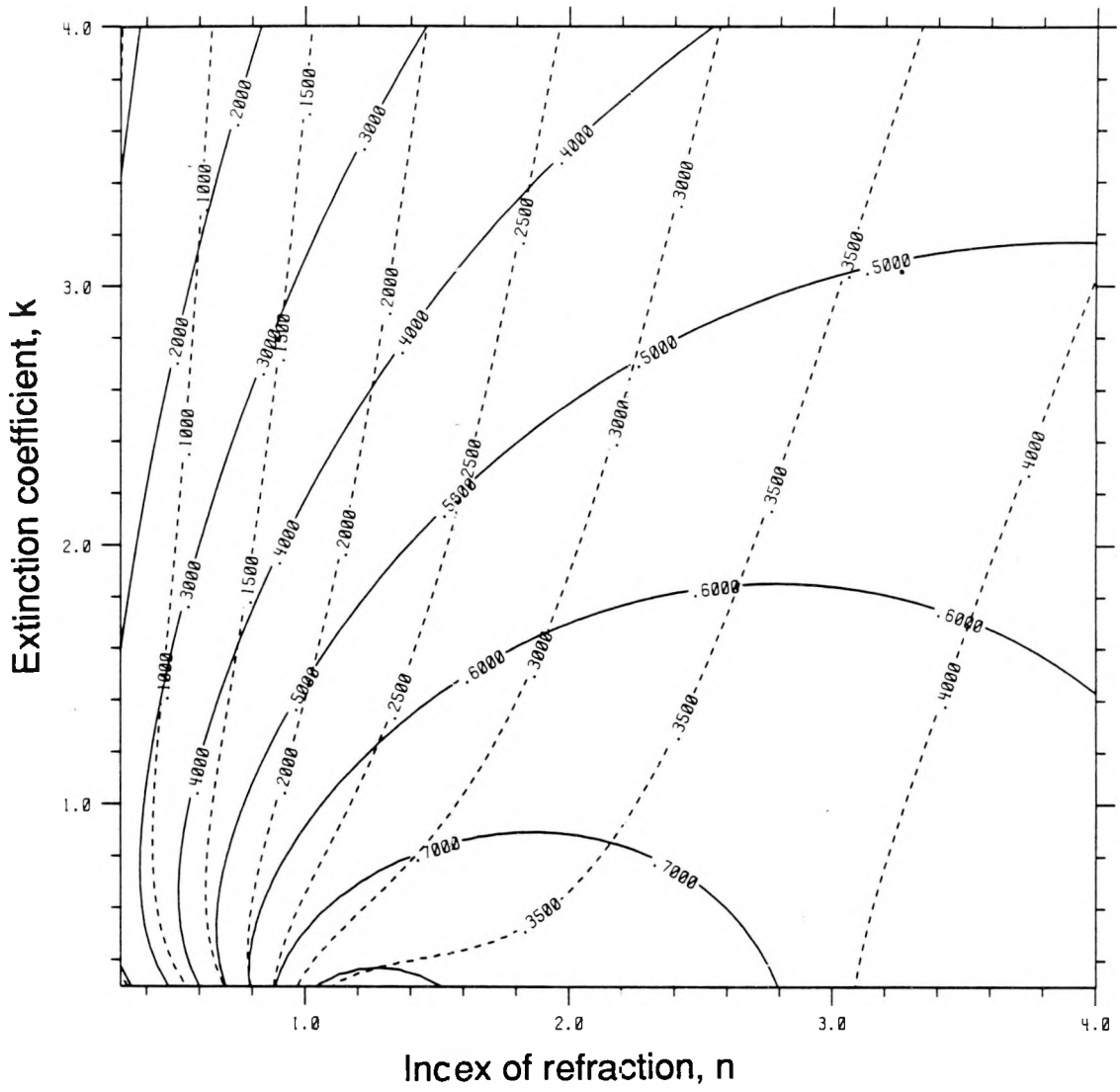

Figure 7.6 Lines of constant $\varepsilon(\theta_1)$ and $\varepsilon(\theta_2)$ for $4<n,k<10$.
$\theta_1=70^o$, solid lines; $\theta_2=85^o$, dashed lines

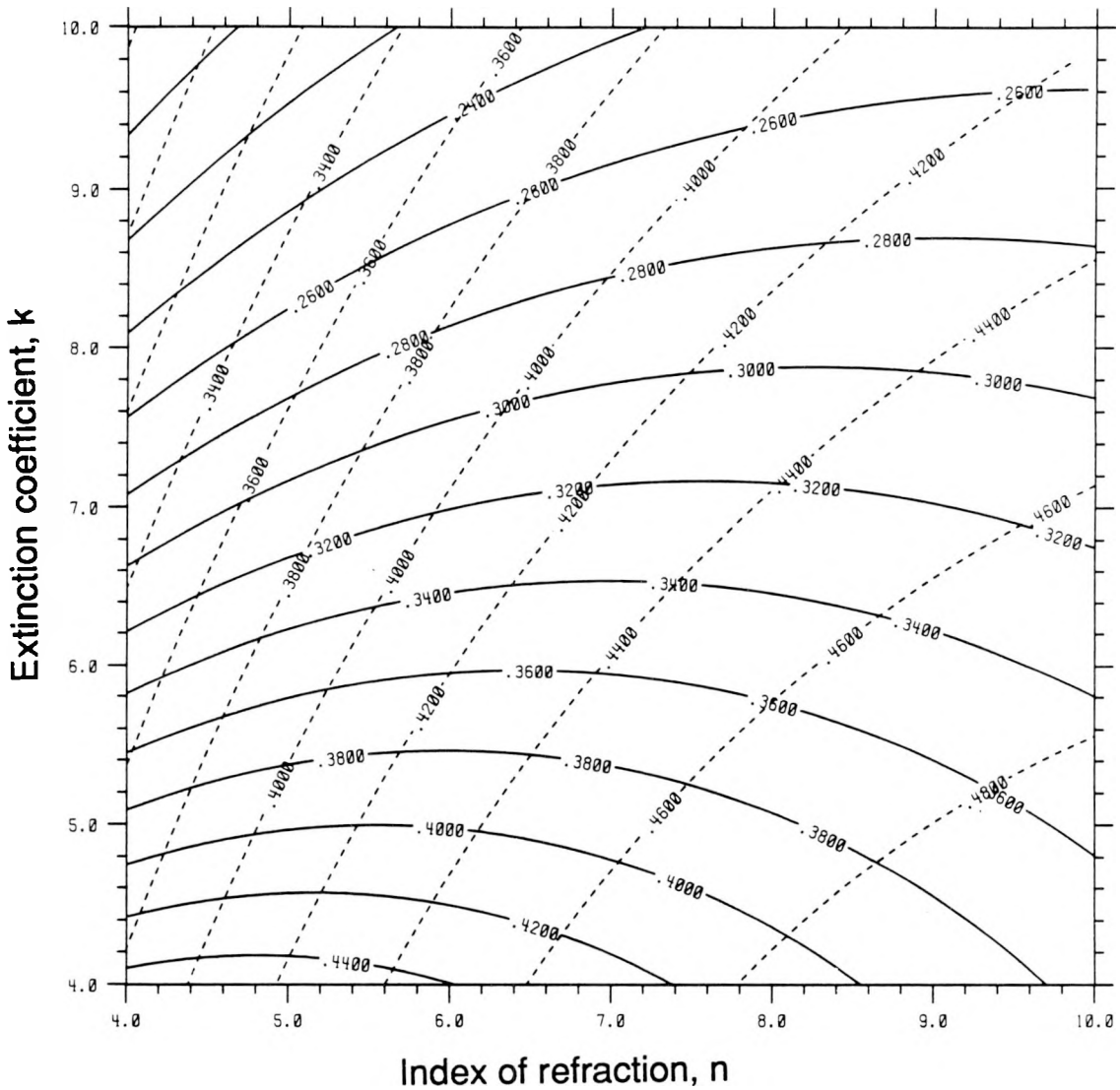

region of nearly parallel contours but this corresponds to the blue end of the visible range and more often the ultraviolet and vacuum ultraviolet.

In Fig. 7-6 both sets of contours indicate good sensitivity over the full range plotted. The results of Figs. 7-5 and 7-6 indicate that this method could be adequate through the visible and some way into the infrared. However the method does not maintain high sensitivity for the highest ranges of n and k of interest here. Fig. 7-7 shows contours similar to those of Figs. 7-5 and 7-6 but for the range $10 < n,k < 40$. Once again the contours are nearly parallel, indicating poor sensitivity for discerning two unknowns from the two measurements. Thus, method B has adequate sensitivity over a wider spectral range than method A and is probably much simpler experimentally but good results cannot be expected in the 3 to 10 μm spectral range.

7.3.3 Measurements of the ratio of perpendicular to parallel polarized reflectivity (method C). Measurements of the ratio of polarized reflectivities possess greater sensitivity over a wider spectral range and can be experimentally simpler than absolute reflectivity measurements such as those described above. As in method A, two angles of incidence are selected for the measurement positions. With this method, the results are fitted to the ratio of the two Fresnel equations given above. Figure 7-8 shows what corresponds to a visible spectral range ($0.3 < n,k < 4$). Once again other pairs of measurement angles could have been selected but this pair is representative. The contour lines are well spaced for good sensitivity and the orthogonality is improved over method A. Since this method does not require an absolute reflectivity measurement it is clearly to be preferred to method A in the visible region. For liquid samples, method C is particularly suited to the visible range because the meniscus makes absolute measurements very difficult.

Figure 7.7 Lines of constant $\varepsilon(\theta_1)$ and $\varepsilon(\theta_2)$ for $10<n,k<40$. $\theta_1=70^o$, solid lines; $\theta_2=85^o$, dashed lines

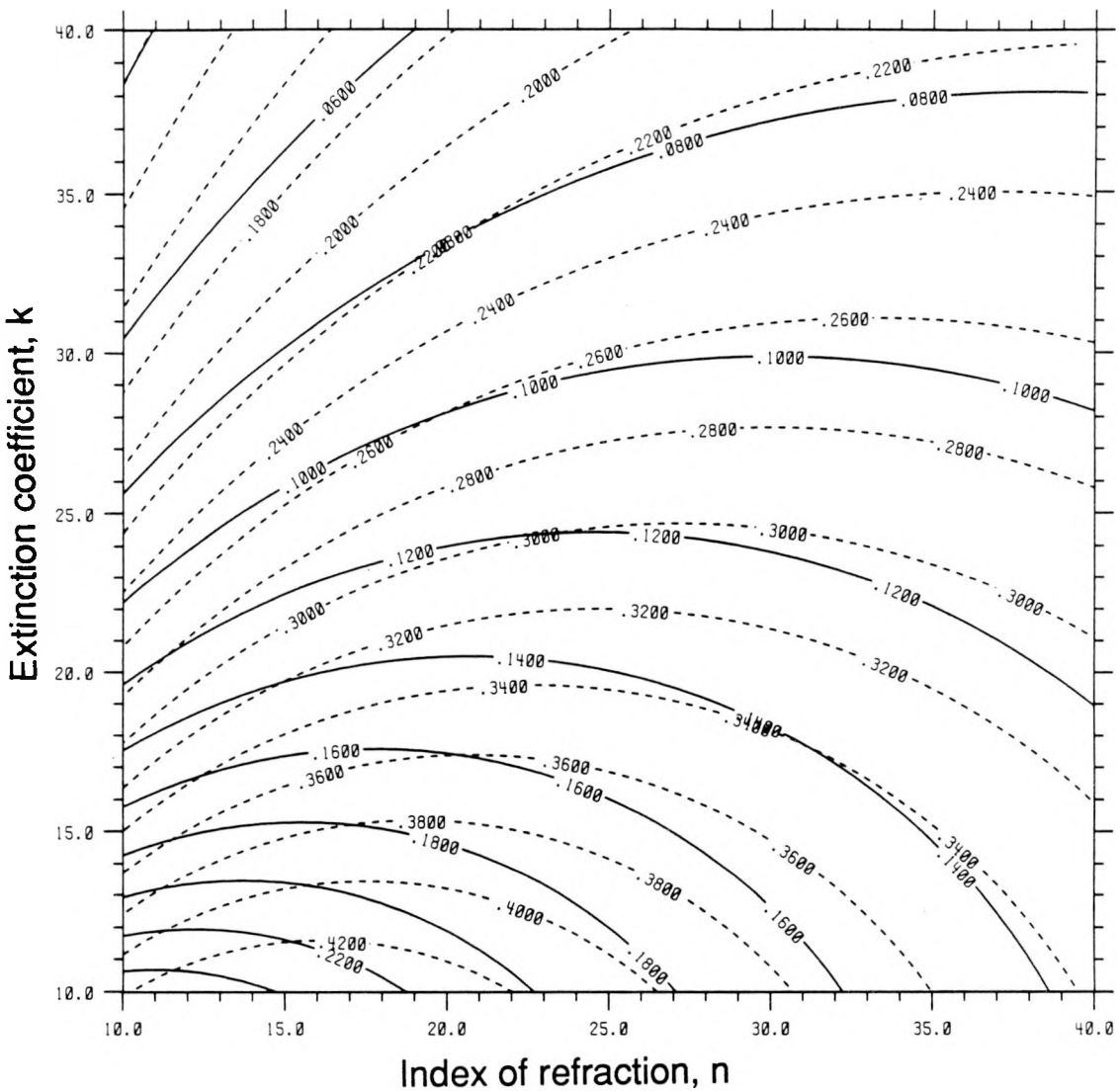

Figure 7.8 Lines of constant $\rho_p(\theta_1)/\rho_s(\theta_1)$ and $\rho_p(\theta_2)/\rho_s(\theta_2)$ for $0.3<n,k<4$.
$\theta_1=20^o$, solid lines; $\theta_2=75^o$, dashed lines

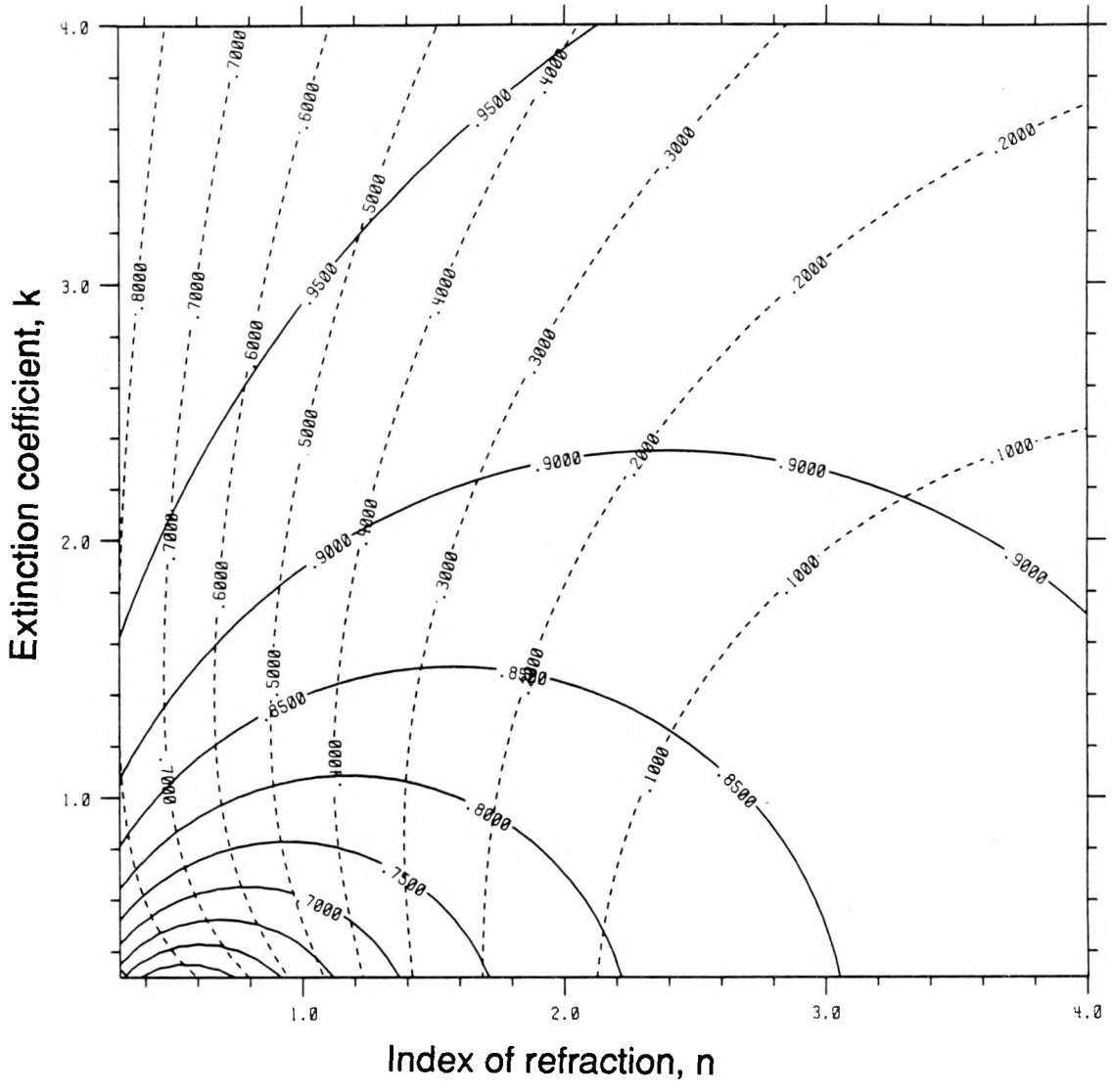

Figure 7-9 shows contours for an infrared spectral range ($4 < n,k < 10$). The contours are more orthogonal in this range for method C than method A (Fig. 7-4) but the difference is not substantial. For larger n,k this method gives nearly parallel contours and is therefore inadequate. In summary, this method has improved sensitivity over method A but still has poor sensitivity in the long wavelength extreme ($\lambda > 5$ μm or n, k $> \sim 20$).

7.3.4 Measurement of the ratio of the perpendicular to parallel polarized emissivity at two angles of incidence (method D). This method is the emissivity counterpart to method C and again possesses significant experimental advantages over A and B. No input optical system is required, absolute measurements are not required and grazing emission is preferred to grazing reflection. The extensive use of this method was noted in Chapter 4. Tingwaldt et. al. [99] were particularly successful in applying this approach (Data from 14 incidence angles between zero and 70^o were fitted to the Fresnel equations.) Their results for tungsten agreed well with the direct emissivity measurements of DeVos [92], Larrabee [93], and Latyev et. al. [94] using the hole-in-tube technique.

The sensitivity results for this method using angles of 20^o and 75^o, are shown in Figs. 7-10 and 7-11. For the lower values of n,k shown in Fig. 7-10, the contours are well spaced but not adequately perpendicular. This is not a severe handicap for this method since only for very hot samples is there substantial emission in the wavelength range (UV) corresponding to these n,k pairs. For intermediate n,k values typical of the visible and near infrared this figure shows acceptable contour spacing and orthogonality.

In Fig. 7-11 the contours are much more nearly parallel, just as occurred in the 4 to 10 range for n and k for method C. For the most extreme values of n and k in consideration here ($10 < n,k < 40$), Fig. 7-12 shows the contours to be yet closer to parallel. The upper left corner of this figure contains n,k pairs appropriate for many

Figure 7.9 Lines of constant $\rho_p(\theta_1)/\rho_s(\theta_1)$ and $\rho_p(\theta_2)/\rho_s(\theta_2)$ for 4<n,k<10.
$\theta_1=20^o$, solid lines; $\theta_2=75^o$, dashed lines

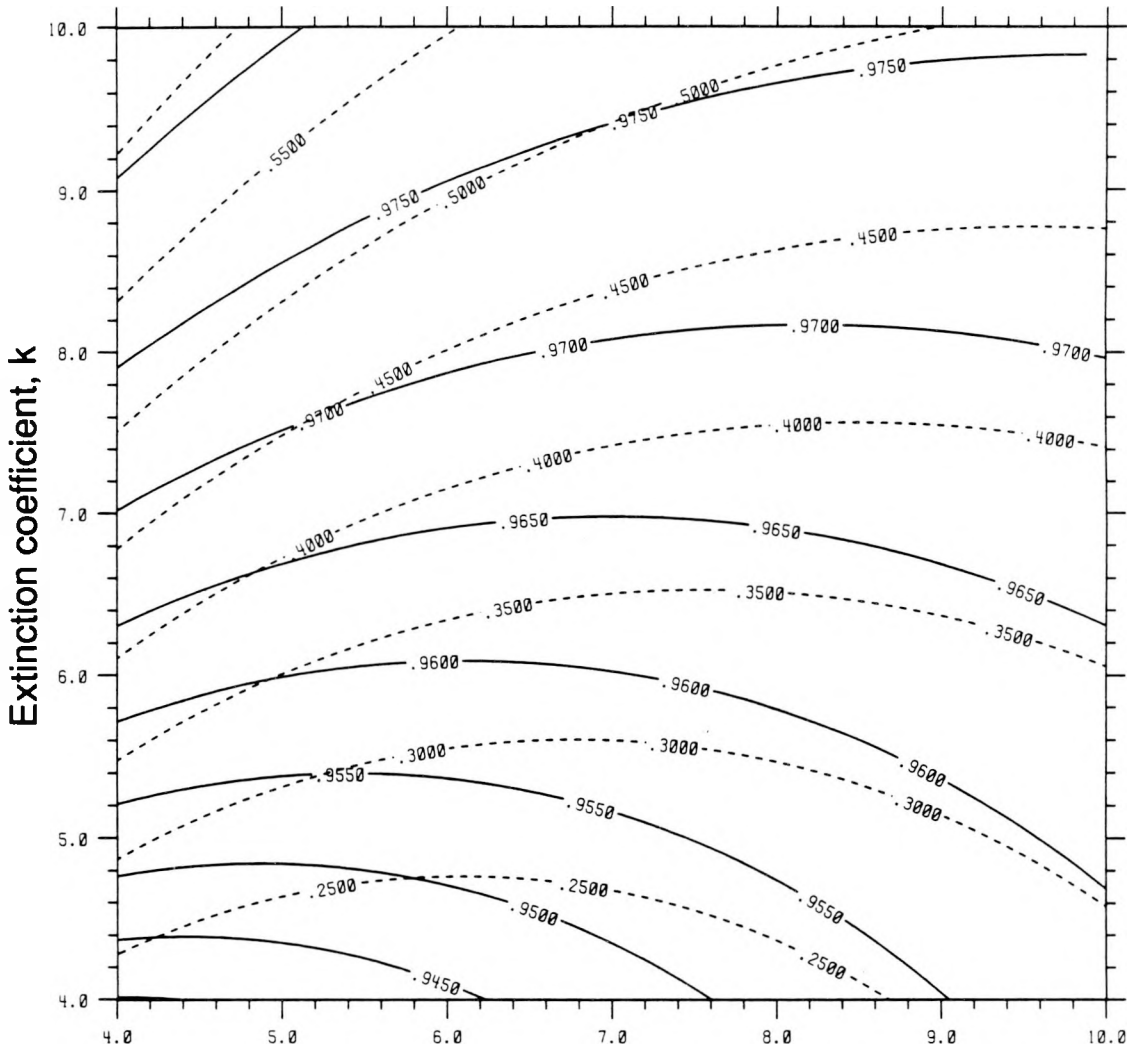

Figure 7.10 Lines of constant $\varepsilon_s(\theta_1)/\varepsilon_p(\theta_1)$ and $\varepsilon_s(\theta_2)/\varepsilon_p(\theta_2)$ for $0.3<n,k<4$.
$\theta_1=20^o$, solid lines; $\theta_2=75^o$, dashed lines

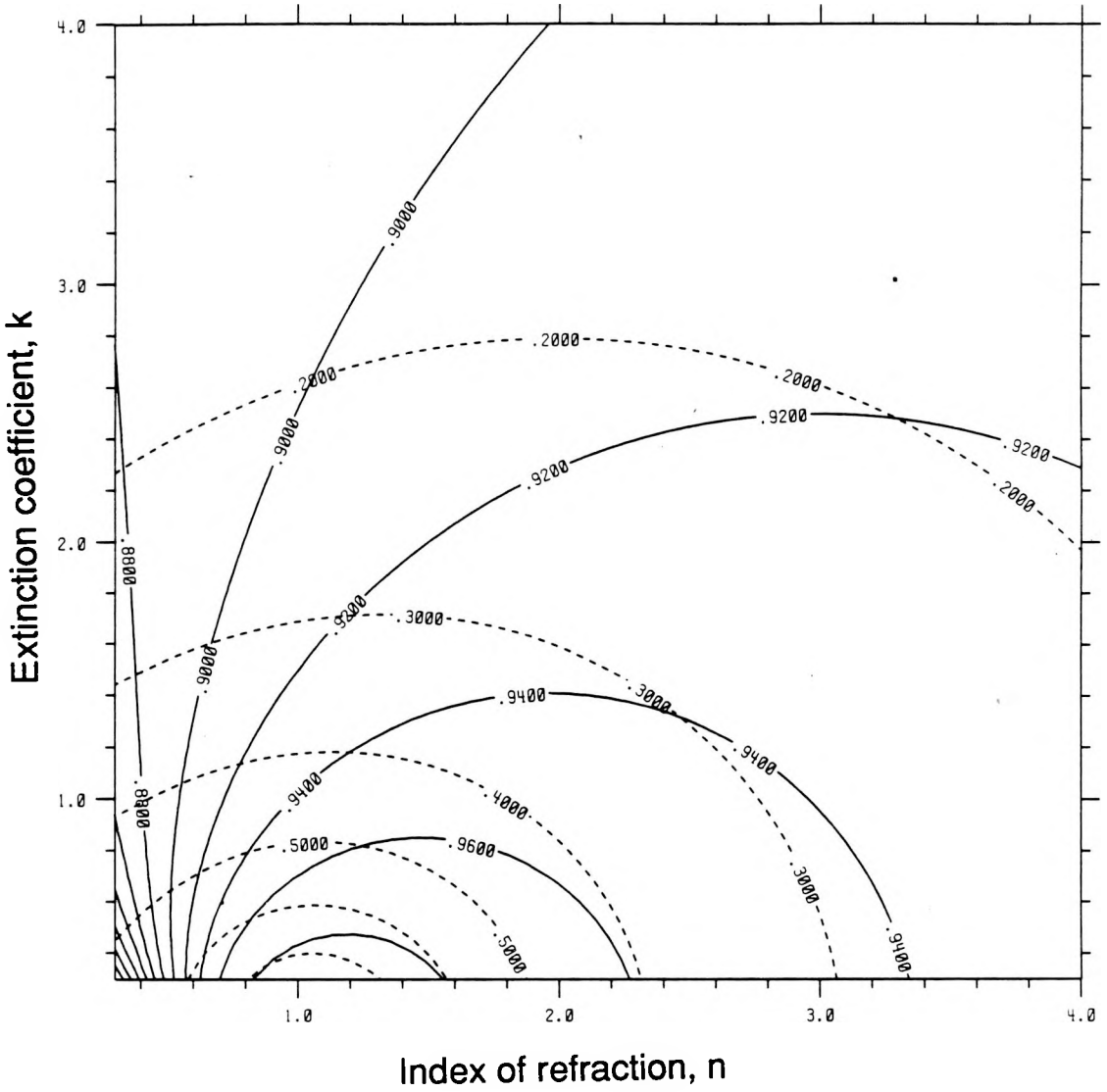

Figure 7.11 Lines of constant $\varepsilon_s(\theta_1)/\varepsilon_p(\theta_1)$ and $\varepsilon_s(\theta_2)/\varepsilon_p(\theta_2)$ for 4<n,k<10.
$\theta_1=20^o$, solid lines; $\theta_2=75^o$, dashed lines

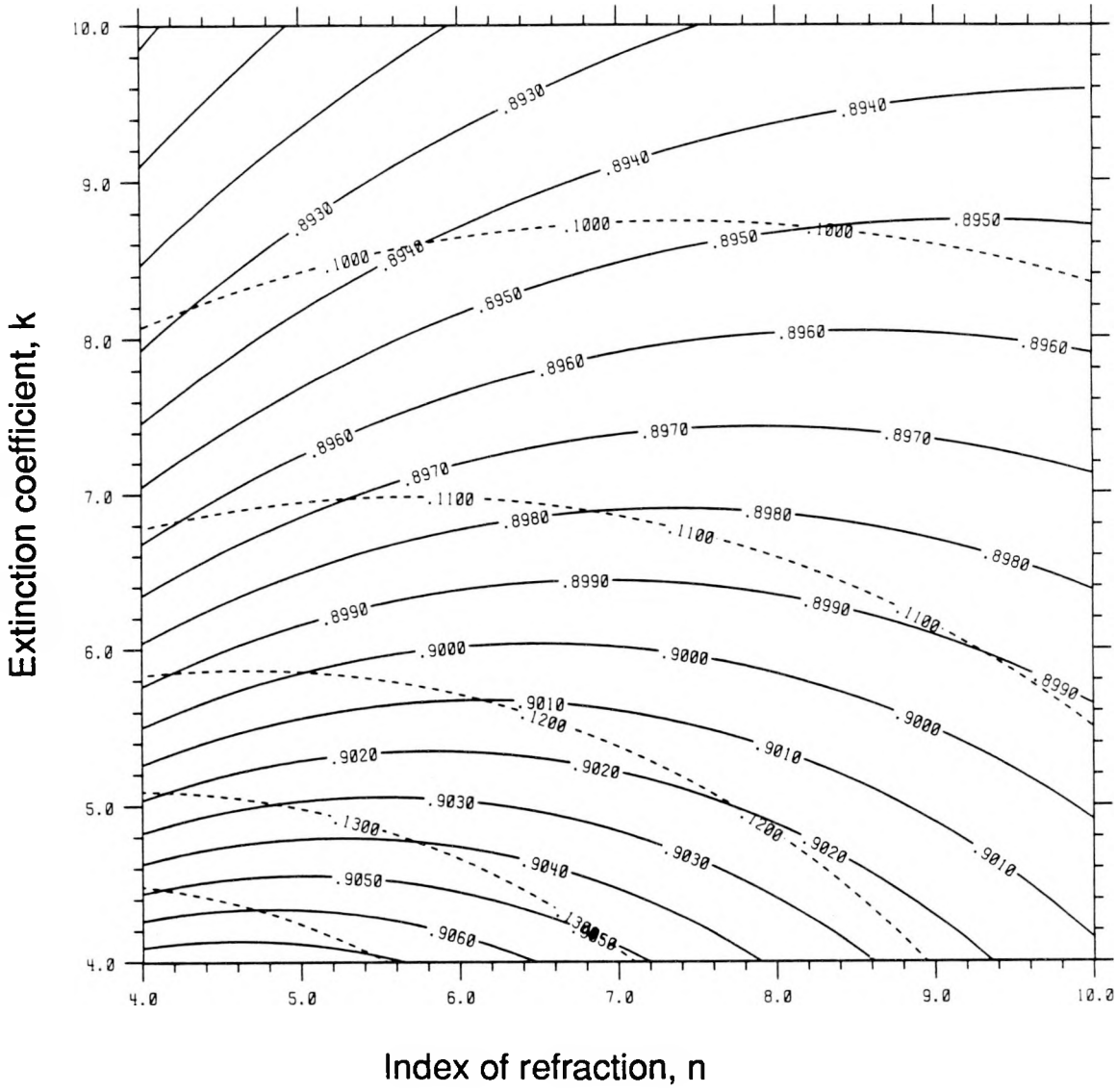

Figure 7.12 Lines of constant $\varepsilon_s(\theta_1)/\varepsilon_p(\theta_1)$ and $\varepsilon_s(\theta_2)/\varepsilon_p(\theta_2)$ for 10<n,k<40.
$\theta_1=20^o$, solid lines; $\theta_2=75^o$, dashed lines

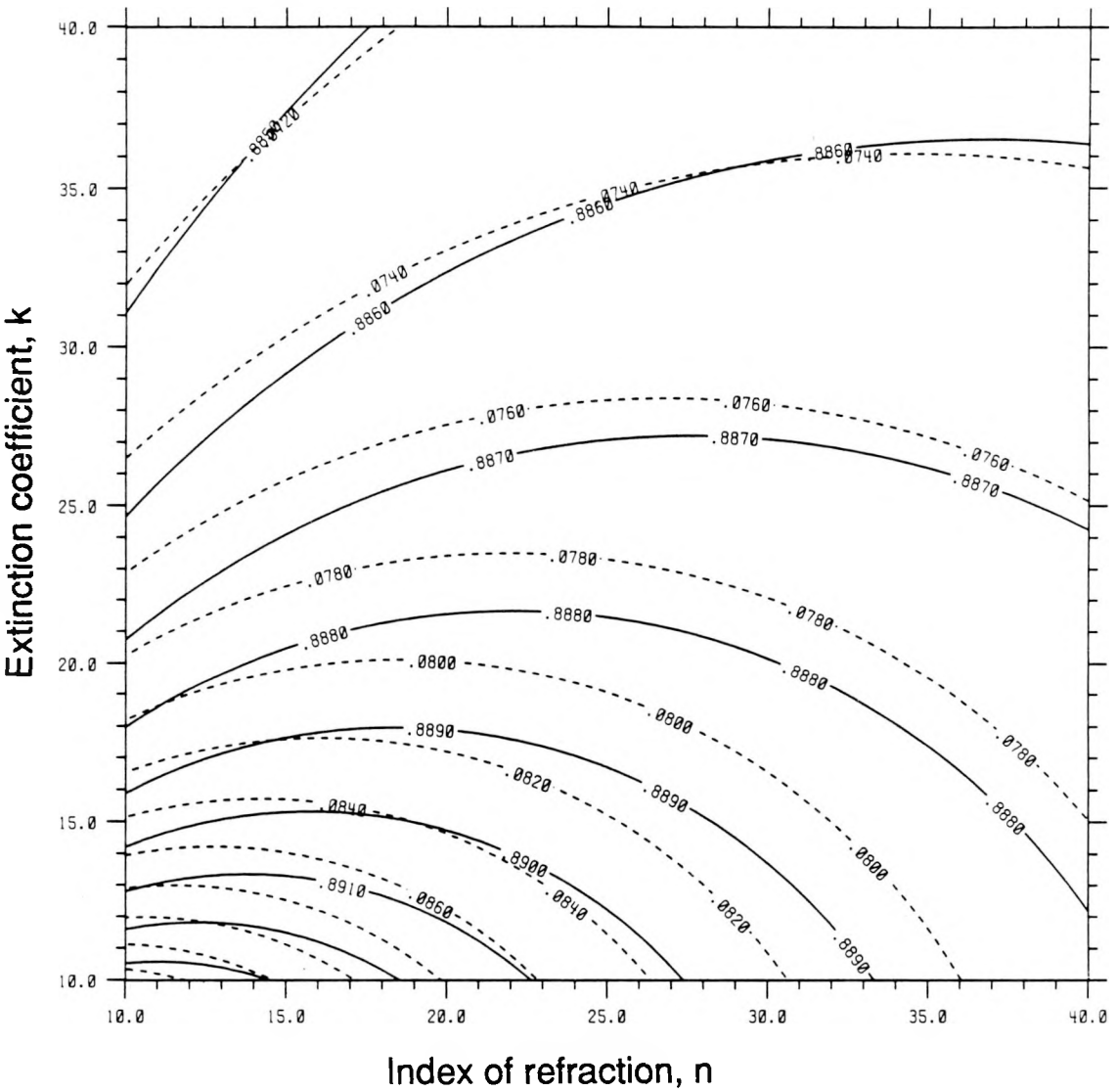

metals in the 8 to 10 μm range. The spacing between contours in this range shows that very small errors in the measured variables will result in substantial changes in both n and k. For example, the contours corresponding to measurements at 20° are 0.885 and 0.886 in this corner of the figure. For a change of 0.001 in the ratio of polarized emissivities measured for this angle, the appropriate contour for determining n and k changes from the 0.885 line to the 0.886 line. Moving from one to the other of these two contours represents a large change in both n and k. The combination of the separation of these two contours in n,k space and the near parallel contours for the two measurement angles makes it clear that this method is not viable at the long wavelength extreme.

7.3.5 The method of Beattie and Conn (method E). Sensitivity results for this method are shown in Figs. 7-13, 7-14 and 7-15. The angle of incidence for the computations was 75°. The use of larger angles of incidence has been reported [108] but was not considered here because of the small crucible size required for use with the Auger spectrometer. All of the calculations used a polarizer azimuth of 45°. The contours of constant measured values shown on the figures are M_1 and M_2, where:

$$M_1 = \sqrt{\frac{I_2}{I_1}} \quad ; \quad M_2 = \frac{I_3 - I_4}{I_3 + I_4} \tag{7–6}$$

In a strict sense, then, M_1 and M_2 are reduced rather than measured quantities. Plotting contours for each of the four actual measured variables was considered too cumbersome.

The orthogonality of the contours of M_1 and M_2 in Fig. 7-13 indicate the potential effectiveness of Method E. The range of n and k on the abscissa and ordinate are the visible range ($0.3 < n,k < 4$) as discussed earlier. Although both sets of contours curve, they remain very close to orthogonal over the entire range plotted in the figure. The n,k

Figure 7.13 Lines of constant M_1 and M_2 for $0.3<n,k<4$.
M_1, solid lines; M_2, dashed lines

M_1 and M_2 are formed from the four measured values, I_1 to I_4, in the method of Beattie and Conn. The angle of incidence is 75^o.

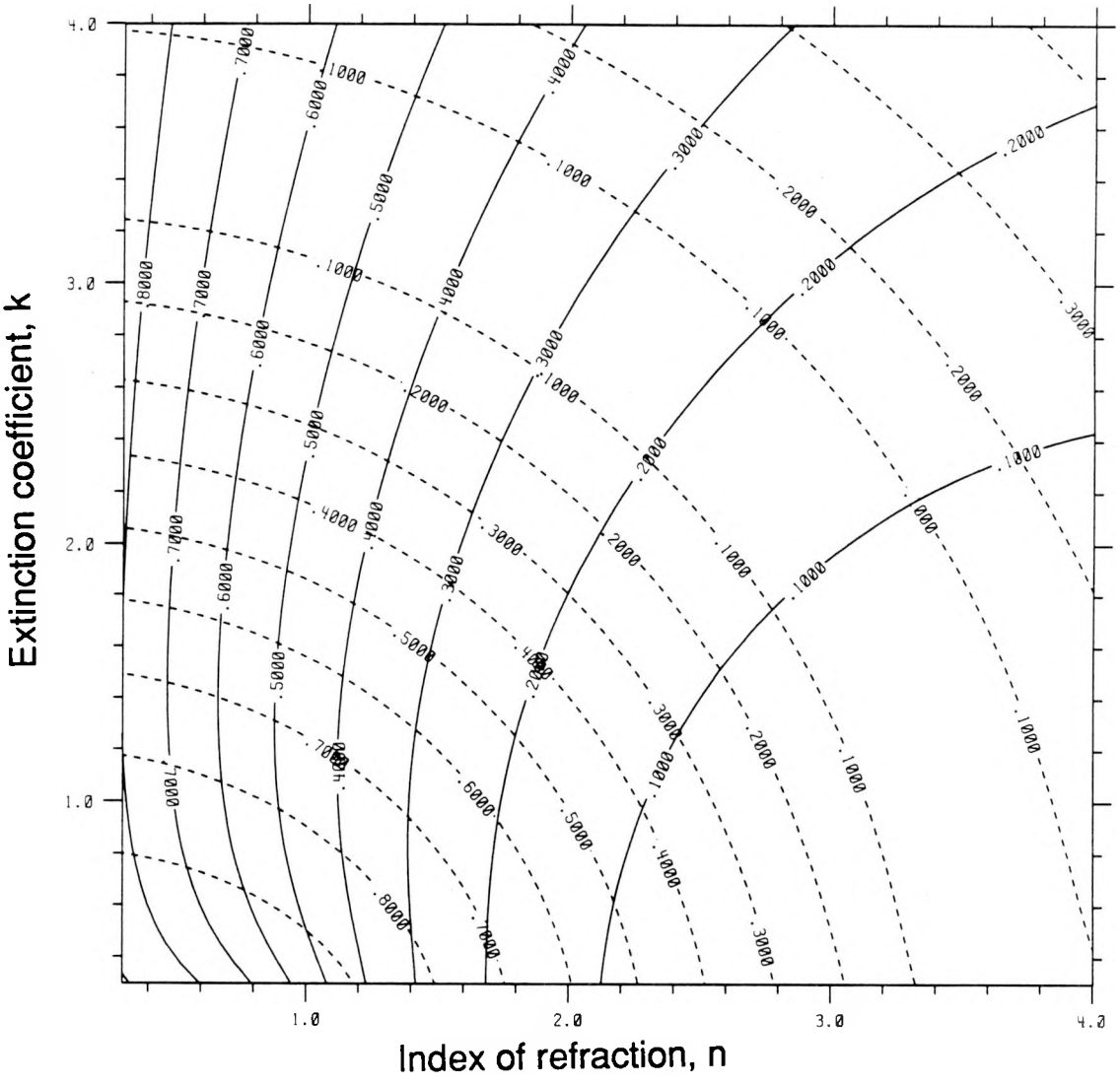

Figure 7.14 Lines of constant M_1 and M_2 for $4<n,k<10$.
M_1, solid lines; M_2, dashed lines

M_1 and M_2 are formed from the four measured values, I_1 to I_4, in the method of Beattie and Conn. The angle of incidence is 75^o.

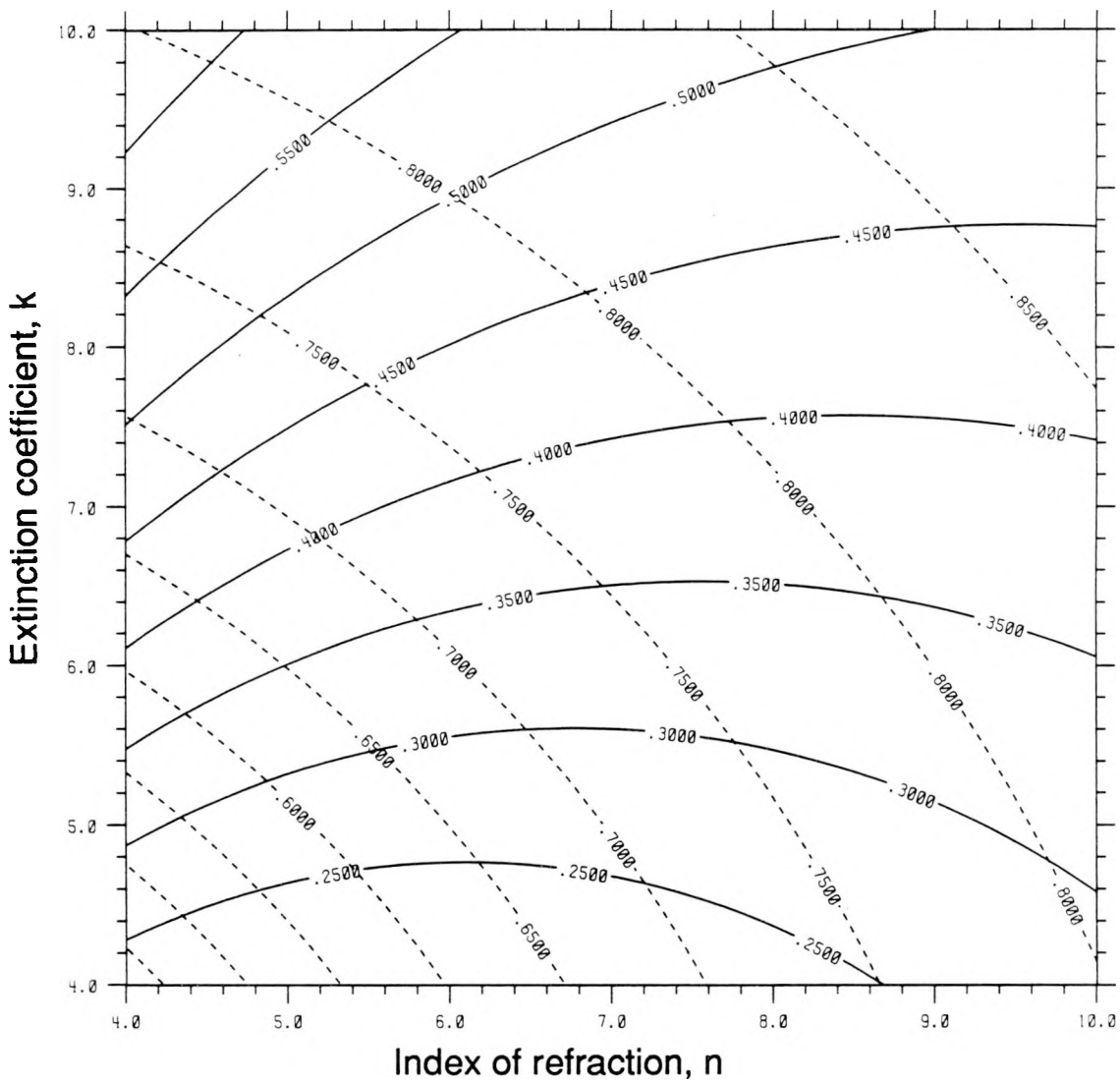

Figure 7.15 Lines of constant M_1 and M_2 for $10<n,k<40$.
M_1, solid lines; M_2, dashed lines

M_1 and M_2 are formed from the four measured values, I_1 to I_4, in the method of Beattie and Conn. The angle of incidence is 75^o.

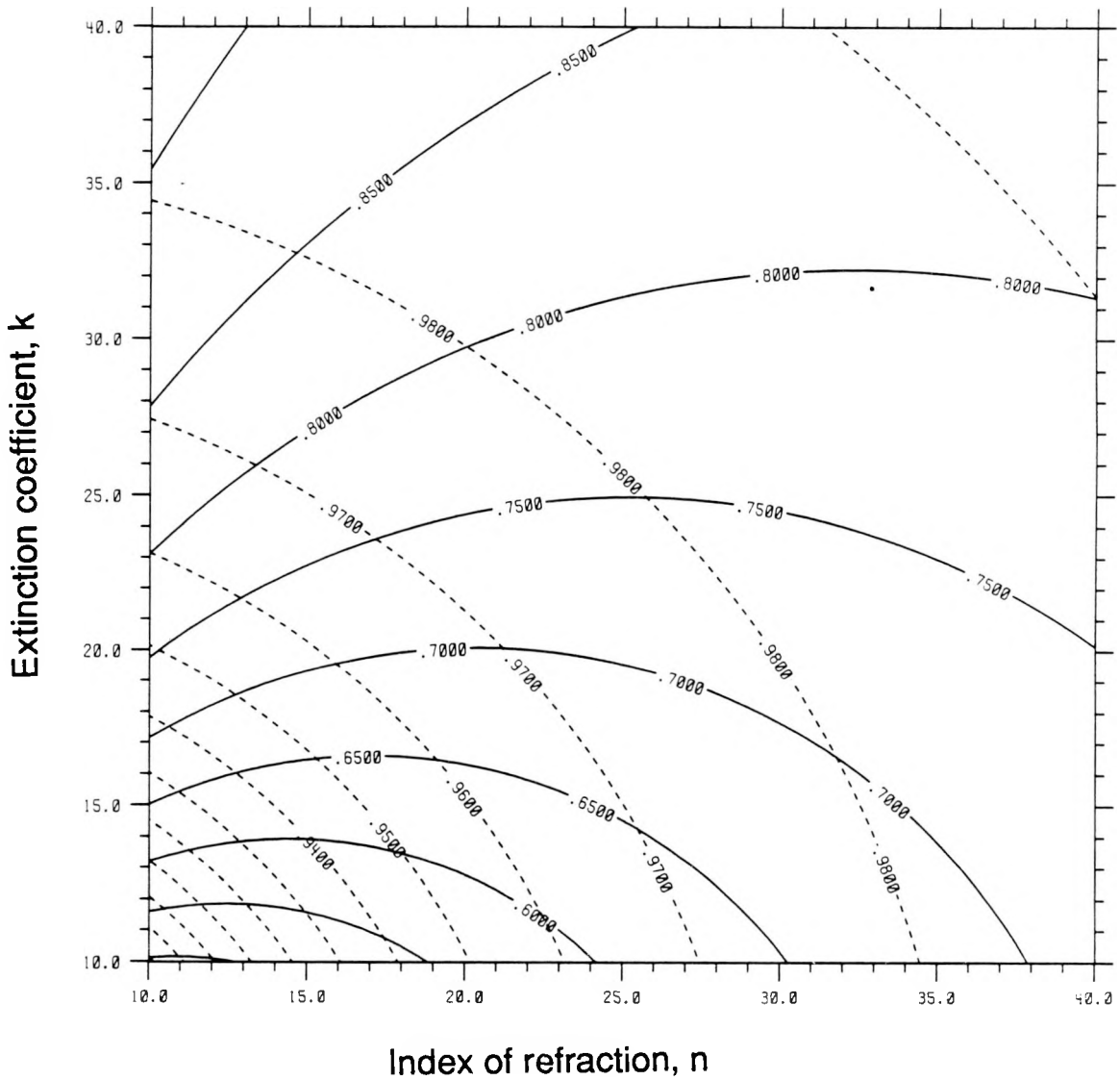

range of 4 to 10 is shown in Fig. 7-14. Both the contour spacing and orthogonality indicate good sensitivity.

The potential sensitivity of the method of Beattie and Conn in the extreme long wavelength limit of this work ($10 < n,k < 40$) is shown in Fig. 7-15. The contours are still intersecting at a reasonably large angle.

Thus, the ellipsometric method of Beattie and Conn retains adequate sensitivity to much larger (n,k) values and hence to longer infrared wavelengths than methods A through D.

7.3.6 The method of Miller (method F). This method is a variation on method E. The values of ρ and Δ are determined from measurements of the two angles of the analyzer for which the intensities are equal for two given settings of the polarizer. However, finding the positions of equal intensity is not as convenient and is considerably slower than recording four intensities at regular polarizer positions as in the method of Beattie and Conn.

Sensitivity plots for method F are shown in Figs. 7-16, 7-17, 7-18 and 7-19. In Figs. 7-16, 7-17 and 7-18, the angle of incidence is again 75^o and the polarizer azimuth was fixed at 45^o. In Fig. 7-19 the angle of incidence was changed to 84^o. The contours on all the plots are lines of constant values of polarizer azimuth for equal intensities. These angles are termed Q_1 and Q_2 and are given in radians on the labels of the contours. In Fig. 7-16 the contour lines are nearly orthogonal over the entire plotted field ($0.3 < n,k < 4$). Methods E and F are very similar in this range for the same (75^o) angle of incidence. Fig. 7-17 presents contours for the n,k range ($4 < n,k < 10$). The contours are also adequately orthogonal on this figure and sensitivity is comparable to method E. However in the highest n,k range, shown in Fig. 7-18, the lines of constant measured position are decidedly more parallel than in Fig. 7-15, the corresponding case for method

Figure 7.16 Lines of constant Q_1 and Q_2 for 0.3<n,k<4.
Q_1, solid lines; Q_2, dashed lines

Q_1 and Q_2 are the angles of equal intensity measured in the Miller method.
The angle of incidence is 75^0.

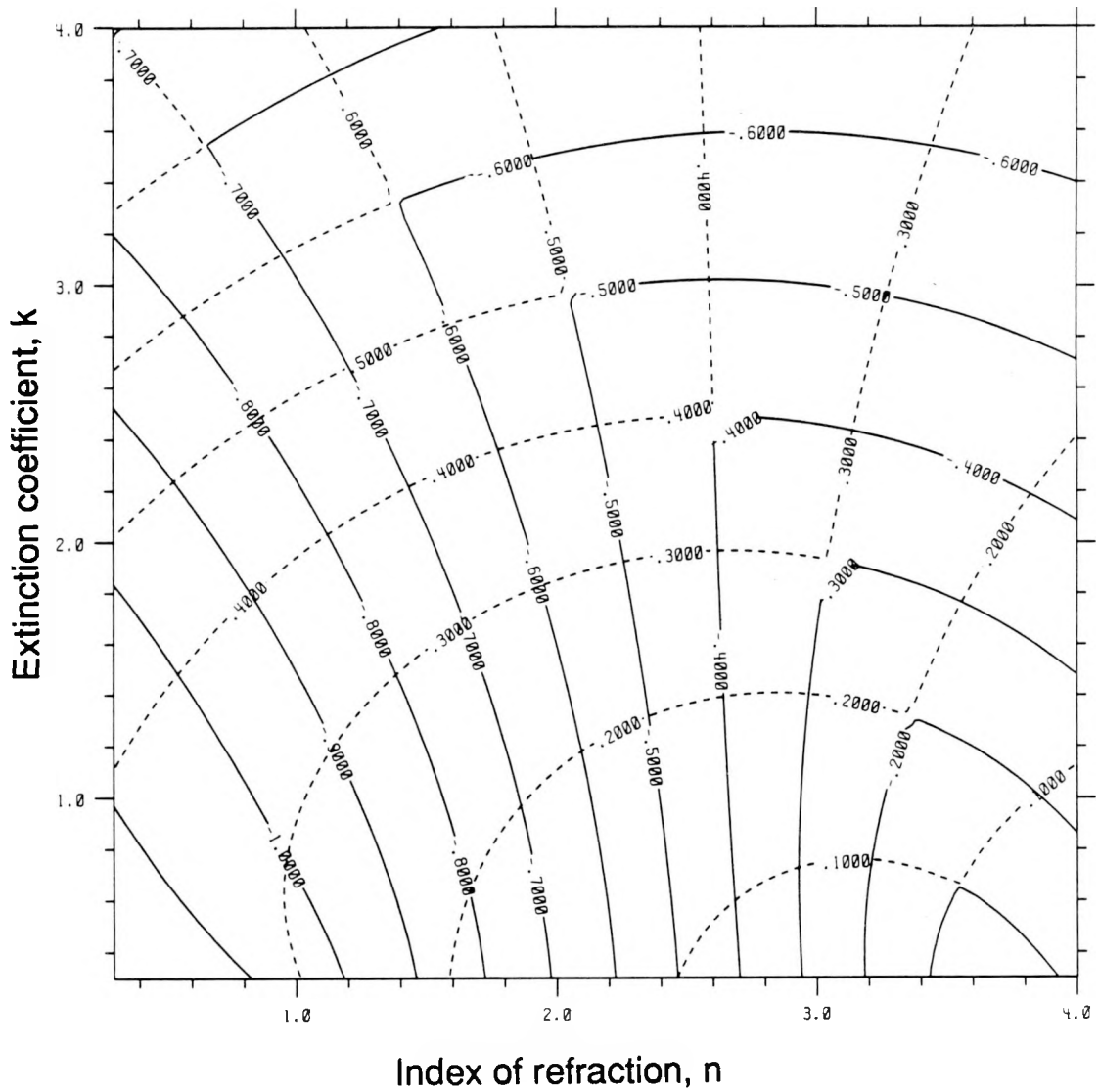

Figure 7.17 Lines of constant Q_1 and Q_2 for 4<n,k<10.
Q_1, solid lines; Q_2, dashed lines

Q_1 and Q_2 are the angles of equal intensity measured in the Miller method.
The angle of incidence is 75^o.

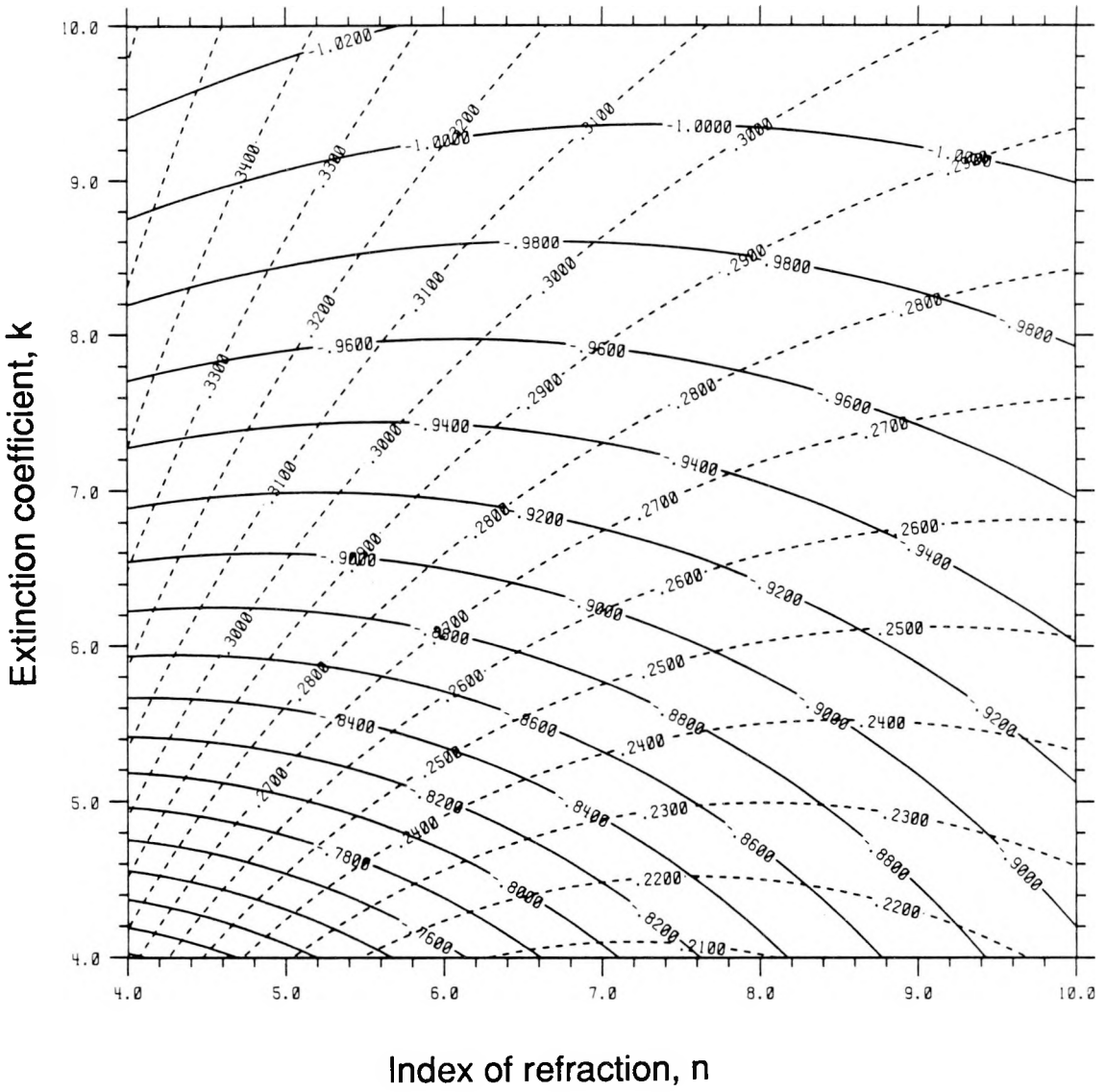

Figure 7.18 Lines of constant Q_1 and Q_2 for 10<n,k<40.
Q_1, solid lines; Q_2, dashed lines

Q_1 and Q_2 are the angles of equal intensity measured in the Miller method.
The angle of incidence is 75^o.

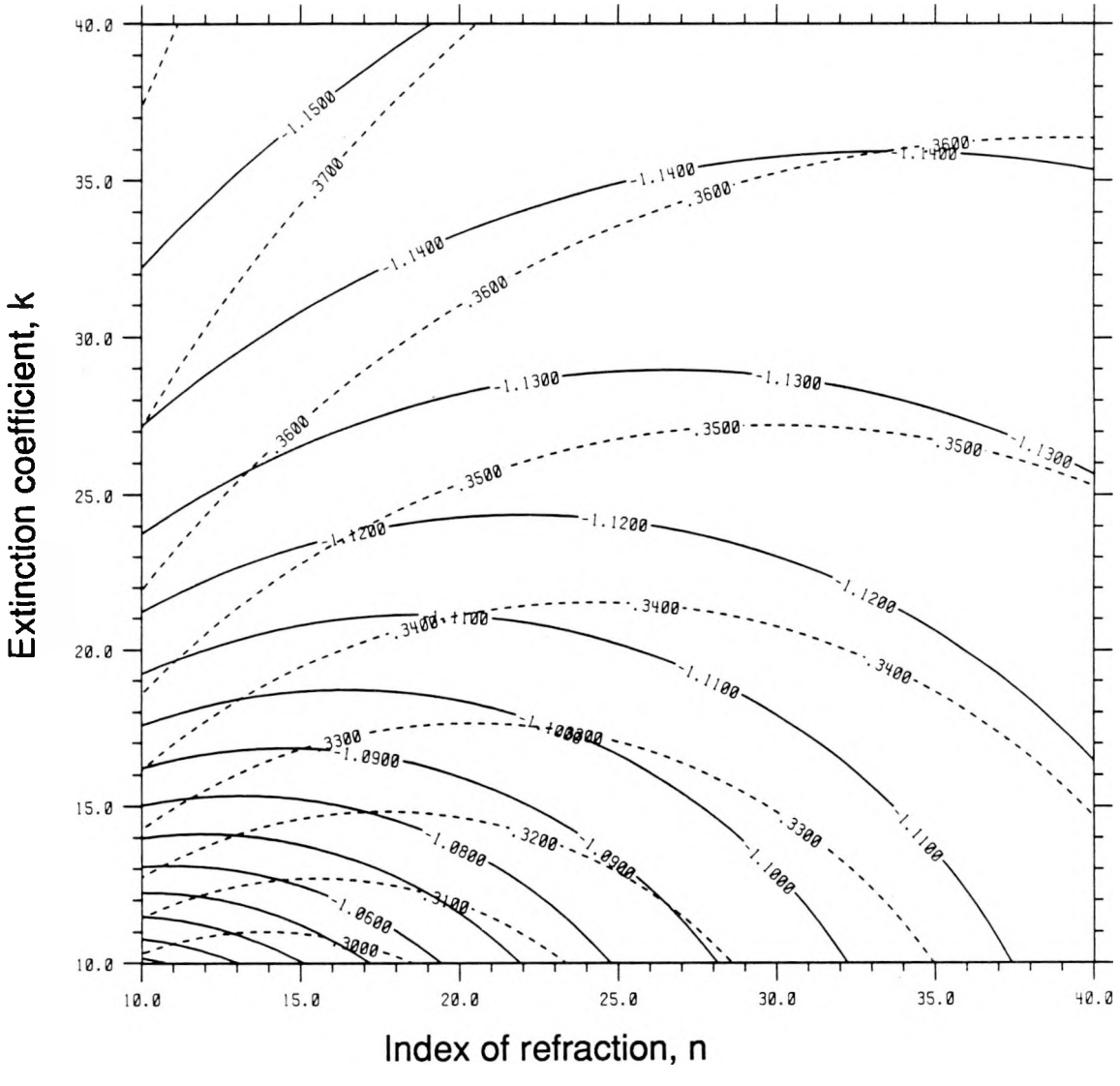

Figure 7.19 Lines of constant Q_1 and Q_2 for $10<n,k<40$, ($\theta_i=84^o$). Q_1, solid lines; Q_2, dashed lines

Q_1 and Q_2 are the angles of equal intensity measured in the Miller method.
The angle of incidence is 84^o.

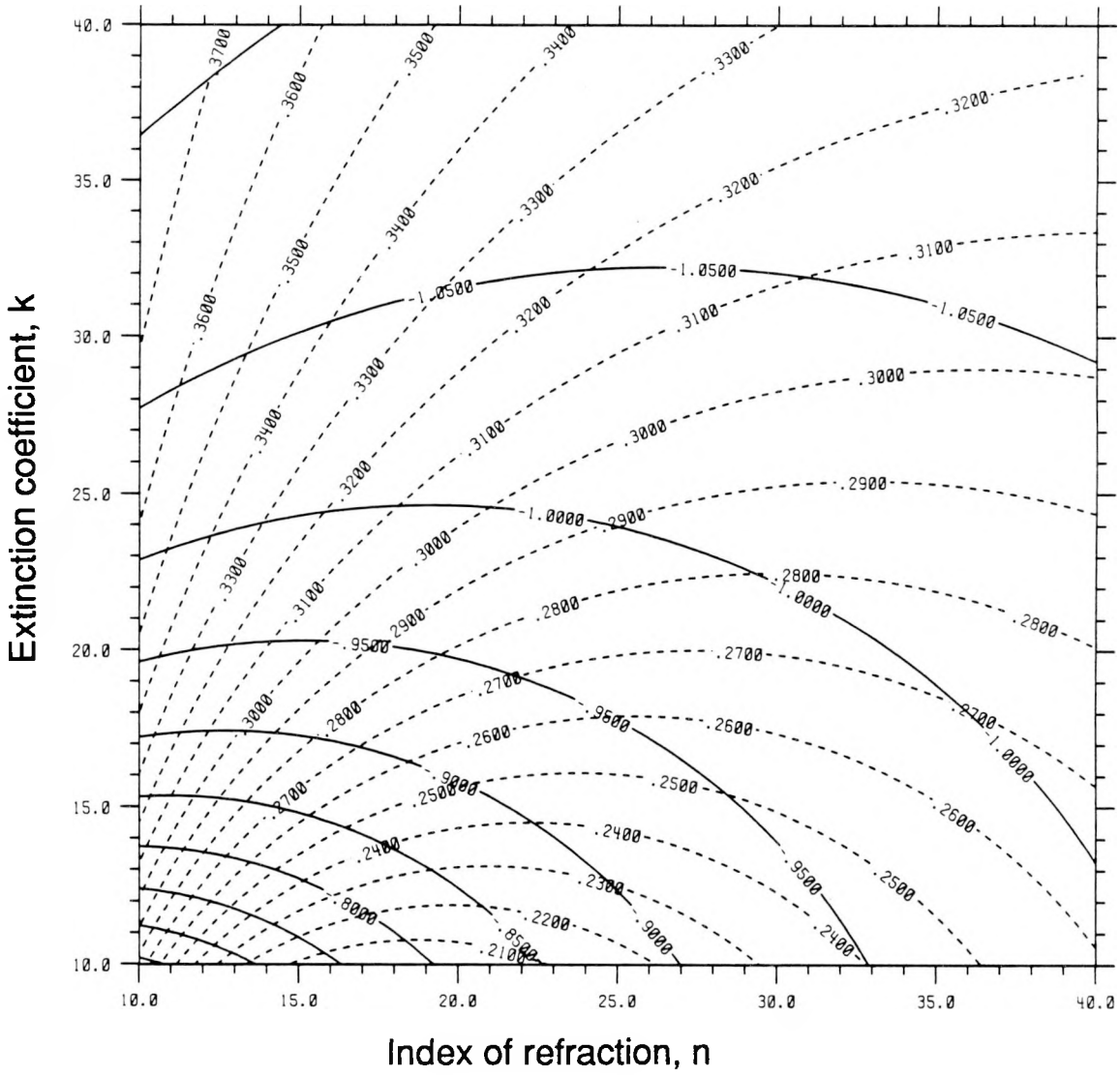

E. This indicates that method F has lower sensitivity than method E in the long wavelength extreme when employing a 75° angle of incidence. Other practical factors may override the indications from these figures but from a fundamental standpoint, the method of Beattie and Conn appears superior.

Sensitivity results for method F in the highest n,k range with the angle of incidence increased to 84° (the angle used by Miller [4] in some of her experiments) are given in Fig. 7-19. The orthogonality of the contours on this figure is comparable to that of method E with a 75° angle of incidence (shown in Fig. 7-15). Substantial advantages in fundamental sensitivity would require working even closer to grazing incidence than 75°. The difficulties associated with such work makes the method of Beattie and Conn (method E) the method of choice.

8. Apparatus and techniques

8.1 General considerations guiding experimental design

Three considerations directed the experimental design from its inception:

1. Sample surface purity and surface composition are required to make measurements on well characterized samples.

2. Redundant and independent measurement methods are required to allow the accuracy of the results to be assessed.

3. Both liquid and solid high temperature samples must be accommodated by the measurement techniques.

Even a brief review of the literature on thermal radiative properties readily confirms the need for the first two requirements [1]. Agreement between studies is rarely consistent with the reported uncertainty. Either surface conditions vary widely or errors are understated. Because of various applications involving molten metals, the third requirement was a consequence of the project interest rather than the problems observed in the literature.

8.1.1 The need for ultra high vacuum. The project interest in a particularly reactive liquid metal, uranium, strengthened the emphasis on the first maxim above. Ultra high vacuum is necesary when working with molten uranium (M.P. 1406 K) surfaces. The importance to experimental design of surface purity considerations is readily illustrated by an order of magnitude calculation of gas collision rates. The flux of gas molecules onto a surface is given by kinetic theory as:

$$\Gamma = \frac{N\bar{c}}{4} \; ; \text{ where } \bar{c} = \sqrt{\frac{8\kappa T}{\pi M}} \quad \text{and } p = N\kappa T \qquad (8\text{–}1)$$

Here, N is the number density, $\bar{c}$ is the mean thermal molecular speed, κ is Boltzmann's constant, p is the pressure, T is the temperature in Kelvin, and M is the molecular mass. For oxygen at 300 K and a pressure of 1.0×10^{-5} torr the flux density of gas molecules onto a sample surface is

$$\Gamma = 0.372 \times 10^{16} \text{ molecules/(cm}^2 \text{ sec)} \qquad (8\text{–}2)$$

Now consider a sample surface in more detail. The lattice spacing of uranium atoms in the solid is ~1.5 Angstroms; hence the surface atomic density is $\sim 0.14 \times 10^{16}$ atoms/cm^2. Thus if uranium were a perfect getter (and it is an excellent one [174]) at $p = 1 \times 10^{-5}$ torr, a pure metal surface would be completely covered by impurities in a time $t \sim 0.4$ seconds. A single monolayer is nearly invisible to a normal emissivity measurement at the wavelengths of interest here but a reactive surface will develop a thicker layer continually. If a monolayer is taken as 3 Angstroms thick (twice the lattice spacing), there are only 6500/3 monolayers to the standard wavelength for spectral emissivity measurement and only ~3 minutes is needed to develop an oxide a quarter wave thick which would strongly modify the surface properties. One would not expect the successive layers to form as fast as the first because the impurity must diffuse through the existing layer, and moreover these calculations are only order of magnitude estimates, but clearly at 1×10^{-5} torr or even 1×10^{-6} torr, the possible measurement time with reactive materials is on the order of minutes or less. Thin surface layers can have much greater effect on oblique reflection than on normal emission so that the vacuum system base pressure and surface cleaning are yet more important and measurement times must be still

shorter for ellipsometry. Hodgson [2] gives the variation of skin depth with angle of incidence as

$$\delta = \delta_n \left(1 - \frac{1}{2\ |\epsilon''|} \sin^2 \theta \right) \qquad (8\text{–}3)$$

Here θ is the angle of incidence, $|\epsilon''|$ is the magnitude of the complex dielectric constant and δ_n is skin depth at the normal incidence given in Chapter 2. For liquid metals, $|\epsilon''|$ is very large and the skin depth variation with θ is small, but for oxides and other common surface contaminants $|\epsilon''|$ is small so that the skin depth is much reduced at oblique incidence. Thus, thin oxide layers can easily perturb ellipsometric measurements intended to yield the properties of the pure substrate .

8.1.2 The need for independent optical property measurements. The common compendiums of data on thermal radiative properties of materials show a wide range of results for the properties of any one material. It is widely acknowledged that much of this variation is due to differing surface preparations and contamination. However, even with materials where surface preparation and composition might be thought to be very similar, the reported results sometimes vary widely. A possible explanation for such discrepancies is that the experimenters did not detect significant errors with their technique. A possible means of avoiding this problem is to make multiple independent measurements of radiant properties. Studies of thermal radiant properties are particularly well suited to this approach because of the interrelationships between the three basic properties (absorptivity, reflectivity and emissivity). For some samples and measurement ranges it is conceivable that three independent sets of results, one for each property type, could be obtained and compared to check for errors.

However, absorptivity measurements are very difficult except at cryogenic temperatures. In the present study two independent measurement methods were deemed sufficient. In results chapters 9 to 11 errors are discussed in more detail.

8.1.3 The need for complete rather than limited property data. The literature for the thermal radiative properties of materials contains results in various forms, some of which were noted in Chapter 2. In many cases however individual researchers give only the normal spectral emissivity for a material. Sometimes this type of data is useful because the total and/or hemispherical properties can be reasonably estimated from the normal spectral emissivity. In other cases or for other parameter regimes (temperature and phase for example), the limited nature of the data makes it of very little use. The range of applications for the materials of interest here made it desirable to get as complete a set of optical and radiative properties as possible from this study. The nature of the samples, smooth pure liquid metals, and the two methods chosen, oblique ellipsometry and normal spectral emissivity combine to make the measurements reported here reasonably complete. All types of emissivity, reflectivity and absorptivity can be computed from the complex index of refraction results given in Chapters 9, 10 and 11.

8.2 The vacuum system and optical access

8.2.1 Vacuum materials. The vacuum chamber was made from stainless steel plate and cleaned by a proprietary process for UHV use. Both aluminum and stainless steel parts were used for the many supports, platforms and other hardware inside the chamber. Brass, bronze or other materials with high vapor pressure constituents such as zinc were entirely avoided. Several sliding and rotating mechanisms are contained in the chamber. Sapphire ball bearings allow these systems to move freely without

lubrication. Anodized and cadmium plated nuts and bolts are not used because of their tendency to outgas. Magnetic steels are not used in the vicinity of the Auger spectrometer because magnetic fields perturb the path of low energy electrons. Valves with all metal seals are used wherever bakeout will be required because non-metal seals, such as viton or rubber, harden at elevated bakeout temperatures. All ports are sealed with copper conflat gaskets. The inner walls and many of the optical parts of the chamber are coated with aerodag (carbon particles suspended in isopropyl alchohol). This material was applied to reduce stray reflected light during optical measurements. After application of this coating, the entire chamber was baked for several days. The pumping system's ultimate pressure was not significantly higher following this bakeout, so outgassing of the coating was neglible.

8.2.2 The pumping equipment. The need for measurements on high purity samples led to the design of an ultra-high vacuum (UHV) system with a base pressure of $\sim 2 \times 10^{-10}$ Torr. Figure 8-1 is a schematic of the vacuum pumping and gas bleed system. The roughing pump is a 50-cfm free air displacement, two-stage mechanical pump with an ultimate pressure of 2×10^{-4} Torr. A liquid nitrogen cold trap framed by isolation valves is located upstream of the mechanical pump. Both pump and trap are mounted on a concrete pad outside the laboratory to minimize mechanical vibration of the optical systems. The valves on either side of the trap are interlocked to the building electrical supply and function pneumatically from a compressed air bottle. When electrical power to the mechanical pump is lost both valves automatically shut to prevent backstreaming of contaminants to the test chamber.

A thermocouple gauge located in the vacuum line between the trap and the turbomolecular pump senses the fore line pressure. In this line, pressures above ~0.03 torr indicate a problem in the roughing system.

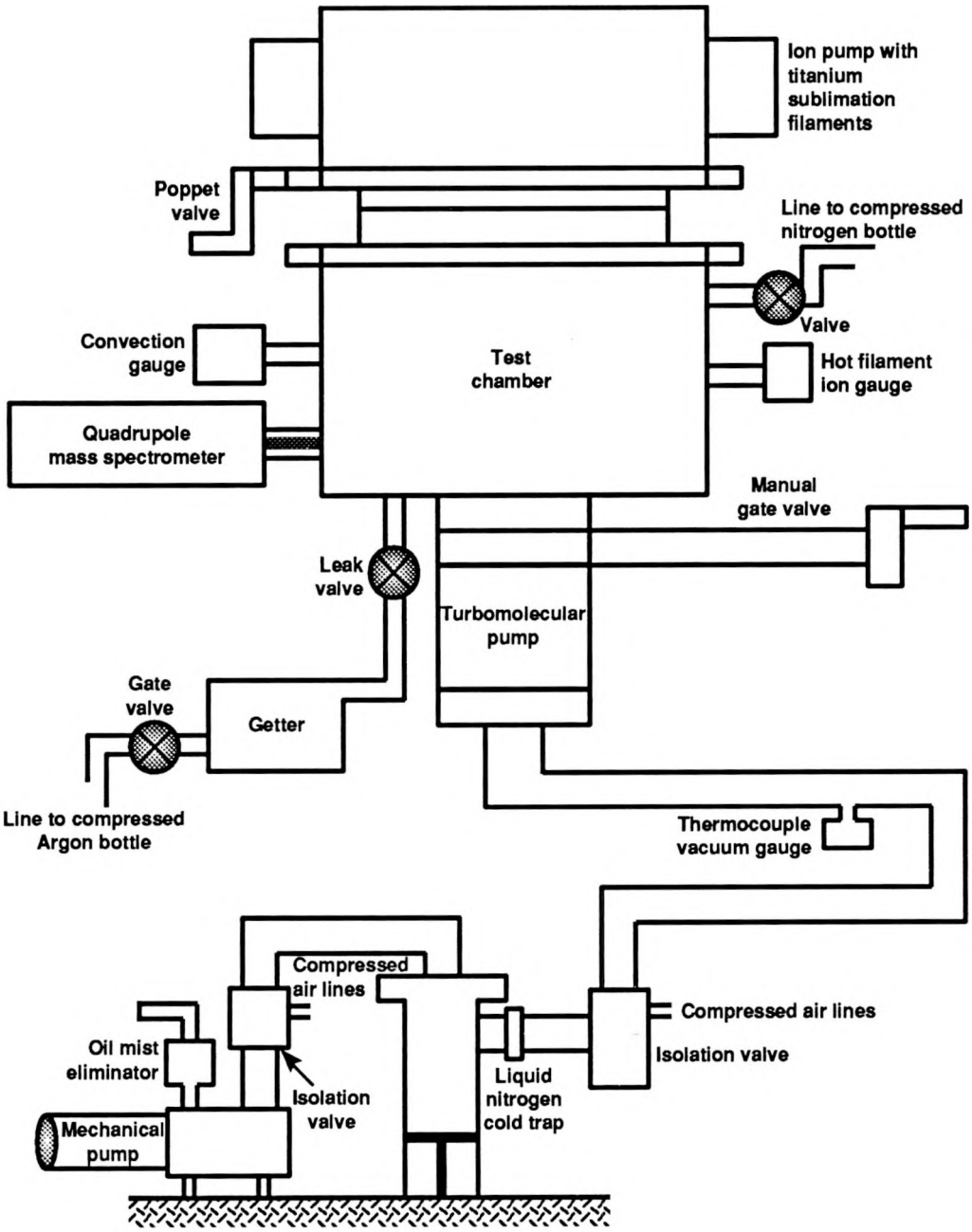

Fig. 8-1. Schematic of the vacuum system.

The turbomolecular pump is rated at 300 liters/sec and is magnetically levitated so there are no lubricated bearings. The rotors run at 48,000 rpm. After bakeout, the ultimate pressure of the pump is 10^{-10} torr. Maximum bakeout temperature of the pump is 120°C. Upstream of the turbomolecular pump is a manually operated 8-in. gate valve with all metal seals. This valve isolates the test chamber from the mechanical pumping system and throttles the loss of sputtered gases from the system during ion sputter cleaning of the sample surface.

The main volume of the test chamber is also pumped by a 300 l/sec ion pump mounted at one end of the system. The permanent magnets mounted outside the chamber around the ion pump are visible in Fig. 8-2. A poppet valve is used to isolate the test chamber from the ion pump which also incorporates a titanium sublimation pump. Near the ion pump are ion and convection gauges. The ion gauge senses the operating pressure in the vacuum system and is used when setting the bleed pressure of sputter gas. The convection gauge senses the pressure level when filling the test chamber with dry nitrogen. Also, at this end of the chamber is a quadrupole type mass spectrometer, used to analyze the composition of the background gas in the vacuum chamber, detect leaks, and check the purity of the sputter gas during cleaning operations.

Figure 8-1 also shows two gas lines feeding the test chamber through needle valves. One line provides dry nitrogen for bringing the system up to atmospheric pressure without exposing the chamber walls to the water vapor in ambient air. The second gas inlet provides high purity argon during sputter cleaning. A precision leak valve is used to set the sputter gas pressure.

Argon (of research grade purity) from a high pressure bottle is admitted periodically to the getter through the gate valve shown. Reactive metal alloy in the getter removes the trace impurities from the gas stream.

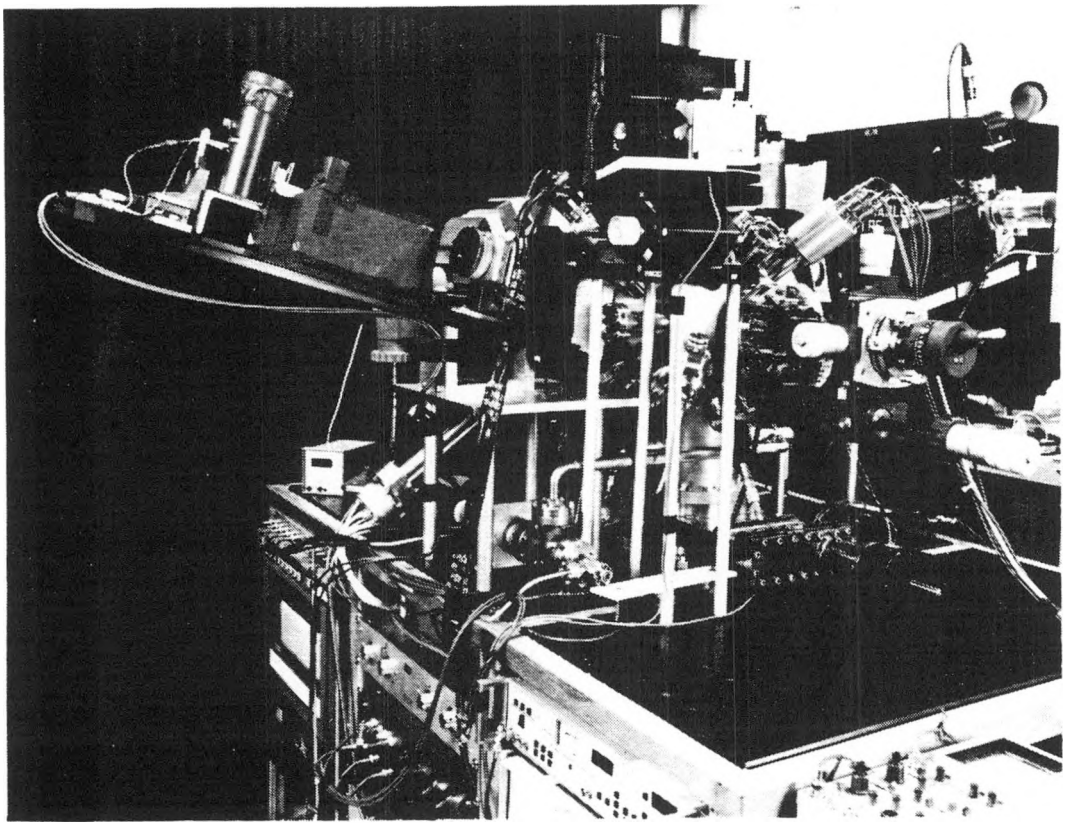

Figure 8-2. The apparatus. The output portion of the ellipsometric optical system is at upper left. The crucible manipulator is on the right.

8.2.3 Bakeout equipment and procedures. Bakeout, to remove water vapor and other high vapor pressure condensates from the vacuum chamber walls, was performed each time the system was opened to atmospheric pressure. Heat sources for bakeout were 1) resistive heating elements, 2) tungsten filament lamps in sealed quartz envelopes and 3) a heat lamp. The resistive heating elements are pliable fiberglass insulated tapes which were wrapped about the chamber walls. Usually, four 100 watt units were used and the entire chamber was covered with aluminum foil. The two tungsten filament lamps were mounted inside the chamber and powered through two current feedthroughs mounted on a 2.75" conflat flange. These were run at 200 watts each for the duration of the bakeout. The heat lamp, a 250 watt bulb, was mounted over the bellows of the sample manipulator stage (see section 8.7.4) and the whole part was covered with aluminum foil. The manipulator stage and the large surface area of its welded bellows was usually exposed to ambient air for extended periods while the sample was being mounted. In contrast, the rest of the chamber was only open to ambient while the stage was being removed or installed. This extra exposure and the high surface area of the bellows made it necessary to apply the extra heat from the lamp directly to the sample manipulator.

The normal duration of bakeout was 14 hours but in some instances longer periods were used. The ion pump portion of the vacuum system was rarely baked because the poppet valve adjacent to it was usually shut when the chamber was opened. This portion of the system was never baked at elevated temperatures because the poppet valve includes a viton O-ring. The turbo-molecular pump includes a permanently installed bakeout jacket which was also activated during chamber bakeout.

8.2.4 Vacuum system interlocks. The apparatus has two interlock systems. In one system, any loss of electrical power to the mechanical pump (shown in Fig. 8-1) causes the two valves on either side of the liquid nitrogen cold trap to close. This feature isolates the chamber from the contaminants in the trap and mechanical pump oil.

In the second interlock system the electrical power to critical systems within the test chamber is interrupted if the chamber pressure exceeds 9×10^{-5} torr. The systems deemed critical were the Auger spectrometer, the ion sputter guns and the sample heater. This interlock system protected the sensitive filaments of these components and the electronic systems which supplied them.

8.2.5 The optical access ports. Calcium fluoride windows mounted in conflat flanges were used to pass light into and out of the vacuum chamber. The normal spectral emissivity system used a 0.14" thick, 1.39" diameter viewport mounted in a 2.75" conflat flange. The ellipsometric system used two 0.1" thick, 0.465" diameter viewports mounted in 1.33" conflat flanges.

The vacuum joint between each window and its flange may determine whether or not the windows altered the state of polarization of the light they transmitted. Stress induced birefringence is particularly critical with the ellipsometry system viewports. Calcium fluoride has a face-centered cubic crystal structure so that when stress-free it exhibits no birefringence. However, the CaF_2 windows are brazed to a silver seat welded to the conflat flange. (Annealed silver is very soft so it will deform easily rather than transmit much stress to the window. The brazing material is silver chloride and the brazing operation takes place at 770 K. Silver displays a linear thermal expansion of 0.85% between 770 K and room temperature and that of CaF_2 is 1.0%. Thus, the cooling process subsequent to the formation of the braze joint may create thermal stresses in the

windows. Raw material for the window slabs is cut by the manufacturer to give the maximum number of parts from each piece of stock. Therefore, the effect of stresses produced by fabrication may vary widely from part to part depending on the orientation of the slab cut. The stress-induced birefringence may also vary from part to part.

Stress birefringence information for CaF_2 and a few other common optical materials is given in Appendix C. The data indicate that CaF_2 is more forgiving in this respect than many other materials.

In order to show that stress induced birefringence did not affect the results shown here, ellipsometric measurements were made on a tungsten sample with the vacuum system at both 5×10^{-9} torr and 760 torr (of nitrogen). There was no detectable change in the optical constants inferred from these tests, which varied over a wide range of window stress.

8.3 Surface analysis equipment

8.3.1 Auger spectrometer. Quantitative analysis of surface composition was an initial requirement of this work and Auger spectroscopy is particularly suited for the task. Uniform sample purity from the bulk to the topmost surface layer was required to obtain the optical constants representative of pure molten metals. Since Auger spectroscopy averages the elemental composition over the top ~10 to 20 Å of a sample and because, when samples (especially dense ones such as uranium) liquefy, most impurities rise to the surface, this technique was ideal. The spectrometer used here requires UHV conditions or very pure inert gas environments at $\sim 10^{-5}$ torr or lower, so it was compatible with the conditions required for the molten metals of interest.

Auger spectroscopy is so named because it uses the Auger radiationless process to determine the mass constituents of a sample at and very near a vacuum-surface interface. The Auger process describes the decay to a lower energy state of an atom which has been

stripped of a core electron by an energetic perturbation such as an impinging electron beam [175]. The energy levels and electronic transitions of such an ionized atom are shown in Fig. 8-3. The process begins when a core level electron is removed from an atom at or near the surface by the high energy electron beam. The core level vacancy is rapidly filled by an electron dropping down from a higher lying shell of the same atom. The electron which fills the core vacancy moves from energy level E_K to level E_L Since the atom has gone from a highly energetic ionized state to a less energetic but still

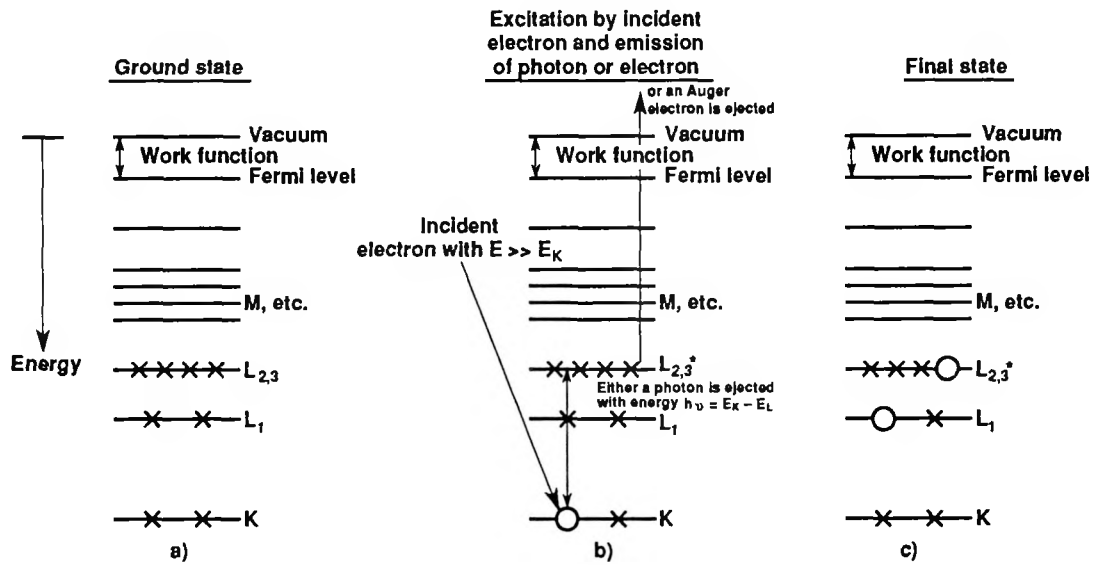

Fig. 8-3. The Auger process. The ground state is shown in a). In b), an energetic electron creates a vacancy in a core (K) atomic shell. A higher lying shell donates an electron to the K shell and either a photon of appropriate energy is ejected or a higher lying shell ejects an Auger electron. The final state is doubly ionized. $E_{L_{2,3}}$ is starred because the appropriate binding energy is for the atom with a hole at L_1 rather than for the atom in the ground state.

ionized state, there is energy to be released. Often this energy appears as a photon ejected by the atom; however there is a probability, depending on the atom, that electrons will be ejected. Their kinetic energy, if they escape the material and reach the vacuum level, is given by the amount of energy available after the initial core level filling process, $E_K - E_{L1}$, less the energy required to free the Auger electron from its bound position within the atom, $E_{L2,3}$. Since the electron energy levels are unique to each element, so are the energies of the ejected Auger electrons. Although not all Auger electrons escape from the material and reach the energy analyzer in the spectrometer, a sufficient number do so to allow surface elemental analysis to be performed with about 5 % precision.

The principal parts of the Auger spectrometer, shown in Fig. 8-4, are the electron gun, the Auger electron energy analyzer and the electron detector. The electron gun employs a hot tungsten filament and a biased grid for accelerating electrons toward the focusing portion of the gun. The electrons are accelerated toward the target, typically with 5 kV while the focus electrodes are used to produce a tightly focused beam at the sample. The focus of the electron beam is coincident with the source point for the cylindrical mirror energy analyzer (CMA). Electrons ejected from the sample move radially outward from the point of excitation and those which enter the analyzer pass through a grid covered aperture on the inner cylinder. The negative potential on the outer cylinder directs electrons with certain energies back through another aperture in the inner cylinder and then into the electron detector. The energy of those electrons brought to the electron detector is controlled by the negative bias applied to the outer cylinder and is scanned over the range of Auger electron energies, typically 0 to 2kV. Typical electron detectors are electron multipliers, of either the continuous or discrete dynode type. The

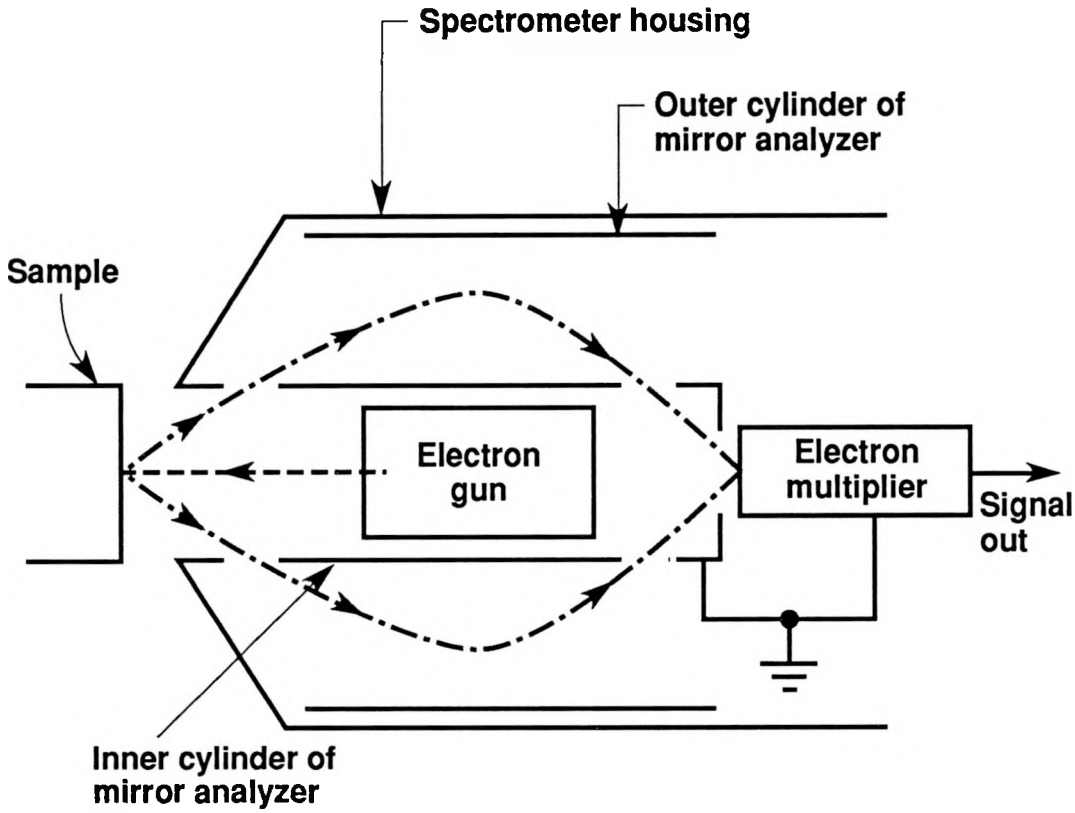

Fig. 8-4. Principal components of an Auger spectrometer.

current to the dynode is amplified by repeated collisions with a surface coated with a material such as CuBe which ejects more than one electron for every impacting electron. Current gain of 10^6 is typical in such detectors.

In operation, the spectrometer's electron gun provides 1 to 5 μamps of current to the sample at 2 to 5 keV. The beam diameter at the sample may be as small as a few μm or as large as 1 mm. Electron beam deflection or scanning at the sample surface are common in newer models but the instrument used here had neither of these capabilities.

Auger electron currents through the CMA are usually in the nA range but the high gain of the electron detector together with phase sensitive detection (the outer cylinder of the CMA is modulated) make these small current levels adequate for good signal to noise performance.

An example of an Auger spectrum of a tungsten sample is shown in Fig. 8-5. The discontinuities in the spectrum are the result of changing the lock-in amplifier gain to obtain a large displayed peak height for each of the elements present in the sample. The peaks on the plot are identified with particular elements using handbooks which show the Auger spectra for most of the elements in their pure state. One peak height is measured for each element identified as present in the sample. Preferably the largest peak is used with a sensitivity factor given in a handbook. The peak height, sensitivity factor and lock-in amplifier gain applicable to each of the identified elements are given in Table 8.1.

To obtain the sample surface mass distribution the peak heights are all normalized with the sensitivity factors and gains as shown below:

$$P_{hn}(i) = \frac{P_h(i)}{S_f(i)\,G(i)} \qquad (8\text{–}4)$$

Here P_h is the peak height, S_f is the sensitivity factor, G is the amplifier gain and P_{hn} is the normalized peak height.

The fraction of element i on the surface is then given by its fractional contribution to the sum of the normalized peak heights:

$$\text{atomic fraction of species i} = \frac{P_{hn}(i)}{\sum_{i=1}^{m} P_{hn}(i)} \qquad (8\text{–}5)$$

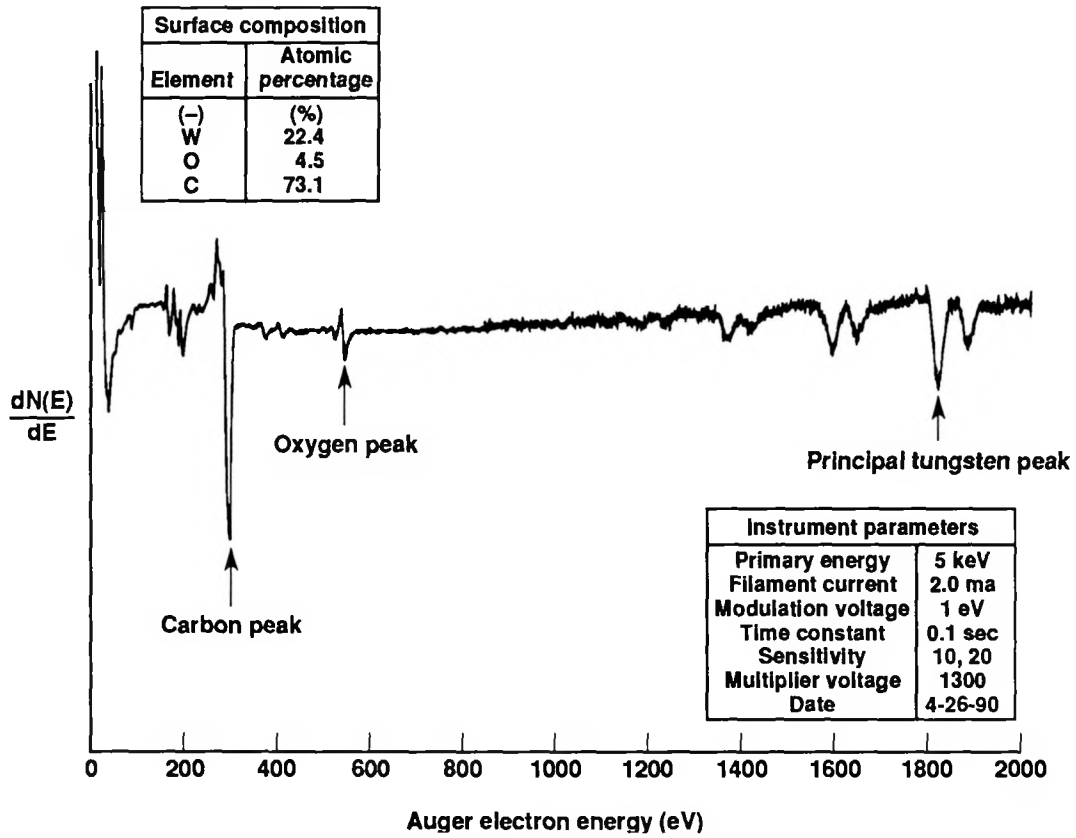

Fig. 8-5. Auger spectrum of a "dirty" tungsten sample.

TABLE 8.1

Auger spectra analysis for tungsten sample of Fig. 8.5

Element (-)	Peak Height (-)	Lock-in Amplifier Gain (-)	Peak Sensitivity Factor (-)	Normalized Peak Height (-)	Surface Atomic Percentage (%)
W	1.108	40	0.080	.34625	22.4
O	0.557	20	0.40	.0696	4.5
C	3.155	20	0.14	1.127	73.1

For the sample shown in Fig. 8-5 further cleaning operations were required to remove the surface contaminants and obtain a purity comparable to that of the bulk material. Carbon is a common impurity in many metals because of the widespread use of carbon crucibles in metallurgical processing.

For solid tungsten, these operations were a combination of a slight oxygen bleed ($p = 2 \times 10^{-7}$ torr) and short periods of ion sputtering (~5 minutes or less) on a hot (~1070 K) surface to remove both the carbon and oxygen contamination.

For uranium and aluminum, ion sputtering was the sole cleaning operation, usually with the sample at ~2/3 of the melting temperature (in Kelvin). Figure 8-6 shows an Auger spectrum for a uranium sample early in the cleaning process. Oxygen and carbon impurities were both common at this stage. Figure 8-7 shows a spectrum for a cleaned uranium surface. Samples in this condition were used for optical measurements.

8.3.2 Ion sputter guns During ion sputter cleaning, energetic (0.5 to 5.0 keV) noble gas ions bombard a surface and physically knock off the surface atoms. Noble gas ions are used because they do not react with the surface material, although a small fraction are implanted in the sample. The principal elements of a sputter gun are shown in Figure 8-8. A hot tungsten filament is used as a source of electrons to ionize argon atoms which are then accelerated toward the sample. Electrodes in the body of the gun focus and deflect the ion beam in a raster pattern.

During typical operation, the entire vacuum system is filled with very pure argon to a pressure of 2 to 7×10^{-5} torr. When the raster function of the ion beam is off, a 2 mm diameter beam is achievable for a current density of 280 $\mu A/cm^2$ at the beam center and 80 $\mu A/cm^2$ at full width half maximum (FWHM). With the full raster on, the gun provides 8 $\mu A/cm^2$ at maximum and 5 $\mu A/cm^2$ at FWHM while sputtering over a ~12 mm x ~12 mm square.

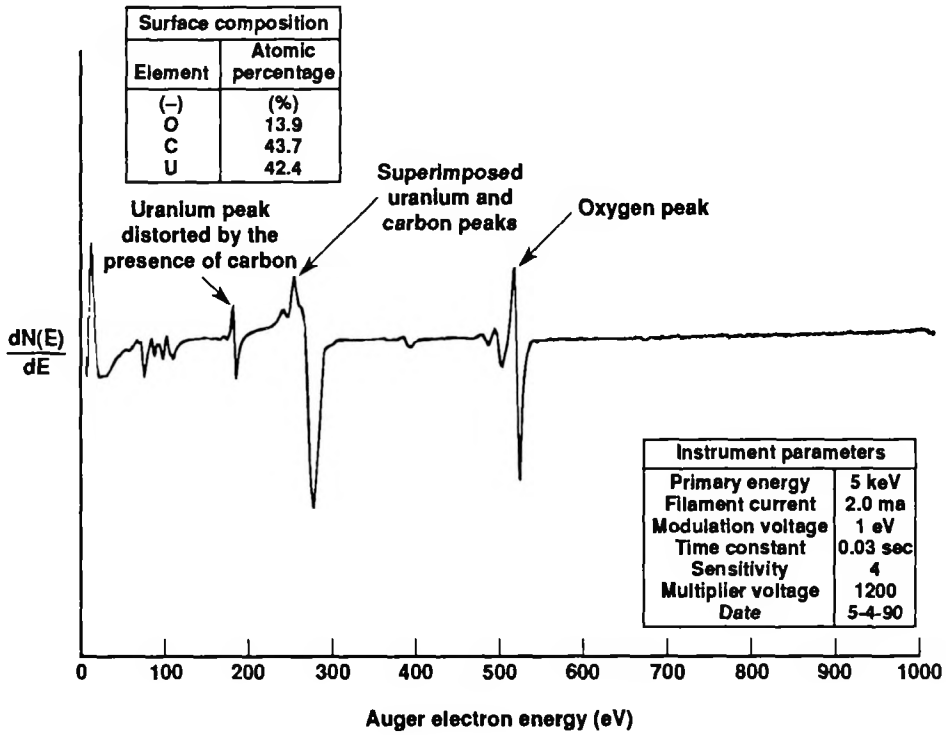

Fig. 8-6. Auger spectrum of a "dirty" uranium sample.

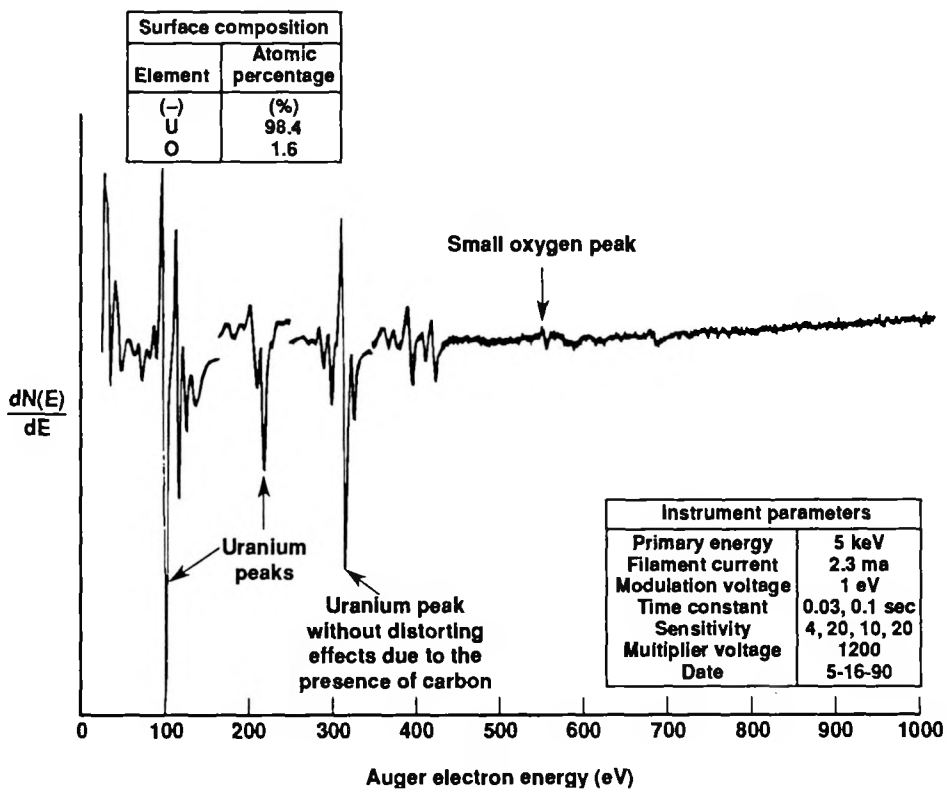

Fig. 8-7. Auger spectrum of a "clean" uranium sample.

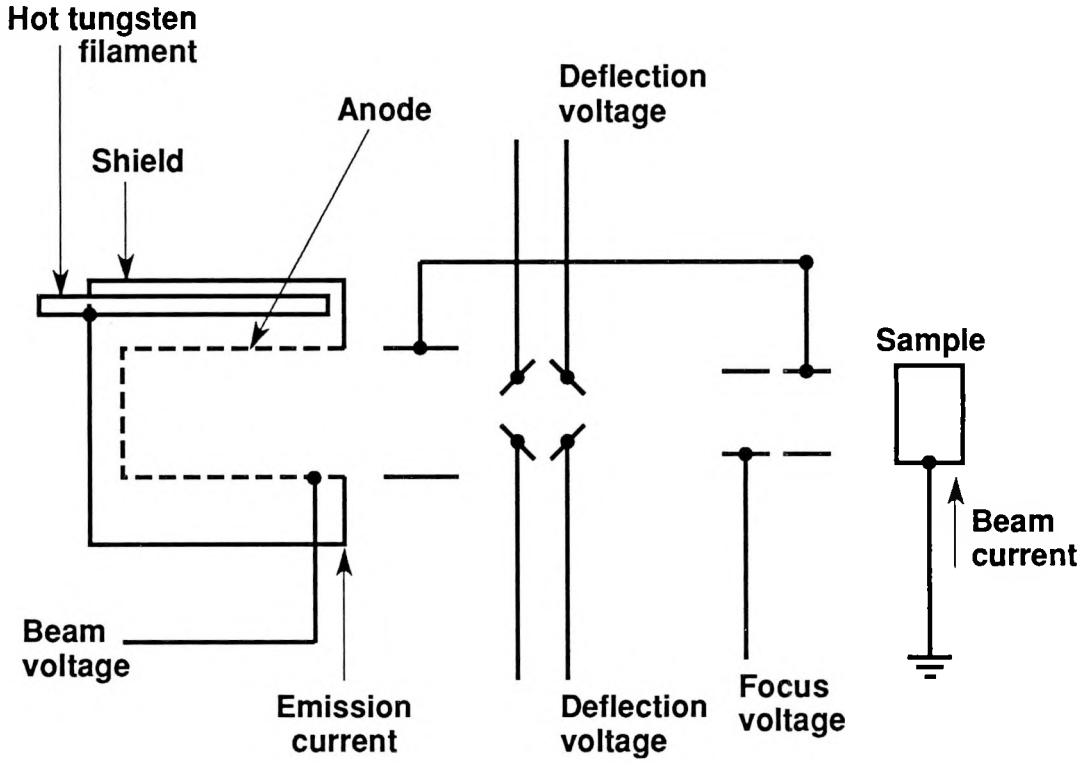

Figue 8-8. Principal components of an ion sputter gun.

Sputter rate, R, is estimated from the following relation [176]:

$$R = 6.24 \times 10^{-2} \frac{JfM}{\rho} \text{ angstroms/minute} \qquad (8\text{–}6)$$

where f = sputter yield- atoms out per ions in

J = ion current density in amps/cm^2

M = atomic weight of sputtering gas in gm/mole

ρ = density of material being sputtered in gm/cm^3

The sputter yield, f, is a strong function of both the accelerating voltage and the ion molecular mass and is empirically determined. Approximate sputter yields for metals and oxides, including uranium and uranium oxide are given in the literature [175].

While cleaning the surface of uranium, the sputter rate is typically tens of angstroms per minute or hundreds of mono-layers per hour. In practice, two weeks were usually required to produce a clean molten uranium surface from uranium bar stock which was nominally 99.999% pure or better. The material purity rating refers to the bulk, not the surface, which is invariably oxidized. Several melt and solidification cycles (each followed by prolonged sputtering) were required to produce a clean molten metal surface. While the metal is liquid, most impurities float to the free surface, but some redissolve on freezing. Sputtering must be performed on solid uranium because the liquid destroys crucibles in a matter of hours. With other less corrosive liquid metals, such as aluminum, solid sputtering is often still preferred because the liquid may slowly wick its way out of the crucible by progressively wetting more and more of the crucible surface area. Sputter yields for solids also depend on crystal orientation and the bonding strength of the surface atoms. Sometimes atoms near or in the grain boundaries are removed at a different rate than those at the center of a grain. The carbon and nitrogen surface impurities often have higher sputter yields than the bulk metal. These sputtering effects are particularly relevant to the work in this study with tungsten. The preferential sputter yield around grain boundaries and other defects produced roughened surfaces. This phenomenon limited the amount of sputter cleaning that could be performed on solid tungsten before surface roughening made ellipsometric measurements impractical.

8.4 A brief account of early versions of the optical system

The original optical system planned for this work was designed to directly measure the spectral reflectivity and emissivity as functions of angle. This concept is shown in Fig. 8-9. In the reflection measurement system the light source was imaged into the vacuum system through a calcium fluoride window. An image of the hot filament of

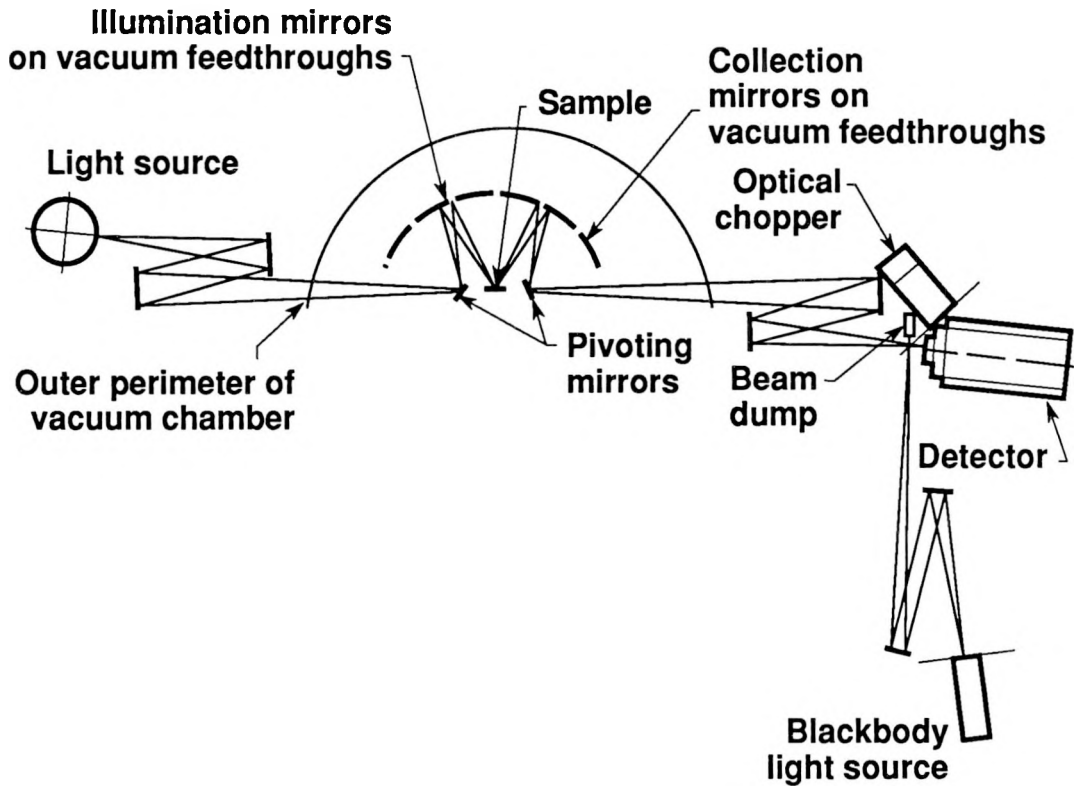

Fig. 8-9. An early version of the optical system.

the light source was formed at an aperture in front of a tilting mirror which could direct the beam onto any of five focusing mirrors. These mirrors were adjustable from outside the vacuum so that the light source could be re-imaged at the sample. The use of reflective optics eliminated chromatic aberration. After reflection from the sample a similar optical system was used to bring the reflected light out and focus it onto a detector. Bandpass filters immediately preceding the detector facilitated spectral measurements. The focusing mirrors were mounted at 15^{o} intervals and were gold coated glass discs. This arrangement permitted reflection measurements relative to a gold

reference mirror which was mounted below the sample position on a vacuum feedthrough. The gold mirror was moved up and the sample moved back to the Auger measurement station when reference reflection measurements were to be made.

This optical system could also be used to measure emissivity as a function of angle. With the light source off and the sample heated, its emission into any of the collection mirrors could be directed out of the vacuum system via the tilting output mirror, and focused at the detector. Normal emissivity as well as directional emissivity measurements, at 15^{o} increments out to 75^{o}, were performed. This system worked well, although errors due to polarization induced by multiple oblique reflections on the gold mirrors may have introduced some error. The tilting mirror and each of the mirrors in the collection optics reflected differing amounts of parallel and perpendicularly polarized light since they were arranged to reflect at off normal incidence. This induced polarization biased the emission measurements recorded at the detector.

The original optical system was abandoned because the curvature of the molten metal samples altered the focal properties of the optical system and prevented use of the flat gold mirror as a reference during reflection measurements. In the first revised optical system, a rotatable polarizer was placed in front of the detector. By rotating the polarizer through 90^{o} increments referenced to the plane of incidence (or the plane of collected emission), the ratio of perpendicular to parallel polarized reflectivity (or emissivity) could be measured. The gold mirror was used to estimate the polarization induced by the oblique reflection from the optical system's mirrors. This system gave reasonable results for molten indium in the visible spectrum despite the approximations involved in the correction technique using the plane gold mirror. However, the procedure for correcting for the polarization in the optical system was judged too approximate to give results of

acceptable precision. Furthermore, this method of fitting polarized reflection results as a function of angle to the Fresnel equations (often referred to as Avery's method [74]) has poor sensitivity in the infrared. This aspect of measurement sensitivity was discussed in Chapter 7.

8.5 Optical system for ellipsometry

8.5.1 The radiation source The wide spectral band of interest here was not well covered by a single available radiation sources. Common visible sources were inadequate because their windows are opaque to infrared radiation. Attempts to refit a tungsten strip lamp with a CaF_2 window were unsuccessful. Common infrared sources were inadequate because their low operating temperatures makes their visible output low. The useful life of Nernst glowers decreases rapidly with operating temperature so that their maximum output is only comparable to a blackbody at ~1170 K. Since higher temperatures were required for adequate signal to noise ratio in the visible, the design of an original source was begun.

After extensive testing, a graphitized carbon filament in a vacuum chamber equipped with a CaF_2 window displayed excellent emission over the whole spectrum. The high total hemispherical emissivity of graphite (~0.85) combined with its high operating temperature (~2000 K) makes it superior to tungsten in the infrared and to Nernst glowers in the visible. The hot portion of the filament is 0.120" wide and ~0.63" long. Filaments are cut from 0.025" thick sheet and bolted to copper rods mounted on commercially provided vacuum feedthroughs. During typical operation the filament is supplied with 11 volts and 26 amps. Operation at 28 amps and higher was occasionally attempted to improve signal to noise at 0.4 and 0.45 μm but twice this resulted in a torn filament.

Since the source was constructed of common vacuum materials, its maintainance and repair were quick and simple operations. After extended use (hundreds of hours) a thin film of carbon developed on the inner surfce of the CaF_2 window. This film was easily removed by wiping with an alchohol-dampened cloth. The filament, mounted in one leg of a standard 5 way vacuum cross, was also readily replaced. On the other legs are the CaF_2 window, a pyrex window for viewing the back side of the filament, a valve to allow pumping the cross to rough vacuum and lastly an ion pump for maintaining the cross at vacuum once it is disconnected from roughing and mounted on the ellipsometer.

8.5.2 The System. The optical system for ellipsometry was designed to measure the relative phase shift and amplitude attenuation on reflection to allow computation of the complex index of refraction of the sample surface. Calcium fluoride lenses were selected to manipulate the emission from the radiation source. The full optical system is shown schematically in Fig. 8-10. A CaF_2 lens (2" diam) in front of the lamp forms an image of the hot filament at an aperture ~6" from the lamp exit window. This aperture rejects emission from the hot filament edges where non-random polarization was expected. An optical chopper placed just behind the aperture allows phase sensitive detection. Beyond the chopper is a second CaF_2 lens which collimates the chopped beam for passage through the polarizer. Distances, focal lengths and other specifications of this optical system are given in Tables 8.2 and 8.3.

Two types of polarizers were used to allow ellipsometric experiments over the full wavelength range of interest. Calcite ($CaCO_3$) polarizers, which have an excellent extinction ratio (10^{-5} or better), were used from the ultraviolet to 2.3 μm. Beyond

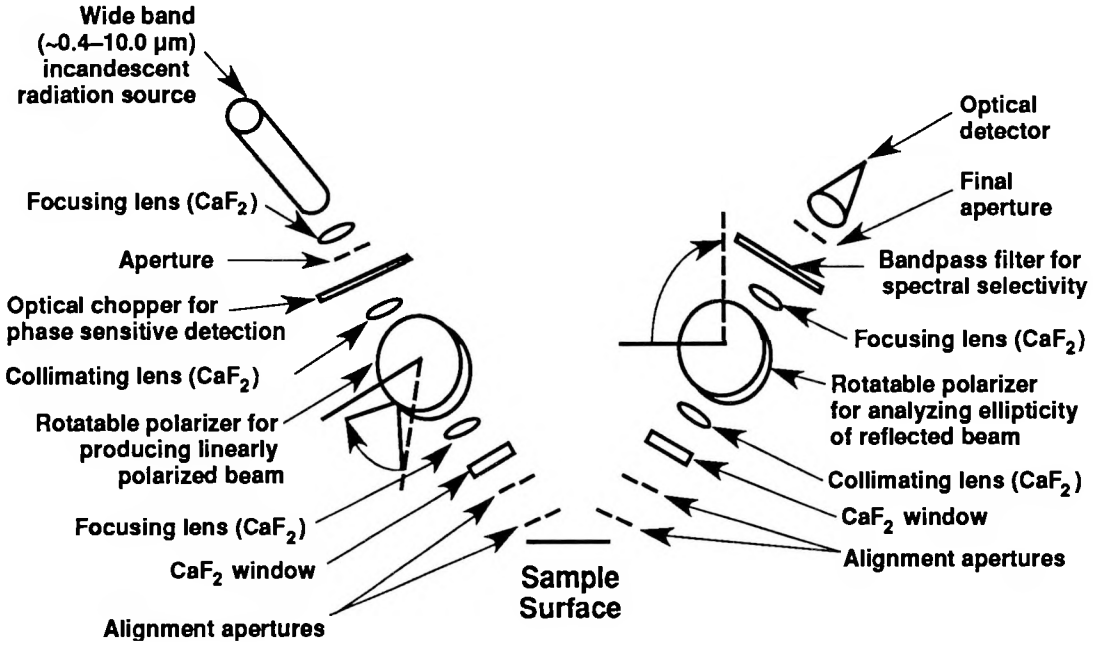

Fig. 8-10. Schematic of the ellipsometry measurement system.

2.3 μm, calcite becomes absorbing so wire grid polarizers were used from 2.3 to ~10 μm. The extinction properties of these polarizers were given in Fig. 5-1. Transmission losses of the CaF_2 elements of the system prevented measurements at wavelengths greater than ~10 μm.

The polarizers were mounted in a special mount of original design which allowed them to be centered in the incoming beam and aligned with their rotation axis coincident with the beam axis. Either type of polarizer could be positioned in these mounts and translated in two directions perpendicular to the beam axis. Two axes of tilt adjustment on the mounts permitted alignment of the rotation axis relative to the beam axis. High precision rotary stages were used to rotate the polarizers about the beam axis. Graduations on the rotators were every degree, with a vernier scale marked in minutes of arc.

Table 8.2
Ellipsometry System Input Optics

Element (-)	Distance from last element (mm)	Focal length (mm)	Size (mm)	Aperture diameter (mm)	f/d (-)
Lamp Filament	0	—	16 x	—	—
Focusing Lens #1	114	50	25	—	2
Lamp Aperture	95	—	—	2.29	—
Optical Chopper Blade	19	—	—	13	—
Collimator Lens	241	250	25	—	9.8
Polarizer Mount	95	—	—	—	—
Focusing Lens # 2	133	250	25	—	9.8
CaF_2 Window	13	—	12	—	—
Input Alignment Aperture #1	89	—	—	8.74	—
Input Alignment Aperture #2	104	—	—	5.74	—
Sample	28	—	7.5	—	—

Table 8.3
Ellipsometry System Output Optics

Element (-)	Distance from last element (mm)	Focal length (mm)	Size (mm)	Apeture diameter (mm)	f/d (-)
Sample	0	—	7.5	—	—
Aperture #1	28	—	—	5.7	—
Output Alignment Apeture #2	104	—	—	8.8	—
Caf_2 Window	90	—	—	11.8	—
Collimating Lens	44	250	25	—	9.8
Polarizer Mount	178	—	—	—	—
Focusing Lens	279	62.5	25	—	2.5
Bandpass Optical Filter Mount	32	—	22.5	—	—
Detector Aperture	16	—	—	1.45	—
Dectector	19	—	2×2	—	—

Following the polarizer on the input portion of the optical system, a focusing lens forms an image of the hot filament of the radiation source at the sample surface inside the vacuum chamber. This focusing lens was a 25 mm diameter CaF_2 lens with a focal length of 250 mm (at 5 μm).

All the focusing elements used in this optical system were simple plano-concave lenses. Thus, their focal lengths varied over the spectral range of measurements. (The variation of refractive index with wavelength of CaF_2 is given in Appendix C.) Images that appeared sharp during alignment in the visible were not nearly as sharp in the infrared where they could not be seen with the eye. However, errors due to chromatic effects were small because in the ellipsometric measurement technique all data was obtained merely by rotating a single polarizer about the beam axis. Chromatic effects caused 1) a loss of signal due to vignetting at the apertures and 2) a variation in polarizer extinction ratio due to a variation in the beam collimation at both the polarizer and the analyzer. Loss of signal due to vignetting had much the same effect as the curvature of the molten metal pool; the effective focal length of the optics varied, but this did not affect the critical consideration, the rotational positioning of the analyzer of the ellipsometer.

The incident beam entered the vacuum system through a 0.435" diameter CaF_2 window, mounted in a UHV vacuum flange. Inside the vacuum chamber, on either side of the sample, was a pair of apertures which facilitated the alignment process . Lines through the aperture centers were fixed at a 150^o angle so that when maximizing the optical signal through the system the angles of incidence and reflection were each 75^o. The layout of these apertures is shown in Fig. 8-11.

After reflection from the sample and passage through the second set of alignment apertures, the beam passed through a second CaF_2 window and exited the vacuum system (Particulars of the sample surface, the crucible and its integral blackbody cavity are

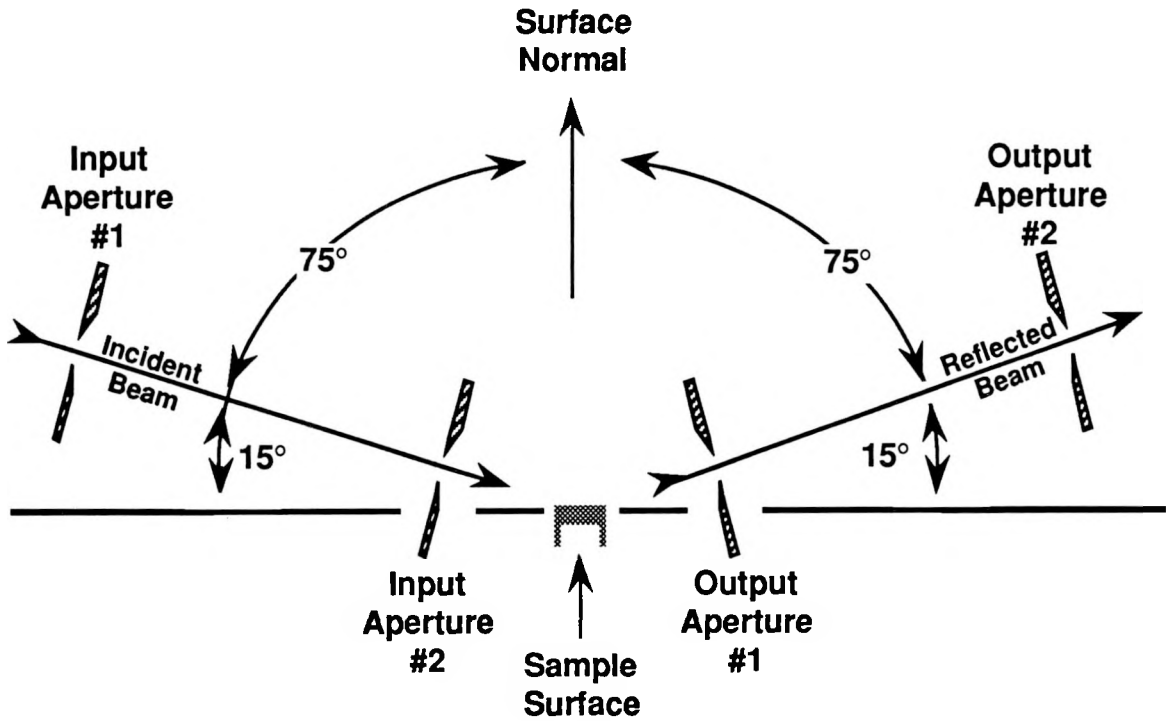

Fig. 8-11. Layout of the ellipsometer apertures within the vacuum system.

given in Sec. 8.8). Another CaF_2 lens , identical to the preceding focusing lens, was positioned just beyond the exit window. This lens produced a collimated beam for passage through the second polarizer, referred to as the analyzer. The analyzer, in the same type of mount as the polarizer, was aligned with the axis of the reflected beam.

A final focusing lens (also of CaF_2) accepted the light transmitted by the analyzer and formed an image of the hot filament source at an aperture immediately in front of the detector. Band pass filters (described below) were placed directly in front of this last aperture. With hot samples, both sample emission and radiation source emission (within the filter spectral bandpass) reached the detector, but only the component from the

radiation source was chopped and therefore processed as signal by the lock-in amplifier. The unchopped sample emission causes shot noise but this is small for the sample temperatures achieved here.

The detector consists of an indium antimonide (InSb) photo-diode backed by a mercury cadmium telluride (HgCdTe) strip operated as a photoconductor (this is referred to as a sandwich configuration). The front element of the sandwich, the InSb diode, is sensitive from 0.5 to 6 μm and transmitts longer wavelength radiation. The HgCdTe photoconductor is sensitive from ~6 to 12 μm. When extra sensitivity was desired in the visible spectral range, a silicon photo-diode was used to cover the range from 0.4 to 1.1 μm.

8.5.3 The band-pass filters. Spectral intervals were selected by using a set of more than 30 commercially produced narrow and wide band-pass filters. A monochromator would have provided the finer spectral resolution needed for a study of the electronic structure of the metals of interest but would have been more complex and less portable between the two optical systems. In the visible, a 10 nm bandpass was typical. In the infrared, filters with larger bandwidths were possible (50 to 300 nm from 0.8 μm to 9.5 μm), because the reflectivity changes more slowly there, and desirable, because other effects tend to make signal to noise ratio decline rapidly there.

During initial measurements, out-of-band transmission by some of the filters produced errors. These were eliminated by using, in series, a second filter of specifications similar to the first (same nominal bandwidth and center wavelength) or by adding a low pass filter. With this approach, out-of-band transmission was generally reduced by ~0.01 while only roughly halving the in-band transmission.

8.5.4 Alignment of the ellipsometric system. Alignment was mostly performed with the room lights out so that the source radiation could be observed on a white card held in the beam path. The positions of the optical elements were adjusted to give the sharpest images at the desired positions and magnifications. This procedure ignored the dependence of focal length on wavelength discussed above. The unseen infrared wavelengths were not as well focused as the visible range, but the radiation source gave very large signal in most of the infrared so the losses in signal due to chromatic aberration were not significant. Three additional alignment operations were: 1) centering the beam in the two pairs of alignment apertures on either side of the sample within the vacuum system, 2) centering the beam in both the polarizer and analyzer, and 3) conforming the beam axis to the rotational axes of the polarizers.

The throughput of the ellipsometric system was peaked by adjusting the detector and sample positions every time the sample was moved into the position for optical measurements. This adjustment ensured that the sample was at the correct position relative to the four alignment apertures within the vacuum system.

The axis of peak transmission of each polarizer relative to the plane of incidence had to be determined before each set of measurements. This was always the last operation before data was taken. Procedures for this alignment have been given in the literature [122,123,124] but a variant of the method described by Aspnes [177] was found to be accurate, fast and easy. One of the two polarizers was rotated until its plane of transmission was roughly in the plane of incidence (as defined by the beam axis and the normal to the sample surface). The other polarizer was then rotated until minimum detector signal was obtained. The second polarizer was then rotated 90^{o} and the first polarizer rotated until another detector minimum signal was obtained. Since light polarized parallel or perpendicular to the plane of incidence remains so after reflection,

this procedure identifies the orthogonal positions of the two sets of polarizers. The minima decrease as the polarizer positions get closer to the plane of incidence so the procedure converges to the correct positions. This procedure was applied iteratively and performed whenever the sample was moved or the polarizers were removed from the rotation mounts.

8.6 Optical system for emissivity measurements

8.6.1 The System. The optical system for the normal emissivity measurements is shown in Fig. 8-12. Focal lengths, aperture sizes and other optical specifications for this system are given in Table 8.4. This system used reflective rather than refractive optics so there is no chromatic aberration. The emission from the sample (and the integral blackbody cavity) into the normal direction exited the vacuum chamber through a CaF_2 window. This window, with a clear aperture of ~1", was mounted in a larger flange (2 .75 ") than those used in the ellipsometric system. A plane mirror ~3" above the window folded the sample emission toward a focusing mirror. An aperture at the face of this mirror was the aperture stop for the system (The half angle of the beam is 1.24^{o}). The focusing mirror directed light from the sample and the blackbody toward the detector. The beam passed through an optical chopper and a bandpass filter (see Section 8.5.3) before reaching the aperture immediately in front of the detector. This aperture was the limiting field stop of this optical system. The entire top surface of the crucible including both the sample and the exit face of the cavity were imaged at the plane of this field stop so that by lateral motion of the sample, radiation from either the sample or the integral blackbody cavity could be positioned at the last aperture. The diameter of this aperture was 0.060 in. and the cavity opening was 0.100 in. Since the

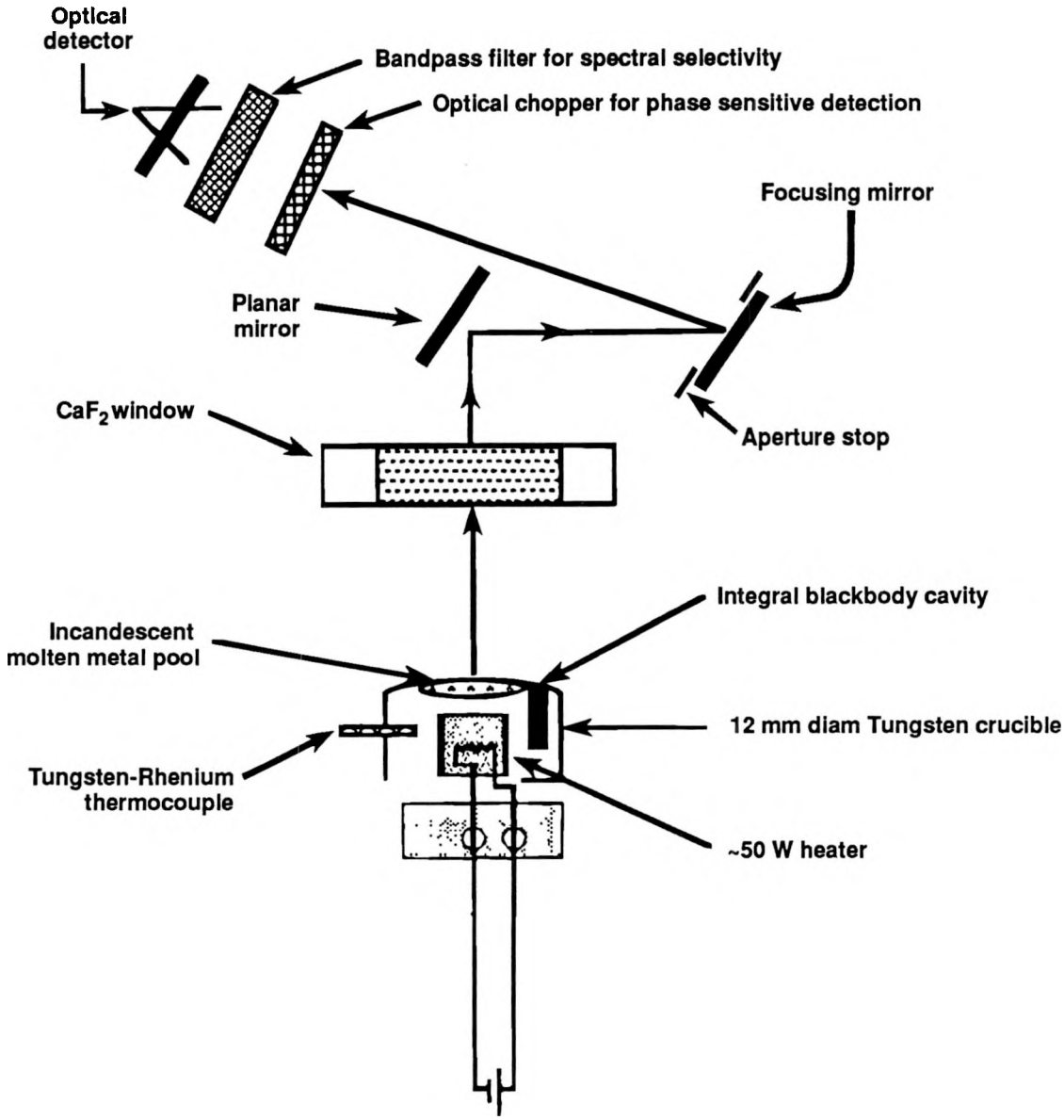

Fig. 8-12. Schematic of the apparatus for measurements of normal spectral emissivity.

Table 8.4
Emissivity Measurement System Optics

Element	Distance From Last Element (mm)	Focal Length (mm)	Size (mm)	Apeture Diameter (mm)	f/d (-)
Sample	0	—	7.5	—	—
CaF_2 Window	203	—	—	32.5	—
Planar Folding Mirror	108	~∞	25	—	~∞
Focusing Mirror	83	200	25	17.1	8
Optical Chopper Blade	311	—	—	25	—
Bandpass Optical Filter Mount	400	—	—	22	—
Detector Aperture	50	—	13	1.45	—
Detector	19	—	2×2	—	—

image and object distances were nearly equal, the cavity image overfilled the aperture and the detector received only the desired signal.

For sample temperatures of ~1175 K or hotter an image of the sample and hohlraum were readily visible when the room lights were off. When the bandpass filters were removed, the hohlraum's image could be centered on the field stop. With reflective optics, the alignment held for all wavelengths of measurement.

8.6.2 Alignment of the emissivity system optics. The emissivity system was aligned by a simple procedure. The sample was roughly centered under the CaF_2 window. The folding mirror was centered over this window and tilted at roughly 45^o to the normal emission direction. This mirror was positioned to direct both sample and cavity emission to the focusing mirror. With the room lights turned off and an aperture on the face of this mirror, the folding mirror was adjusted to center the light from the crucible in the focusing mirror. The focusing mirror was positioned on the axis of an

optical rail which held the rest of the optical components. The chopper blade openings were centered in the beam and the chopper motor mount bolted to the rail. The detector was positioned on this rail with the image of the hot crucible visible on the aperture immediately in front of the detector.

8.7 Crucible design and positioning

8.7.1 Design constraints. The twelve principal guidelines for the crucible design were:

1. Crucible lifetime with corrosive liquid metal long enough for optical measurements to be made.
2. Crucible geometry, thermal conductivity and surface radiative properties should minimize the temperature difference between the pool surface and the blackbody cavity
3. Molten pool larger than image of radiation source formed upon it.
4. Molten pool flat enough for sufficient signal to noise ratio at detector.
5. Crucible large enough to include an integral blackbody cavity.
6. Crucible size compatible with available heater.
7. Crucible overall dimensions small enough to fit at the focus of the Auger spectrometer.
8. Crucible capable of being instrumented with thermocouples.
9. Crucible fabrication cost moderate.
10. Rate of alloying of molten sample with crucible material consistent with typical measurement time.
11. Molten sample contact angle with the crucible surface gives adequate molten pool flatness.

12. Crucible melting temperature must be significantly above the highest desirable measurement temperature.

Some of these criteria are obvious but the complete set of constraints meant that there were very few candidate materials and severe size limits on the crucible. The corrosion lifetime criterion was particularly restrictive, as discussed in more detail in section 8.7.3. The wetting condition was also difficult, largely because of its unpredictability. The wetting of solids by liquid metals is variable and substrate processing history and temperature are influential. Molten aluminum was exceedingly difficult to control. In some cases it would not wet the crucible and remained in a sessile drop for hours or even days. In other, seemingly identical, cases it would spread over the crucible, fully wetting its top surface, and then drain out because wetting had extended to the crucible sides or an adjacent thermal shield. Crucibles for uranium and aluminum melts were machined from tungsten and niobium rod respectively. For the optical measurements on (solid) tungsten, the sample and the crucible were a single integral part. With aluminum, there was no destruction of the crucible by the molten metal but the liquid tended to wet the niobium substrate more readily over time so that sample surface stability declined.

8.7.2 The crucible design. An ensemble of crucibles and heaters are shown in Fig. 8-13. At the lower left is a view of the underside of a crucible. The large diameter hole is provided for a heater and the small hole is for a thermocouple. The other three items across the bottom row of parts in the photograph are a broken-off heater inside a damaged crucible, a single heater standing free and upside down and lastly a crucible sectioned in half to show its blackbody cavity and heater cavity in more detail. When in use, the blackbody cavity is coated with aquadag (a colloidal graphite suspension in water) to enhance its emissivity. Above these four parts are a heater mounting stage

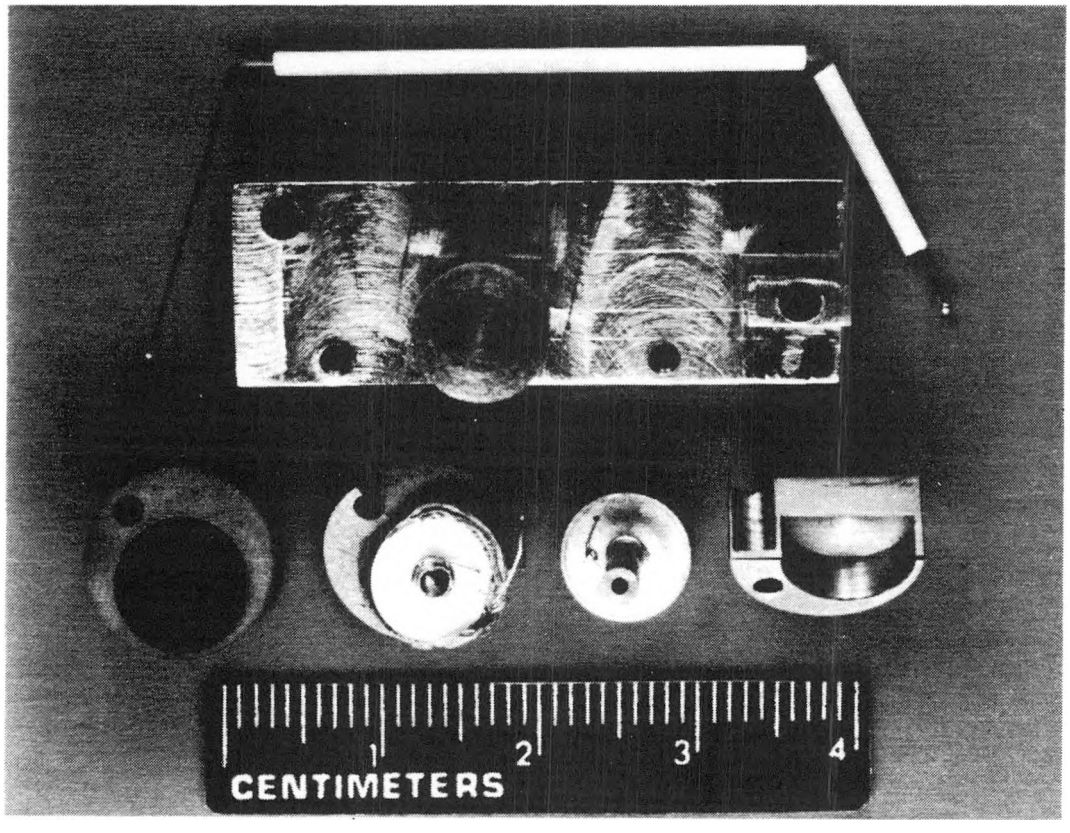

Figure 8-13. An ensemble of crucibles, and associated equipment. A thermocouple is at the top above the heater mounting stage. A broken heater and a heater in a broken crucible are shown in the foreground.

and a thermocouple. The round top surface of the heater is visible above the stainless steel heater stage. A set screw is used to hold the stem of the heater to the stage. The heaters consist of a molybdenum case with 0.005" tungsten wire wound helically as the dissipation element. The heater wire is potted into the case with alumina (the white material visible on the heater underside in the photograph). When ~50 W of electric power is dissipated in the heater, the metal samples in the crucible reach ~1500 K. Figure 8-14 shows two crucibles mounted on a heater stage and surrounded by molybdenum heat shields. The concave surface on the sample at right is an extreme example of the curvature possible with molten samples. In this case, more material would be added to the crucible to obtain a flatter surface before attempting optical measurements.

The crucible design is important for its influence on measurement error. Such errors typically arise from two sources. First, any temperature difference between the integral blackbody cavity and the sample leads to error in measurements of normal spectral emissivity. These errors are strongly dependent on wavelength as given by the Planck function. For a well designed crucible, errors are small because the cavity and sample are close and well connected thermally. Second, for every percent that the blackbody's emissivity is less than ideal (apparent emissivity less than one), measurements of normal spectral emissivity are in error by the same amount. Size constraints on the crucible limited the depth to diameter ratio of the cavity to 2 so that an analysis of these errors was warranted.

Since these errors are determined by three dimensional conductive effects which are coupled to thermal radiative interchance in and out of the cavity, finite element methods were chosen for the analysis. These methods allowed approximation of errors due to these effects on a normal spectral basis. The calculations, described in Appendix A, indicate that temperature differences on the order of 6 K are likely between the sample and the cavity (for a sample temperature of 1400 K) and that errors due to

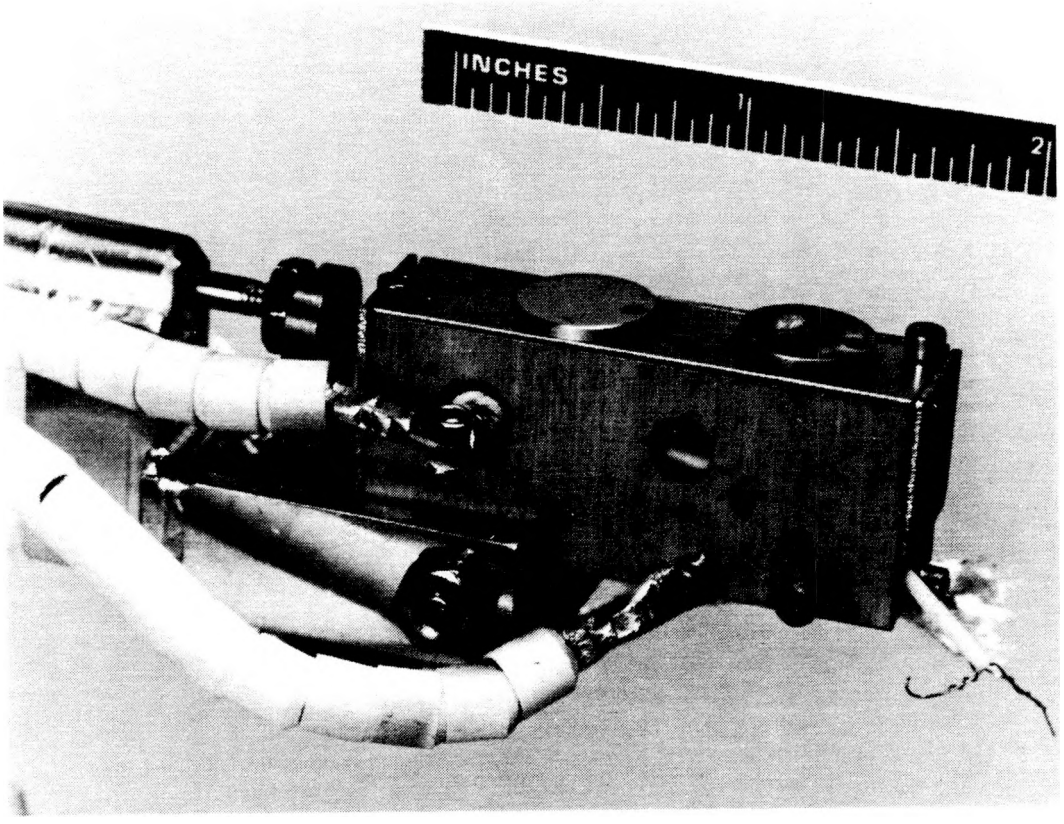

Figure 8-14. Two crucibles mounted on the manipulator stage.

thermal gradients and non-ideal cavity emission combine to give measurement errors which vary from ~7 % at 0.6 μm to ~2 % at 9.5 μm. The variation in estimated error in normal spectral emissivity with wavelength and sample temperature is shown in Fig. 8-15. These error estimates were useful during crucible design but the true test of the design is given by the agreement between the direct measurements of normal spectral emissivity and the values computed from the ellipsometric system (which are independent of the errors discussed above). In particular, for disagreement with strong wavelength dependence such as that shown in Fig. 8-15, errors due to crucible design are likely. In fact, disagreement on the order of 5% and less is observed for most measurements in the visible and near infrared, and larger values for the 4 to 10 μm range. Thus, errors due to thermal gradients and non-ideal cavity emission appear small compared to those due to other effects and the crucible design is adequate.

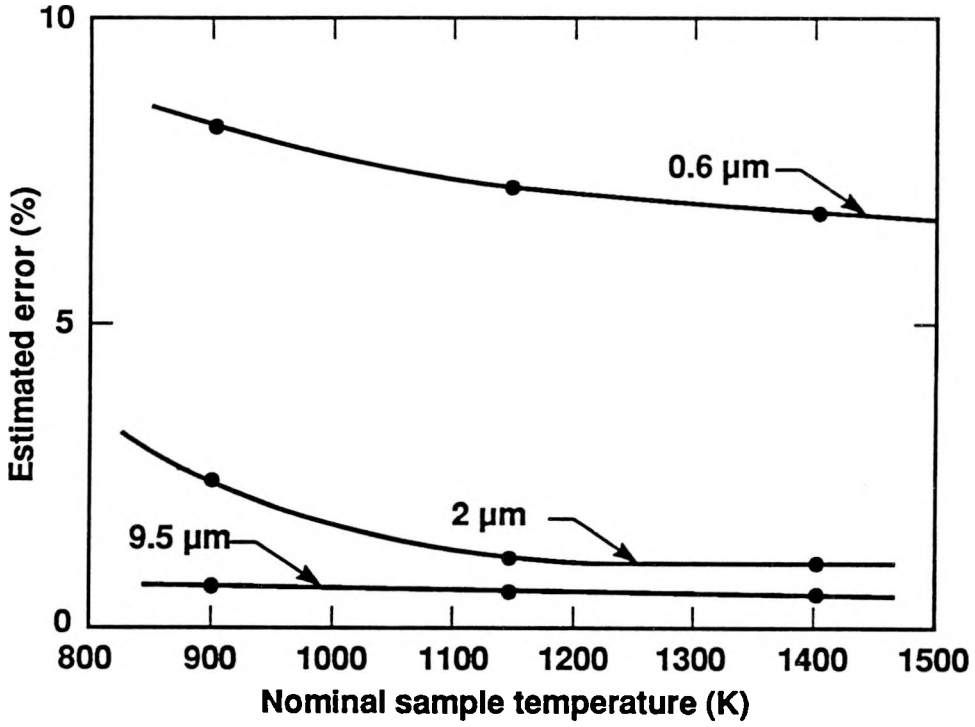

Figure 8-15 Estimated error in normal spectral emissivity due to non-ideal cavity emission.

8.7.3 Crucible corrosion and lifetime issues. Molten uranium is a highly reactive material [178] and there are few materials known to contain it for periods of more than a few hours [179]. For the few materials for which reaction with the liquid metal is slow there is often grain boundary attack. In this study, the pure tungsten crucibles used to contain molten uranium were eventually destroyed by dissolution of grain boundaries. The impurities and the bulk atoms in the vicinity of the grain boundaries are less strongly bonded than the atoms in the bulk so that as the exposure time to molten metal increases the liquid dissolves the material around more and more entire grains. The grains which are freed from the bulk drift away to float around in the pool of denser liquid. This process exposes more crucible material which had originally been below the solid-liquid interface. Crucibles eventually fail when enough grain boundaries are dissolved for the liquid metal to penetrate the crucible. This mode of attack has been documented for crucibles of tungsten as well as other refractory metals [180].

8.7.4 Surface tension and curvature effects. The shape of the surface of a liquid when contained in a wide cylinder was analyzed by Rayleigh [181]. His results were used by Ebert [182] to obtain some estimates of the surface curvature due to surface tension and liquid wetting angle, the angle between the cylinder wall and the fluid surface at the wall. Solutions for the liquid shape are given in the form of Bessel functions. The radius of curvature of this shape is the relevant quantity for the samples effect on the ellipsometric optical system because it determines the focal properties of the molten sample pool. Ebert used a series expansion for the Bessel function solution and the method of matched asymptotic expansions to obtain estimates of the radius of curvature. He showed that very large molten pools (10 cm or larger) would be required to give a focal length large compared those of the optical system. Pools of this size would not fit

under the Auger spectrometer and would be very slow to clean by sputtering. It was concluded that no practical size of crucible could give a focal length long enough to have a negligible focusing effect on the optical beam. These findings led to a search for reflection methods which did not entail comparison with a standard reflector, because no standard reflector could match the varying curvature of the molten pool surface. Ultimately, ellipsometry was the reflection method chosen, partly because the defocusing properties of the liquid surface would have negligible effect on the results and partly because of its superior sensitivity for determining the optical constants as discussed in Chapter 7.

There are several other aspects of surface tension and curvature which are worth noting. First, the results of Rayleigh and Ebert are dependent on the wetting properties of the sample-crucible combination. These properties vary over the experiment time as surfaces are sputter cleaned or coated with evaporated or sputtered material. As the crucible became less full during an experiment, due to leakage or loss of material by sputtering, the curvature changed. No single value (or small range) of curvature could be maintained. Surface curvature also varies as the sample material wets more and more of the crucible surface. This effect was most noticeable with aluminum, but even with uranium, the molten metal would slowly wet portions of the crucible top and migrate down the sides.

8.7.5 Sample positioning for optical measurements and surface analysis. The vacuum system was designed so that the sample could be studied at either of two positions. At the surface analysis station, the sample was located at the focus of the Auger spectrometer. A sputter gun was also aimed toward this location, so sample cleaning could be performed, simultaneously with Auger spectroscopy. At the second station, ~100 mm from the first, the optical measurements were made and a second ion sputter gun was also focused at this position.

The sample was moved between these two stations by a vacuum feedthrough manipulator shown in Fig. 8-16. The manipulator is connected to the crucible by a long stainless steel rod visible in the photograph.

The crucible has five degrees of freedom when connected to this manipulator. It can be moved in three orthogonal directions and has two axes of tilt. Motion in the direction of the rod, referred to as the traverse direction in later sections of this report, translated the crucible between the two measurement stations. The sample could be translated ~112 mm in this direction and ~25 mm in the two perpendicular directions. The manipulator also allowed roll and a limited amount (~$\pm 20^{o}$) of pitch. These degrees of freedom allowed the sample to be positioned at the Auger spectrometer focus and at the position for maximum signal through the ellipsometric system. The sample position was not as critical in emission measurements, since the detector could be moved to the desired position on the image of the hot crucible.

The manipulator was commercially supplied and used bellows to allow its motion in vacuum with control from the ambient. The pitch mechanism was added to the device later. All motions are controlled by precision micrometer movements, except the 100 mm traverse motion which is controlled by an uncalibrated lead screw.

8.8 Optical signal detection system

The emissivity and ellipsometric measurement systems employed the same detector and signal processing equipment, shown in Fig. 8-17. Both systems had optical choppers for phase sensitive detection. In the emissivity system, the chopper is located between the focusing mirror and the bandpass filter. In the ellipsometric system the chopper is at the input aperture field stop. This placement caused only reflected radiation to be chopped and recorded as signal. Sample emission was not chopped and was therefore rejected by the lock-in amplifier. In the emissivity system, the chopper was

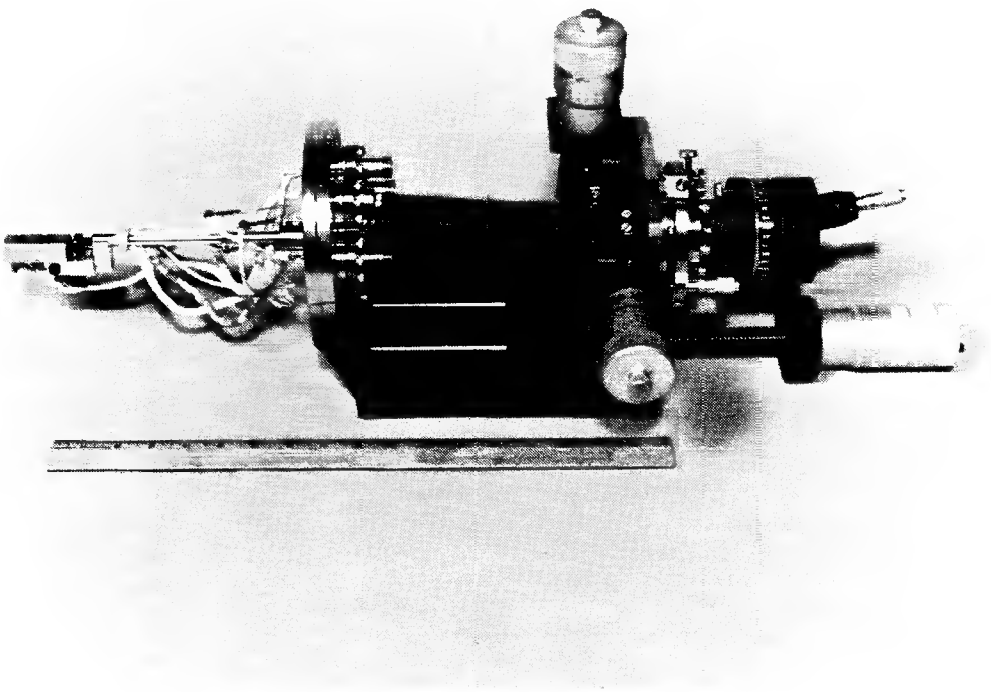

Figure 8-16. The crucible manipulator. The two crucibles mounted at left can be translated in three directions and rotated about two axes.

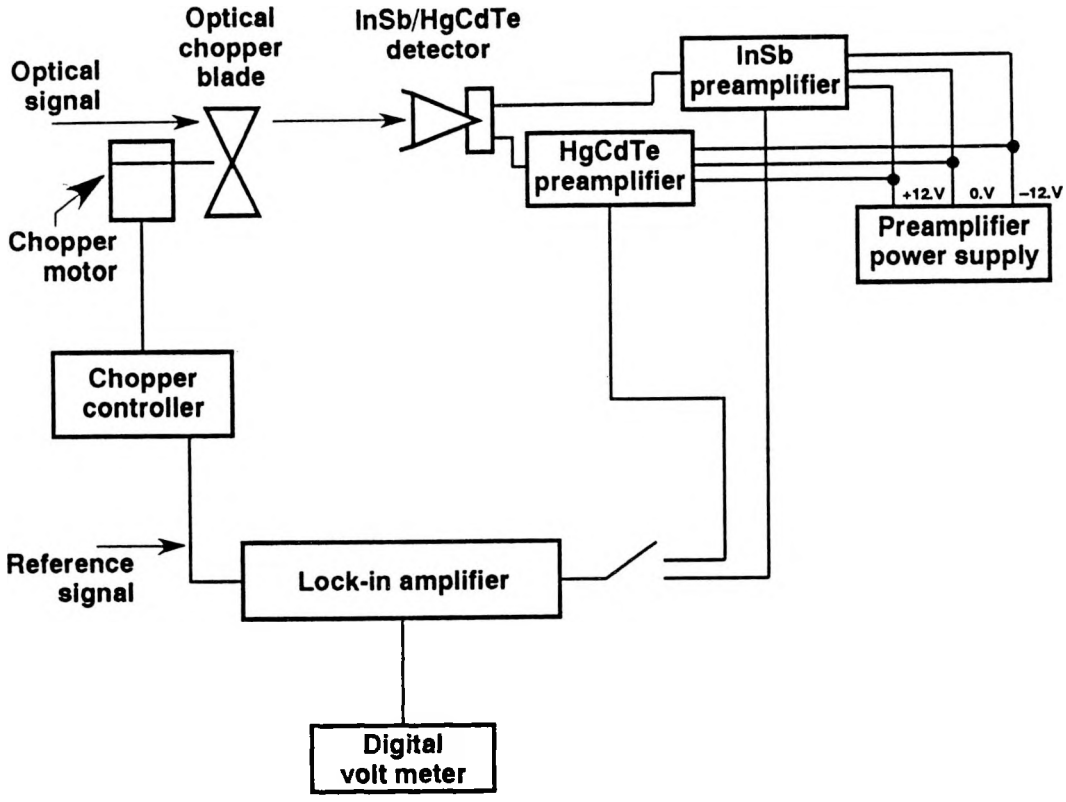

Figure 8-17 The optical signal detection system.

placed as close as possible to the light source of interest, the hot sample. Chopping within the UHV vacuum system was not practical. Figure 8-17 represents both these chopper placements as equivalent and displays the rest of the signal detection system.

The optical detectors described above were connected to matched preamplifiers. Each preamplifier was powered by chemical storage batteries as shown. The batteries were charged while the detector was not in use. When the detector was in use, the charging system was turned off and disconnected from the batteries. Output from the preamplifiers and the reference signal from the chopper controller was fed to the lock-in amplifier where only the signal from the preamplifier in phase with the reference signal was amplified and rectified at the lock-in amplifier. The lock-in amplifier had a galvanometer display, a zero to 10 V output BNC connector and a digital liquid crystal

display (LCD). For some experiments the LCD was used and in others the BNC output jack was connected to a digital multimeter for readout and recording. The time constant of the lock-in detector was usually 1 or 3 seconds but for some of the long wavelength measurements (3–10 μm) values of 10 and 30 were used.

The optical chopper blades are 100 mm in diameter. The ellipsometric system used a blade with ten evenly spaced slots. The emissivity system used a blade with five evenly spaced slots. The chopping frequencies used with these blades were typically 550 and 250 Hz respectively. Frequencies as high as 1000 Hz with the 10 slot blade and 500 Hz with the 5 slot blade were possible but at these maximum values, chopper controller overheating was observed. The reference signal provided by the chopper controller was a square wave at the chopping frequency.

9. Experimental results for the radiative properties and optical constants of tungsten

9.1 Background

This chapter presents measurements of the normal spectral emissivity and the complex index of refraction of pure tungsten at elevated temperatures (940 K to 1450 K). These measurements were made to establish confidence in the techniques selected for optical studies of molten uranium and aluminum. Comparisons between the present work and the most accurate previous studies (reviewed in chapter 6) are made here but given less emphasis than those between the two techniques of the present work, oblique spectral ellipsometry and direct measurements of normal spectral emissivity.

Comparisons between this study and prior ones is facilitated by the fact that tungsten in ultra high vacuum and within the above temperature range is relatively inert and grain growth is slow. Although such stability makes the optical properties fairly reproducible, variations in sample preparation can produce significant differences in the measured normal spectral emissivity [1]. Although careful consideration of surface polish, grain size and sample bulk purity in this study has limited these differences to several percent (or less), these surface non-idealities are not discussed in depth here because they are largely irrelevant to liquid metals which are smooth and sputter cleaned. Interpretation of the results in terms of the theories of the optical constants is not stressed, although it is treated briefly in the later sections, because of the purpose of the measurements stated above and because numerous prior works have done so [183,184].

9.2 Surface mass analysis of solid tungsten samples

The surface cleaning operations for solid tungsten were described in section 8.3.1. (Figure 8-5 gave a typical Auger scan for a "dirty" tungsten surface.) More extensive use of the sputtering methods so well suited to liquid metals was impossible here because, with solids, surface roughness is increased by sputtering. This roughening reduces the specular reflectivity and enhances the emissivity. Hence, for solid tungsten the surface condition was not so easily controlled as it was for liquids; the sample mass analysis varied by 5 to 10% between experiments. Figure 9-1 shows an Auger spectrum for a representative "clean" tungsten surface. As discussed earlier, since the Auger electrons collected by the spectrometer are principally from the top 50 angstroms of the sample, the indicated impurity levels are low. In summary, the good agreement between this work and earlier studies indicates that surface impurities were well controlled.

The samples for this study were disks cut from 99.99% pure tungsten rod and polished with successively finer grits. The final polish was obtained with a 0.1 micron grit but considerable roughening was later created, primarily by recrystallization during sample heating at 1450 K but also during brief periods of surface sputtering.

9.3 The normal spectral emissivity of tungsten as a function of wavelength and temperature

The normal spectral emissivity of polished tungsten at 1450 K and in the wavelength range of interest (0.4–10 μm) is reported in Fig. 9-2. The results of Latyev et. al. [134] for the wavelength range, 0.4–5 μm, and a sample temperature of 1400 K are also given. The results obtained by direct measurement of normal spectral emissivity are represented with triangles, those obtained from the ellipsometric system are represented by circles and the values given by Latyev et. al. are the squares. The

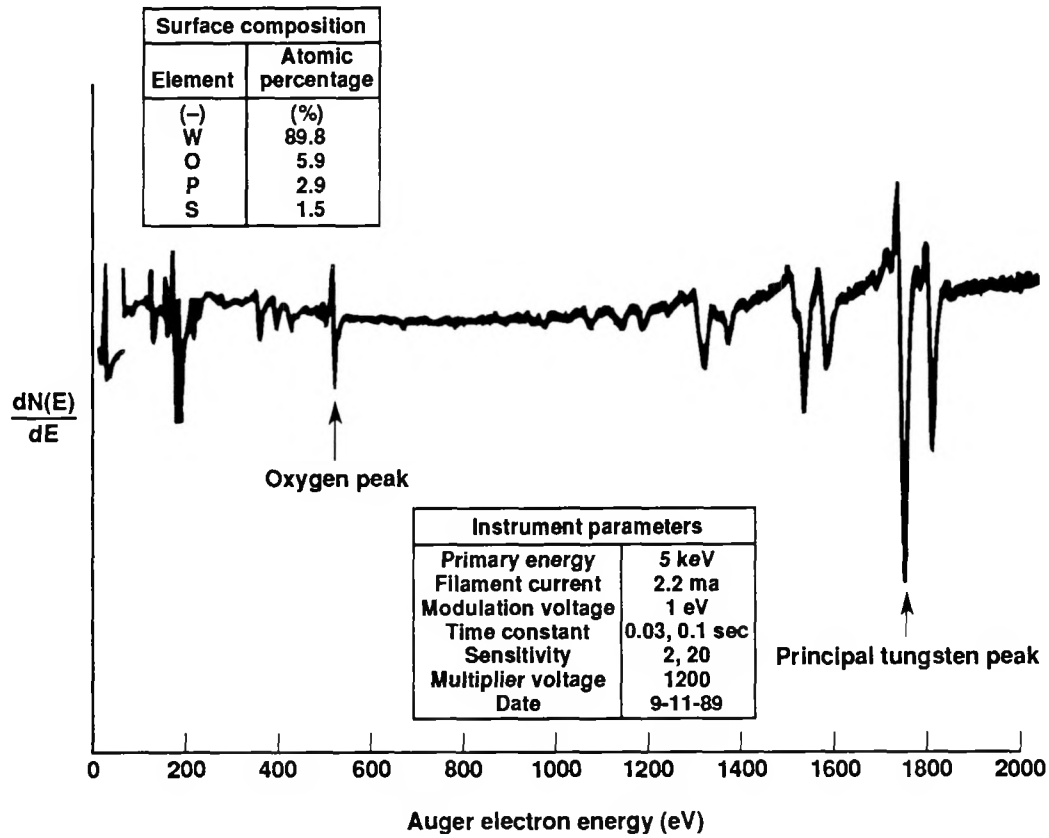

Fig. 9-1. Auger spectrum of a "clean" tungsten sample.

curves drawn through the data of this work are least squares fits to the following equation:

$$\varepsilon_n(\lambda) = a_o + \frac{1}{a_1\lambda^2 + a_2\lambda + a_3} \qquad (9\text{–}1)$$

This equation is not a theoretical result, although it is similar to forms derived by Edwards and De Volo [185] from the work of Roberts [138] (assuming contributions to the normal spectral emissivity from both free and bound electrons).

The results from both measurement techniques compare quite well with the earlier work. The actual percentage differences between the curve fits and the results reported

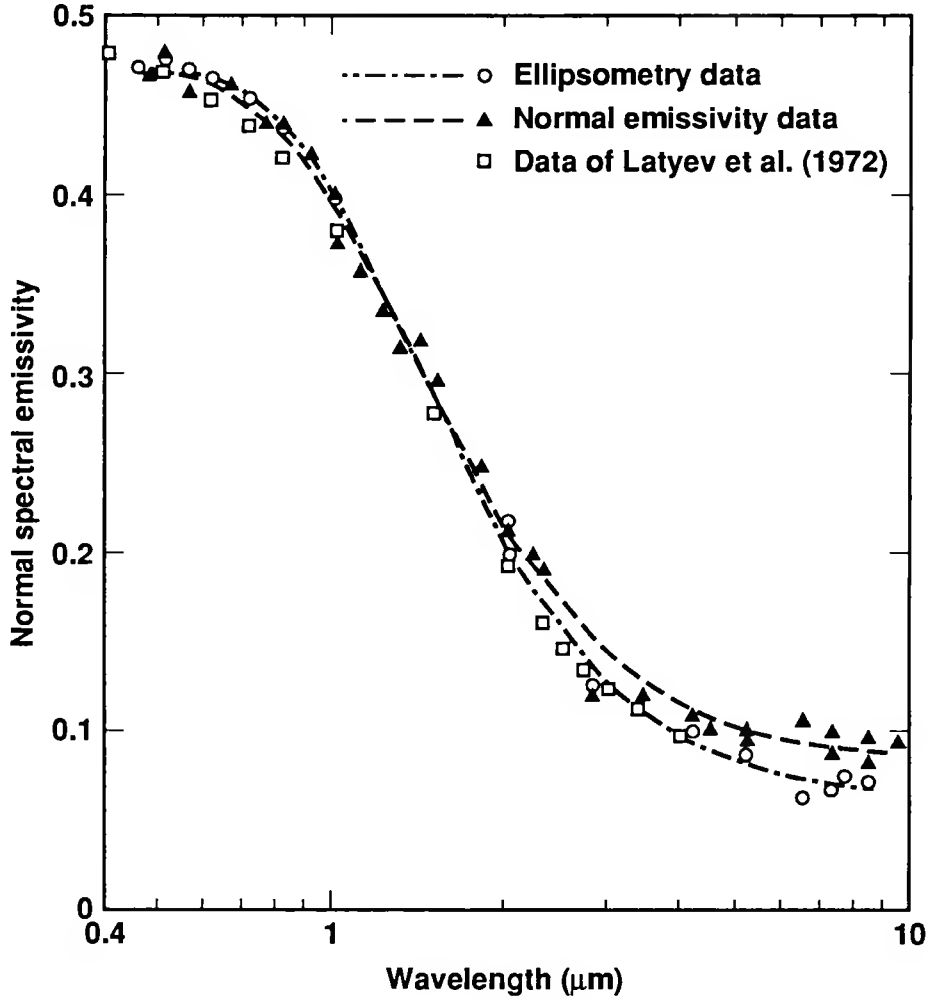

Fig. 9-2. The normal spectral emissivity of polished tungsten at 1450 K. The lines are least-squares fits to a form given in the text. See text for full citation.

by Latyev et. al. are given in Table 9.1. The results in the visible spectrum agree to better than 5% despite the fact that both signal strength and detector responsivity decrease rapidly here for both the ellipsometric and direct normal spectral emissivity measurement systems. The larger differences between the results at the long wavelength extreme are due to three factors which lead to rapidly declining signal strength. For ellipsometric measurements, the lamp emission and the optical element transmissivity decline with increasing wavelength. The lamp emission declines relatively slowly, as shown by the Planck function (see Fig. 2-11) but the CaF_2 windows and lenses cut off rapidly beyond

TABLE 9.1

Differences in normal spectral emissivity between this work and that of Laytev et. al. [94] for a sample temperature of 1450 K

Wavelength (μm)	Percent difference from ellipsometric measurements (%)	Percent difference from direct normal spectral emissivity measurements (%)
0.4	3.0	–1.7
0.5	–0.1	–0.4
0.6	–2.5	–1.9
0.7	–3.8	–2.5
0.8	–4.6	–2.8
1.0	–4.7	–2.8
1.5	–1.4	–2.4
2.0	–3.4	–8.9
2.3	–4.7	–13.2
2.5	–4.4	–14.7
2.7	–4.0	–15.9
3.0	–1.6	–15.5
3.4	0.7	–15.5
4.0	1.4	–17.9
5.0	6.6	–15.1

percent difference = $[\,(\varepsilon_{Latyev} - \varepsilon_{Havstad})/\varepsilon_{Latyev}\,] \times 100$

about 8 μm (see Fig. B-1). Furthermore, chromatic aberration increases rapidly with wavelength beyond about 5 μm in the ellipsometric optical system (see Fig. B-2). This effect causes vignetting and produces a beam size at the detector which increases with wavelength in the long wavelength extreme. In the normal emissivity system, chromatic aberration is avoided but sample emission again declines for long wavelength and there are two CaF_2 windows in the beam path, one at the vacuum chamber exit and one at the detector. These three effects produce a rapidly decreasing signal to noise ratio in the

infrared. From a comparison of the two curve fits (in Fig. 9-2) with the trend in the results of Latyev et. al., it is reasonable to be confident in the average of the long wavelength results of the two measurement systems used here.

The pattern of agreement between the ellipsometric and emissivity measurement systems indicates that errors due to temperature differences between the tungsten surface and the blackbody cavity are small. The two systems give essentially equal results at two wavelengths, ~0.5 and ~1.3 μm (see Fig. 9-2). If the blackbody cavity were either higher or lower in effective radiating temperature, the errors in measured normal spectral emissivity would be monotonically dependent on wavelength. To explain the ~20% difference between the emission and ellipsometric techniques at long wavelengths (8 μm say), a cavity temperature of ~150 K less than the sample is required. The heat transfer calculations described in chapter 8 and Appendix A show that temperature differences on the order of 5 to 10 K are reasonable and that larger differences would produce large errors at shorter wavelengths. Thus, the close agreement at the two wavelengths noted indicates that, at this nominal sample temperature at least, cavity and sample agree in temperature to the extent required of the measurement system.

The differences between this work and Latyev et. al.'s are small considering both sample preparation and measurement systems were very different. The earlier work was done with tungsten rolled into foil and then curled into a tube to form a high quality blackbody cavity behind the sample surface (see ch. 4). The samples for this study were polished disks as described in section 9.2. Differences in the measurement methods, due to a desire to treat small molten metal surfaces in this work, were discussed in chapter 8. The errors due to using these methods rather than those of Latyev et. al. can be gauged from Fig. 9.1, the difference between the two curve fits indicates that the systematic error (assuming Latyev et. al.'s results are exact) in the 0.4 to 2 μm range is less than 5%. Only a small part of this discrepancy may be attributed to the different sample temperatures.

The normal spectral emissivity of tungsten at a lower sample temperature (1270 K) is given in Fig. 9-3. Results from Latyev et. al., this time for a sample temperature of 1200 K, are again shown for comparison. The same symbol conventions and least squares fitting forms have been used as in Fig. 9-2. As before, the scatter in the results for both measurement systems employed here increases in the long wavelength

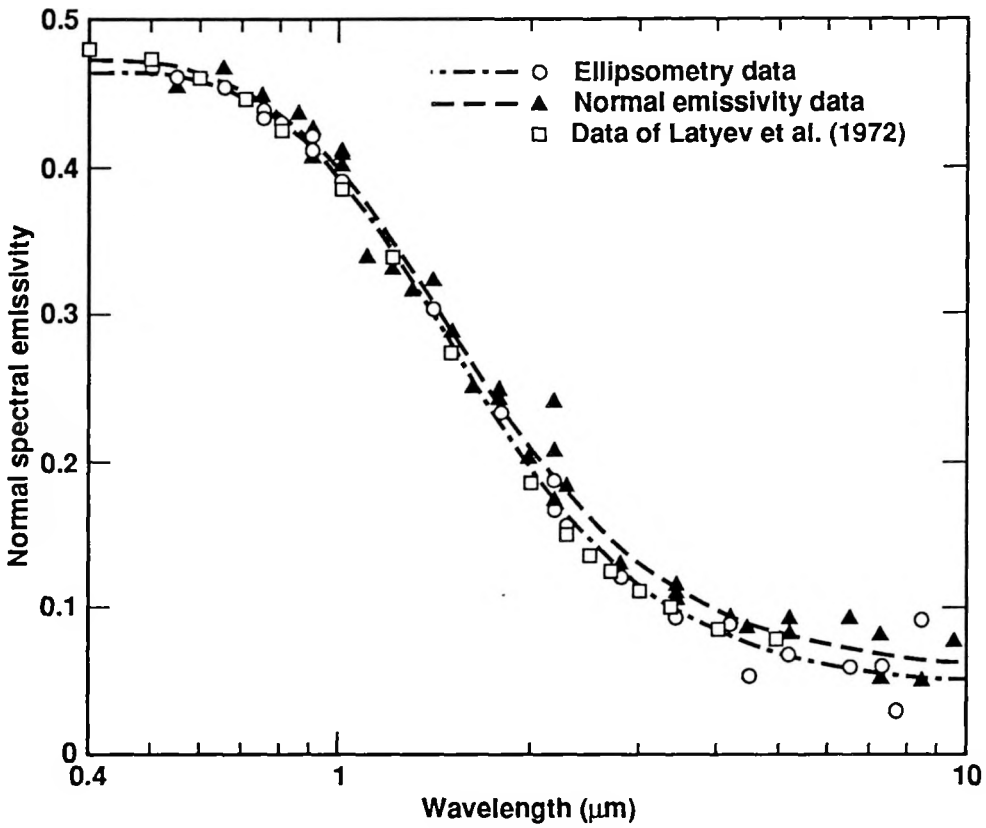

Fig. 9-3. The normal spectral emissivity of polished tungsten at 1270 K. The lines are least-squares fits to a form given in the text. See text for full citation.

extreme and the direct measurements of normal spectral emissivity indicate higher values of emissivity than the ellipsometric measurements. The differences in the three data sets at selected wavelengths are tabulated in Table 9.2. In general, the results for this nominal sample temperature are comparable to the one described earlier.

Results for a yet lower sample temperature (1040 K) are given in Fig. 9-4. In this case only the results of this work are shown (the lowest temperature reported by Latyev et. al. was 1200 K). The circles represent the ellipsometric work and the triangles the direct measurements of normal spectral emissivity. The single curve fit shown is of the same form as those described above but the fit is shown only for the ellipsometric results. The lower sample temperature of this case limited the direct emissivity work to wavelengths greater than 1.55 μm, at lower wavelengths signal to noise ratio was on the order of unity.

Surprisingly, the two measurement methods still show exellent agreement in the 3 to 10 μm range. More scatter and less accuracy were expected from the direct normal spectral emissivity system here because of the decrease in signal due to the lower sample temperature. More scatter was expected because signal to noise was lower and less accuracy because systematic errors would be larger (the data reduction equation given in chapter 6, eqn. 6-1, is increasingly inadequate for decreasing sample temperature). With the exception of the normal emissivity measurements in the 1 to 2 μm range, where decreasing signal is clearly causing larger errors, the results for normal spectral emissivity at this sample temperature display even better agreement than those given earlier. The percent differences between the direct emissivity measurements and the curve fit to the ellipsometric data are given in Table 9.3.

Experimental results for a fourth and yet lower sample temperature (940 K) are given in Fig. 9-5. The same symbol conventions are used and the curve is again a fit to only the ellipsometric work. Increased scatter in the directly measured normal spectral emissivity is apparent in the long wavelength extreme (5 to 10 μm) as expected from the

TABLE 9.2

Differences in normal spectral emissivity between this work and that of Laytev et. al. [94] for a sample temperature of 1270 K

Wavelength (μm)	Percent difference from ellipsometric measurements (%)	Percent difference from direct normal spectral emissivity measurements (%)
0.4	3.6	1.5
0.5	1.8	0.2
0.6	0.2	–1.0
0.7	–0.7	–1.6
0.8	–1.2	–2.1
1.0	–1.5	–2.6
1.5	–0.9	–4.3
2.0	–6.4	–13.4
2.3	–9.9	–19.2
2.5	–9.5	–20.0
2.7	–7.9	–19.4
3.0	–4.7	–17.5
3.4	–1.1	–15.3
4.0	1.2	–15.0
5.0	10.6	–6.7

percent difference = $[(\varepsilon_{Latyev} - \varepsilon_{Havstad})/\varepsilon_{Latyev}] \times 100$

lower sample temperature. Large and increasing errors are also obtained in the shorter wavelength ranges (1 to 2 μm) of these measurements. In the region between the two extremes, there is still good agreement between the two measurement methods. The percentage differences between the curve fit to the ellipsometric work and the direct emission measurememts are given in Table 9.3. The coefficients for this curve fit and those of the preceeding figures are given in Table 9.4.

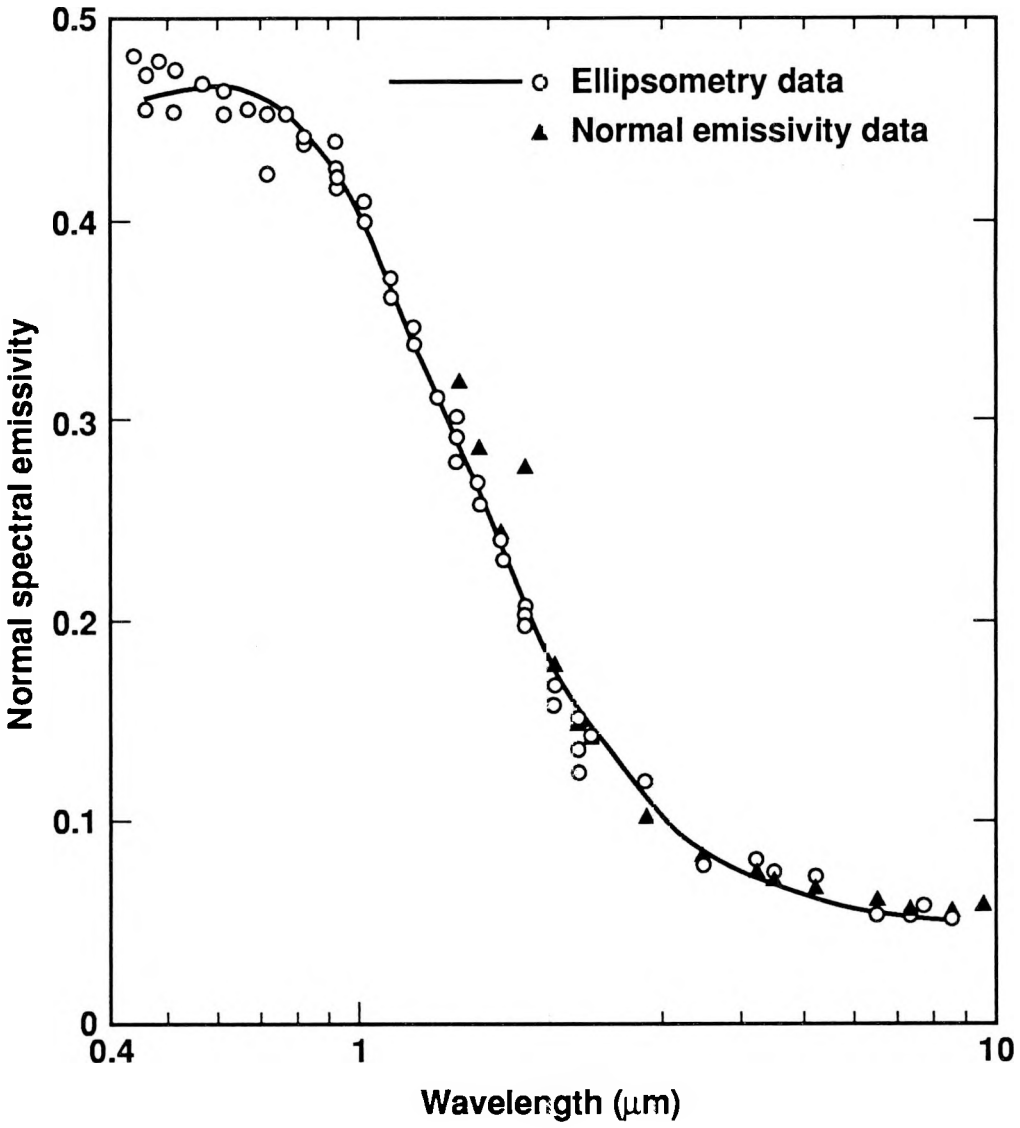

Fig. 9-4. The normal spectral emissivity of polished tungsten at 1040 K. The line is a least-squares fit to the ellipsometry data to a form given in the text.

Table 9.3

Difference between ellipsometric and direct normal spectral emissivity measurements for a sample temperature of 1040 K

Wavelength (μm)	Percent difference between ellipsometric and direct normal spectral emissivity measurement (%)
1.4	–11.5
1.53	–11.7
1.65	–5.6
1.8	–35.2
2.0	–2.7
2.2	0.4
2.3	–1.2
2.8	6.1
3.45	2.1
4.2	–4.0
4.5	–4.0
5.2	–6.6
5.2	–8.3
6.5	–12.3
7.3	–5.8
8.45	–8.6
9.5	–17.8

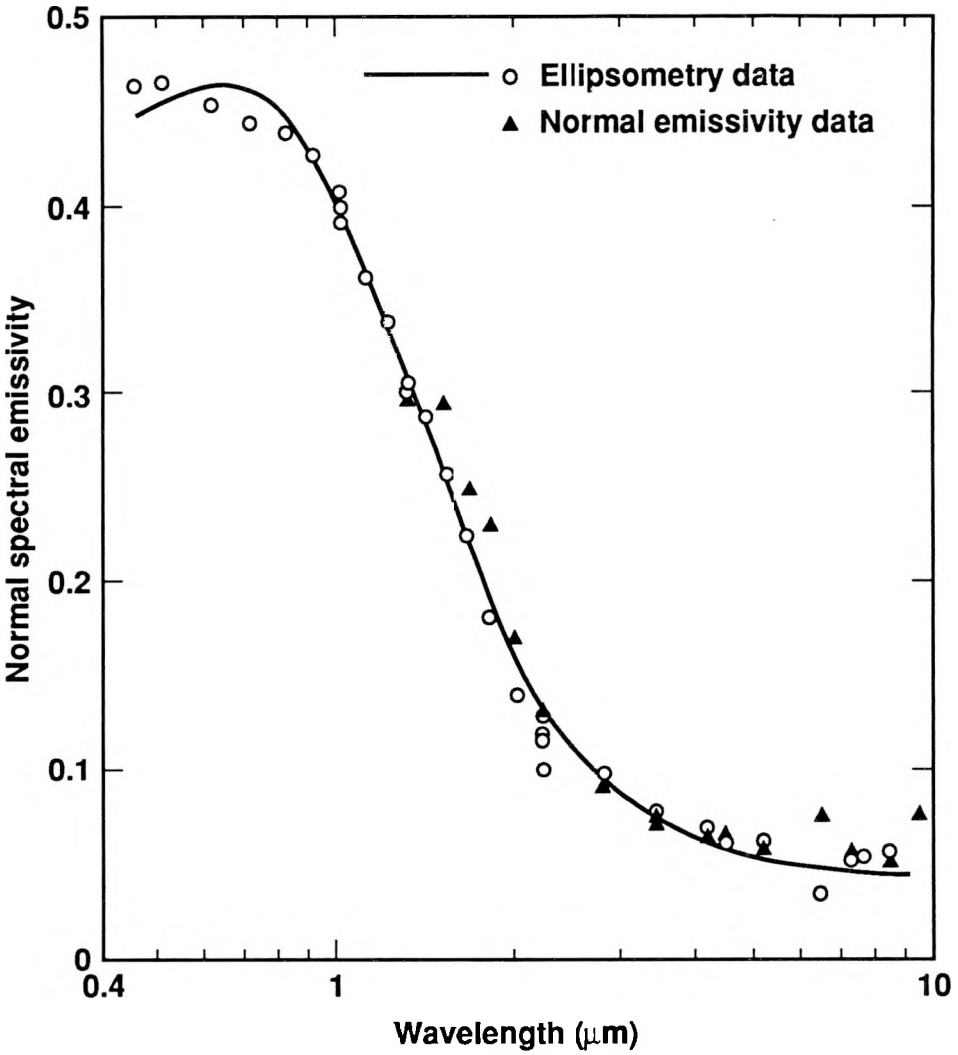

Fig. 9-5. The normal spectral emissivity of polished tungsten at 940 K. The line is a least-squares fit to the ellipsometry data to a form given in the text.

TABLE 9.4

Coefficients for curve fits to the normal spectral emissivity of tungsten as a function of wavelength

Coefficient (-)	Ellipsometric Data (-)	Direct normal spectral emissivity data (-)
	sample temperature 1450 K	
a_0	0.0594	0.0789
a_1	0.06	2.02
a_2	–2.08	–1.74
a_3	0.96	2.91
	sample temperature 1270 K	
a_0	0.0434	0.0557
a_1	1.74	1.62
a_2	–1.62	–1.35
a_3	2.74	2.66
	sample temperature 1040 K	
a_0	0.0436	
a_1	2.59	
a_2	2.96	
a_3	3.20	
	sample temperature 940 K	
a_0	0.0382	
a_1	3.21	
a_2	–4.00	
a_3	3.58	

Wavelength must be given in μm.

The curve fits are of the form:

$$\varepsilon_n(\lambda) = a_o + \frac{1}{a_1\lambda^2 + a_2\lambda + a_3}$$

9.4 The dependence of normal spectral emissivity on temperature in the infrared spectral region.

Measured and predicted variations in normal spectral emissivity with temperature are shown in Fig. 9-6. The direct measurements of normal spectral emissivity in the 1.8 to 5.2 μm range are shown as a function of sample temperature (The scatter in the results at longer wavelengths was greater than the temperature dependence being investigated). Also shown in the figure are the results of Dmitriev and Kholopov [186] and those of Latyev et. al. [134]. Qualitatively, the Hagen-Rubens relation correctly predicts emissivity increasing with temperature and decreasing with wavelength (beyond 1.3 μm).

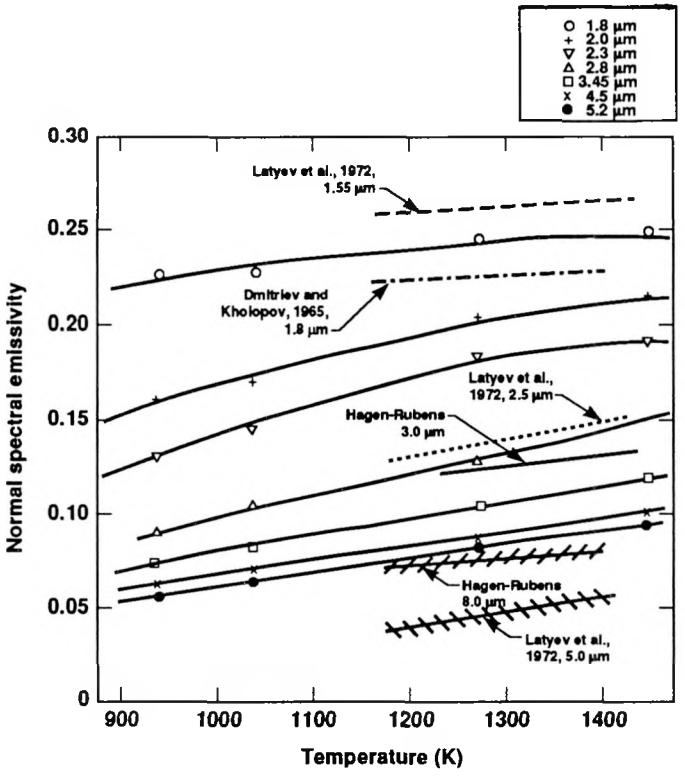

Fig. 9-6. The normal spectral emissivity of polished tungsten as a function of temperature. See text for full citations.

The dependence on temperature results from the temperature variation of the resistivity. From the data in a standard reference on the thermophysical properties of high temperature materials [40], the variation in the electrical resistivity of tungsten with temperature in the 900 K to 1500 K range is well approximated by the linear relation:

$$r_e(T) \approx 3.12 \times 10^{-4}\, T \; - 0.068 \tag{9–2}$$

Here, temperature is given in Kelvin, and resistivity is in ohm-m. (Variations in resistivity with material purity and sample forming techniques are relatively minor.) Substituting eqn. 9-2 into the Hagen-Rubens result for the normal spectral emissivity (eqn. 3-24) yields:

$$\varepsilon_n(\lambda) = 0.365 \sqrt{\frac{3.12 \times 10^{-4}(T) - 0.068}{\lambda}}$$

$$- (0.0464)\left[\frac{3.12 \times 10^{-4}\,(T) - 0.068}{\lambda}\right] \tag{9–3}$$

Wavelength is given in μm. Differentiating yields the rate of change of normal spectral emissivity with temperature:

$$\frac{\partial \varepsilon_n(\lambda)}{\partial T} \approx \frac{5.69 \times 10^{-5}}{\sqrt{\lambda}}\left[\frac{1}{\sqrt{3.12 \times 10^{-4} T - 0.068}}\right] \tag{9–4}$$

The rate is in 1/K. The rate of change of emissivity with temperature decreases with wavelength for all of the measurements but the Hagen-Rubens relation predicts even lower rates of change (and lower values of emissivity) than are observed. This is not

surprising since all the measurement wavelengths are for $\lambda < 10$ μm. Optical systems designed specifically for work at even longer wavelengths would be required to yield experimental results more closely approaching the predictions of the Hagen-Rubens relation.

The performance of the Hagen-Rubens relation for predicting the radiative properties of tungsten in the spectral range of interest to this work is more clearly illustrated in Fig. 9-7. The normal spectral emissivity predicted from the (direct current) electrical resistivity of tungsten at 1040 K is compared to that measured. Using the resistivity measured at this temperature [40] ($r_e = 26 \times 10^{-6}$ ohm-cm) gives predicted values (dashed line) consistently greater than the measured values (diamond symbols),

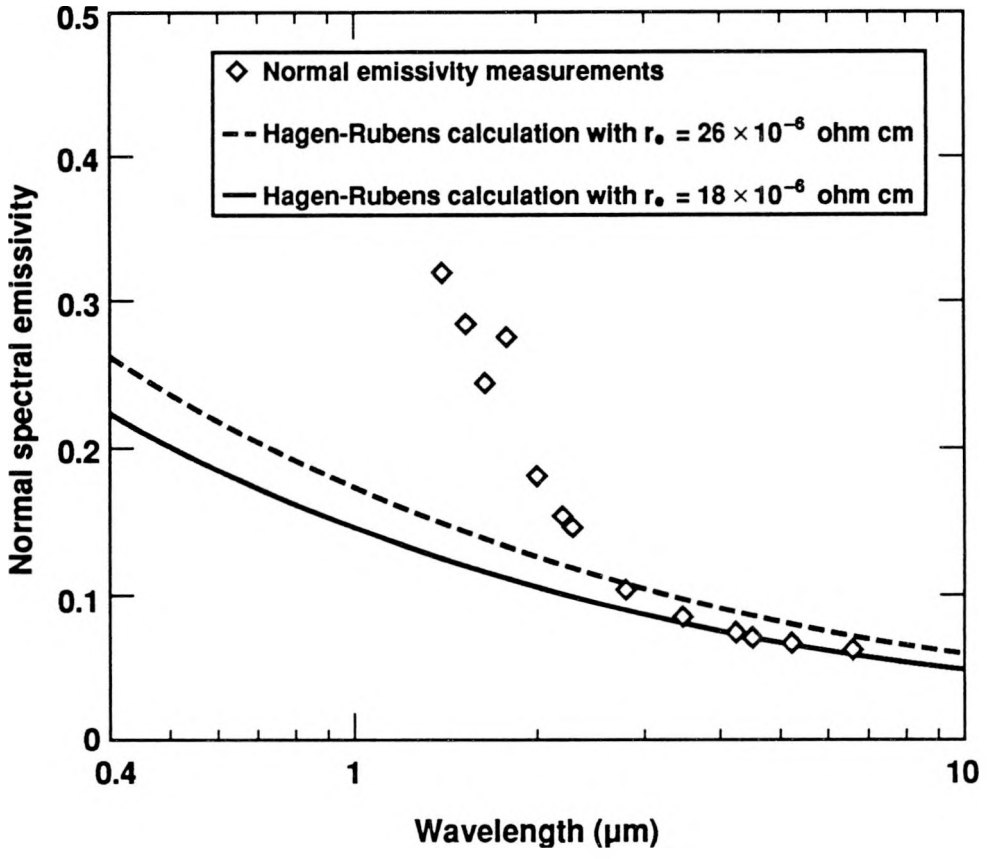

Fig. 9-7. The normal spectral emissivity of polished tungsten at 1040 K compared to the Hagen-Rubens approximation.

although the discrepancy decreases with wavelength. A resistivity of 18×10^{-6} ohm-cm, more than 30% lower, is required to obtain a good fit (solid line) to the measurements between 3 and 10 μm. However, of greater importance than the comparison to the Hagen-Rubens prediction is the reasonable agreement between the two techniques and the correct dependence on wavelength for $\lambda < \sim 4$ μm.

9.5 The optical constants of polished tungsten at elevated temperature in the visible spectral range

The optical constants of tungsten between 0.45 and 0.75 μm have been extensively studied. The results of a comprehensive review [100] are compared to the present study for the two highest nominal sample temperatures, 1270 K and 1450 K) in Figs. 9-8 and 9-9. The small differences between the results for k in Fig. 9-9 could be due to a combination of sample purity (both bulk and surface), surface grain (both size and boundary depth) and surface roughness effects, or measurement errors, but, in general, the agreement is good. Except for the work of Barnes [187], the results for k agree to within 6% over most of the plotted range.

The results for index of refraction, n (shown in Fig. 9-8), do not agree as well as those for k (for the five studies), but the agreement between Roberts' data [138] and this work is better than 2% over the whole range. The level of agreement shown here for both n and k indicates a high level of confidence in the visible wavelength ellipsometry is warranted. Since all of the ellipsometric results from 0.4 to 2.3 μm, were obtained with the same (calcite) polarizers, and the only difference in the optical system over this whole wavelength range was the bandpass filters placed directly in front of the detector, the ellipsometeric results to 2.3 μm deserve comparable confidence.

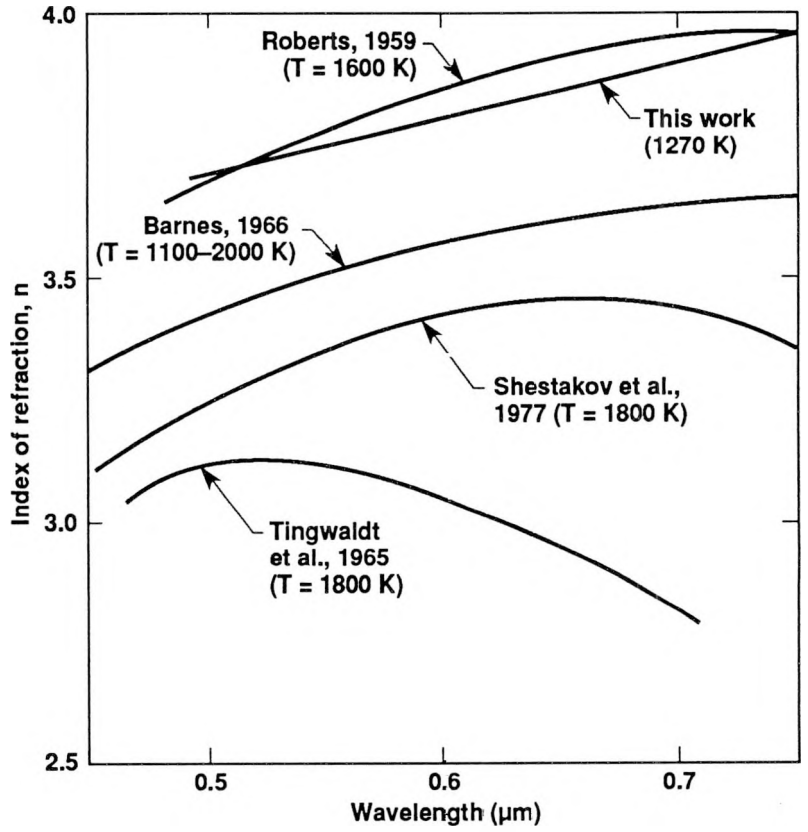

Fig. 9-8. The index of refraction of polished tungsten in the visible spectral region. See text for full citations.

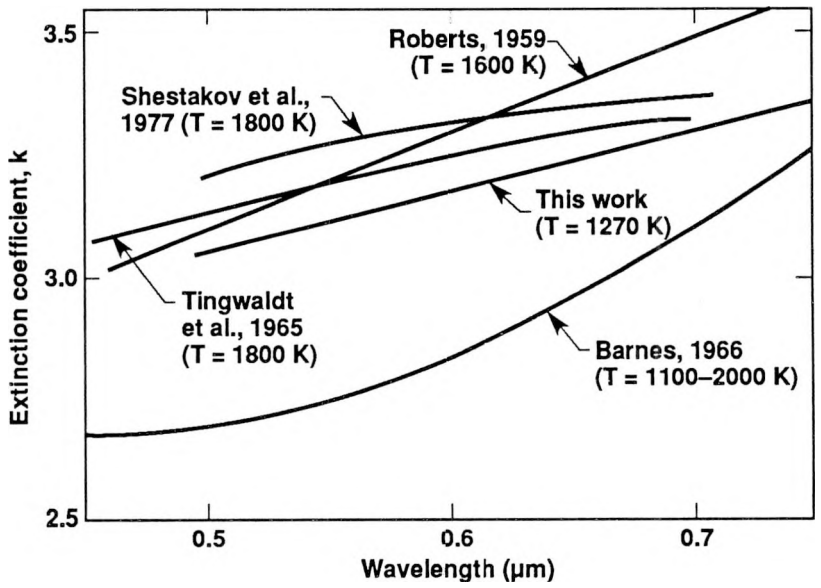

Fig. 9-9. The extinction coefficient of polished tungsten in the visible spectral region. See text for full citations.

9.6 The optical constants of polished tungsten at elevated temperature over the entire spectral range (0.4 to10μm)

The optical constants of hot tungsten in the infrared and the visible spectral ranges are shown in Figs. 9-10 and 9-11. In Fig. 9-11, the variation of extinction coefficient with wavelength is compared with the results of Nomerovannaya, Kirillova and Noskov (at room temperature) [137], Aksyutov and Pavlyukov (at 620 K) [136], and Roberts (at 1100 K and 1600 K) [138]. The close agreement of the data through the visible to 2 μm reflects both the high signal to noise ratio in the measurement system and the weak dependence of k on temperature at these shorter wavelengths. For wavelengths less than 2 to 3 μm the variation in k with λ is due to bound electron effects as discussed for molybdenum in chapter 3. For $\lambda > \sim 3$ μm, free and bound electron effects both contribute. For tungsten, the lowest energy bound electron effects occur at ~0.3 eV (4.1 μm) [137] so that measurements at wavelengths beyond 10 μm are required for successful fits to the free electron relations (either the Drude model or its long wavelength asymptote, the Hagen-Rubens relation). The rapid increase of k with λ in this range is an indication of convergence toward agreement with such models but true quantitative agreeement requires longer wavelengths than are of interest to radiation heat transfer. The variation of index of refraction, n, with wavelength is given in Fig. 9-10. Bound electron effects are even more apparent here than with k. The monotonic increase in n with λ does not begin so soon and unlike k, the index of refraction increases monotonically with temperature in the 2 to 6 μm range. The Hagen-Rubens result for n

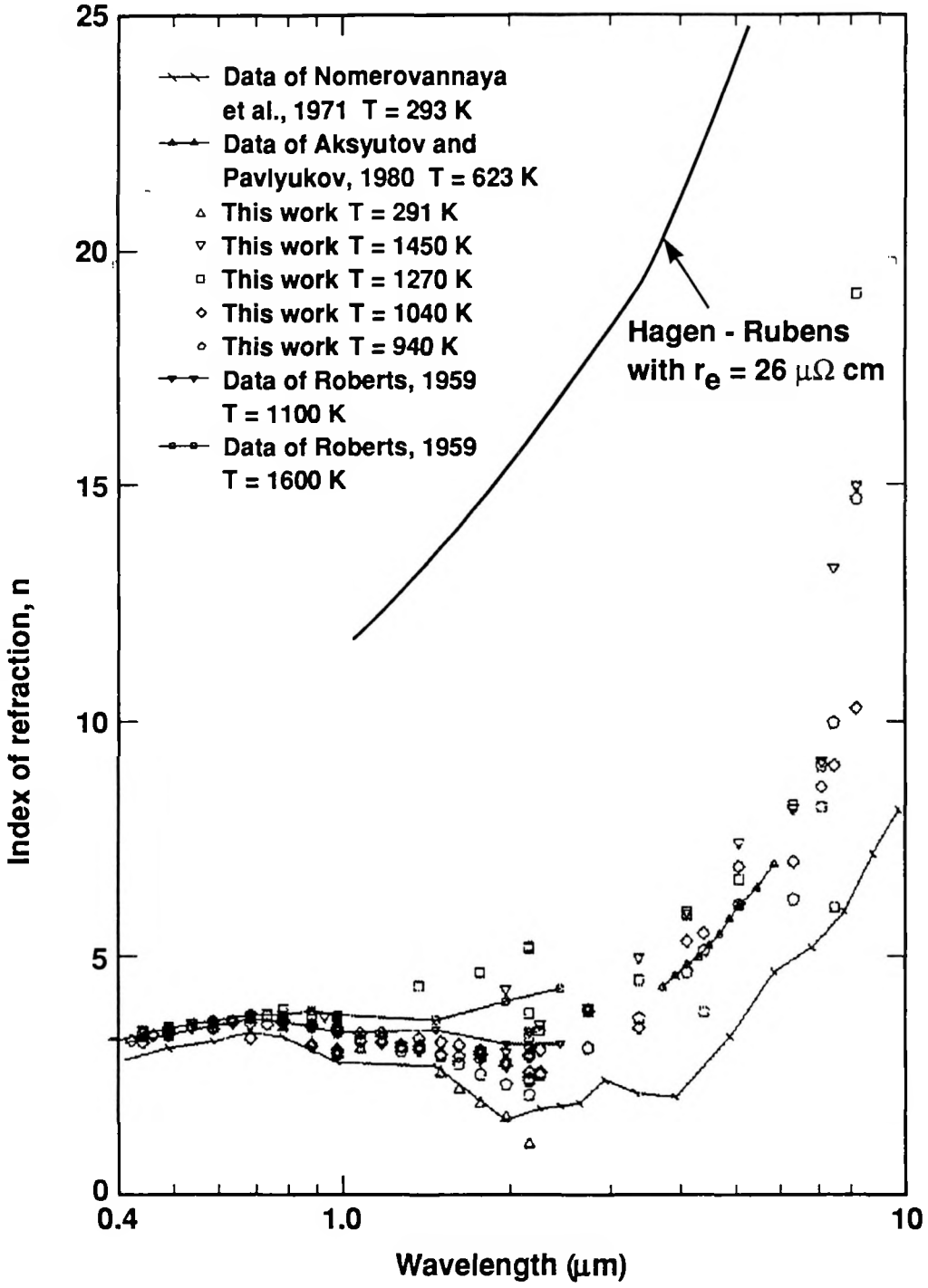

Fig. 9-10. The index of refraction of polished tungsten. See text for full citations.

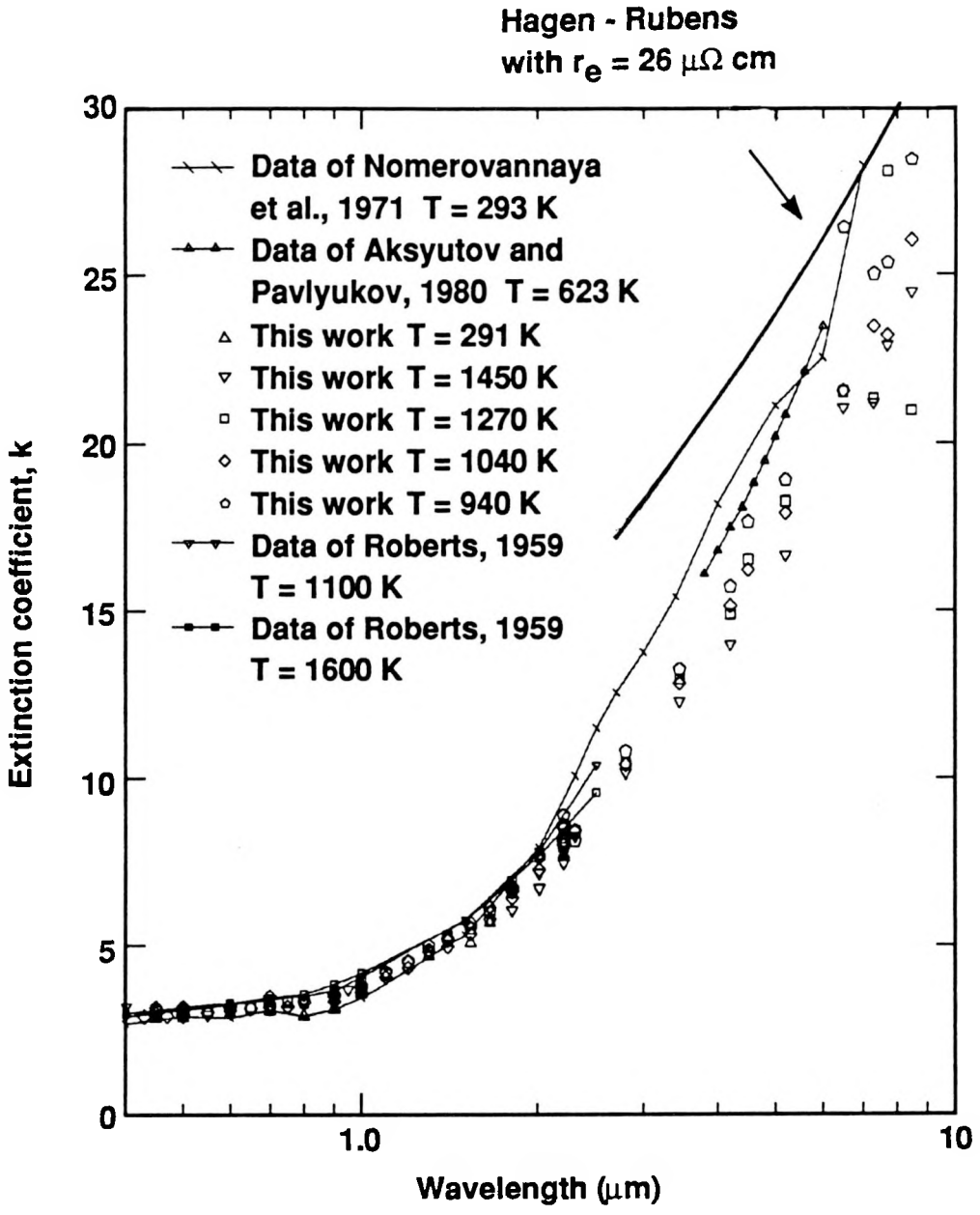

Fig. 9-11. The extinction coefficient of polished tungsten. See text for full citations.

and k in terms of wavelength and resistivity predicts their long wavelength dependence on temperature:

$$n = k = \sqrt{\frac{0.0030\lambda_o(\mu m)}{r_e(\Omega\text{–cm})}} \qquad (9\text{–}5)$$

Since resistivity increases with temperature this relation predicts both n and k decreasing monotonically with temperature. Only for wavelengths beyond 10 μm is good agreement with this relation observed.

With measurements of the complex index of refraction for tungsten in hand (despite their failure to conform to classical theory) over the entire range of wavelengths, it is now possible to illustrate the reflective, emissive and absorptive properties of this material over the full range of interest. Figures 9-12 to 9-15 display the directional spectral reflectivity as a function of angle for tungsten at 1273 K for four wavelengths from the visible to 5.2 μm. Reflectivity increases toward unity as wavelength increases and the pseudo-Brewster angle tends toward 90°.

The effect of the temperature dependence of the complex index of refraction on reflectivity in the infrared is understood by comparing Figs. 9.15, 9-16 and 9-17, which show the polarized reflectivity at 5.2 μm at temperatures of 1270 K, 1450 K and 940 K respectively. Reflectivity decreases with increasing temperature in the infrared.

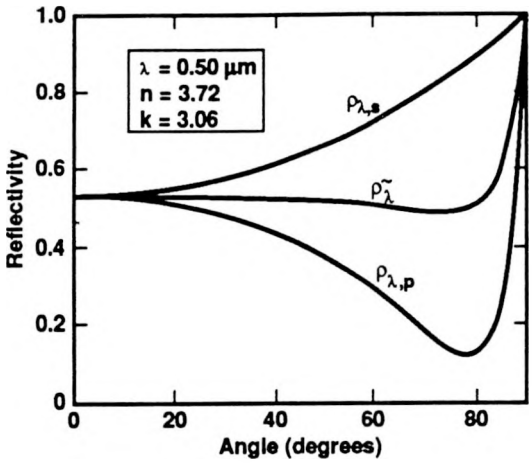

Fig. 9-12. The reflectivity of polished tungsten at 0.50 μm and 1270 K.

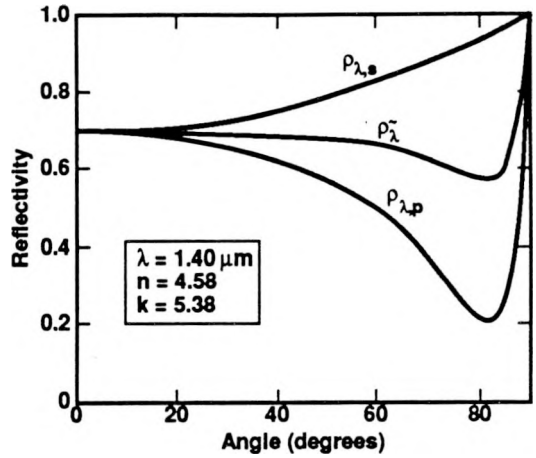

Fig. 9-13. The reflectivity of polished tungsten at 1.40 μm and 1270 K.

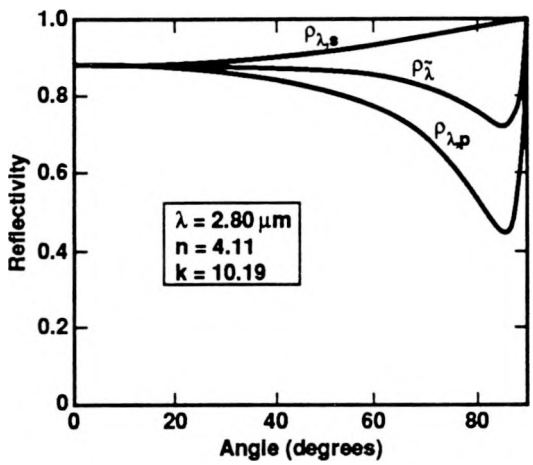

Fig. 9-14. The reflectivity of polished tungsten at 2.80 μm and 1270 K.

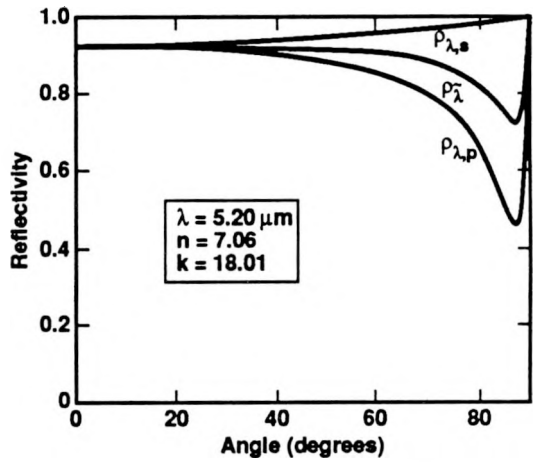

Fig. 9-15. The reflectivity of polished tungsten at 5.20 μm and 1270 K.

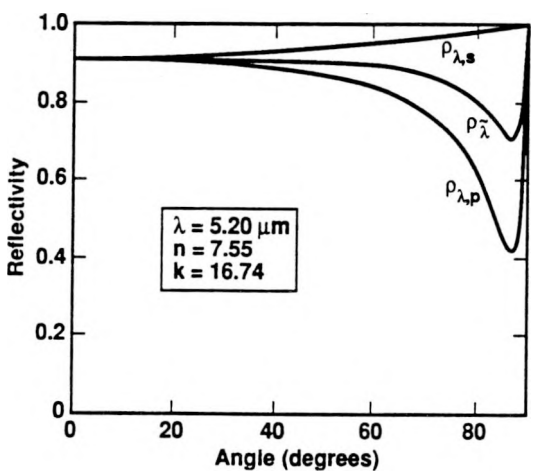

Fig. 9-16. The reflectivity of polished tungsten at 5.20 μm and 1450 K.

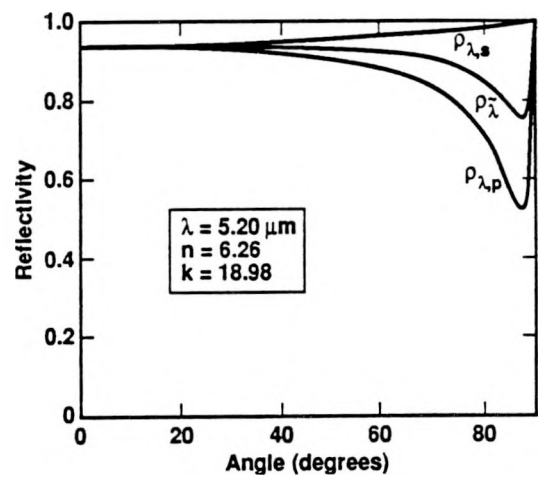

Fig. 9-17. The reflectivity of polished tungsten at 5.20 μm and 940 K.

9.7 The complex dielectric function of polished tungsten at elevated temperatures

Figures 9-18 and 9-19 present the experimental results for tungsten (described above) in terms of ϵ and σ rather than n and k and as functions of photon energy rather than wavelength. The essentially equivalent specifications of the optical constants of materials by the complex dielectric function and the complex index of refraction were given in chapter 2:

$$\epsilon = [\epsilon_0 \mu_o / \mu][n^2 - k^2] \quad ; \quad \epsilon' = [\epsilon_o \mu_o / \mu][2nk] \qquad (9\text{–}6)$$

The common representation using optical conductivity, σ, in place of ϵ' was given in chapter 3:

$$\sigma = \omega \epsilon' \qquad (9\text{–}7)$$

Optical conductivity is sometimes preferred because, unlike ϵ', σ remains finite as wavelength goes to infinity. In the visible and shorter infrared spectral regions, the weak dependence of both n and k on temperature produces no observable variation in ϵ with temperature but at longer wavelengths the tendency for n to increase and k to decrease with temperature produces a noticeable increase in the magnitude of ϵ as sample temperature rises.

The results for conductivity (Fig. 9-19) show no consistent variation with temperature over the whole spectral range of interest. Since the components of the complex index of refraction have opposite dependences on temperature, and, because the conductivity varies as their product, little change with temperature results. As with n and k, the presence of low energy bound charge effects prevents correspondence between predictions from free carrier models (given in ch. 3) and the data.

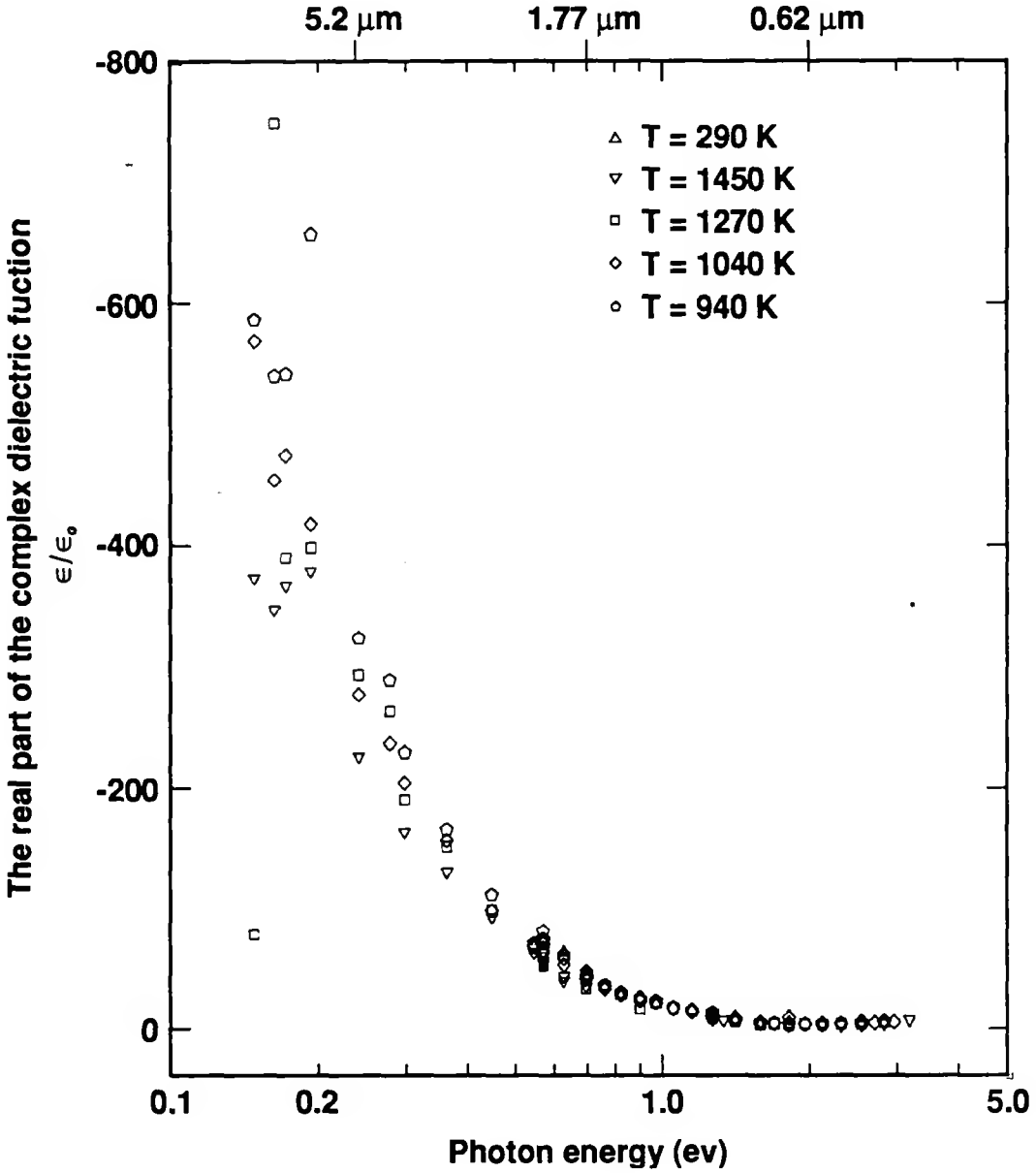

Fig. 9-18. The real part of the complex dielectric function, ϵ/ϵ_0, as a function of photon energy for polished tungsten.

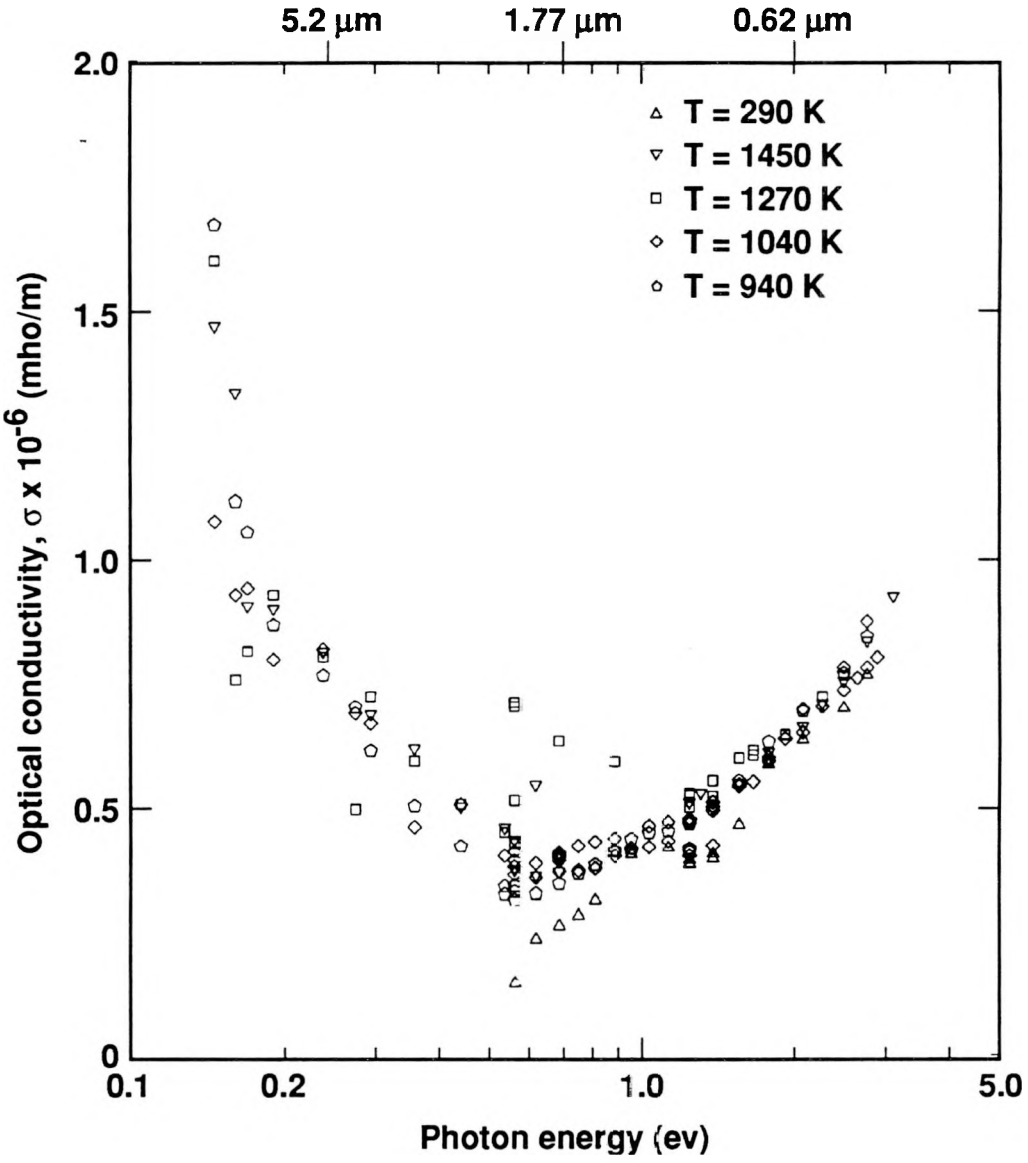

Fig. 9-19 Optical conductivity, σ, as a function of photon energy for polished tungsten.

9.8 Summary

The thermal radiative properties of tungsten at elevated temperature have been measured by two essentially independent methods. Comparisons between the two methods and to previously published work show reasonably good agreement. The variations in ε_n, n and k with wavelength, in the long wavelength extreme of this work (5 to 10 μm), are only in qualitative agreement with the Hagen-Rubens relations. Variations in ε_n, n and k with temperature are 1) not large, 2) consistent with those of other experimental efforts, and 3) in the case of k and normal spectral emissivity (but not n) in agreement qualitatively with expectations derived from the Hagen-Rubens relation. In summary, the results for tungsten justify confidence in the measurement system to be applied to molten uranium and aluminum. Errors depend on wavelength, and have been tabulated. Over the entire spectral range of interest the uncertainties in the results are small enough that the thermal radiative properties of tungsten are accurately enough known for most heat transfer calculations.

10. Experimental results for the radiative properties and optical constants of uranium

10.1 Background

The thermal radiative properties and optical constants of uranium have not been well studied. The literature review given in chapter 5 included only seven references, all of which were either of questionable quality or limited to ambient temperatures and lower. Of the four studies treating uranium at elevated (1100 to 1410 K) temperature, three were simply measurements of normal spectral emissivity (0.65 μm) and all were performed in inadequate vacuum. In the three studies of uranium at ambient temperature or lower, considerable efforts were expended to maintain sample purity, but reliable methods for predicting the radiative properties of high temperature metals from their room temperature values do not exist.

This chapter reports the first measurements of the optical constants of molten uranium. With the exception of Burgess and Waltenberg's result [161] for the normal spectral emissivity of liquid uranium at 0.65 μm reported in 1915, these are also the first measurements of the thermal radiative properties of molten uranium. Measurements of the normal spectral emissivity of solid uranium at temperatures approaching the melting point (1406 K) are also given here (for contrast with the molten results) but these are for rough surfaces resulting from resolidification within the tungsten crucible. Since rough solid surfaces can exhibit emissivity enhancement of several percent or more relative to solid ones [188,189], the results given here for the normal spectral emissivity of high temperature solid uranium are probably high by at least several percent. The considerable difficulties of producing and maintaining a high purity solid uranium surface with a fine polish were not addressed in this work. However, the results for solid uranium given

here are sufficiently close to those for the liquid that it seems unlikely that any of the thermal radiative or optical properties of the two phases are appreciably different.

The surface cleaning operations and Auger spectrometer scans for "dirty" and "clean" uranium were given in section 8.3.1. All measurements were made on "clean" samples while they were being sputtered to maintain their purity.

10.2 The normal spectral emissivity of uranium as a function of wavelength at 1410 K

The normal spectral emissivity of liquid uranium at 1410 K is given in Fig. 10-1. The direct measurements of normal spectral emissivity are represented by triangles and the ellipsometric results by diamonds. The curves shown are least squares fits (of the same form as that used with tungsten in the preceeding chapter) to the results from each of the two independent measurement systems. Differences between the two curve fits indicate the magnitude of systematic errors. Table 10.1 gives the percent difference between the two curves at selected wavelengths over the range of interest. Errors are small over the 0.8 to 3.5 μm range, where both measurement systems have good signal to noise ratios and the ellipsometric sysem has good sensitivity. Outside of this range larger errors were expected, both from the sensitivity considerations treated in ch. 7 and for the experimental reasons discussed in the preceeding two chapters. The impact of discrepancies at the long wavelengths (beyond 3.5 μm) between the two sets of results is not severe for the principal applications which motivated this work: the peak in the Planck function for material at the melting point of uranium (1406 K) is at 2.06 μm and 62% of blackbody emission from a surface at 1406 K is below 3.5 μm. With the spectral dependence of the emissivity included (because the emissivity decreases quite strongly with wavelength) even a 20% uncertainty in the normal spectral emissivity at wavelengths greater than 3.5 μm involves only a small fraction of the emitted energy in

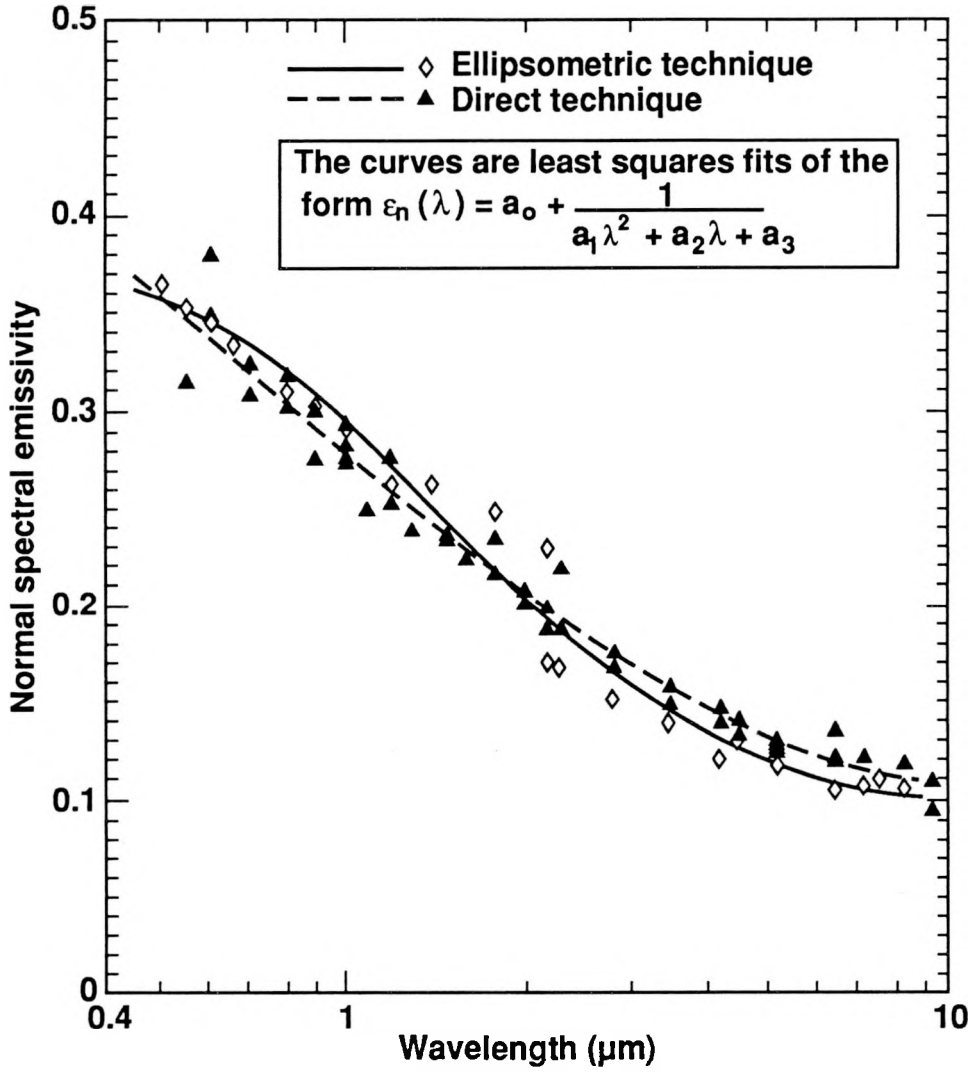

Fig. 10-1. The normal spectral emissivity of liquid uranium at 1410 K.

the whole spectrum. In summary, the small systematic errors indicated by Fig. 10-1 and the data in Table 10.1 indicate that confidence is warranted in the results given here for normal spectral emissivity.

Random errors are indicated by the magnitude of the deviations of the measured results from the curve fits shown. These deviations are shown as a function of wavelength in Figs. 10-2 and 10-3. The first of these figures gives the deviations of the ellipsometric results and the second, the direct measurements of normal spectral emissivity. The

standard deviations (the square root of the mean of the deviations squared) of the results for each data set are, 6.78% and 6.77% for the ellipsometry and direct sets respectively.

The results for both measurement methods at 1410 K, matched to a single curve of the same form as that used above, are shown in Fig. 10-4. The standard deviation of the results considered in this way is 6.4%.

TABLE 10.1

Difference between ellipsometric and direct measurements of normal spectral emissivity for liquid uranium at 1410 K

Wavelength (μm)	Percent difference between curve fits to the two measurement techniques (%)
0.45	–1.8
0.5	–0.4
0.6	1.8
0.7	3.3
0.8	4.4
0.9	5.0
1.0	5.3
2.0	0.5
3.0	–5.9
3.5	–8.0
4.0	–9.5
4.5	10.3
5.0	10.7
6.0	10.6
7.0	–9.9
8.0	–9.0
9.0	–8.0

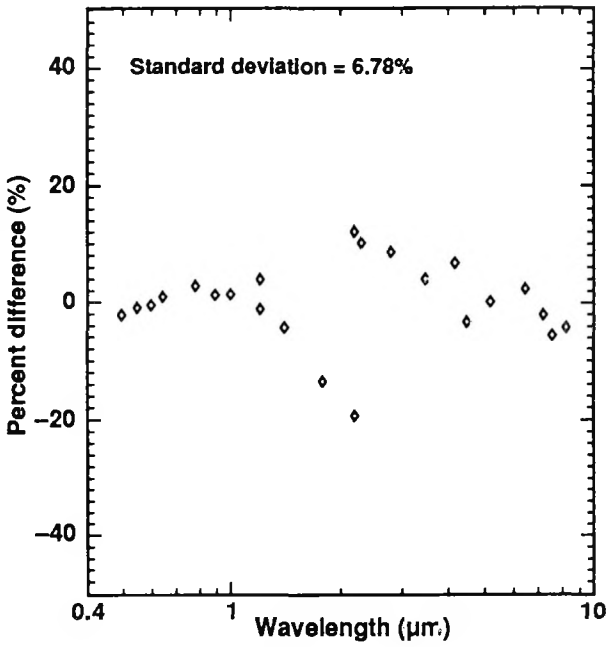

Fig. 10-2. The difference between the ellipsometry data and its curve fit for a sample temperature of 1410 K.

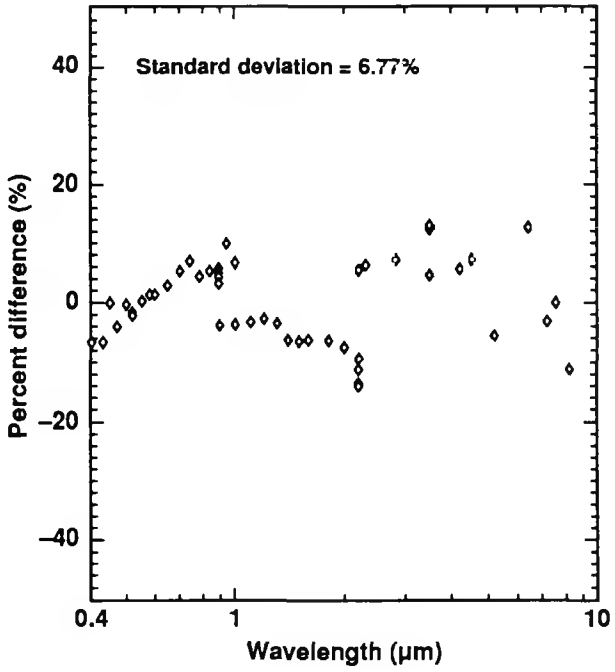

Fig. 10-3. The difference between the direct measurements of normal spectral emissivity and its curve fit for a sample temperature of 1410 K.

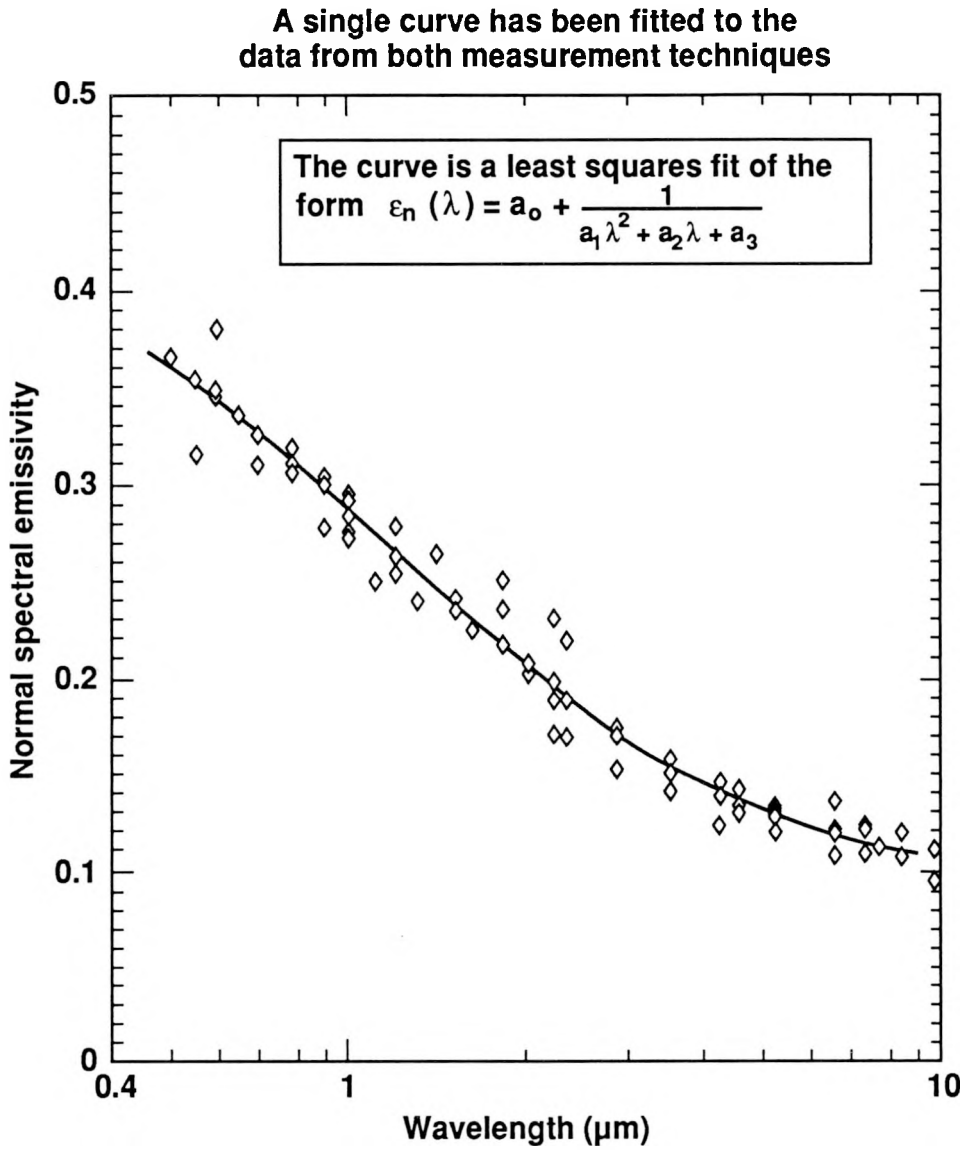

Fig. 10-4. The normal spectral emissivity of liquid uranium at 1410 K (with a single curve fit).

10.3 The normal spectral emissivity of uranium as a function of wavelength at 1480 K

The normal spectral emissivity of molten uranium obtained from the two measurement techniques with a sample temperature of 1480 K is given in Fig. 10-5. The presentation follows that of Fig. 10-1 and good agreement is again observed in the 0.8 to 3.5 μm range but greater differences are evident here in both the short and the long wavelength extremes. The four data points obtained by ellipsometry for wavelengths greater than 6 μm are approximately 20% low relative to the direct emissivity work at this temperature and all of the work at 1410 K. Small increases in emissivity are expected with temperature at these wavelengths (from the Hagen-Rubens relation) so a sharply lowered emissivity here causes these four ellipsometry results to be suspect. For completeness, these data are retained in the work which follows, but the curve fit for the direct emissivity work for this temperature is to be preferred over that from the ellipsometry.

The deviations of each data set from the respective curve fits for the sample temperature of 1480 K are given in Figs. 10-6 and 10-7. These figures indicate that the random error for this sample temperature is similar to that observed at 1410 K. The standard deviations for the ellipsometric and direct measurement systems were 5.06% and 3.88%.

In addition to 1410 and 1480 K, measurements at sample temperatures up to 1630 K were obtained. All of these measurements (from both measurement methods) are shown in figure 10-8. The single curve fit shown represents the best fit to normal spectral emissivity of molten uranium between 1410 and 1630 K. The coefficients for this curve fit are given in table 10.2

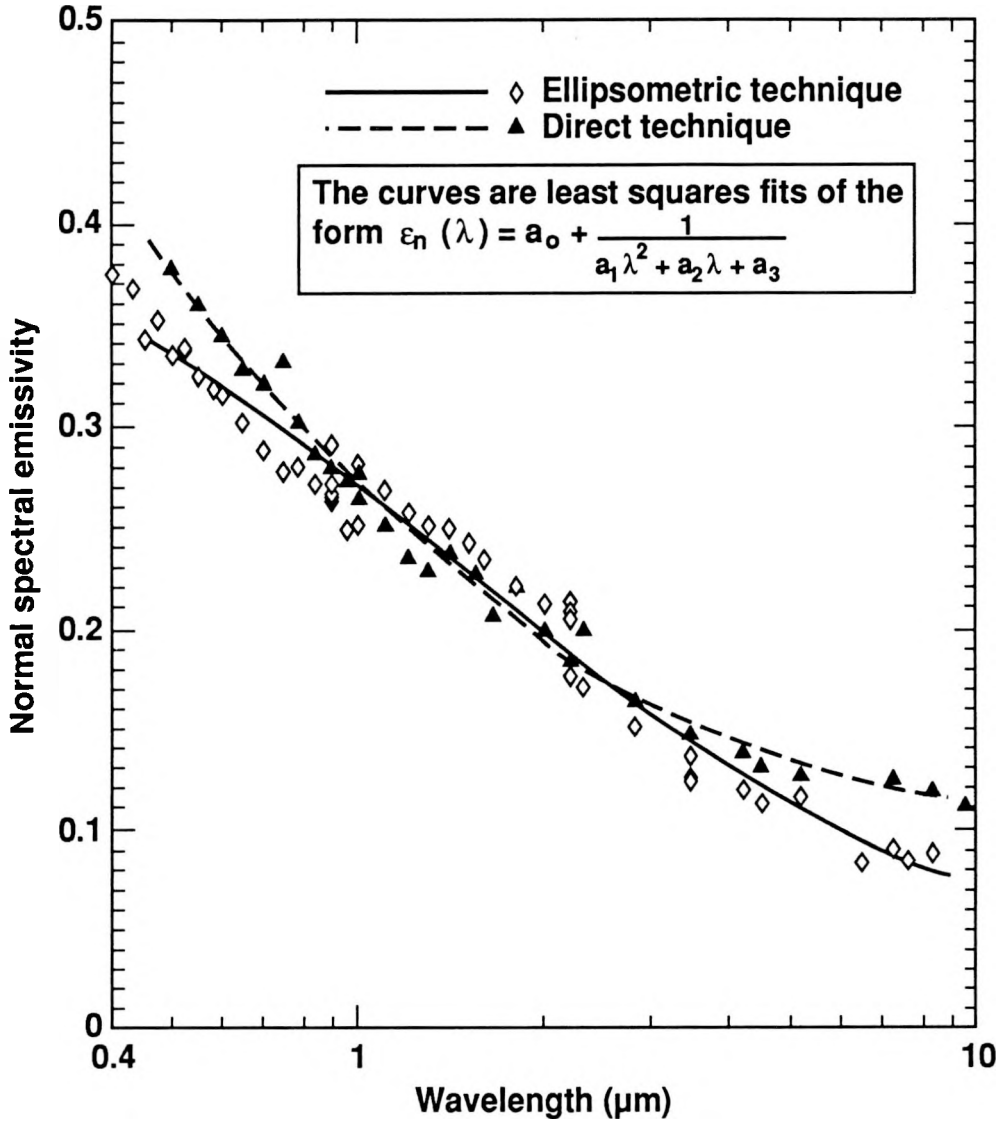

Fig. 10-5. The normal spectral emissivity of liquid uranium at 1480 K.

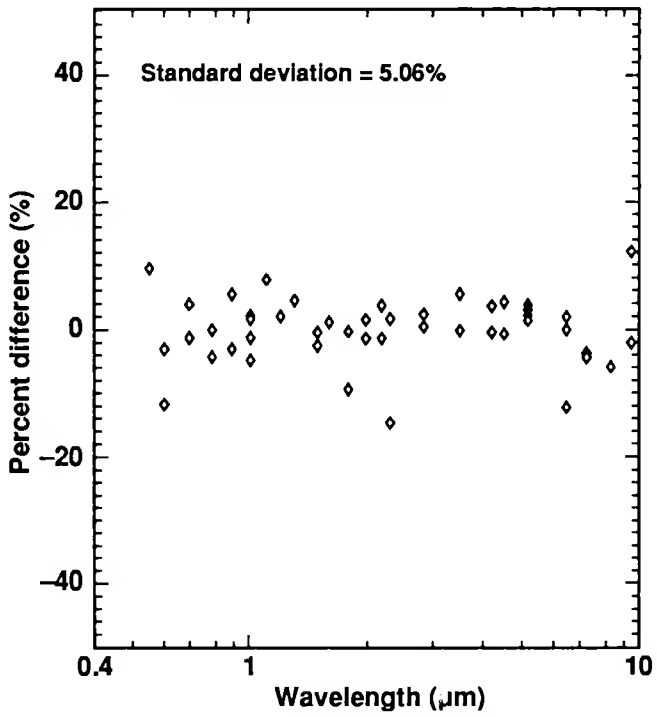

Fig. 10-6. The difference between the ellipsometry data and its curve fit for a sample temperature of 1480 K.

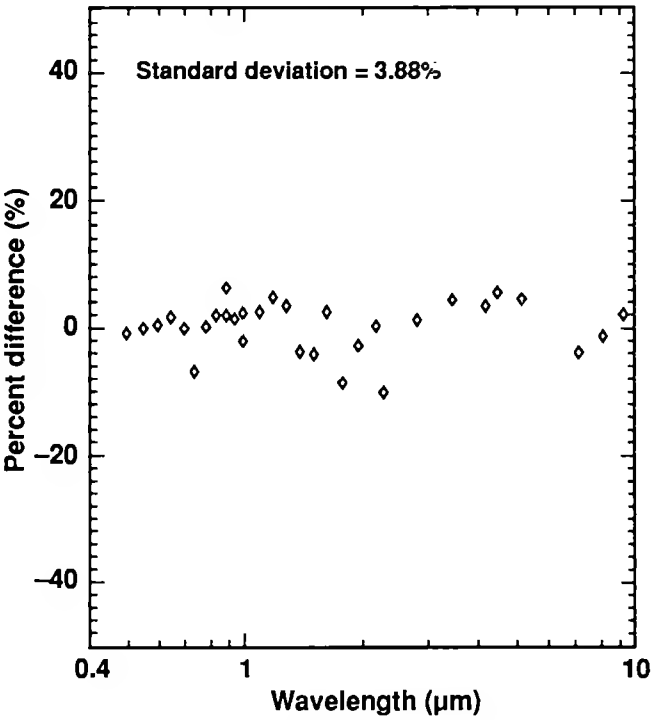

Fig. 10-7. The difference between the direct measurements of normal spectral emissivity and its curve fit for a sample temperature of 1480 K.

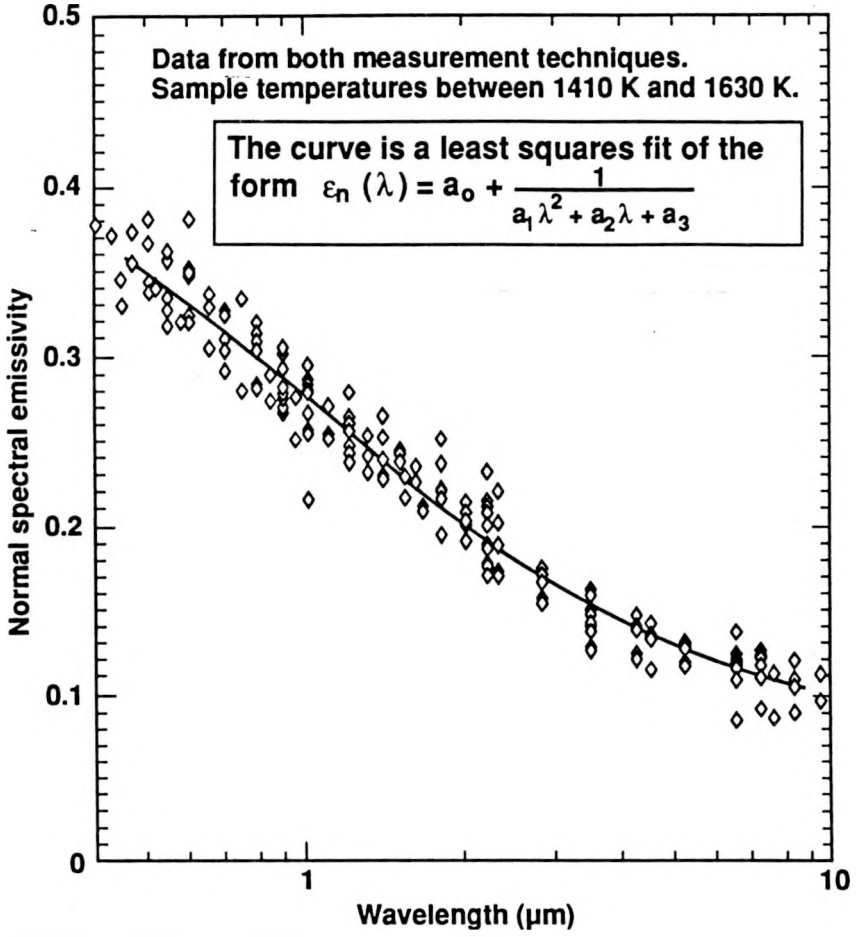

Fig. 10-8. The normal spectral emissivity of uranium

TABLE 10.2

Coefficients for the curve fit to the normal spectral emissivity of liquid uranium as a function of wavelength (1410 to 1630 K)

Coefficient	value
a_0	0.0793
a_1	0.254
a_2	2.50
a_3	2.42

Wavelength must be given in μm. The curve fit is of the form:

$$\varepsilon_n(\lambda) = a_o + \frac{1}{a_1\lambda^2 + a_2\lambda + a_3}$$

10.4 The dependence of the normal spectral emissivity on temperature in the infrared spectral region

The results of direct measurements of normal spectral emissivity in the infrared (beyond 2 μm) at six sample temperatures are shown in Fig. 10-9. The three sets of data obtained with molten uranium indicate emissivity increasing with temperature in the infrared but the solid uranium results have the opposite dependence. Since the solidified samples used here were not smooth polished specimens (they were simply solified samples which had been studied in the liquid state) the emissivity enhancement due to surface roughness may have been variable and significant enough to obscure the true dependence of the normal spectral emissivity on temperature for pure solid uranium. The decrease in emissivity with temperature shown in Fig. 10-9 for solid uranium is small and monotonic, but also of the same order of magnitude as would be expected for roughness effects, several percent. The experimental difficulties inherent to resolving the sign of the temperature dependence for solid uranium are extreme. The chemical reactivity of the uranium surface makes polishing difficult and only of limited value, while sputter cleaning produces roughening which masks the effect to be measured.

The temperature dependence of the resistivity of uranium was studied by Busch, Guntherodt and Kunzi [190] over a wide temperature range (288 to 1473 K). From their data, the resistivity at the melting temperature is 64 μohm-cm and the resistivity increases with temperature at a rate of about 0.043 μohm-cm per K. These values were used with the Hagen-Rubens relation (eqn. 3-24) to predict the variation with temperature of the normal spectral emissivity (also shown in Fig. 10-9). Both the magnitude of the emissivity and its rate of change with temperature are moderately well represented by the Hagen-Rubens relation.

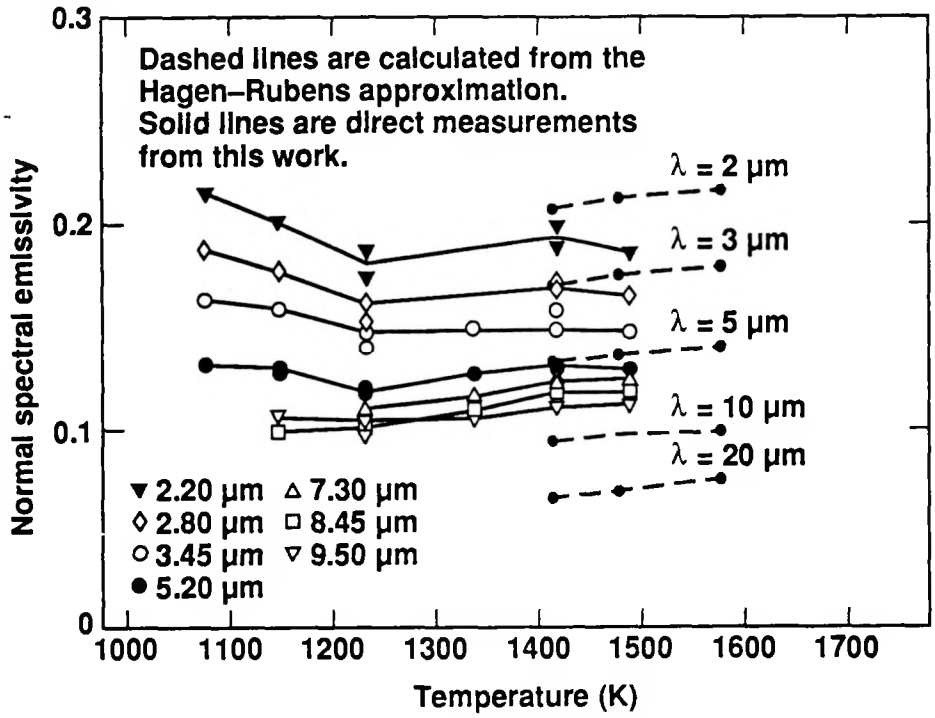

Fig. 10-9. The normal spectral emissivity of uranium as a function of temperature.

A Hagen-Rubens prediction and experimental results for the normal spectral emissivity of uranium are also compared in Fig. 10-10. The normal spectral emissivity (from direct measurements) at 1410 K is given along with 1) a Hagen-Rubens calculation using the resistivity reported for uranium at the melting point and 2) a least squares fit of the form of the Hagen-Rubens approximation with the single free parameter corresponding to the resistivity. The resistivity obtained from the fitting routine, 73 μohm cm (15% higher than the measured value), provides an excellent fit to the measurements over the entire spectral range of interest. However, the success of the fit does not mean that the Hagen-Rubens relation holds over the range of wavelengths used

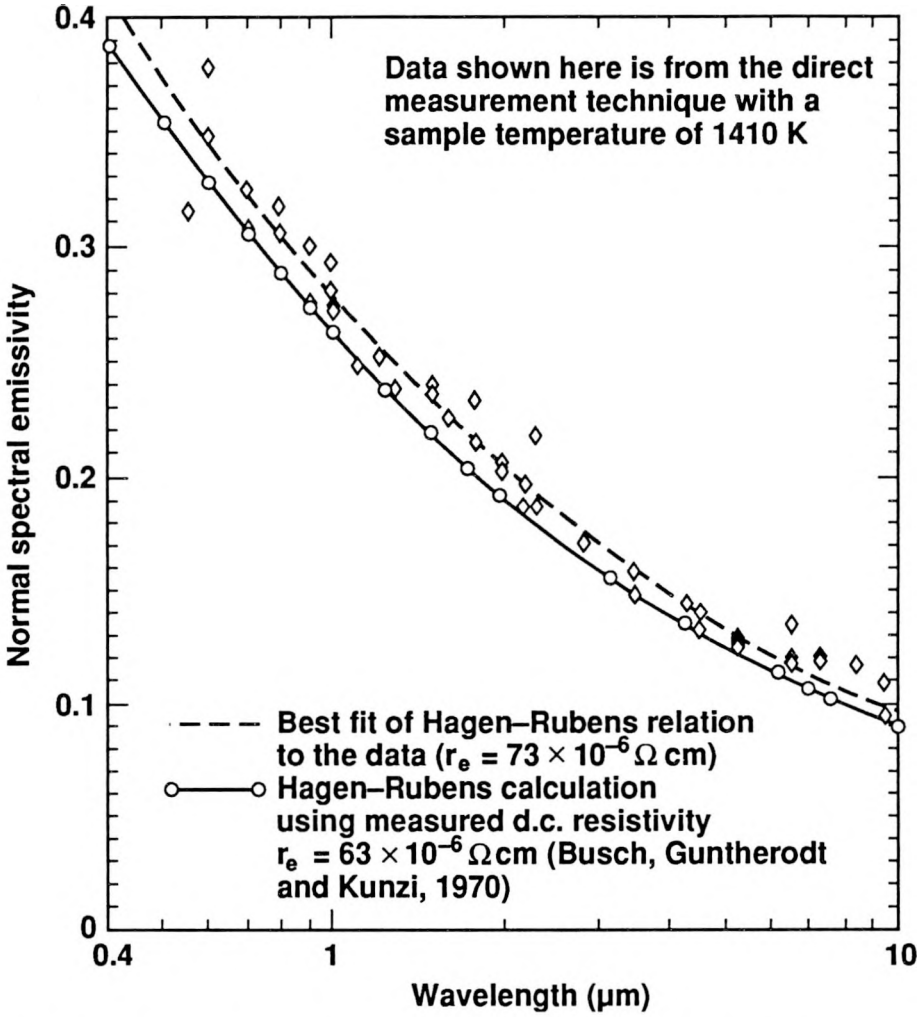

Fig. 10-10. A comparison of data and the Hagen-Rubens approximation.

here. The variation of n and k (which determine the spectral dependendence of the normal spectral emissivity) shown below are not quantitatively consistent with the predictions.

10.5 The optical constants of liquid uranium in the visible spectral range

The off-normal reflecting, absorbing and emitting properties of uranium in the visible spectrum are of particular importance because visible wavelength radiation

constitutes a large unwanted heat load in laser isotope separators. The visible range optical constants determine these off-normal properties.

The variation in the index of refraction of molten uranium with wavelength in the visible spectral range is given in Fig. 10-11. The index increases uniformly from 0.5 to 0.80 μm. The deviations from monotonic variation in the 0.4 to 0.5 μm range for the squares (1480 K) are probably due to the low signal to noise ratios of the ellipsometric measurement system at short wavelengths, but could be due to bound electron effects. (Weaver [159] noted bound effects at 0.95 μm, 1.6 μm, 3.65 μm and 8.27 μm.) Two measurements given by Weaver for uranium at 4.2 K are also given in the figure but the extreme difference in sample temperatures precludes significant comparison. The results of Faldt and Nillson [160] for wavelengths less than 0.5 μm and a sample temperature of 293 K lie below the range shown for the ordinate. The data of Weaver and Faldt and Nillson are the only reported optical constants for uranium.

Results for the extinction coefficient of liquid uranium, given in Fig. 10-12, exhibit less scatter than those for the index of refraction, as was also found in the experimental results for tungsten. The results of Faldt and Nillson for the 0.4 to 0.5 μm region (and a sample temperature of 293 K) are given as well as more results from Weaver between 0.6 and 0.8 μm. Both n and k increase monotonically over the visible range, as was also observed for tungsten earlier.

10.6 The optical constants of liquid uranium over the entire spectral range (0.4 to 10 μm)

The optical constants of liquid uranium in the visible and infrared spectral ranges are given in Figs. 10-13 and 10-14. The figures include data obtained at visible and

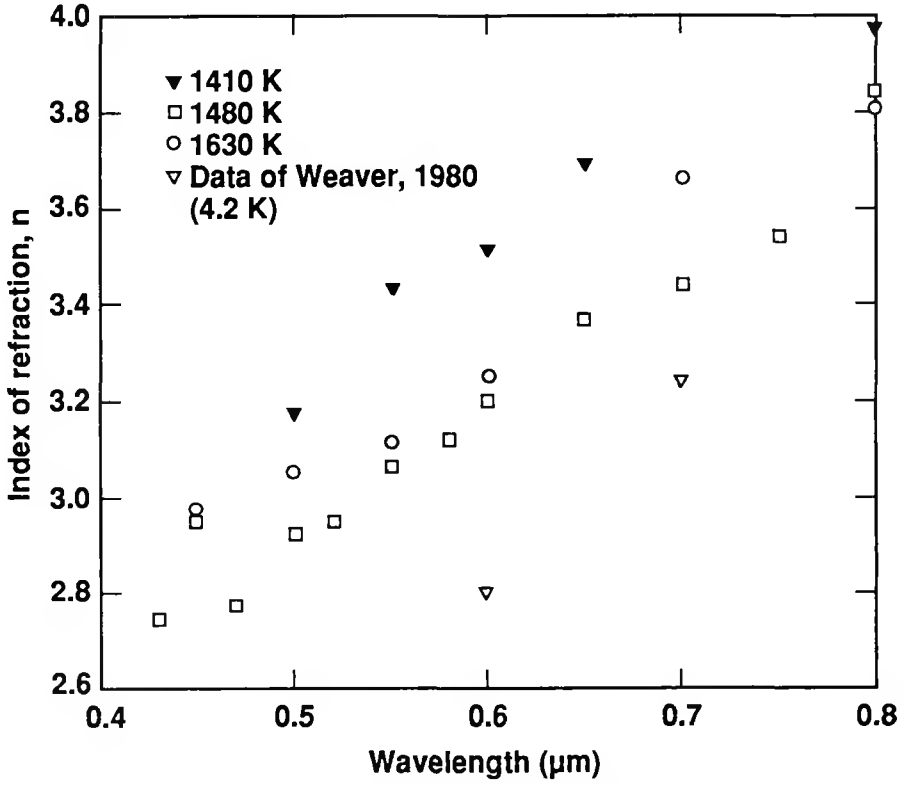

Fig. 10-11. The index of refraction of molten uranium in the visible spectral range.

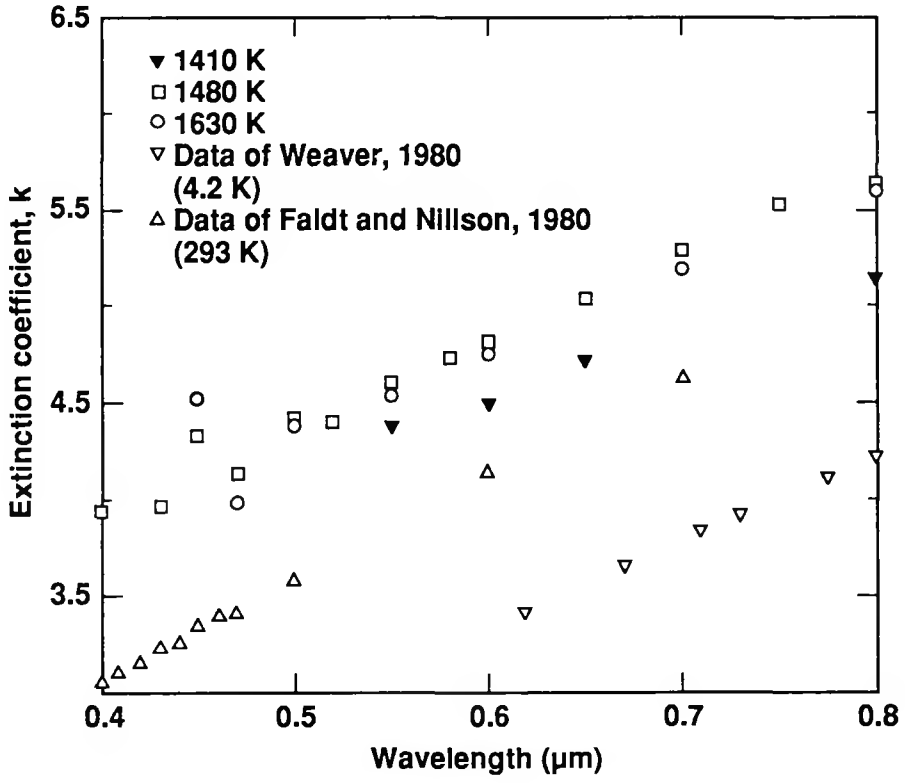

Fig. 10-12. The extinction coefficient of molten uranium in the visible spectral range.

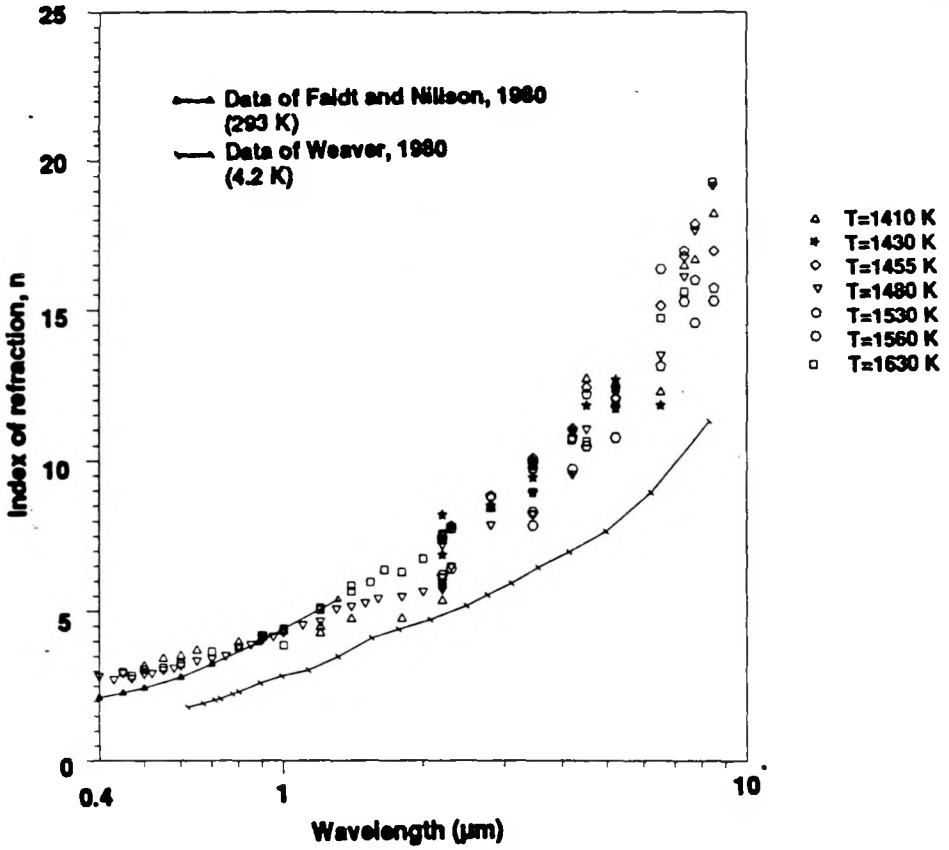

Fig. 10-13. The index of refraction of molten uranium.

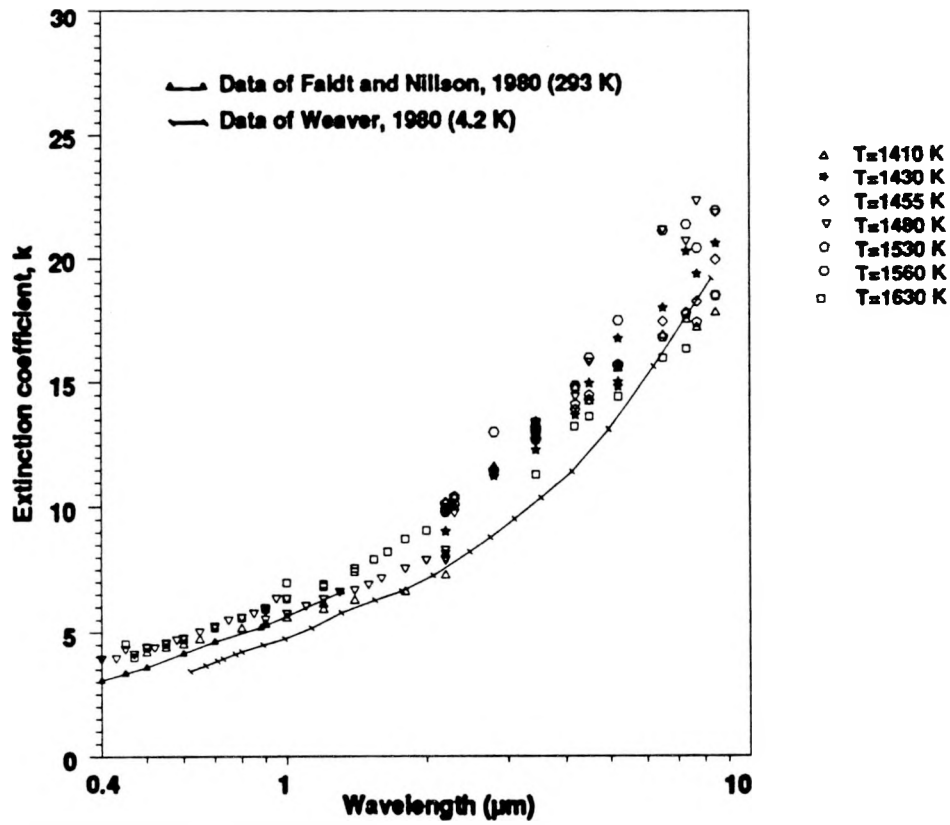

Fig. 10-14. The extinction coefficient of molten uranium.

infrared wavelengths for sample temperatures of 1410 K, 1480 K and 1630 K in addition to four sets of infrared measurements (2.8 to 8.5 μm) at temperatures ranging from 1430 K to 1560 K. The scatter in the results in the long wavelength region, which is as large or larger than the temperature dependence of the optical constants, is due to 1) the combination of optical effects (discussed in ch. 8) that produce declining signal to noise ratio and 2) declining measurement sensitivity with wavelength (discussed in chapter 7). The results of Faldt and Nilsson [160] and Weaver [159] are again given but their sample temperatures are so much lower that comparisons are of limited value.

The dominant aspect of Figs. 10-13 and 10-14 is the monotonic increase of n and k with wavelength which was not observed with tungsten until beyond 4 μm (for n) and beyond 1 μm (for k). Uranium is more "Drude-like" at shorter wavelengths but the low energy bound transitions first noted by Weaver exert sufficient strength to preclude good fits to the free electron picture. Computations using the Hagen-Rubens relation with two values for the resistivity, 64 μohm-cm (corresponding to the published value for molten uranium) and 73 μohm-cm (corresponding to the result of the fit to the ellipsometry data in Fig. 10-9) are compared to the measured results for n and k in Figs. 10-15 and 10-16. The Hagen-Rubens computations provide a good approximation for k over the entire measurement range but over estimate n significantly. The difference in slopes between the curve fits and the theoretical results for k in the 8 to 10 μm range is probably due to scatter in the data. The agreement in the slopes for n are excellent. Bound electron effects, although weaker in molten uranium than hot solid tungsten, are still significant.

10.7 The complex dielectric function of molten uranium at elevated temperatures

The results of the ellipsometric measurements of the optical constants of liquid uranium are given in terms of the optical conductivity and the real part of the complex

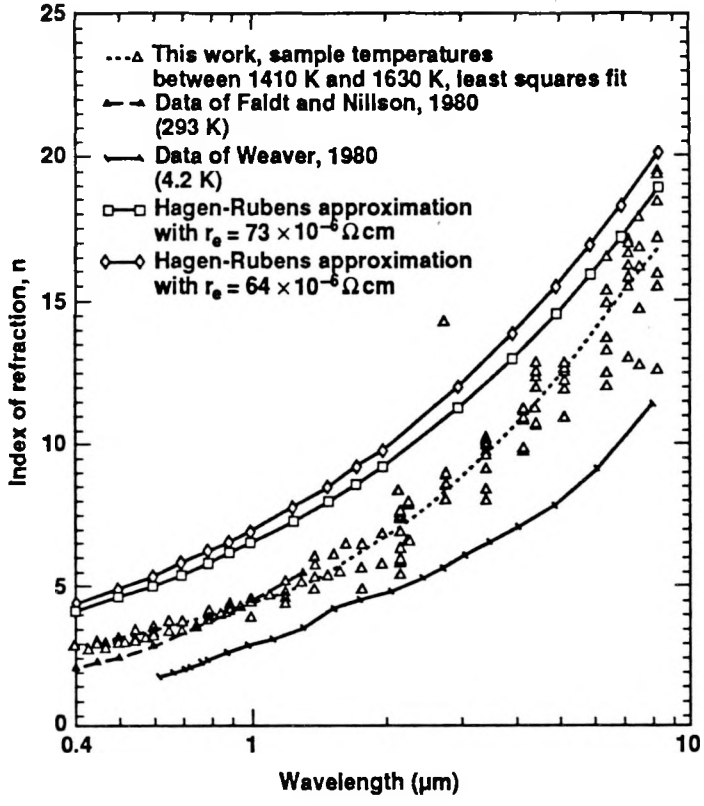

Fig. 10-15. The index of refraction of molten uranium vs the H-R approximation.

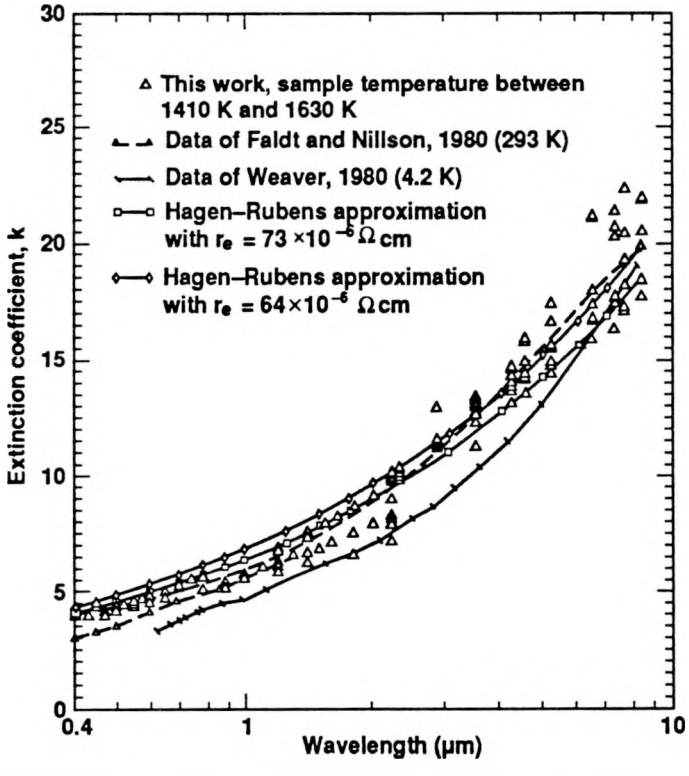

Fig. 10-16. The extinction coefficient of molten uranium vs the H-R approximation.

dielectric function respectively in Figs. 10-17 and 10-18. The relations between these constants and those used above (n and k) were given earlier (eqn 9-6). The squared and product terms in the relations for ϵ and σ cause the random errors (which were evident in results for n and k) to be amplified in presentations of ϵ and σ. This increased scatter in the results in this form was evident at long wavelengths with tungsten but is more severe here. Since the optical constant values are roughly similar for the two metals, the increased scatter is attributed to the liquid uranium surface being less stable mechanically than the solid tungsten surface.

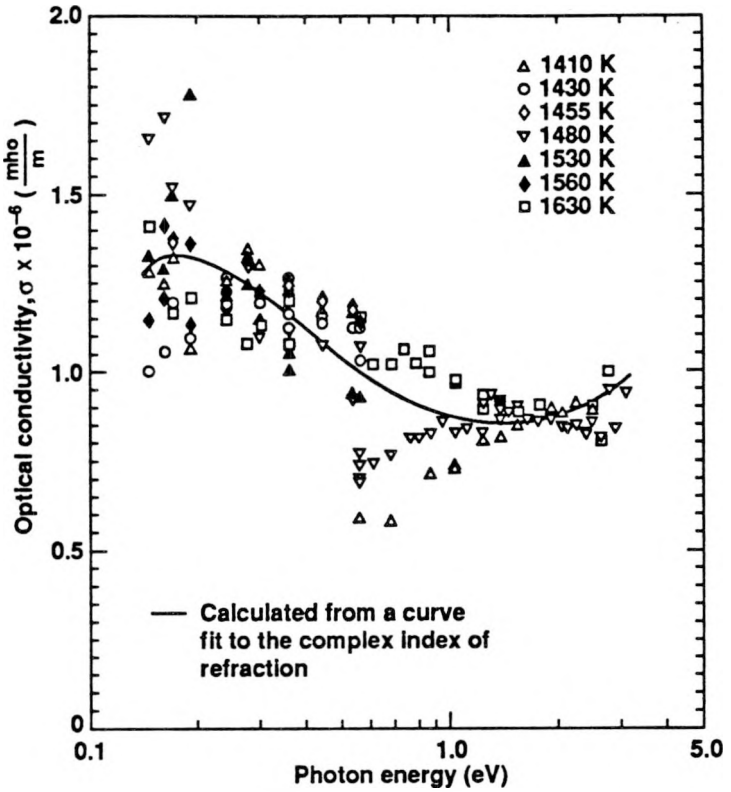

Fig. 10-17. The optical conductivity of molten uranium.

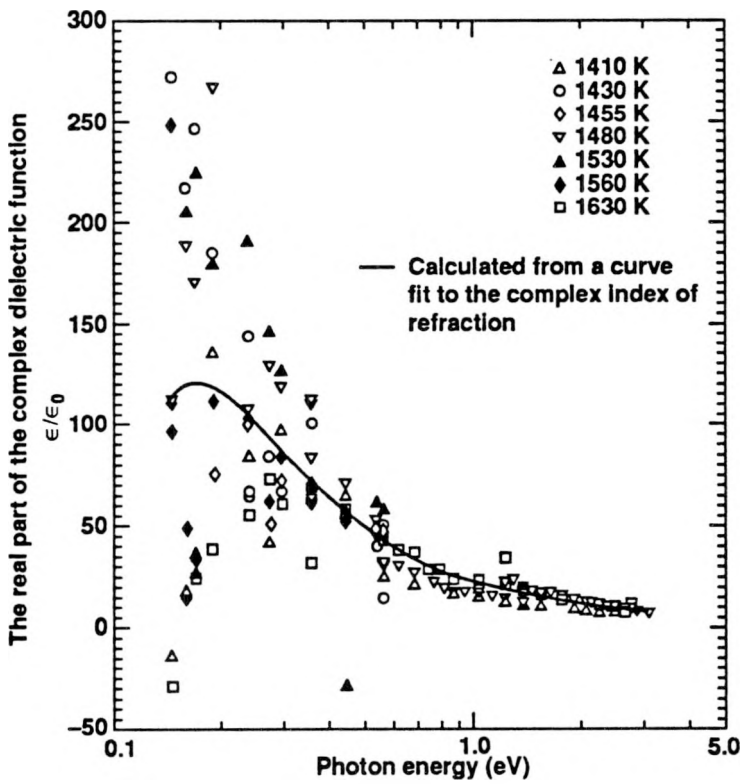

Fig. 10-18. The real part of the complex dielectric function of molten uranium.

11. Experimental results for the optical constants of molten aluminum

11.1 Background

The optical properties of metallic aluminum have been widely measured and analyzed to at least three distinct ends. First, the optical properties of aluminum combine both bound and unbound electron effects in ways which are inherently interesting. The wavelengths and strengths of the bound electron effects in aluminum have been investigated repeatedly. Second, the reflective properties of aluminum make it a much used mirror material. Aluminum reflectors with a protective overcoat provide high quality and stable performance over a wide wavelength band. Third, the thermal radiative properties of solid and molten aluminum influence the design and performance of many technical activities. These include smelting, casting, welding by TIG, E-beam and laser methods and thermal and E-beam evaporative sources.

Although the interpretation of the optical properties of aluminum has been recently summarized in detail in terms of intraband and interband quantum calculations [3], the presentation here will focus on the classical models described in chapter 3 because the properties of liquid aluminum in the wavelength range of interest here are adequately described from the classical viewpoint.

The decline of the importance of bound effects on the optical constants as temperature increases for solid aluminum has been well documented [191] and the disappearance of the most prominent absorption peak (the principal bound effect) at 1.5eV (0.8 μm) on melting was reported by Miller [4]. A classical approach (the Drude model) fits the optical constant data for liquid aluminum in the 0.4 to 10 μm range very well.

The results given here for molten aluminum cover a spectral range which was partially treated by two earlier investigations, but without the benefit of surface analysis.

Miller made measurements between 0.25 and 1.6 μm but was unsure if surface oxide effects made her deduced free electron density erroneous. Comins [5] made measurements in the infrared (3.9 to 8 μm) using a modified version of Miller's apparatus and then fitted his and Miller's data to the Drude model, apparently assuming that oxide effects were negligible. The new work reported here covers the 0.4 to 8.5 μm region (including the 1.6 to 3.9 μm band not treated earlier) with demonstrably clean surfaces and finds good agreement with both the data and the deduced parameters of the Drude fit given by Comins.

Aluminum proved to be a particularly difficult metal in this apparatus. Size constraints prevented using the same crucible material as Miller and Comins; Aluminum samples in alumina crucibles gave sessile drops. Niobium proved barely adequate as a material for containing aluminum: no alloying with the sample was observed but with increasing exposure time and temperature, the molten metal would creep across the top of the crucible to the vertical edges and then drain over the side. Stable signal levels from the ellipsometric optical system were difficult to achieve. Early in the life of the crucible, the migration of aluminum across the niobium surface beside the molten metal pool was significantly slower than in the later experimental work. Unfortunately the later work included the infrared ellipsometry, where signal levels and sensitivity also worked to the detriment of measurement precision. For these reasons the ellipsometric results for molten aluminum at wavelengths in excess of 2.2 μm are not as reliable as those given earlier for tungsten and uranium. Fortunately, the 0.4 to 2.2 μm band was sufficiently broad to be fitted to the Drude model, and the Drude parameters obtained here are in good agreement with those of Comins (using both his own and Miller's data).

The fact that molten aluminum fits a Drude model well for wavelengths in the visible and longer means that the Drude parameters determined from calcite polarizer ellipsometry (0.4 to 2.2 μm) completely specify the optical constants and thermal radiative properties of molten aluminum in the entire wavelength range of interest (0.4 to

10 μm). Using only an optically determined free electron density, N_e, and a collision time for electrons, τ, the emissivities, absorptivities and reflectivities needed for heat transfer calculations are fully specified.

Experimental difficulties limited the range of sample temperatures achieved. Several sputter guns were rendered inoperative by aluminum vapor condensed on their high voltage insulators. Because the vapor pressure of aluminum increases rapidly with temperature, 1030 K was taken as an upper bound. Lower temperatures were also preferred because molten metal creep, noted above, increased with sample temperatures, presumably due to the decrease of surface tension with temperature. In summary, although both the wavelength and temperature ranges of the data are more limited than for uranium, the spectral range of the deduced results is at least as wide. The good fit to the Drude model has given the radiative properties over the full range of interest.

11.2 Surface mass analysis of liquid aluminum samples

As with the molten uranium studies, the cleanliness of the aluminum samples was determined in-situ by Auger spectroscopy just prior to and just after each set of optical measurements. Separate argon ion sputter guns (5 kV each) produced and maintained the surface purity at the optics and surface analysis positions. The operating parameters of the sputter guns and the Auger spectrometer were given in chapter 8.

The impurity content of the aluminum surfaces was negligible during all optical work. During sample preparation, oxides were removed by sputtering. Figure 11-1 shows an Auger spectrum for a typical sample of "clean" liquid aluminum . The aluminum peaks are noted on the figure and the location of an oxide peak is marked but not present. Since oxides float to the sample surface and the Auger spectrometer samples the mass constituents of the top ~10 to 20 Å of the surface, it is clear that the samples were oxide free.

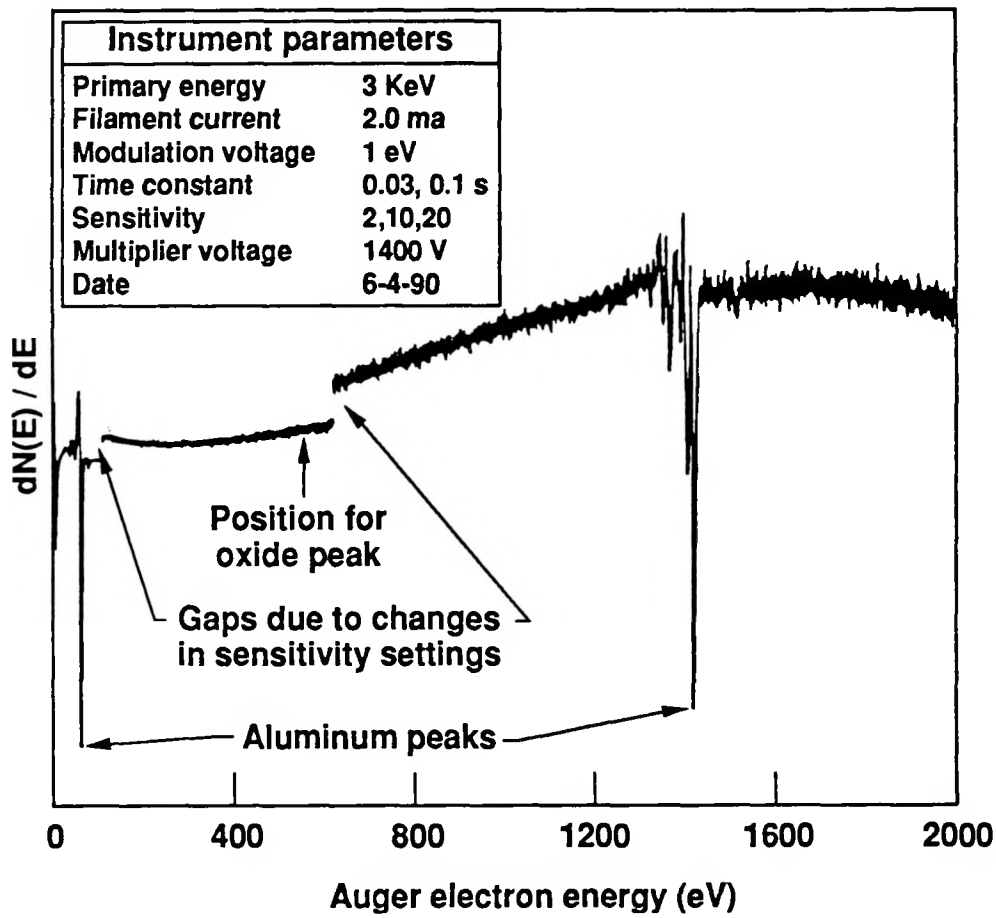

Fig. 11-1. Auger spectrum for a typical liquid aluminum sample.

11.3 The normal spectral emissivity of molten aluminum as a function of wavelength

Accurate direct measurements of normal spectral emissivity were not obtained with aluminum because of a combination of the following four factors:

1) Aluminum condensed on the CaF_2 window.
2) Sample temperatures were moderately low.
3) The emissivity of aluminum is relatively low.
4) Aluminum metal migrated into the blackbody cavity and lowered its apparent emissivity.

Thus, only ellipsometric measurements of normal spectral emissivity (in the temperature range 940 to 1030 K) are shown in Fig. 11-2. Wavelength and temperature effects are important in these data. First, the emissivity decreases with wavelength as expected from the free electron model. (Since n and k increase monotonically with wavelength, reflectivity increases uniformly.) Second, at the long wavelength extreme, no consistent variation in emissivity with temperature is present. As discussed in preceeding chapters, the Hagen-Rubens relation predicts emissivity increasing with temperature through the direct current resistivity:

$$\varepsilon_n(\lambda) = 0.365\sqrt{\frac{r_e}{\lambda}} - 0.0464\,\frac{r_e}{\lambda} \qquad (11\text{–}1)$$

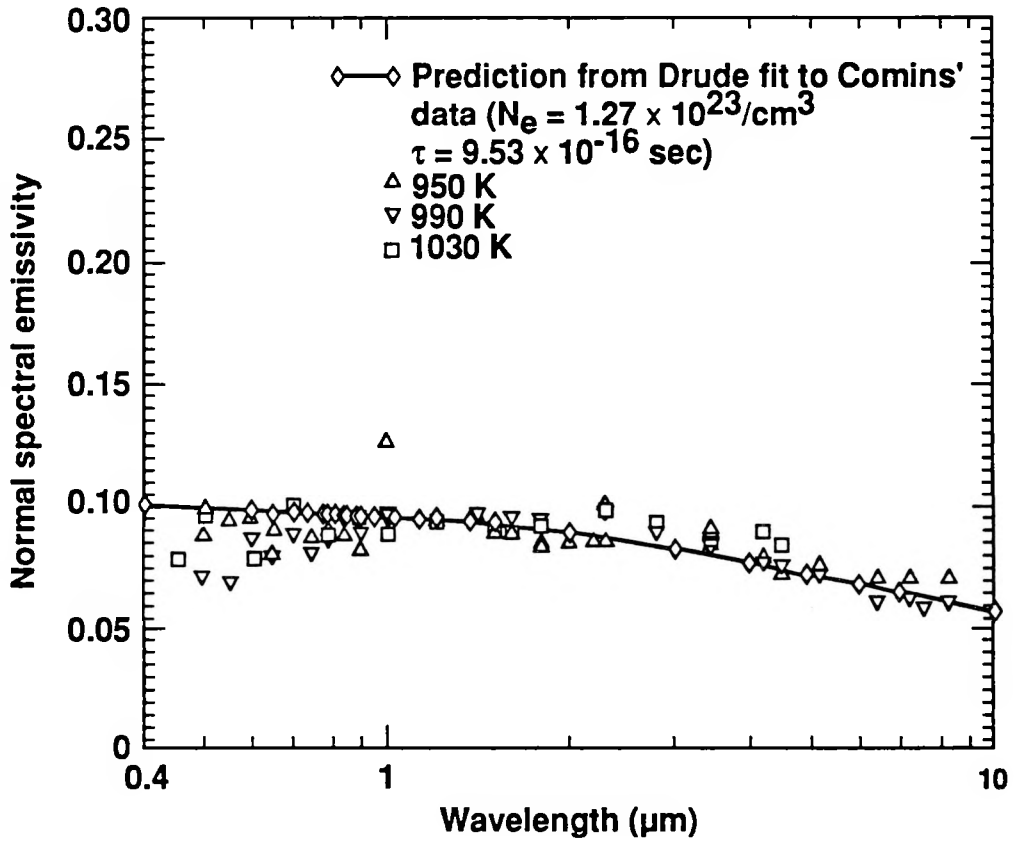

Fig. 11-2. The normal spectral emissivity of molten aluminum.

However, using the variation in resistivity with temperature reported by Guntherodt and Kunzi [192] a change in the normal spectral emissivity of only 0.002 (from 0.060 to 0.062) would be expected from a temperature rise from 940 to 1030 K.

Calculations using the Drude parameters of Comins [5] and those of this work are given in Fig. 11-3 and contrasted to the room temperature emissivity taken from several sources and reported by Smith et. al. [166]. Comins gave $N_e = 1.27 \times 10^{23}$ cm^{-3} and $\tau = 9.5 \times 10^{-16}$ sec while a least squares fit to the Drude relations (eqn. 3-16) using the data from this work (for wavelengths less than 2.25 μm because the longer wavelength measurements display too much scatter) gives $N_e = 1.38 \times 10^{23}$ cm^{-3} and $\tau = 9.35 \times 10^{-16}$. (When ellipsometry measurements out to 8.45 μm are included in the fitting calculations, the values $N_e = 1.24 \times 10^{23}$ cm^{-3} and $\tau = 7.85 \times 10^{-16}$ are obtained.) The agreement between the two sets of results shown for liquid aluminum is good, especially considering the different sample temperatures. Using the resistivity results noted above and the Hagen-Rubens approximation, one expects an increase in normal spectral emissivity of 0.003 at 10 μm when the sample temperature rises from 970 to 1170 K. The difference in the two "Drude metal" fits to the molten metal data is 0.0016 at 10 μm. Thus, the small difference in the two sets of results is about half as large as might have been expected from the the Hagen-Rubens relation.

11.4 The complex index of refraction of pure molten aluminum between 0.4 and 10 μm

The agreement of the Drude fits of Comins and the present work suggests that the thermal radiative properties in the normal direction have been well determined. However, the two components of the refractive index must be given for a complete specification of radiative properties at angles departing from the normal. The influence

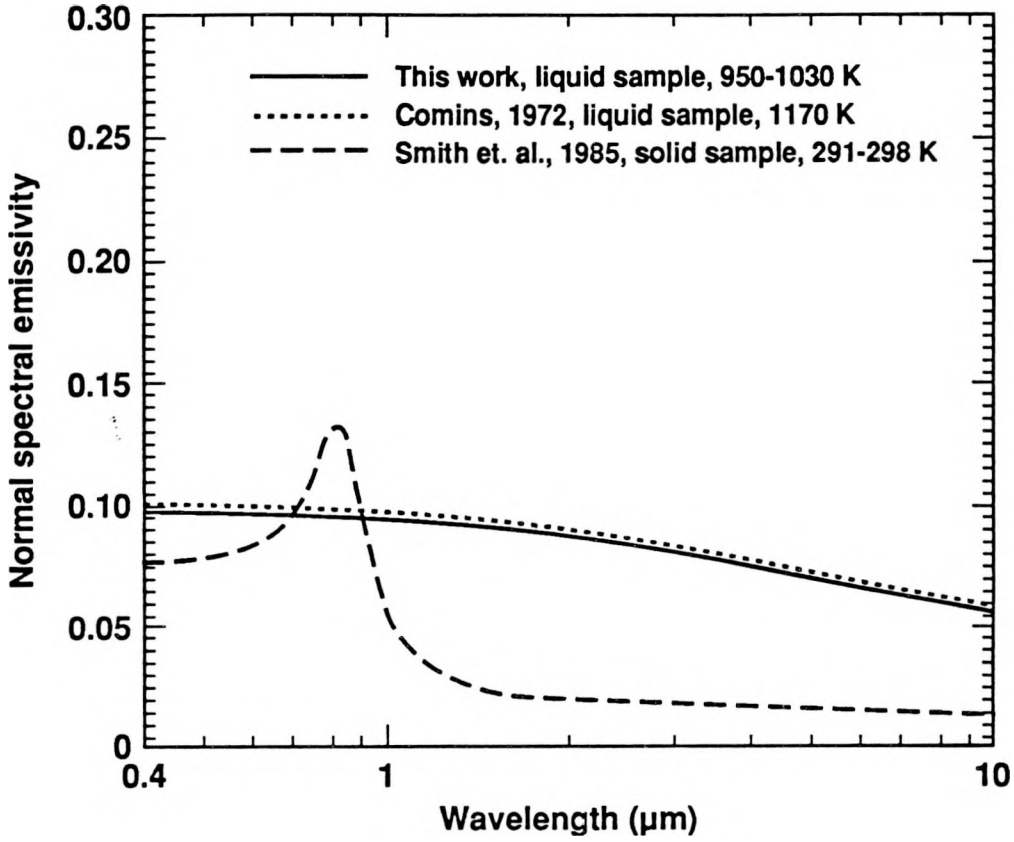

Fig. 11-3. The normal spectral emissivity of solid and molten aluminum calculated from published optical constants.

of n and k on the oblique reflectivity was shown in chapter 9 for n,k pairs appropriate for tungsten.

The variations of n and k with wavelength for liquid aluminum are given in figures 11-4 and 11-5. The points shown are the results of ellipsometric work over the full wavelength range of interest but the curve was derived by fitting only the data for wavelengths between 0.4 and 2.25 μm to the Drude model. The qualitative variation of both n and k is consistent with the free electron picture for three reasons. First, both n and k increase monotonically. There is no structure to the variation of either n or k which would indicate bound electron effects. Second, k is everywhere greater than n. Both these features were described in connection with the Drude model in chapter 3. Third,

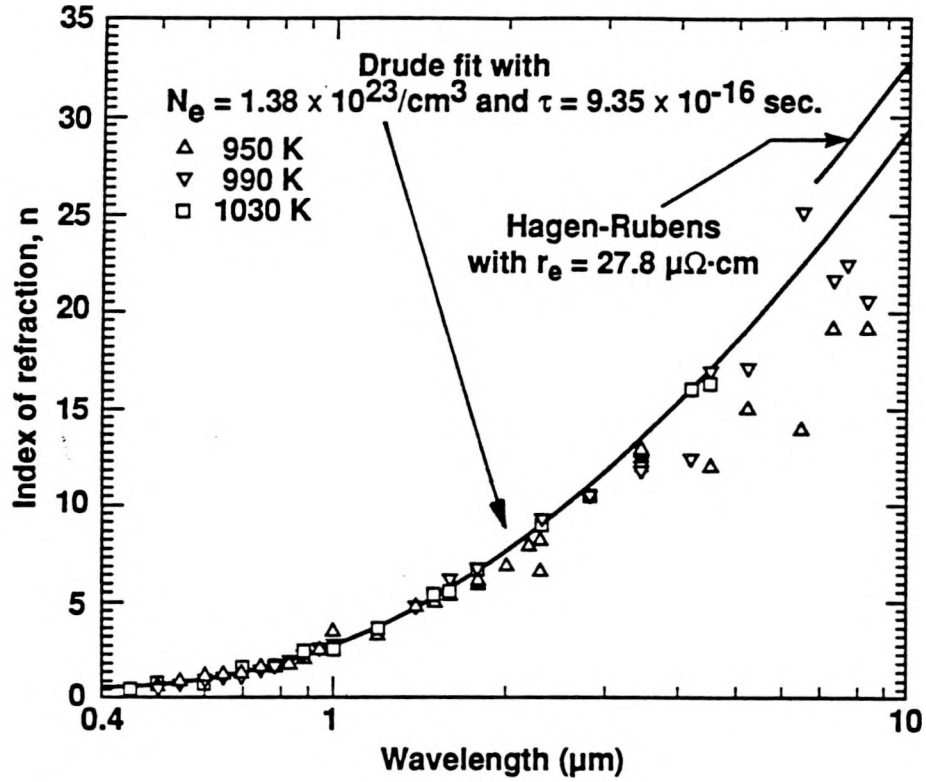

Fig. 11-4. The index of refraction of molten aluminum.

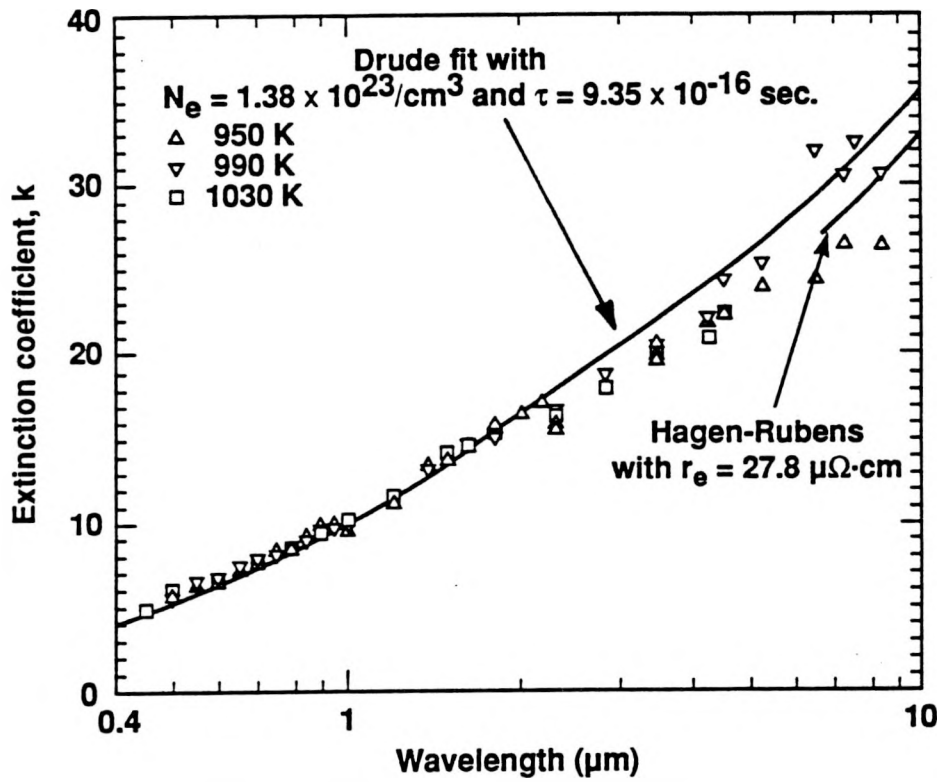

Fig. 11-5. The extinction coefficient of molten aluminum.

beyond ~3 μm, n converges toward k: the Hagen-Rubens limit of the Drude model gives n = k at very long wavelengths.

The Drude fit to the molten aluminum data of the present work is compared to that of Comins in Figs. 11-6 and 11-7. The variation in extinction coefficient predicted by the two curves (Fig. 11-7) are in good agreement. As with the normal spectral emissivity discussed above, the differing sample temperatures are a concern. At long wavelengths the Hagen-Rubens relations predict both n and k declining with temperature. For a wavelength of 10 μm, a change in n or k of 1.9 (from 34.9 to 33.0) is predicted for a sample temperature rise from 970 to 1170 K.

The variation in k for room temperature aluminum, also given in Fig. 11-7, contrasts strongly to the results for liquid. The elimination of bound electron effects (principally at 0.8 μm) was necessary for the liquid results to fit the free carrier model.

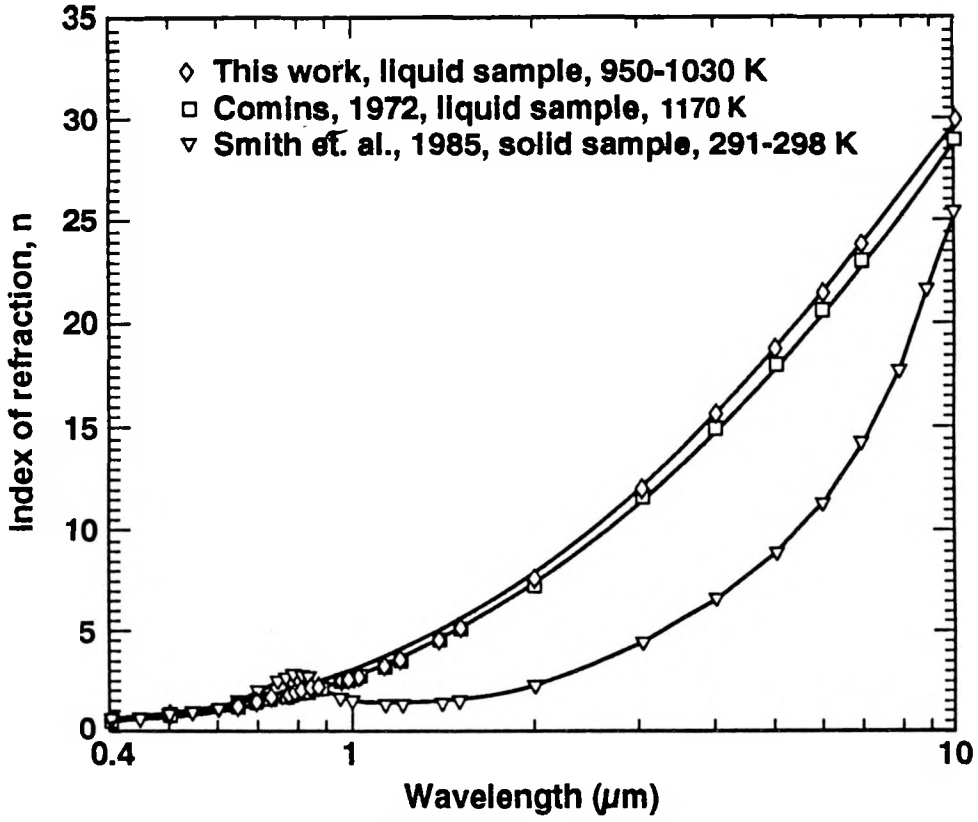

Fig. 11-6. Comparison of published results for the index of refraction of aluminum.

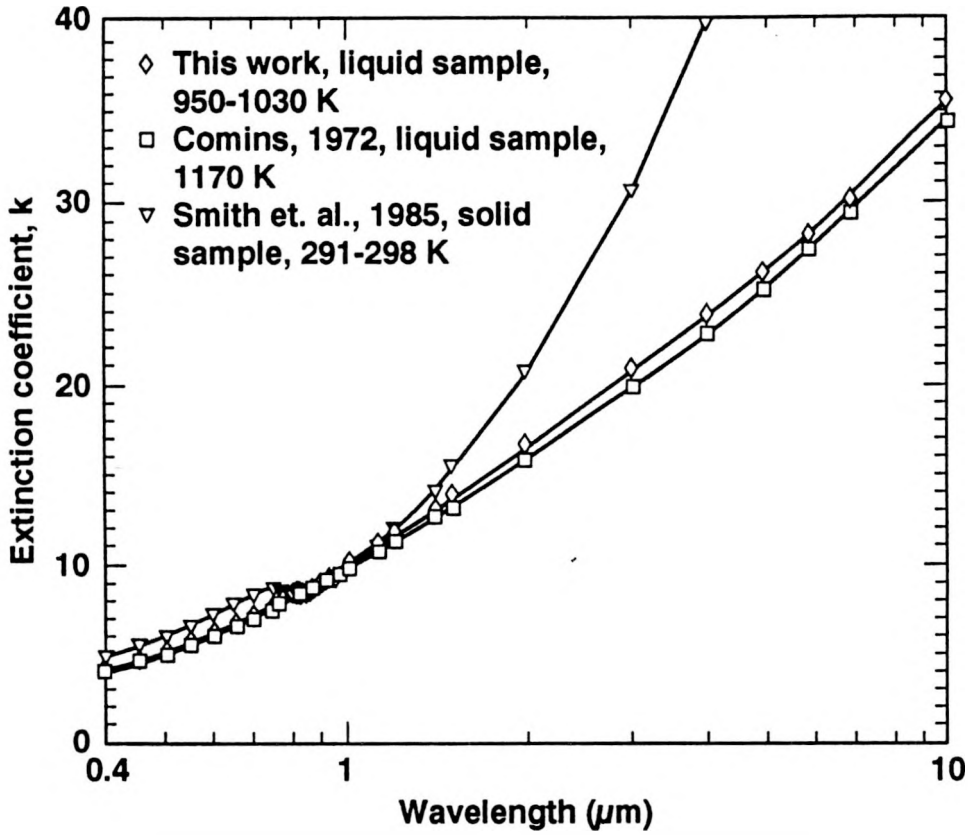

Fig. 11-7. Comparison of published results for the extinction coefficient of aluminum.

The variation in index of refraction for the two Drude fits and the room temperature work (all given in Fig. 11-6) lead to similar observations as were given above concerning the variation in k. The structure in the variation for both n and k with room temperature material resembles that shown for the Lorentz model with a single bound charge.

11.5 The complex dielectric function of pure molten aluminum between 0.4 and 10 μm

The real part of the complex dielectric function, ϵ/ϵ_0, and the optical conductivity are given in Figs. 11-8 and 11-9 as functions of photon energy. As above, the data for all wavelengths is shown but the curves were derived from least squares fits to the Drude model using data for wavelengths less than 2.25 μm. The variations of both

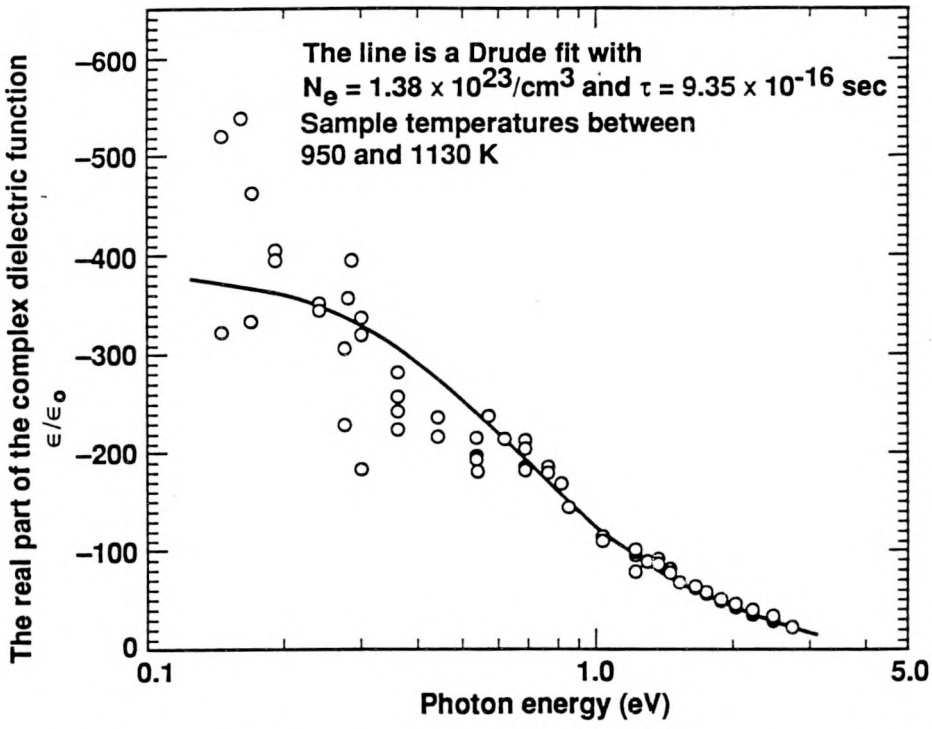

Fig. 11-8. The real part of the complex dielectric function of molten aluminum.

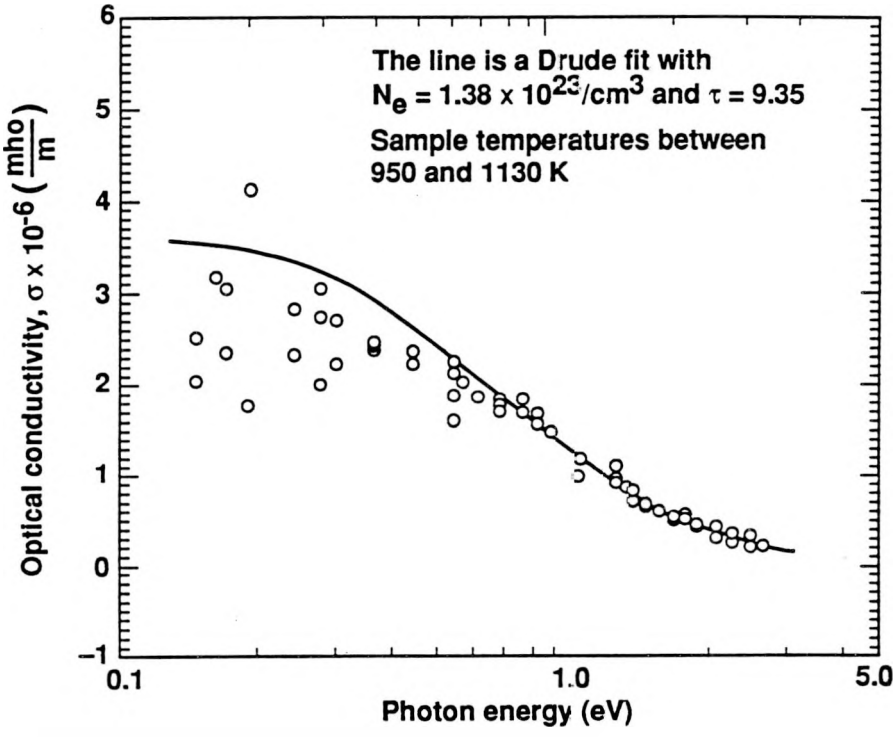

Fig. 11-9. The optical conductivity of molten aluminum.

ϵ and σ for the Drude fits correspond closely to that shown for a typical "Drude metal" in chapter 3. Variations in both ϵ/ϵ_0 and σ with temperature are small for wavelengths below 2.2 μm, as indicated by the spread in the results for the three temperatures noted. Thus it is reasonable to fit all of the data points to a single pair of Drude parameters.

The Drude fit given by Comins is compared to that of this work in Figs. 11-10 and 11-11. For both figures the agreement is good at higher photon energies and less close for lower energies (long wavelength). This condition is a consequence of the present work lacking precision at long wavelengths.

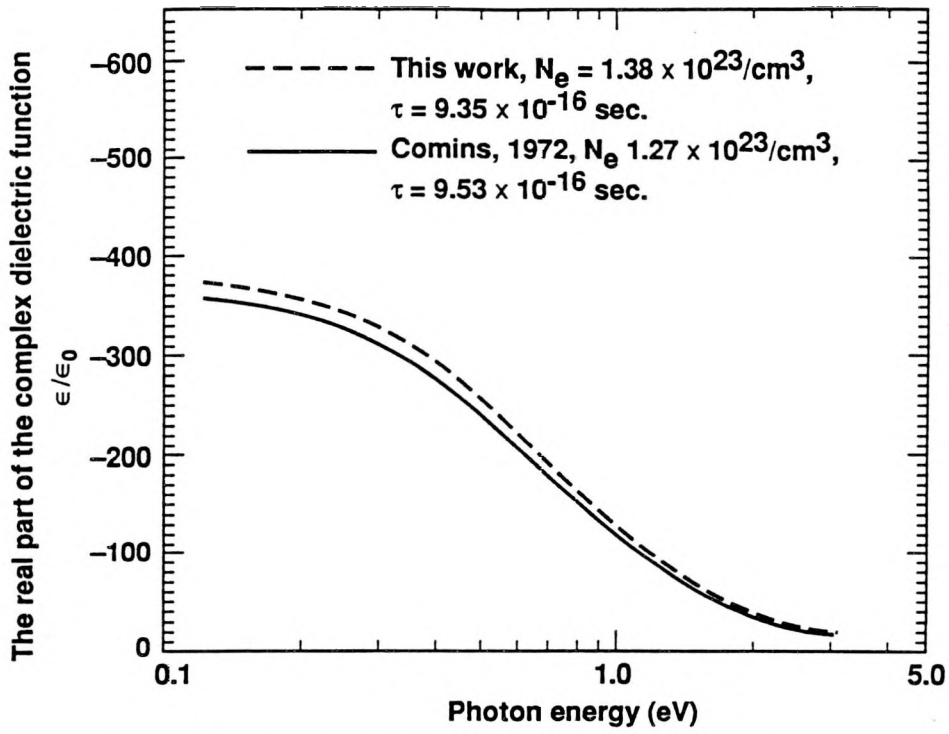

Figure 11-10. Comparison of published results for the real part of the complex dielectric function deduced from the Drude parameters for molten aluminum.

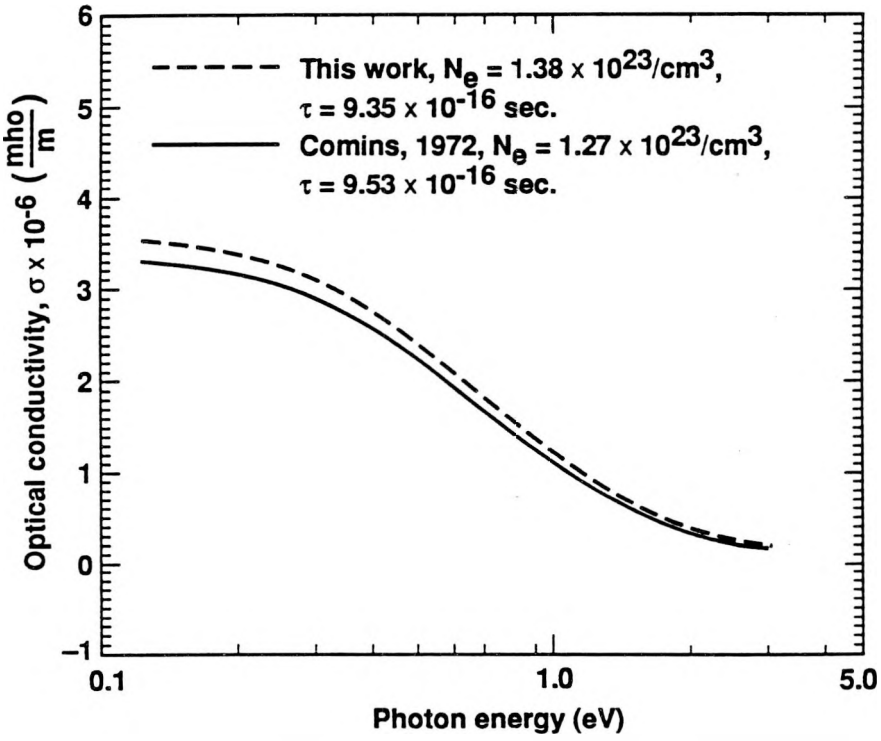

Fig. 11-11. Comparison of published results for the optical conductivity deduced from the Drude parameters for molten aluminum.

12. Summary and conclusions

12.1 Focus of the work

This study's original goal was simply to obtain the thermal radiative properties of liquid uranium. The influence of these properties on the performance and economic viability of the Laser Isotope Separation process for uranium enrichment warranted significant expenditures of time, money and effort. However, a review of typical results for the thermal radiative properties of many common metals revealed a need for improved experimental approaches within the entire field. Thus, a more general perspective and a more widely useful set of goals were formulated. These goals were:

1) To devote sufficient equipment and care to control and characterize the sample surface condition so that measurements could be reported on known samples.

2) To design and use multiple redundant measurement techniques so that unbiased error estimates could be made.

3) To use the most general measurement techniques practical over a wide wavelength range so the results could be useful to as many technologies, materials and situations as possible.

The first goal reflected a desire to minimize errors due to surface contamination or other surface effects. Such errors are widespread in published results for the thermal radiative properties of metals. The second goal reflected a desire to accurately quantify measurement errors. The wide scatter between published results in this field often exceeds

the error bars, no doubt sometimes due to undetected systematic errors as well as to variable surface contamination. The third goal reflected a desire to get complete results for as many applications as possible. Many results in this area are very limited; often only the normal spectral emissivity at a single wavelength for a material is given. Energy balance computations performed for process development almost always require a more complete specification of radiant characteristics. In many laser and electron beam processing applications there are two characteristic temperatures. Very high temperatures (2000 K to 4000 K) may be attained so that visible optical emission is dominant in regions where very high heat fluxes are delivered to the material. Cooler regions (700 K and lower) where infrared emission is dominant characterize regions somewhat removed from the high heat flux regions. Construction of a spectrally broad band instrument with good sensitivity for obtaining the optical constants insured that the results would be widely useful for detailed process development calculations.

12.2 Capabilities of the apparatus

Many of the unique features of the apparatus developed in this work and described in chapter 8 constitute advances over methods commonly used to measure the thermal radiative properties of metals. Some capabilities of the apparatus are common to other specific areas of inquiry but their combination with other features of this apparatus makes it uniquely suitable for determining thermal radiative properties at high temperatures with greater certainty than had previously been obtained. The principal features of the apparatus are:

1) Ultra high vacuum (~5 x 10^{-10} torr) is maintained, which is instrumental in producing and maintaining sample purity.

2) Auger spectroscopy is used in-situ to obtain surface mass composition. Unlike previous work in this area the sample itself is known with certainty.

3) Ion sputtering is used to remove surface contamination. Solids form surface impurity layers when exposed to ambient and contaminants often float to the surface when metals are melted.

4) Direct measurements of normal spectral emissivity can be made using an integral blackbody technique over the wavelength range 0.4 to 10 μm and for sample temperatures from 900 K to 1630 K.

5) Spectroscopic ellipsometric measurements can be made with an angle of incidence of 75^{o}. This optical system allows determination of the complex index of refraction of pure metal substrates over the spectral range given above, although precision decreases with wavelength past ~3 μm due to declining detector responsivity, chromatic aberration and declining radiation source output. Sample temperature can vary from ambient to 1630 K.

The combination of the five features listed above make this instrument capable of forming pure metal surfaces and then measuring their optical constants and thermal radiative properties. Unbiased error estimates are computed by comparing the results of two independent measurement systems. The instrument has been used with 3 metals of significant technical importance, tungsten, uranium and aluminum. The results and their relation to prior work and theoretical relations for the optical properties of metals are summarized in the next section.

12.3 Summary of experimental results

12.3.1 Tungsten

Comparisons between the present work and earlier work on the optical and radiative properties of high temperature tungsten were very favorable over the entire spectral range of interest. The somewhat lower precision in the results of the present study for the normal spectral emissivity and both components of the complex refractive index was an expected consequence of the compromises necessary to allow measurements on liquid metals with surface science capabilities.

The measured optical properties of high temperature tungsten display the effects of both bound and free electrons as noted in earlier work. Both n and k increase monotonically with wavelength beyond ~5 μm, due to free electrons. At shorter wavelengths the structure in the results for n and k indicates bound electron effects.

The dependence of the normal spectral emissivity on wavelength showed good agreement with earlier work despite the inevitable differences in sample preparation. As expected from the indication of bound electron effects noted earlier, neither the Hagen-Rubens relation nor the Drude relations for the optical constants could be fitted to the measurements.

12.3.2 Uranium

The data for the normal spectral emissivity of molten uranium determined using the two methods displayed excellent agreement over the entire spectral range of interest. Although, the Hagen-Rubens relation's prediction of normal spectral emissivity based on the measured resistivity of liquid uranium showed better agreement with the data than was observed with tungsten, the long wavelength asymptote clearly does not apply

here because of the inequality of the two measured components of the complex refractive index. Only as n and k approach equality are the optical and radiative properties rigorously given by a single parameter, the direct current resistivity.

The combination of a weak dependence of the complex index on temperature and a moderate range of test temperatures (1400 K to 1630 K) prevented determination of a dependence of n and k on temperature. It would be both interesting and valuable to engineering development work to obtain this dependence at elevated temperatures (to ~4000 K). However, another sample heating system is required for such work and condensing uranium would damage the optics and surface science equipment.

12.3.3 Aluminum

The optical constants and thermal radiative properties of liquid aluminum determined by ellipsometry here are fit well to Drude model relations. Although experimental difficulties with the sample molten aluminum surface greatly decreased the precision of the measurements in the long wavelength portion of the infrared, the measurements from 0.5 to 2.25 μm were sufficient to determine the two Drude parameters with high accuracy. Good agreement was obtained for these two parameters between values from this work and those obtained by Comins [5] using both his own data and that of Miller [4]. The goodness of fit to the Drude equations means that the two Drude parameters completely specify the thermal radiative properties of molten aluminum over the entire wavelength range of interest for many engineering development activities such as those noted earlier.

Comparisons between the two independent measurement systems such as those given earlier with tungsten and uranium were not made with aluminum because the low sample temperatures of this work prevented accurate direct measurements of normal spectral emissivity. Higher sample temperatures would have given better signal to noise

ratios but the high vapor pressure of aluminum led to coating of the optical access ports and the surface science tools.

12.4 Directions for future work

Additional work with pure liquid metals is needed. Most metals have not been fully treated in the temperature and spectral ranges of interest to engineering development work. The rare earth Lanthanides are almost completely unstudied and their melting points and vapor pressures are ideally suited to this apparatus. The lanthanides are of interest to a particular technology in development at the Lawrence Livermore National Laboratory and studies of them have been initiated.

Very little work has been done on the optical radiative properties of molten alloys. Low melting point combinations using tin, lead, mercury and gallium have been treated but high melting point alloys used in welding applications need study. Interpretation of the variation of optical properties with alloy composition and wavelength would be challenging.

Future work with the present apparatus may also involve modification of its optics to improve precision in the infrared spectral range. A greater angle of incidence would improve sensitivity but would require changes to the vacuum chamber. Reflective rather than transmissive optics would eliminate chromatic aberration and increase signal strength in the infrared but would also introduce unwanted polarization. At present, errors are highest between 3 and 10 μm. Although precision is excellent on the short wavelength side of this range and the Hagen-Rubens relation often gives good estimates of the long wavelength asymptote of the optical properties, the importance of this intermediate range to many applications may warrant testing with mirrors rather than the calcium fluoride windows now installed. For studies of the complex dielectric function of metals rather than their thermal radiative properties greater precision is certainly required.

The apparatus in its present form will also be used for measuring the thermal radiative properties of many common engineering materials. Although some instruments can give particular radiative properties in narrow spectral bands with less random error, the surface science and broad band capability of this apparatus make it more precise in a general sense. More than 10 solid materials of interest to various development activites at LLNL have been measured to date and more will be studied in the future.

Appendix A
Calculations of Heat Transfer in the Crucible

A.1 Purpose

Heat transfer in the crucible is important for its influence on errors in measurements of normal spectral emissivity. Errors due to thermal effects can arise due to a temperature difference between the sample and the integral blackbody cavity or due to non-ideal emission from the integral blackbody cavity. Reported efforts to estimate these effects have considered them seperately. Often the apparatus justifies such an approach, as with the hole-in-tube method where the thickness of the tube is only ~0.005" or less and therefore errors due to temperature gradients are negligible. However, in this apparatus part thickness is much larger and significant temperature gradients within the blackbody cavity itself are expected. Errors due to the two effects noted above then combine in a complex way to determine total error. Although specific in that it is relevant only to the cavity and crucible geometry defined here, the analysis is general in that it considers these effects together and estimates error on a normal spectral basis rather than the more common but limited normal total or even total hemispherical basis.

In order to consider all the non-ideal thermal effects noted above, with a crucible geometry void of symmetry, finite element methods were required. Although simpler analytical approches were possible for individual thermal effects only a fully three dimensional finite element model of the crucible could practically estimate the interaction of all of them together.

A.2 The model

The crucible geometry and its representation in a finite element mesh are given in Figs. A-1 and A-2 respectively. The blind hole on the right hand side of Fig. A-2 is the blackbody cavity. The mesh is more finely divided in the region surrounding the cavity to better resolve the temperature gradients there. A bottom view (Fig. A-3) shows the

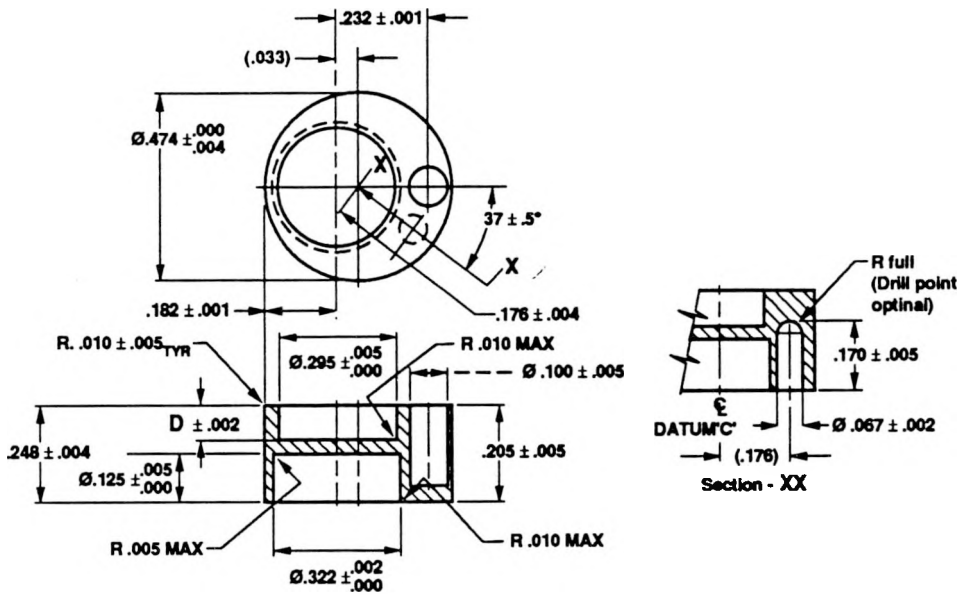

Tab No.	Dim. D
-01	0.01
-02	0.02
-03	0.04
-04	0.06
-05	0.09
-06	0

Figure A-1. The crucible geometry.

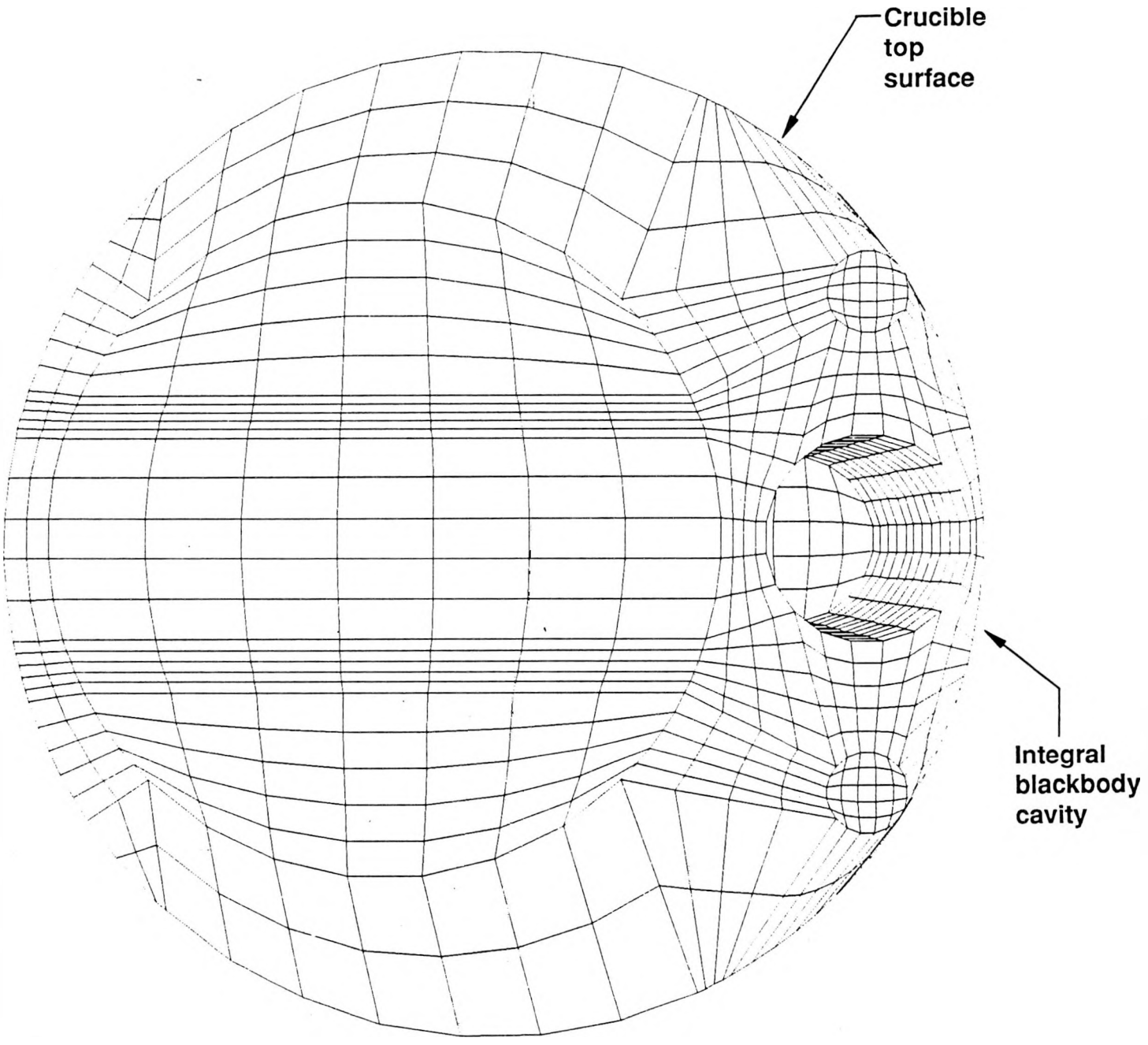

Figure A-2. A top view of the finite element mesh.

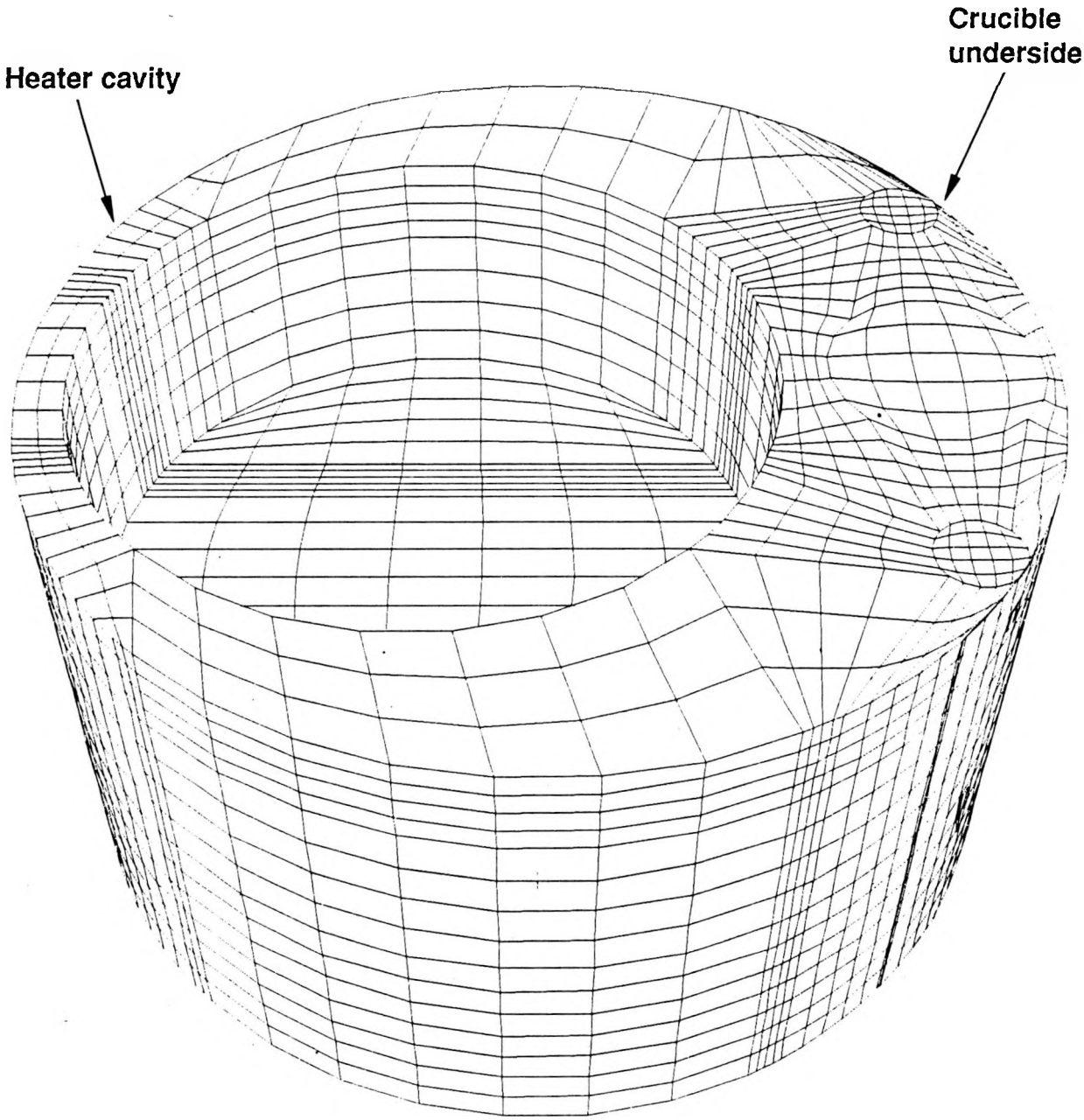

Figure A-3. A bottom view of the finite element mesh.

underside of the mesh and the heater cavity. Heat loss from the crucible to the surroundings is modelled by radiation boundary conditions on the top, bottom and side surfaces of this model:

$$q'' = F_{12}\,\sigma\,(T_1^4 - T_2^4) \qquad \text{(A–1)}$$

Where F_{12} is the radiative exchange coefficient for radiation from the crucible surface, T_1 to the cooler surroundings, T_2. The surroundings are the walls of the vacuum chamber (T ~ 300 K) and F_{12} was determined using the assumption that the radiating surface was small compared to the much larger enclosure.

The surfaces of the blackbody cavity are coupled to crucible conduction and to each other by diffuse radiant exchange using a view factor matrix [25] . The diffuse assumption is reasonable since the surfaces of the cavity are coated by aquadag. Heat gain to the crucible from its heater is modelled by heat flux or temperature boundary conditions on the surfaces of the heater cavity.

A.3 Results

Figure A-4 gives the crucible temperature profile resulting from this mesh, boundary conditions and representative tungsten properties [thermal conductivity = 0.84 w/cm K and ε (hemispherical,total) = 0.17]. The mesh slice shown is through the center of the blackbody cavity and the temperatures noted are the highest value present within the band of the corresponding type of shading. The blackbody cavity shows a significant temperature variation, including a relatively cool extreme edge. This slice is the most pessimistic in the sense that it includes the position on the cavity which is

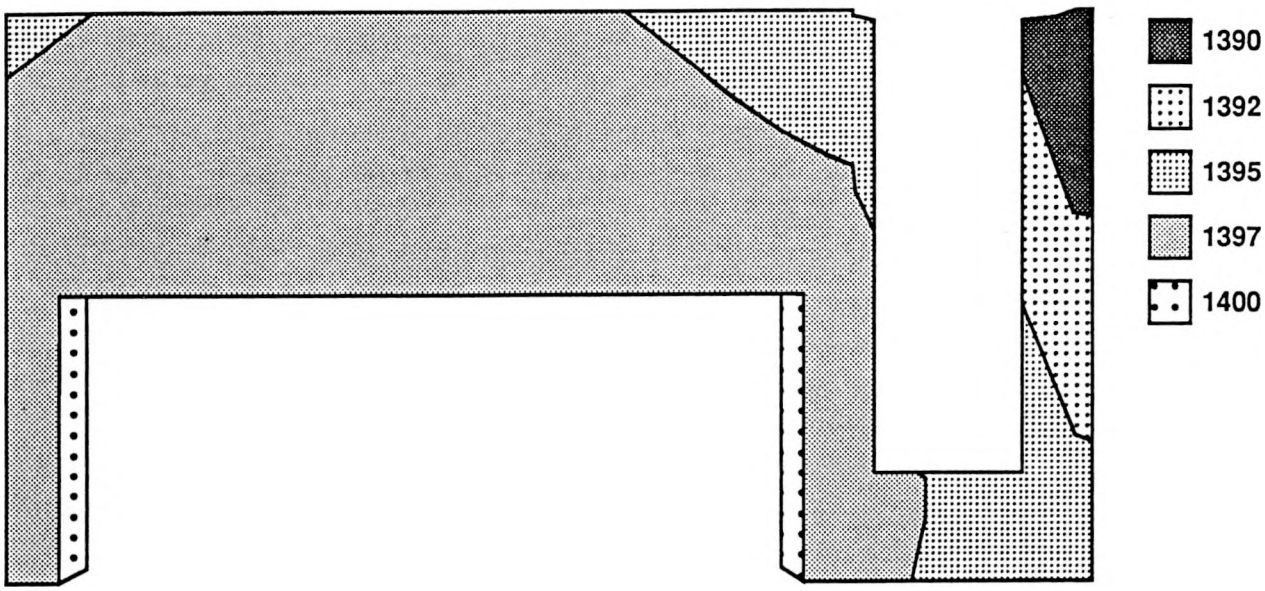

Figure A-4. Temperature contours for representative conditions. Temperatures noted are in K and are the highest value present within the band of the corresponding type of shading. The slice shown is a cut through the center of the crucible.

furthest from the heat source. Slices through other portions of the cavity are closer to the heater cavity and their conductive connection to it is better (the part is thicker there).

To estimate measurement errors due to conductive and radiative effects in the crucible and cavity, a fourth power average of the temperature distribution in the blackbody is required (only a portion of which is shown in Fig. A-4). Ideally, one would obtain the spectral emissive power into the normal direction (defined as the normal to the opening of the cavity) from each of the surfaces of the model of the blackbody cavity. Such an approach is not computationally practical, so the heat radiated out of the cavity to a surface above the cavity which subtended a solid angle comparable to that of the folding mirror (see Fig. 8-12) was computed using the cavity temperature profile. This calculation was then repeated but with the cavity walls given an emissivity of unity and a uniform temperature equal to that of the center of the top surface of the crucible (i. e. the sample measurement point). The ratio of these two heat loads is an estimate of the normal total apparent emissivity of the blackbody cavity (particular to the boundary conditions specified):

$$\varepsilon_a\,(\text{normal,total}) = \frac{Q\,(\text{normal,total})\,|_{\text{gray,non-isothermal}}}{Q\,(\text{normal,total})\,|_{\text{black, isothermal}}} \qquad \text{(A–2)}$$

Using ε_a and the sample temperature, an effective temperature for the cavity can be obtained:

$$\varepsilon_a\,(\text{normal, total}) = \frac{T_{bb}^4}{T_{\text{sample}}^4} \qquad \text{(A–3)}$$

This temperature, T_{cavity}, is a fourth power average of the cavity surface temperatures with weighting which varies with solid angle subtended by the folding mirror of the

apparatus. The Planck function can then be used with this temperature to estimate the cavity's shortcomings on a spectral basis. The derivative of the Planck function (eqn 2-36) with respect to temperature is:

$$\frac{\partial i_\lambda}{\partial T} = \frac{2C_1C_2\exp(C_2/\lambda T)}{\lambda^6 T^2 [\exp(C_2/\lambda T) - 1]^2} \qquad \text{(A–4)}$$

For a given (small) temperature difference between two blackbodies, the temperature difference multiplied by the above quantity estimates the change in spectral intensity:

$$\frac{i-i_o}{i_o} = \frac{C_2 \exp[C_2/\lambda T]}{\lambda T^2 (\exp[C_2/\lambda T] - 1)} \Delta T \qquad \text{(A–5)}$$

Figure A-5 shows the variation of fractional change in intensity with wavelength for a temperature of 1400 K and six values of ΔT. For a 5.6 K temperature difference between the sample and the cavity then, the resulting error in a measurement of normal spectral emissivity varies from 9.1% at 0.45 μm to 4.1% at 1 μm to 0.65% at 9.5 μm. For a lower sample temperature (Fig. A-6), such as encountered with molten aluminum here, the variation in error with wavelength is similar. With a sample temperature of 900 K (aluminum melts at 933 K) a 5.6 K temperature difference yields a 22% error at 0.45 μm and a 1.3% error at 9 μm. At lower temperatures, the spectral intensity is lower and the same temperature difference is a greater fraction of the sample temperature.

The estimated errors for other crucible conditions (such as different thermal conductivity) are given in Table A-1. The principle inputs to the analysis were varied over a reasonable range of uncertainty and operating conditions. The largest temperature difference between the sample and the cavity was 9.1 K and occurred for the cavity

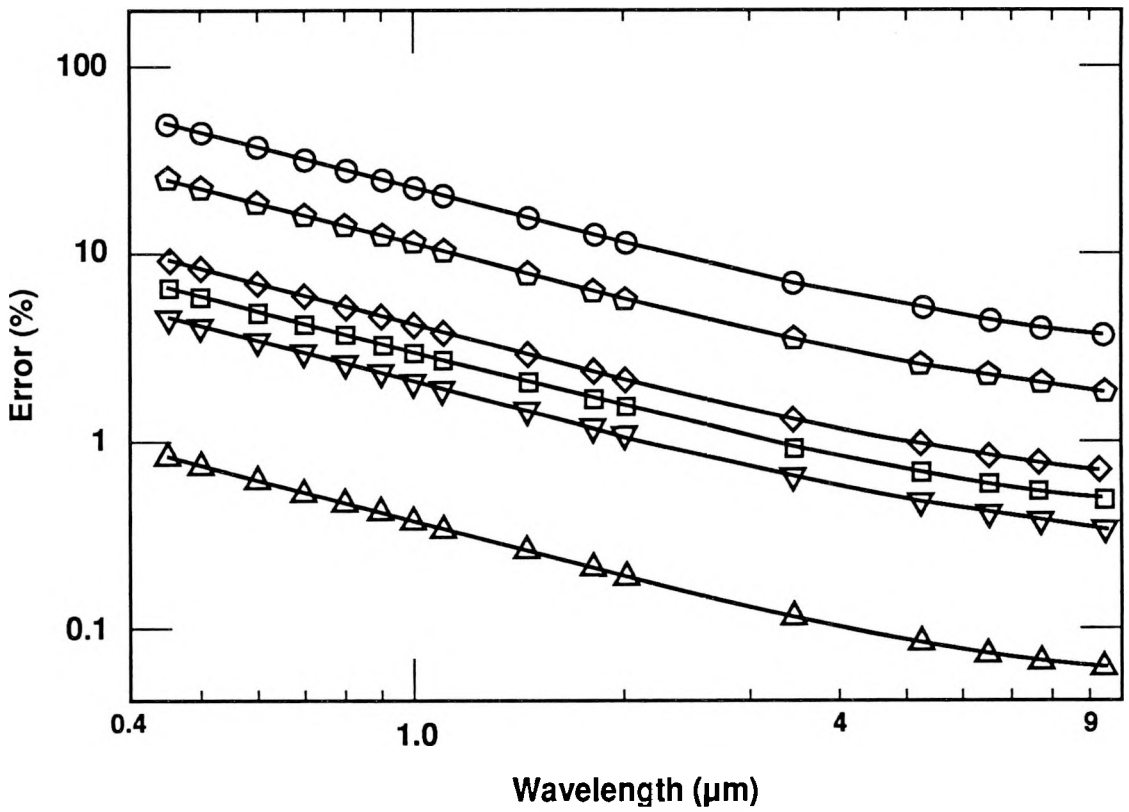

Figure A-5. Estimated error in normal spectral emissivity due to thermal effects for a sample temperature of 1400 K.

surface emissivity (total and hemispherical) set to 0.75. Such a low value for this emissivity could occur if the sample remained at temperature for several days, allowing a substantial portion of the aquadag coating to evaporate from the cavity walls. The blackbody was periodically repainted after extended periods at temperature to prevent this.

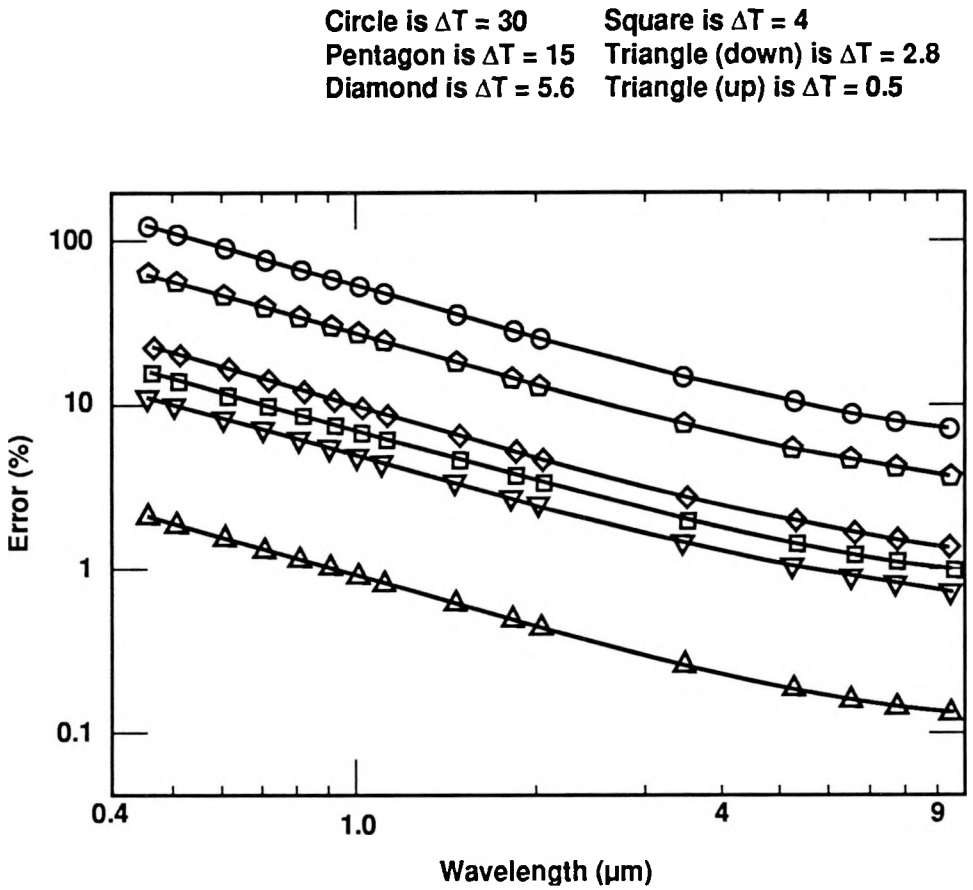

Figure A-6. Estimated error in normal spectral emissivity due to thermal effects for a sample temperature of 900 K.

The calculations reported in Table A-1 show that the apparent emissivity varies moderately over the range of possible operating conditions in physically reasonable ways. The temperature drop from sample to cavity increases as thermal conductivity decreases because the cavity becomes less well connected thermally to the heat source. As cavity wall emissivity drops so does the cavity's output: higher surface emissivities produce better cavities. As the total hemispherical emissivity of the crucible sides, top and bottom declines, less heat is supplied to the crucible to maintain it at a given temperature so that heat fluxes are reduced and therefore temperature gradients in the crucible are reduced. Smaller temperature gradients in the crucible result in higher apparent emissivity for the cavity. The results summarized in table A-1 and calculations of fractional change in intensity with wavelength were combined to produce Fig. 8-15.

Table A-1. Finite element calculations of heat transfer in the crucible

Case number (–)	Case designation (–)	Thermal conductivity (w/cm K)	Crucible total hemispherical emissivity (–)	Total hemispherical emissivity of cavity walls (–)	Heater temperature (K)	Cavity total normal apparent emissivity (–)	Effective sample to cavity temperature drop based on cavity total normal quality (K)
1	ff	0.84	0.17	0.85	1400	0.984	5.6
2	hh	0.67	0.17	0.85	1400	0.983	6.0
3	ii	1.01	0.17	0.85	1400	0.985	5.3
4	jj	0.84	0.17	0.75	1400	0.974	9.1
5	kk	0.84	0.17	0.95	1400	0.992	2.8
6	ll	0.84	0.27	0.85	1400	0.983	6.0
7	nn	0.84	0.07	0.85	1400	0.986	4.9
8	uu	0.84	0.17	0.85	900	0.988	2.8
9	150	0.84	0.17	0.85	1150	0.986	4.9

Appendix B. Some transmissive and chromatic properties of calcium fluoride

The transmissive characteristics of calcium fluoride in both the ultraviolet and the infrared make it a common optical material. These wide transmissive characteristics, shown in Fig. B-1, were ideally suited to the present study. However, the variation in the index of refraction over this range complicates its use. Qualitatively, this variation, shown in Fig. B-2, is similar to many other glasses, including those commonly used in infrared applications. A material with less variation in index of refraction in the infrared would display reduced chromatic effects here (vignetting and loss of signal described in chapter 8 and 9) but is not presently available.

Chromatic effects can be estimated using the lensmaker's equation:

$$\frac{1}{f(\lambda)} = (n(\lambda) - 1)\left(\frac{1}{r''} - \frac{1}{r'}\right) \qquad \text{(C–1)}$$

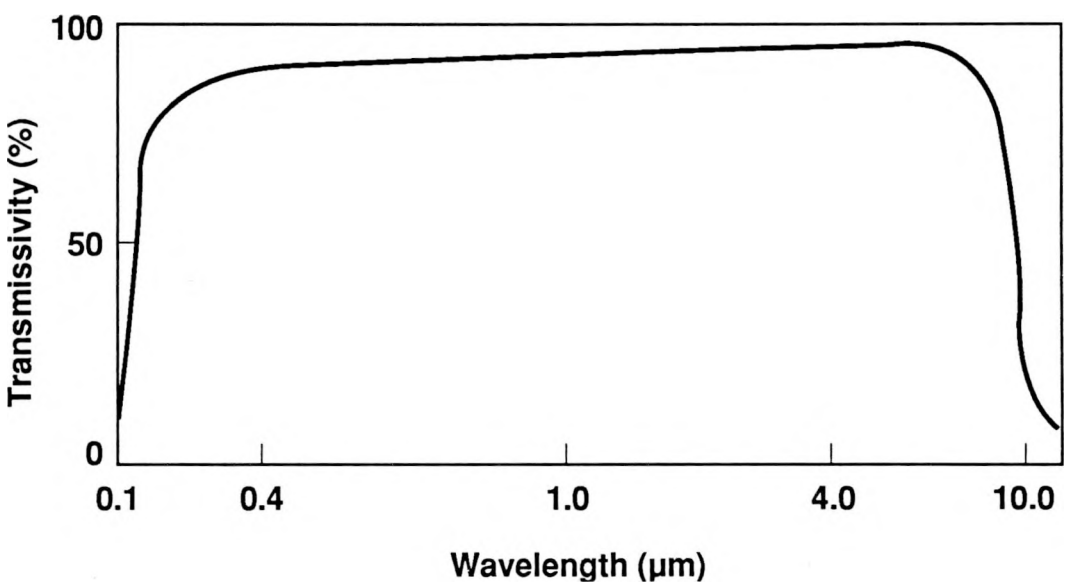

Figure B-1. The transmissivity of calcium fluoride (thickness=4mm).

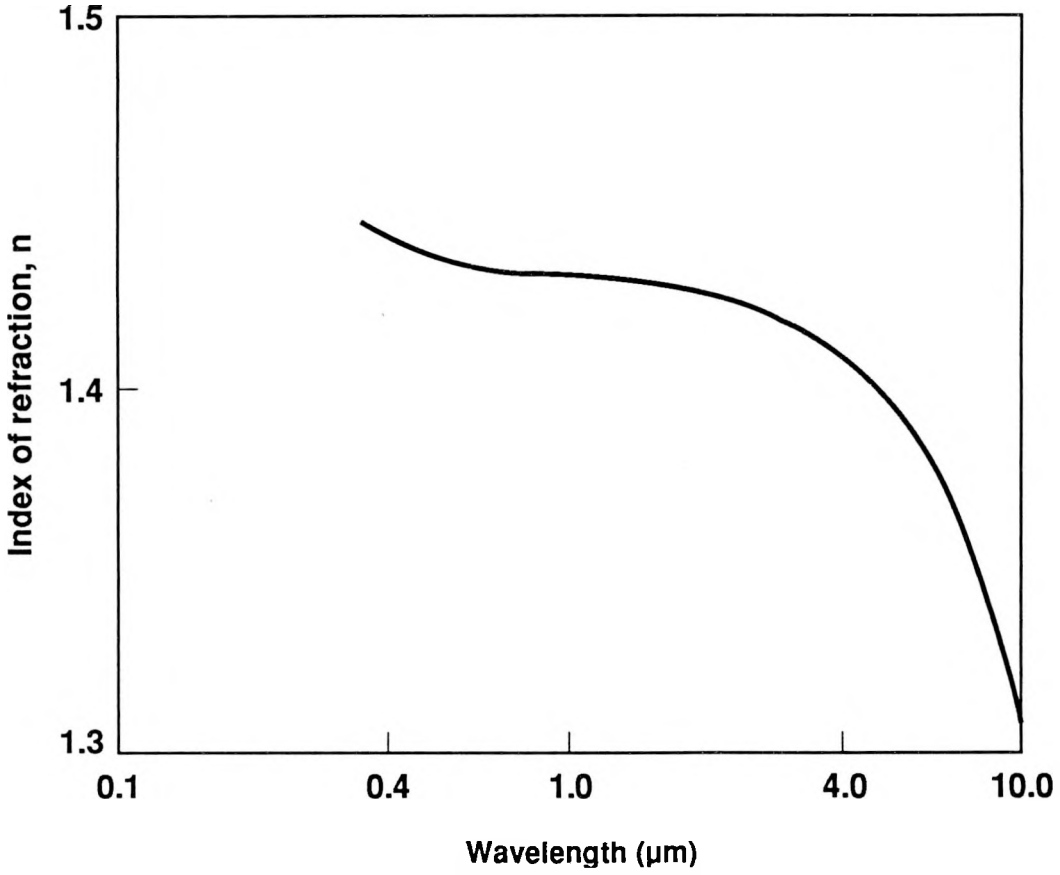

Figure B-2. The index of refraction of calcium fluoride as a function of wavelength

The focal length is f, n is the index of refraction of the lens material and r' and r'' are the radii of curvature of the two sides of the lens. The fractional change in focal length with wavelength for a fixed lens is given by:

$$\Delta f(\lambda) = \frac{1/(n(\lambda)-1)}{1/(n_d-1)} \qquad \text{(C–2)}$$

where n_d is the index of refraction for the design wavelength, in this case 5 μm. This quantity is shown in Fig. B-3 as a function of wavelength in the visible and infrared (to 10 μm). The rapid change in focal length beyond 6 μm accounts, in part, for the decline in precision in the infrared ellipsometry at the longer wavelengths. The ellipsometry

system's optics are aligned in the visible with each aperture slightly overfilled. The variation in focal length with wavelength causes each aperture to be more overfilled than

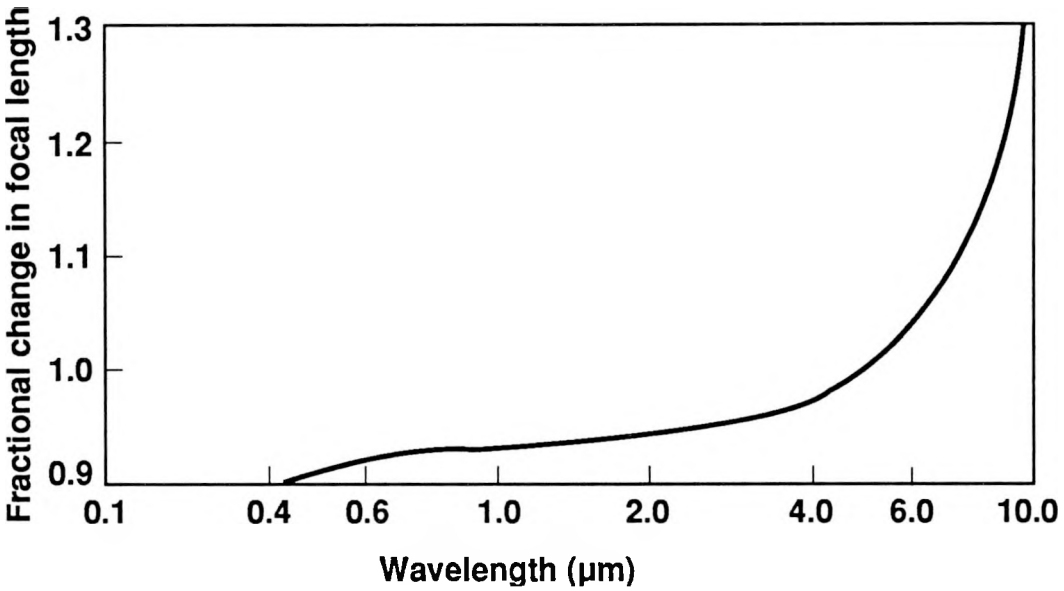

Figure B-3. The fractional change in focal length of a calcium fluoride lens as a function of wavelength

it had been in the visible. Thus, for wavelengths greater than 6 μm, signal strength declines and with it signal to noise ratio. Adjustment of the lens positions for each new wavelength would have been too tedious. Reflective optics avoid chromatic aberration but would have necessitated the use of corrections to every measured Ψ and Δ parameter due to the polarization produced by each of the oblique reflections at the mirrors.

References

1. Y.S. Touloukian and D.P. DeWitt, Thermal Radiative Properties, volume 7 of Thermophysical Properties of Matter, IFI/Plenum, New York (1970).
2. J.N. Hodgson, "The Optical Properties of Liquid Metals," Chapter 7, Liquid Metals, Sylvan Z. Beer, Editor, Marcel Dekker, Inc., New York (1972).
3. D.Y. Smith and B. Segall, "Intraband and Interband Processes in the Infrared Spectrum of Metallic Aluminum," Physical Review B, **34**, 5191 (1986).
4. J.C. Miller, "The Optical Properties of Liquid Metals at High Temperature," Phil. Mag., **20,** 1115 (1969).
5. N.R. Comins, "The Optical Properties of Liquid Metals," Phil. Mag., **25**, 817 (1972).
6. J.D. Jackson, Classical Electrodynamics, 2nd ed., John Wiley and Sons, New York (1975).
7. S. Ramo, J.R. Whinnery and T. Van Duzer, Fields and Waves in Communication Electronics, 2nd ed., John Wiley and Sons, New York (1984).
8. C. F. Bohren and D. R. Huffman, Absorption and Scattering of Light by Small Particles, Wiley-Interscience, New York (1983).
9. R. Siegel and J.R. Howell, Thermal Radiation Heat Transfer, 2nd ed., McGraw Hill, New York (1981).
10. D. Clarke and J.F. Grainger, Polarized Light and Optical Measurement, Pergammon Press, Oxford (1971).
11. D. Halliday and R. Resnick, Fundamentals of Physics, John Wiley and Sons, New York (1970).
12. J.H. Weaver, C. Krafka, D.W. Lynch and E.E. Koch, "Optical Properties of Metals," Physics Data, Fach-Informations-Zentrum, Karlsruhe (1981).

13. S. S. Mitra, "Optical Properties of Nonmetallic Solids for Photon Energies below the Fundamental Band Gap," Chapter 11, Handbook of Optical Constants of Solids, E.D. Palik, Editor, Academic Press, Inc., New York (1985).

14. R.W. Ditchburn, Light, 2nd ed., Interscience Publishers, London, (1963).

15. P. Drude, "The Optical Constants of Metals," Annals of Physics and Chemistry, **39**, 481, (1890).

16. E. Hagen and H. Rubens, "Reflection and Emission of Metals," Annals of Physics, **11**, 873, (1903).

17. F.A. Jenkins and H.E. White, Fundamentals of Optics, 4th ed., McGraw Hill, New York (1965).

18. K.E. Torrance and E.M. Sparrow, "Theory for Off-Specular Reflection from Roughened Surfaces," J. Opt.Soc.Am., **57**, 1105, (1967).

19. T. F. Smith and R.G. Hering, "Comparison of Bidirectional Measurements and Model for Rough Metallic Surfaces," Fifth Symposium on Thermophysical Properties, ASME, Boston, (1970).

20. R.C. Birkebak and E.R.G. Eckert, "Effects of Roughness of Metal Surfaces on Angular Distribution of Monochromatic Reflected Radiation," Transactions of the ASME, paper no. 64-HT-26, (1964).

21. H.E. Bennett and J.O. Porteus, "Relation Between Surface Roughness and Specular Reflectance at Normal Incidence," J. Opt. Soc. Am., **51**, 123, (1961).

22. R.H. Bube, Electronic Properties of Crystalline Solids, Academic Press, New York (1974).

23. N.W. Ashcroft and N.D. Mermin, Solid State Physics, Saunders College, Philadelphia (1976).

24. C. Kittel, Introduction to Solid State Physics, John Wiley and Sons, New York, (1986).

25. E. M. Sparrow and R. D. Cess, Radiation Heat Transfer, Augmented edition, McGraw-Hill Book Co., New York (1978).

26. M. Planck, "Distribution of Energy in the Spectrum," Annals of Physics, **4**,No. 3, 553, (1901).

27. T. S. Moss, Optical Properties of Semi-Conductors, Butterworths, London (1961).

28. H. R. Phillip, "Optical Properties of Silicon Nitride," J. Electrochem. Soc., **120**, 295 (1973).

29. R. L. Sproull, Modern Physics, Second Edition, John Wiley and Sons, Inc.,New York (1963).

30. L. G. Schulz, "The experimental study of the optical properties of metals and the relation of the results to the Drude free electron theory," Advances in Physics, **6**,102 (1957)

31. F. Wooten, Optical Properties of Solids, Academic Press, New York (1972).

32. R. H. Bube, Electrons in Solids, Academic Press, New York (1981).

33. C. Kittel, Elementary Solid State Physics, John Wiley and Sons, New York (1962).

34. D. W. Lynch and W. R. Hunter, "Comments on the Optical Constants of Metals and an Introduction to the Data for Several Metals," Part II subpart 1, Handbook of Optical Constants of Solids, E. D. Palik, Editor, Academic Press, New York (1985).

35. T. L. Loucks, "Fermi Surfaces of Cr, Mo, and W by the Augmented-Plane wave Method," Phys. Rev., **139**, No. 4a, 1181 (1965).

36. M. M. Kirillova, L. V. Nomerovannaya, and M. M. Noskov, "Optical Properties of Molybdenum Single Crystals," Soviet Physics JETP, **33**, 1210 (1971).

37. J. C. Slater, Insulators, Semiconductors and Metals, McGraw-Hill Book Co., New York (1967).

38. N. F. Mott and H. Jones, The Theory of the Properties of Metals and Alloys, Dover, New York (1936).

39. W. J. Parker and G. L. Abbott, "Theoretical and Experimental Studies of the Total Emittance of Metals," Symposium on Thermal Radiation of Solids (S. Katzoff, Editor), NASA SP-55, 11 (1965).

40. Y. S. Touloukian, Thermophysical Properties of High Temperature Solid Materials, Volume 1: Elements, Macmillan, New York (1967).

41. R. W. Seward, NBS Standard Reference Materials Catalog 1988-89, U.S. Government Printing Office, Washington (1988).

42. R.V. Dunkle, "Spectral Reflectance Measurements," Surface Effects on Spacecraft Materials, F.J. Clauss, Editor, Wiley and Sons, (1960).

43. S.T. Dunn, J.C. Richmond and J.F. Parmer, "Survey of Infrared Techniques and Computational Methods in Radiant Heat Transfer," J. Spacecraft and Rockets, **3**, 961 (1966).

44. P. Fowler, "Far Infrared Absorptance of Gold," AD 418 456, (1960).

45. D.M. Gates, C.C. Shaw and D. Beaumont, "Infrared Reflectance of Evaporated Metal Films," J. Opt. Soc. Am., **48** (2), 88 (1958).

46. H.E. Bennett and W.F. Koehler, "Precision Measurement of Absolute Specular Reflectance with Minimized Systematic Errors," J. Opt. Soc. Am., **50**, 1 (1960).

47. J. Strong, Procedures in Experimental Physics, Prentice Hall, New York (1938).

48. J.J. Hsia and J.C. Richmond, "Bidirectional Reflectometry Part I," J. Res. Nat. Bur. Std., **80A**, 189 (1976).

49. S.F. Johnston and B.P. Claxman, "Reflectivity Measurements on Hot Reactive Liquids Using a FIR Laser," Applied Optics, **19**, 3118 (1980).

50. W.M. Brandenberg, "The Reflectivity of Solids at Grazing Angles," NASA SP-3, 75 (1962).

51. S.T. Dunn, J.C. Richmond and J.A. Wiebelt, "Ellipsoidal Mirror Reflectometer," J. Res. Nat. Bur. Std., **70C** (2), 75 (1966).

52. R.T. Neher and D.K. Edwards, "Far Infrared Reflectometer for Imperfectly Diffuse Specimens," Appl. Opt., **4**, 775 (1965).

53. W.L. Derksen, T.I. Monahan and A.J. Lawes, "Automatic Recording Reflectometer for Measuring Diffuse Reflectance in the Visible and Infrared Regions," J. Opt. Soc. Am., **47**, 995 (1957).

54. W.W. Coblentz, "The Diffuse Reflecting Power of Various Substances," Bull. Nat. Bur. Std., **9**, 283 (1913).

55. J.E. Janssen and R.H. Torborg, "Measurement of Spectral Reflectance Using an Integrating Hemisphere," Measurement of Thermal Radiation Properties of Solids (J.C. Richmond, Editor), NASA SP-31, 169 (1963).

56. B.P. Kozyrev and O.E. Vershinin, "Determination of Spectral Coefficients of Diffuse Reflection of Infrared Radiation from Blackened Surfaces," Optics and Spectroscopy, **6**, 345 (1959).

57. J.U. White, "New Method for Measuring Diffuse Reflectance in the Infrared," J. Opt. Soc. Am., **54**, 1332 (1964).

58. D.G. Goebel, B.P. Caldwell and H.K. Hammond, III, "Use of an Auxiliary Sphere with a Spectroreflectometer to Obtain Absolute Reflectance," J. Opt. Soc. Am., **56**, 783 (1966).

59. G.J. Kneissl, J.C. Richmond and J.A. Wiebelt, "A Laser Source Integrating Sphere for the Measurement of Directional Hemispherical Reflectance at High Temperature," Progress in Aeronautics and Astronautics, **20**, AIAA (G.B. Heller, Editor), Academic Press, 177 (1967).

60. D.K. Edwards, J.T. Gier, E.K. Nelson and R.D. Roddick, "Integrating Sphere for Imperfectly Diffuse Samples," Appl. Opt., **51**, 1279 (1961).

61. B.A. McCullough, B.E. Woods and A.M. Smith, "A Vacuum Integrating Sphere for in-situ Reflectance Measurements at 77 °K from 0.5 to 10.0 μ," Progress in Astronautics and Aeronautics, **20**, AIAA (G.B. Heller, Editor), 137 (1967).

62. G.J. Kneissl and J.C. Richmond, "A Laser Source Integrating Sphere Reflectometer," Nat. Bur. Std. Tech. Note 439 (1968).

63. J.T. Gier, R.V. Dunkle and J.T. Bevans, "Measurement of Absolute Spectral Reflectivity from 1.0 to 15 Microns," J. Opt. Soc. Am., **44**, 558 (1954).

64. R.J. Hembach, L. Hemmerdinger and A.J. Katz, "Heated Cavity Reflectometer Modifications," Measurement of Thermal Radiation Properties of Solids (J.C. Richmond, Editor), NASA SP-31, 153 (1963).

65. R.V. Dunkle, D.K. Edwards, J.T. Gier, K.E. Nelson and R.D. Roddick, "Heated Cavity Reflectometer for Angular Reflectance Measurement," Progress in International Research on Thermodynamic and Transport Properties, ASME, 100 (1962).

66. W.M. Brandenberg and J.T. Neu, "Unidirectional Reflectance of Imperfectly Diffuse Surfaces," J. Opt. Soc. Am., **56** (1), 97 (1966).

67. E.R. Miller and R.S. VunKannon, "Development and Use of a Bidirectional Spectroreflectometer," Progress in Aeronautics and Astronautics, **20** (G.B. Heller, Editor), Academic Press, 219 (1967).

68. G. Pfestorf, "Optical Constants of Metals in the Visible and Ultra-Violet Regions of the Spectrum," Ann. d. Physik, **81**, 906 (1926).

69. C. Boeckner, "A Method of Obtaining the Optical Constants of Metallically Reflecting Substances in the Infrared,"J. Opt. Soc. Am., **19**, 7 (1929).

70. M.R. Querry, "Direct Solution of the Generalized Fresnel Reflectance Equations," J. Opt. Soc. Am., **59**, 876 (1969).

71. R. Tousey, "On Calculating the Optical Constants from Reflection Coefficients," J. Opt. Soc. Am., **29,** 235 (1939).

72. R.E. Lindquist and A.W. Ewald, "Optical Constants from Reflectance Ratios by a Geometrical Construction," J. Opt. Soc. Am., **53,** 247 (1963).

73. D. W. Juenker, "Digital Evaluation of the Complex Index of Refraction from Reflectance Data," J. Opt. Soc. Am., **55**, 295 (1965).

74. D.G. Avery, "An Improved Method for Measurements of Optical Constants by Reflection," Proc. Phys. Soc. B, **65**, 425 (1952).

75. S.P.F. Humphreys-Owen, "Comparison of Reflection Methods for Measuring Optical Constants without Polarimetric Analysis, and Proposal for New Methods," Proceedings of the Physical Society, **77**, 949 (1961).

76. W.R. Hunter, "Measurement of Optical Constants in the Vacuum Ultraviolet Spectral Region," Chapter 4, Handbook of Optical Constants of Solids, E. D. Palik, Editor, Academic Press, New York (1985).

77. I. Simon, "Spectroscopy in Infrared by Reflection and its Use for Highly Absorbing Surfaces," J. Opt. Soc. Am., **41**, 336 (1951).

78. T. Sasaki and K. Ishiguro, "A Spectrophotometer for Determining Optical Constants in the Vacuum Ultraviolet Region," Japanese Journal of Applied Physics, **2**, 289 (1963).

79. L.N. Aksyutov and A.K. Pavlyukov, "Some Distinctive Features of the Temperature Dependence of the Optical Properties of Tungsten in the IR Spectral Region," Journal of Applied Spectroscopy, **32**, 813 (1980).

80. A. Y-C. Yu and W.E. Spicer, "Optical Properties of Platinum," Physical Review, **17**, 834 (1968).

81. P.O. Nilsson and G. Forsell, "Optical Properties of Calcium," Physical Review B, **16**, 3352 (1977).

82. J.H. Weaver, D.W. Lynch and C.G. Olson, "Optical Properties of V, Ta and Mo from 0.1 to 35 ev," Physical Review B, **10**, 501 (1974).

83. V.A. Petrov, V. Ya. Chekhovskoi and A.E. Sheinblin, "Experimental Determination of the Integral Emissivity of Metals and Alloys at High Temperatures," High Temperature, **1**, 19 (1963).

84. J.R. Grammer and E.R. Streed, "Measurement of Normal and Directional High-Temperature Total and Spectral Emittance," Measurement of Thermal Radiation Properties of Solids (J.C. Richmond, Editor), NASA SP-31, 489 (1962).

85. T.R. Riethof and V.J. DeSantis, "Techniques of Measuring Normal Spectral Emissivity of Conductive Refractory Compounds at High Temperatures," Measurement of Thermal Radiation Properties of Solids (J.C. Richmond, Editor), NASA SP-31, 565 (1963).

86. V.E. Peletskii, "Thermophysical Properties of Iron Specimens of Different Purities at High Temperatures," High Temperatures-High Pressures, **21**, 377 (1989).

87. S.X. Cheng, "An Accurate Transient Calorimeter for Measuring the Total Hemispherical Emissivity of Metals and Alloys," High Temperatures-High Pressures, **16**, 459 (1984).

88. R.L. Rudkin, W.J. Parker, R.J. Jenkins, "Measurements of the Thermal Properties of Metals at Elevated Temperature," Measurement of Thermal Radiation Properties of Solids (J.C. Richmond, Editor), NASA SP-31, 523 (1964).

89. A.G. Maki and E.K. Phyler, "Method of Measuring Emissivities of Metals in the Infrared," Journal of Research of the NBS, **66C**, 283 (1962).

90. P.E. Johnson, D.P. Dervitt and R.E. Taylor, "Method for Measuring High Temperature Spectral Emissivity of Non-Conducting Materials," AIAA Journal, **19,** 113 (1981).

91. J.C. Richmond, W.N. Harrison and F.J. Shorten, "An Approach to Thermal Emittance Standards," Measurement of Thermal Radiation Properties of Solids (J.C. Richmond, Editor), NASA SP-31, 403 (1963).

92. J.C. De Vos, "A New Determination of the Emissivity of Tungsten Ribbon," Physica **XX**, 690 (1954).

93. R.D. Larrabee, "Spectral Emissivity of Tungsten," J. Opt. Soc. Am., **49,** 619 (1959).

94. L.N. Latyev, V. Ya Chekhovskoi, and E.N. Shestakov, "Monochromatic Emissivity of Tungsten in the Temperature Range 1200–2600°K and in the Wavelength Range 0.4–4 μm," High Temperatures-High Pressures, **2**, 175 (1970).

95. L.N. Latyev, V. Ya Chekhovskoi, and E.N. Shestakov, "Experimental Determination of Emissive Power of Tungsten in the Visible Region of the Spectrum in the Temperature Range 1200- 2600 K," High Temperatures-High Pressures, **7**, 610 (1969).

96. A. Kinbara, "Variation of the Optical Properties of Iron at Transition Temperature," J. Phys. Soc. of Japan, **13**, 966 (1958).

97. W.S. Martin, E.M. Duchane, and H.H. Blau, "Measurement of Optical Constants at High Temperature," J. Opt. Soc. Am., **55**, 1623 (1965).

98. H.H. Blau, E. Chaffee, J.R. Jasperse, and W.S. Martin, "High Temperature Thermal Radiation Properties of Solid Materials," AFCRC-TN-60-165 (1960).

99. C. Tingwaldt, U. Schley, J. Verch, and S. Takata, "The Optical Constants of Tungsten and Hafnium at Glowing Heat," Optik, **22**, 48 (1965).

100. E.N. Shestakov, L.N. Latyev, V. Ya. Chekhovskoi, "Methods for Determining the Optical Constants of Metals and Alloys at High Temperatures," (Survey), High Temperature, **16**, 140 (1978).

101. E. N. Shestakov, L. N. Latyev and V. Ya. Chekhovskoi, "Optical properties of metals at high temperatures," High Temperature, **15**, 249 (1977).

102. S. Mattei, P. Mosclet, and P. Herve, "Study of Complex Refractive Indices of Gold and Copper Using Emissivity Measurements," Infrared Physics, **29,** 991 (1989).

103. M.C. Jones, D.C. Palmer and C.L. Tien, "Infrared Absorptivities of Transition Metals at Room and Liquid-Helium Temperatures," J. Opt. Soc. Am., **62**, 353 (1972).

104. J.H. Weaver, D.W. Lynch, C.G. Olson, "Optical Properties of Niobium from 0.1 to 36.4 eV," Physical Review B, **7**, 431 (1973).

105. W. Shurcliff, Polarized Light, Harvard University Press, Cambridge (1962).

106. J. M. Bennett and H. E. Bennett, Polarization, Chapter 10, Handbook of Optics, W. G. Driscoll, Editor, McGraw-Hill Inc., New York (1978).

107. J. R. Beattie, "Optical Constants of Metals in the Infra-Red—Experimental Methods," Phil. Mag., **46**, 235 (1955).

108. J. R. Beattie and G. K. T. Conn, "Optical Constants of Metals in the Infra-Red—Principles of Measurement," Phil. Mag., **46**, 222 (1955).

109. J.N. Hodgson, "The Infrared Properties of Some Metallic Films," Proc. Phys. Soc., **9** (B), 593 (1955).

110. E.T. Arakawa, T. Inagaki and M.W. Williams, "Optical Properties of Metals by Spectroscopic Ellipsometry," Surface Science, **96**, 248 (1980).

111. T. Inagaki, E.T. Arakawa, R.D. Birkhoff and M.W. Williams, "Optical Properties of Liquid Na Between 0.6 and 3.8 eV," Physical Review B, **13**, 5610 (1976).

112. P.S. Tuminello, E.T. Arakawa, T. Inagaki and J.E. Parks II, "Optical Reflectance of Liquid Mercury," Physical Review B, **40**, 17 (1989).

113. K.M. Shvarev, B.A. Baum, and P.V. Gel'd, "Optical Properties of Liquid Silicon," Sov. Phys. Solid State, **16**, 2111 (1975).

114. T. Inagaki, E.T. Arakawa and M.W. Williams, "Optical Properties of Liquid Mercury," Physical Review B, **23**, 5246 (1981).

115. H.G. Liljenvall, A.G. Mathewson and H.P. Myers, "The Optical Properties of Lead in the Energy Range 0.6–6 eV," Phil. Mag., **22**, 243 (1970).

116. A. Faldt and P.O. Nilsson, "Optical Properties of Thorium in the Range 0.5–25 eV," Physical Review B, **22**, 1740 (1980).

117. M.M. Kirillova, L.V. Nomerovannaya and M.M. Noskov, "Optical Interband Absorption in Platinum," Fiz. Metal. Metalloved., **34**, 60 (1972).

118. G. K. T. Conn and G. K. Eaton, "On the use of a rotating polarizer to measure optical constants in the infrared," J. Opt. Soc. Am., **44**, 484 (1954).

119. D.J. Price, "Note on the calculation of Optical Constants," Proc. Phys. Soc., **58**, 704, (1948).

120. A.V. Sokolov, Optical Properties of Metals, American Elsevier Publishing Company, New York, (1967).

121. W. L. Wolfe and G. J. Zissis, The Infrared Handbook, Office of Naval Research, Department of the Navy, Arlington (1985).

122. H.G. Liljenvall and A.G. Mathewson, "Two Alignment methods of the Polarizer and Analyzer in an Ellipsometer," Appl. Optics, **9**, 1489 (1970).

123. J.H.P. Castelijns, "Improved Method for Azimuthal Alignment in Ellipsometry," Appl. Optics, **14**, 806 (1975).

124. C. Wijers, "A One-Wavelength, in situ Alignment Method for Rotating Analyser Ellipsometers," Applied Physics B, **27**, 5 (1982).

125. R.M.A. Azzam and N.M. Bashara, Ellipsometry and Polarized Light, North Holland Publishing Co., Amsterdam (1977).

126. M. Born and E. Wolf, Principles of Optics, 6th edition, Pergammon Press, Oxford, (1980).

127. R.C. Jones, "New Calculus for the Treatment of Optical Systems, VIII Electromagnetic Theory," J. Opt. Soc. Am., **46**, 126 (1956).

128. M.J. Walker, "Matrix Calculus and the Stokes Parameters of Polarized Radiation," American Journal of Physics, **22**, 170 (1954).

129. D.W. Weeks. "A study of Sixteen Coherency Matrices,"J. Math. and Physics, **18**, 380 (1957).

130. G. Hass and L. Hadley, Optical Properties of Metals, Section 6G, American Institute of Physics Handbook, 3rd Edition, (E.D. Graig, Coordinating Editor), McGraw-Hill, New York (1972).

131. M.A. Ordal, R.J. Bell, R.W. Alexander, Jr., L.A. Newquist and M.R. Querry, "Optical properties of Al, Fe, Ti, Ta, W, and Mo at submillimeter wavelengths," Appl. Optics, **27**, 1203 (1988).

132. M.A. Ordal, R.J. Bell, R.W. Alexander, Jr., L.L. Long and M.R. Querry, "Optical Properties of Fourteen Metals in the Infrared and Far Infrared: Al, Co, Cu, Au, Fe, Pb, Mo, Ni, Pd, Pt, Ag, Ti V, and W," Appl. Optics, **24**, 4493 (1985).

133. E.N. Shestakov, L.N. Latyev and V. Ya. Chekhovskoi, "The Optical Constants of Metals and Alloys at High Temperatures (Review)," in: Thermophysical Properties of Materials at High Temperatures (in Russian), High-Temp. Inst., Academy of Sciences of the USSR, Moscow, 45 (1978).

134. L. N. Latyev, V. Ya. Chekhovskoi and E. N. Shestakov, "Tungsten as a standard material for monochromatic emissivity," High Temperatures-High Pressures, **4**, 679 (1972).

135. J.C. De Vos, "Evaluation of the Quality of a Blackbody," Physica **XX**, 669 (1954).

136. L.N. Aksyutov, "Normal Spectral Emissivity of Gold, Platinum, and Tungsten," Journal of Engineering Physics, **27**, 913 (1976).

137. L.V. Nomerovannaya, M.M. Kirillova and M.M. Noskov, "Optical Properties of Tungsten Monocrystals," Soviet Physics Jetp, **33**, 405 (1971).

138. S. Roberts, "Optical Properties of Nickel and Tungsten and Their Interpretation According to Drude's Formula," Physical Review, **114**, 104 (1955).

139. G.B. Blanchet, P.J. Estrup and P.J. Stiles, "A Study of the H/W(110) Absorption System by Surface Reflectance Spectroscopy," Physical Review B, **23**, 3655 (1981).

140. P. Pigeat, N. Pacia and B. Weber, "Experimental and Theoretical Studies of the Evolution of Normal Spectral Emissivity During Successive Steps of Tungsten Oxidation," Applied Surface Science, **27**, 214 (1986).

141. M.L. Ramalingam and D.L. Jacobson, "Normal Spectral Emittance Data for Thoriated Tungsten, Rhenium Alloys," International Journal of Thermophysics, **2**, 94 (1988).

142. A. Cezairliyan and A.P. Miller, "Radiance Temperature (at 653 nm) of Tungsten at its Melting Point," International Journal of Thermophysics, **3**, 89 (1982).

143. J. Hiernaut, F. Sakuma and C. Ronchi, "Determination of the Melting Point and the Emissivity of Refractory Metals with a Six-Wavelength Pyrometer," High Temperatures-High Pressures, **21**, 139 (1989).

144. J.-P. Hiernaut, R. Beukers, W. Heinz, R. Selfslag, M. Hoch and R. W. Ohse, "Submillisecond six-wavelength pyrometer for high-temperature measurements in the range 2000 to 5000 K," High Temp. - High Press., **18**, 617 (1986).

145. E. Arpaci, G. Betz, M.G. Frohberg, "Determination of the Spectral Emissivities of Niobium, Molybdenum, Tantalum, and Tungsten at their Melting Points," High Temperatures–High Pressures, **17**, 519 (1985).

146. T.H. Allen, "Study of Al with a combined Auger Electron Spectrometer—Ellipsometer System," J. Vac. Sci. Technol., **13**, 112 (1976).

147. H. Allen and J. Sunderland, "Oxide Thickness Measurements by Infrared Ellipsometry," Thin Solid Films, **45**, 169 (1977).

148. J.H. Halford, F.K. Chin and J.E. Norman, "Effects of Vacuum Deposition Conditions on Ellipsometric Parameters, Optical Constants, and Reflectance of Ultrapure Aluminum Films," J. Opt. Soc. Am., **63**, 786 (1973).

149. M.N. Churaeva and Z.M. Zorin, "A Study of the Aluminum Surface and Determination of Its Optical Constants by Ellipsometry," Phys. Chem. Mech. Surfaces, **4** (1), 3349 (1987).

150. G. Gergely, Z. Bodo and P. Croce, "Determination of the Optical Constants of Metals and Semiconductors by Combining Ellipsometry with Electron Spectroscopy Microscopy and X-ray Specular Reflection Analysis," Surface Science, **200**, 527 (1988).

151. D. L. Decker and V. A. Hodgkin, "Wavelength and Temperature Dependence of the Absolute Reflectance of Metals at Visible and Infrared Wavelengths," Laser Induced Damage in Optical Materials: 1980, Proceedings of a Symposium (NBS-SP-620), 190 (1981).

152. H. Masuda and M. Higano, "Transient Calorimetric Technique for Measuring Total Hemispherical Emissivities of Metals with Rigorous Evaluation of Heat Loss Through Thermocouple Leads," J. Opt. Soc. Am. A, **2**, 1877 (1985).

153. J. Grimblot and J.M. Eldridge, "Interaction of Al Films with O_2 at Low Pressures," Journal of the Electrochemical Society: Solid State Science and Technology, **29**, 2366 (1982).

154. A.M. Bradshaw, P. Hofmann and W. Wyrobisch, "The Interaction of Oxygen with Aluminium (111)," Surface Science, **68**, 269 (1977).

155. B.E. Hayden, W. Wyrobisch, W. Oppermann, S. Hachicha, P. Hofmann and A.M. Bradshaw, "The Interaction of Oxygen with Aluminium: Mainly Ellipsometric Aspects," Surface Science, **109**, 207 (1981).

156. M. Bruckner, J.H. Schafer and J. Uhlenbusch, "Ellipsometric Measurement of the Optical Constants of Solid and Molten Aluminum and Copper at $\lambda = 10.6\ \mu m$," Journal of Applied Physics, **66**, 1326 (1989).

157. H.G. Dreehsen, C. Hartwich, J.H. Schaefer and J. Uhlenbusch, "Measurement of the Optical Constants of Al Above the Melting Point at $\lambda = 10.6$ μm," J. Appl. Phys., **56**, 238 (1984).

158. V. I. Konov and V. N. Tokarev, "Temperature dependence of the absorptivity of aluminum targets at the 10.6μ wavelength," Sov. J. Quantum Electron., **13**, 177 (1983).

159. J. H. Weaver, "Low-Energy Optical Absorption in α-U Metal," J. Opt. Soc. Am., **70**, 1030 (1980).

160. A. Faldt and P. O. Nilsson, "Optical Properties of Uranium in the Range 0.6–25 eV," J. Phys. F: Metal Phys., **10**, 2573 (1980).

161. G. K. Burgess and R. C. Waltenberg, "The emissivity of metals and oxides II Measurements with the micropyrometer," National Bureau of Standards Bulletin, **11**, 591 (1915).

162. A. W. Lemmon, "The reaction of steam with uranium and with various Uranium-Niobium-Zirconium alloys at high temperatures," Battelle Memorial Institute-**1192**, 1 (1957).

163. W. L. Hole and R. W. Wright, "Emissive and Thermionic Characteristics of Uranium," Phys. Rev., **56**, 785 (1939).

164. L. Baker, Jr., E. M. Mouradian, and J. D. Bingle, "Determinations of the Total Emissivity of Polished and Oxidized Uranium Surfaces," Nucl. Sci. Eng., **15**, 218 (1963).

165. E. G. Rauh, "Work Function, Ionization Potential, and Emissivity of Uranium," Argonne National Laboratory, Lemont, IL, **ANL-5534** (1956) .

166. D. Y. Smith, E. Shiles and M. Inokuti, "The Optical Properties of Metallic Aluminum," Part II subpart 1, Handbook of Optical Constants of Solids, E. D. Palik, Editor, Academic Press, New York (1985).

167. J.H. Weaver, "Optical Properties of Rh, Pd, Ir, and Pt," Physical Review B, **11**, 1416, (1975).

168. W.R. Hunter, "Errors in using the Reflectance vs. Angle of Incidence Method for Measuring Optical Constants,",J. Opt. Soc. Am., **55**, 1197 (1965).

169. W.R.Hunter, "Measurement of optical properties of materials in the vacuum ultraviolet spectral region,"Appl. Optics, **21**, 2103 (1982).

170. R.F. Miller, A.J. Taylor and L. S. Julien, "The optimum angle of incidence for determining optical constants from reflectance measurements," Journal of Physics D., **3**, 1957, (1970).

171. G.R. Field and E. Murphy, "Method of using the reflectance ratios of different angles of incidence for the determination of Optical constants," Appl. Optics, **10**, 1402 (1971).

172. R.H.W. Graves and A.P. Lenham, "Determination of the Optical Constants of Uniaxial or Isotropic Metals by Measurement of reflectance ratios," J. Opt. Soc. Am., **58**, 884, (1968).

173. E.N. Shestakov, L.N. Latyev and V. Ya. Chekhovskoi, "Experimental determination of the ratio of the polarized components of radiation flux of metals at high temperatures," High Temperature, **15**, 1189 (1977).

174. K. A Winer, "Initial Stages of Uranium Oxidation: A Surface Study," UCRL-53655, Lawrence Livermore National Laboratory, Livermore, California, (1985).

175. A. W. Czanderna, "Methods of Surface Analysis," Volume 1 of "Methods and Phenomena: Their Applications in Science and Technology," Elsevier Scientific Publishing Company, Amsterdam, (1975).

176. W. McLean II, "Lithium Surface Complexes," Ph. D. Thesis, Univ. of North Carolina, Chapel Hill, (1977).

177. D. E. Aspnes, personal communication.

178. R. G. Musket, W. McLean, C. A. Colmenares, D. M. Makowiecki, and W. J. Siekhaus, "Preparation of Atomically Clean Surfaces of Selected Elements: A Review," Applications of Surface Science **10**, 143 (1982).

179. M. Balooch, D. R. Olander, and W. J. Siekhaus, "Reaction of Water Vapor and Oxygen with Liquid Uranium," Oxidation of Metals, **28**, 195 (1987).

180. J. S. Huang, G. G. Gallegos, "Embrittlement by Liquid U in Some Group VB and VIB Metals and Alloys During Tensile Loading at 1473 K," UCRL-101141, Lawrence Livermore National Laboratory, Livermore, California, (1989).

181. Lord Rayleigh, "On The Theory of The Capillary Tube," Proceedings of the Royal Society, **XCII** A, 350 (1915).

182. J. Ebert, personal communication.

183. L. F. Mattheiss, "Fermi Surface in Tungsten," Physical Review, **139**, 1893 (1965).

184. M. M. Kirillova, L. V. Nomerovannaya and M. M. Noskov, "Interband optical absorption and the electronic structure of 5d metals," Sov. Phys. Solid State, **16**, 1425 (1975).

185. D. K. Edwards and N. Bayard de Volo, "Useful Approximations for the Spectral and Total Emissivity of Smooth Bare Metals," Advances in Thermophysical Properties at Extreme Temperatures and Pressures, ASME, New York (1965).

186. V. D. Dmitriev and G. K. Kholopov, "Radiant emissivity of tungsten in the infrared region of the spectrum," Journal of Applied Spectroscopy, **2**, 315 (1965).

187. B. T. Barnes, "Optical Constants of Incandescent Refractory Metals," J. Opt. Soc. Am., **56**, 1546 (1966).

188. T. J. Quinn, "The effect of thermal etching on the emissivity of tungsten," Brit. J. Appl. Phys., **16,** 973 (1965).

189. L. K. Thomas, "Thermal Radiation from Rough Tungsten Surfaces in Normal and Off-Normal Directions," J. Appl. Phys., **39**, 4681 (1968).

190. G. Busch, H.-J. Guntherodt and H. U. Kunzi, "Hall coefficient and electrical resistivity of liquid uranium," Physics Letters, **32A**, 376 (1970).

191. A. G. Mathewson and H. P. Myers, "Optical absorption in aluminum and the effect of temperature," J. Phys. F.: Metal Phys., **2**, 403 (1972).

192. H.-J. Guntherodt and H. U. Kunzi, "Hall-Koeffizient und elektrischer Widerstand flussiger Al-Ga-Legierungen," Phys. kondens. Materie, **10**, 285 (1969).

193. G. M. Kibler, T. F. Lyon, M. J. Linevsky and V. J. DeSantis in Thermophysical Properites of High Temperature Solid Materials, V. S. Touloukian, Editor, **1**, 1038, Macmillan, New York (1967).

194. R. L. Dreshfield and R. D. House, "Spectral Normal Emittance of Single Crystals," AIAA Journal, **4**, 371 (1966).

195. V. D. Dmitriev, Thesis, State Institute of Applied Optics, Kazan, USSR (1967).

196. T. R. Reithof, B. D. Acchione and E. R. Branyan, in Temperature: Its Measurement and Control in Science and Industry, C. M. Herzfeld, Editor, **3**, 515, Reinhold, New York (1962).

197. I. I. Kovalev and G. F. Muchnik, "Normal spectral emissive power of tungsten, niobium, molybdenum, and tantalum in the wavelength range $\lambda = 0.66–5.12$ μm and the temperature interval 1400–3000 K," High Temperature, **8**, 922 (1970).

Technical Information Department · Lawrence Livermore National Laboratory
University of California · Livermore, California 94551